Proliferation, differentiation, and glutamatergic synapses: Communication between neurons and oligodendrocyte precursor cells

Dissertation

zur Erlangung des Grades eines

Doktors der Naturwissenschaften

der Mathematisch-Naturwissenschaftlichen Fakultät

und

der Medizinischen Fakultät

der Eberhard-Karls-Universität Tübingen

vorgelegt

von

Bálint Nagy

aus Budapest, Hungary

November – 2018

Tag der mündlichen Prüfung: 03.07.2019

Dekan der Math.-Nat. Fakultät: Prof. Dr. W. Rosenstiel

Dekan der Medizinischen Fakultät: Prof. Dr. I. B. Autenrieth

1. Berichterstatter: Prof. Dr. / PD Dr. Maria Kukley

2. Berichterstatter: Prof. Dr. / PD Dr. Holger Lerche

Prüfungskommission: Prof. Dr. Marlies Knipper

Dr. Maria Kukley

Prof. Dr. Olga Garaschuk

Prof. Dr. Holger Lerche

Erklärung / Declaration:
Ich erkläre, dass ich die zur Promotion eingereichte Arbeit mit dem Titel:
"**Proliferation, differentiation, and glutamatergic synapses: Communication between neurons and oligodendrocyte precursor cells**"
selbständig verfasst, nur die angegebenen Quellen und Hilfsmittel benutzt und wörtlich oder inhaltlich übernommene Stellen als solche gekennzeichnet habe. Ich versichere an Eides statt, dass diese Angaben wahr sind und dass ich nichts verschwiegen habe. Mir ist bekannt, dass die falsche Abgabe einer Versicherung an Eides statt mit Freiheitsstrafe bis zu drei Jahren oder mit Geldstrafe bestraft wird.

I hereby declare that I have produced the work entitled
*"**Proliferation, differentiation, and glutamatergic synapses: Communication between neurons and oligodendrocyte precursor cells**"*
submitted for the award of a doctorate, on my own (without external help), have used only the sources and aids indicated and have marked passages included from other works, whether verbatim or in content, as such. I swear upon oath that these statements are true and that I have not concealed anything. I am aware that making a false declaration under oath is punishable by a term of imprisonment of up to three years or by a fine.

Tübingen, den 28.11.2018 ……
Datum / Date Unterschrift /Signature

Table of content

I. Abstract

The healthy physiological functioning of the mammalian central nervous system relies on the precise communication between many different cell types. The most general communication channel between neurons is the chemical synapse. Fascinatingly, oligodendrocyte precursor cells also receive synaptic input from glutamatergic neurons. Oligodendrocyte precursor cells are responsible for forming the myelin sheaths by differentiating into oligodendrocytes, and the myelination itself seems to be regulated by neuronal firing patterns. The differentiation and proliferation of oligodendrocyte precursor cells are influenced by transient changes of neuronal firing. Therefore the questions arise: Can oligodendrocyte precursor cells discriminate dissimilar patterns of neuronal firing? How exactly those different patterns would influence their proliferation and differentiation? How the physiological properties of synaptic signaling would influence the cellular behavior of oligodendrocyte precursors?

In my doctoral thesis I analyzed in details the synaptic responses of oligodendrocyte precursors to different, repetitive axonal stimulation patterns; and found that the postsynaptic responses are very diverse upon the various patterns of axonal activation. I showed *in vivo* that these distinct patterns do influence the proliferation and differentiation of oligodendrocyte precursors in a dissimilar way, even though the sum activity and transmitted charge through their synaptic receptors were similar in the applied paradigms. I also demonstrated that the quantal parameters at the axon – OPC synapses are sensitive to the method by which the quantal synaptic events had been triggered. Therefore the different approaches to trigger quantal events are not interchangeable or substitutable with each other. Lastly, with my colleagues we established that the exact physiological parameters of the glutamatergic synaptic transmission matter greatly to these cells: modifications of the AMPA receptors on oligodendrocyte precursors considerably altered their proliferation and differentiation.

The results discussed in this thesis not only show how millisecond-scale events, such as synaptic currents, can influence slow biological processes as cell cycle or cell differentiation; but also carry key implications for various myelin-related diseases, for instance multiple sclerosis.

II. Synopsis

General Introduction

The mammalian central nervous system (CNS) is one of the most structurally and physiologically complex systems of the mammalian organism. It consists of billions of cells with highly specialized functions. The two major cell classes forming the CNS are the neurons and the glial cells. Most non-neuronal cells are called glia, but that does not mean that they are similar morphologically or functionally. Glial cells are further divided into several types: astrocytes, oligodendrocytes, ependymal cells, radial glia, satellite cells, and microglia. They come from different developmental paths: microglia develops from the mesoderm, while all other glia cells form from the neuroectoderm. Glial cells show diverse morphological features; have distinct cell-type functions, and play a number of key roles in physiological and pathological states of the nervous system.
The subjects of this thesis are the cells of the oligodendrocyte-linage. I will mainly focus on the communication of the oligodendrocyte precursor cell (OPC) with the glutamatergic projection axons; and their differentiation into oligodendrocytes (OLs), the myelin-sheath forming insulating cells of the CNS. The myelination plays a crucial role in healthy CNS function; therefore the normal and balanced OPC development, proliferation, differentiation and physiology drastically influences the overall structure and functionality of the adult CNS.

The oligodendrocytes

The myelinating cells of the mammalian CNS are the OLs (Baumann and Pham-Dinh, 2001). Their morphology is unique and easily recognizable: they have relatively large soma, and typically possess many processes. At the tip of these processes they form the myelin sheaths around the adjacent axons. The majority of OLs ensheath several axons (Peters et al., 1978; Peyron et al., 1997).
The myelin sheaths have several important roles. Their segments confine voltage gated Na^+-channels to the nodes of Ranvier (Freeman

et al., 2016; Rasband and Peles, 2015), and have high resistance and low capacitance. Thus they enable saltatory action potential propagation along the axon (Tasaki, 1939). This speeds up the communication between neurons without requiring thicker axons. CNS myelin is mainly found in vertebrates, and is thought to have a major role in the evolution in higher nervous system functions (Hartline and Colman, 2007).
Besides faster action potential propagation, the normal myelin sheaths give trophic and metabolic support to axons (Nave, 2010), and are essential for axon survival and maintenance. Mutant mice for PLP/DM20 (a major component of the myelin) have normally structured, but unstable myelin (Klugmann et al., 1997). Surprisingly, this already causes severe symptoms in axon morphology and pathology (Griffiths et al., 1998). Thus the well-structured and stable myelin sheaths are essential for the solid functioning of the CNS.

The oligodendrocyte precursor cell

The OLs differentiate from OPCs during development (Dimou et al., 2008). Two commonly used markers of OPCs are the chondroitin-sulphate proteoglycan neural/glial antigen 2 (NG2) and receptor alpha for platelet-derived growth factor (PDGF-Rα) (Nishiyama et al., 1996). These cells have multiple, finely branching processes, therefore OPCs are clearly distinguishable from the other NG2-expressing cells of the CNS, the pericytes. They are more or less evenly distributed both in grey and white matter (Nishiyama et al., 1996). Although the main OPC function known to be the generation of OLs during development (Dimou et al., 2008), in the adult brain OPCs still constitute 2–3% of total cells in the grey matter, and 8-9 % in the white matter (Dawson et al., 2003). A peculiar feature of these cells is that they continue to proliferate throughout the lifetime of the mammals (Psachoulia et al., 2009). In fact, OPCs represent one of the most prominent fraction of the proliferating cells in the adult CNS (Fröhlich et al., 2011; Psachoulia et al., 2009). OLs still differentiate from OPCs and then generate myelin in adult mice (Young et al., 2013), although at a much lower rate than in young animals. Blocking adult myelination prevents mice from learning new motoric skills (McKenzie et al., 2014). Therefore, the constantly

renewing pool of OPCs is the basis of certain aspects of the brain's plasticity in adulthood. After myelin damaging injuries or pathological conditions, OPCs are able to repair myelin (Miron et al., 2011), hence the presence of OPCs in the adult brain is crucial to the maintenance and restoration of healthy brain function.

Oligodendrocyte precursor cells and their glutamatergic synapses with neurons

The expression of glutamate receptors by glial cells was suggested about 30 years ago (Usowicz et al., 1989). Oligodendrocyte-type-2 astrocytes isolated from the optic nerve (Barres et al., 1990), complex cells from the hippocampus (Steinhäser et al., 1994), and glial precursors of the corpus callosum (Berger, 1995) all showed inward currents, elicited by AMPA/kainate receptor agonists. Although these studies did not use the NG2 or PDGF-Rα staining as cell identity markers, the studied cells were most likely OPCs (Bergles et al., 2010).

It remained unclear for a long time through which mechanism these AMPA/kainate receptors on OPCs are activated. In 2000., Bergles and his colleagues demonstrated that action potentials in glutamatergic neurons trigger glutamate release onto OPCs and these glutamatergic responses were blocked by AMPA/kainate receptor antagonists (Bergles et al., 2000). Most importantly, they registered events which were proven to be quantal currents (Bergles et al., 2000), and electron microscopy of dye-filled OPCs revealed similar synaptic structures as between neurons (Bergles et al., 2000). Taken together, these data showed that one communication channel between neurons and OPCs is the action potential activated synaptic glutamate release. Since then it was shown that OPCs receive glutamatergic synaptic input in all investigated brain regions, including hippocampus (Bergles et al., 2000), cortex (Chittajallu et al., 2004), corpus callosum (Kukley et al., 2007; Ziskin et al., 2007), and the cerebellum (Káradóttir et al., 2008).

The glutamate is released from highly specialized presynaptic sites at the axon – OPC synapses. The mechanism of the release is very similar to release happening at neuron – neuron synapses: the

presynaptic membrane is depolarized by an action potential, this opens voltage gated Ca^{2+} channels, and the increased intracellular $[Ca^{2+}]$ in the presynaptic axon causes glutamate-filled vesicle fusion with the presynaptic membrane (Kukley et al., 2007). The glutamate release at the callosal axon – OPC synapses have two distinct kinetic components: phasic, which is time-locked to the action potential; and asynchronous or delayed, which keep happening for hundreds of milliseconds after the action potentials ceased (Kukley et al., 2007; Nagy et al., 2017).

The glutamate released by the presynapse is detected primarily by the AMPA receptors on the membrane of the OPCs (Bergles et al., 2000). The AMPA receptors are large macromolecular complexes, consisting of more than thirty proteins in the neurons (Schwenk et al., 2014). The channel pore is formed by a tetramer of four AMPA receptor subunits. There are four known subunit types (GluA1-4), and they are together responsible for the ionotropic function. If present in the receptor-tetramer, the GluA2 subunit regulates Ca^{2+}-permeability (Hume et al., 1991) and single channel conductance (Swanson et al., 1997) of AMPA receptors in neurons. Natural or genetically engineered modifications on the GluA2 subunit drastically influence the final physiological properties of the given receptor: receptor kinetics, single-channel conductance, Ca^{2+}-permeability, and the block by endogenous polyamines (Isaac et al., 2007). OPCs in the corpus callosum express functional GluA2-4-containing receptors in their post-synaptic sites, whereas they only express GluA1 sporadically (Kougioumtzidou et al., 2017).

The nature of the neuron-OPC contact was proven synaptic, but the physiological properties of these synapses remained somewhat controversial. The estimates for the quantal amplitude (the amplitude of a post-synaptic current triggered by the fusion of one glutamate filled vesicle at the presynapse) at axon-OPC synapses have a very wide range of values in the literature (Table 1).

Table 1. Overview of quantal glutamatergic synaptic currents recorded in OPCs in different brain regions (blockers of $GABA_A$ and NMDA receptors are present in the bath in each case)

Publication	Animals	Animal age	Brain area	V_{hold} [mV]	How recordings of quantal currents were performed		Events detection		Mean quantal amplitude [pA]	Amplitude distribution histogram	
					Type of recorded quantal currents	Drugs in the bath	Algorithm /software	Threshold		Peak location	Histogram shape
Bergles et al, 2000	rat	P7, P12-16, P21, P66	hippocampus	-90	spontaneous mEPSCs	TTX + pardaxin (2 µM) or α-latrotoxin (2 nM)	not indicated	not indicated	15 ± 3	~8 pA	skew to larger amplitudes
Lin et al, 2005	mouse	P16-25	cerebellum	-80	spontaneous mEPSCs	TTX + ruthenium red (100 µM)	mini analysis (Synaptosoft)	not indicated	13.5 ± 4.8	not reported	
Lin et al, 2005	mouse	P16-25	cerebellum	-80	delayed EPSCs after train stimulation	5 mM Sr^{2+} (instead of Mg^{+}/Ca^{2+})	mini analysis (Synaptosoft)	not indicated	11.3 ± 3.3	not reported	
Kukley et al, 2007	rat	P8-16	corpus callosum	-80	spontaneous mEPSCs	TTX + ruthenium red (100 µM)	sliding template (IgorPro)	3 pA	4 ± 0.2	~4 pA	skew to larger amplitudes
Ziskin et al, 2007	mouse	P14-15, P19-21, P32-37	corpus callosum	-90	spontaneous mEPSCs	TTX	mini analysis (Synaptosoft)	not indicated	18.4 ± 1.2	not reported	
Ziskin et al, 2007	mouse	P14-15, P19-21, P32-37	corpus callosum	-90	spontaneous mEPSCs	TTX + α-latrotoxin (5 nM)	mini analysis (Synaptosoft)	not indicated	15.1 ± 0.6	first peak ~10 pA, second peak ~18 pA	skew to larger amplitudes

Table 1. (continuation)

Kukley et al, 2008	mouse	P7-12	hippocampus, cortex	-80	spontaneous mEPSCs	TTX+ ruthenium red (100 µM)	sliding template (IgorPro)	not indicated	5.8 ± 1.1 to 7 ± 0.6 (depending on cell cycle stage)	not reported	
Ge et al, 2009	mouse	P25 or P50	neocortex	-60	spontaneous mEPSCs	spont. (no TTX)	not reported	not reported	25±2	not reported	
Kukley et al, 2010	mouse	P9–14	hippocampus	-80	spontaneous mEPSCs	TTX+ ruthenium red (100 µM)	sliding template (IgorPro)	3 pA	6 ± 0.9	not reported	
De Biase et al, 2010	mouse	P5-45	corpus callosum, hippocampus, cerebellum	-80	spontaneous mEPSCs	TTX + focally applied sucrose (500 mM)	mini analysis (Synaptosoft)	5 pA	not indicated	~7pA	skew to larger amplitudes
De Biase et al, 2011	mouse	P40-45	corpus callosum, hippocampus	-80	spontaneous mEPSCs	TTX + focally applied sucrose (500 mM)	mini analysis (Synaptosoft)	5 pA	~8	not reported	
Sahel et al, 2015	mouse	P40-70	corpus callosum	-90	spontaneous mEPSCs	TTX + ruthenium red (75 µM)	Spacan (IgorPro)	3 times the noise standard deviation	10	not reported	
Passlick et al, 2016	mouse	P8-12, >9 months	hippocampus	-80	spontaneous mEPSCs	TTX+ ionomycin (3 µM)	template-based (pClamp)	5 pA	~9	not reported	
Etxeberria et al, 2010	mouse	adult	corpus callosum	-80	spontaneous mEPSCs	TTX+ ruthenium red (100 µM)	Clampfit 9.2	not reported	Not indicated	~8pA	skew to larger amplitudes
Nagy et al, 2017	mouse	P19-22, P50-53	corpus callosum	-80	spontaneous mEPSCs, delayed/asynchronous EPSC	TTX (for the spont. EPSC)	Deconvolution (IgorPrO+FBrain)	3.9 times noise standard deviation	3.3 2.8	small skew to larger amplitudes	

As the quantal amplitude partially defines synaptic strength, the great variability of this parameter implies that the synaptic strength of axon – OPC synapses varies significantly. However, these results come from different experimental conditions and data analysis approaches, therefore it is difficult to compare and confer the different studies. As synaptic strength influences drastically what kind of response the postsynaptic cell has upon synaptic activation transmission, it would be crucial to clarify the factors behind the reported differences. Therefore as one of my goals in my doctoral work has been to reliably estimate the quantal amplitude at axon – OPC synapses: I compared how the different experimental approaches to trigger quantal events influence the parameters of the quantal transmission at the axon – OPC synapses.

Glutamate receptor activation influences the behavior of oligodendrocyte precursor cells

One supposed function of the glutamate receptors was that they regulate the proliferation and differentiation of OPCs. For OPCs, the Ca^{2+}-permeability of AMPA receptors seems particularly important: in the corpus callosum, the OPCs in the young mouse pups contain edited GluA2, therefore their receptors are Ca^{2+}-impermeable; while in older mice AMPA receptors lack the edited GluA2, becoming Ca^{2+}-permeable (Ziskin et al., 2007). This switch of receptor properties coincides with the slowing down of OPC proliferation and differentiation into myelinating OLs (Young et al., 2013).
In cerebellar slice cultures, the number of OPCs (identified by their NG2-expression) was influenced significantly by glutamatergic drugs acting on AMPA receptors (Yuan et al., 1998). The number of OPCs was increased compared to the control in the presence of DNQX, a blocker for AMPA/kainate (Yuan et al., 1998). Reversely, application of agonists (kainate or AMPA, individually) reduced the number of OPCs, in a dose dependent manner (Yuan et al., 1998). They also tested OPC proliferation-rate, using bromodeoxyuridine (BrdU), a thymidine analogue, which is built into the DNA of proliferating cells, thus labeling them. In this study, BrdU labeling revealed that kainate reduced the OPC proliferation (Yuan et al., 1998). The conclusions were that if AMPA receptor activation reduces the proliferation and number of OPCs in cultures, and neurons signal to

OPCs through synapses with AMPA-receptors, then glutamatergic neuronal activity should suppress OPC proliferation, and consequently decrease their number. However, *in vivo* experiments contradict this conclusion. A recent study in vivo demonstrated that the proliferation of OPCs did not change in mice lacking GluA2 and GluA3 subunits; or GluA2, GluA3, and GluA4 subunits of AMPA receptors in OPCs (Kougioumtzidou et al., 2017). However, in both knockouts fewer myelinating OLs survived, and created less myelin sheathes. This latter effect persisted in adulthood in the triple knockout. The authors concluded that OPC proliferation and the differentiation are not influenced by the lack of AMPA receptors, but the AMPA-receptor-mediated signaling enhances OL survival. This latter is probably an indirect or delayed effect, because OLs seem to disassemble their synapses during differentiation, and it appears that they lack functional AMPA receptors completely (Kukley et al., 2010). It is also possible that the lack of GluA2-4 based subunits was compensated by the OPCs with some unknown mechanism. One reason for the contradiction between *in vivo* and *in vitro* studies might be a mechanism described by Hossain et al. in 2014 in cell cultures: upon prolonged exposure to AMPA receptor antagonists (AMPA or kainate), OPCs downregulate their AMPA receptor expression (Hossain et al., 2014). With this, in the presence of AMPA or kainate OPCs may actually *decrease* their AMPA receptor mediated activity, and that leads to decreased proliferation. These controversial findings in cell cultures show that these conclusions and hypothesizes have to be tested in vivo as well. With our own studies (Chen et al., 2018) we clarified how the modifications in the ionotropic function of AMPA receptors would influence the cellular fate of OPCs.

Electrical activity of axons influences the proliferation and differentiation of OPCs

Some studies suggested that neuronal activity might regulate the white matter structure. For example the internal capsule, the corpus callosum and the arcuate fascicle of professional musicians develop differently, as they gain extremely fine motoric skills through excessive practice (Bengtsson et al., 2005). The “practice” is essentially a modification of neuronal activity. Also it would seem

sensible that the axons might be able to regulate their own myelination depending on their activity and needs. The optic nerve was the model system in one of the first studies investigating the correlation between the neuronal activity and OPC proliferation in vivo (Barres and Raff, 1993). In young rodents there are many proliferating OPCs in the optic nerve. Blocking action potential propagation along the optic nerve axons (TTX injection to the eyeball, or severing the optic nerve) drastically reduced the number of proliferating OPCs (Barres and Raff, 1993). Therefore, axonal activity enhances the proliferation of OPCs. It was confirmed that myelination (which is a result of differentiation of OPCs) is also regulated by the electrical activity of the axons (Demerens et al., 1996). This study demonstrated, both in cell cultures and in the optic nerve in vivo, that blocking action potential with TTX reduces the number of myelin segments along the axons.

A recent study using dorsal root ganglion (DRG) neurons co-cultured with OPCs confirmed that electrically active axons are more likely to become myelinated than the non-active ones (Wake et al., 2015). DRG neurons do not build synapses in cultures with each other (B R Ransom et al., 1977; B. R. Ransom et al., 1977). They also fail to establish synaptic connections with OPCs (Wake et al., 2015). OPCs expressing the genetic calcium indicator GCaMP3 showed clear Ca^{2+} transients to electrical stimulation of axons. Thus the electrical activity of axons is still detected by the OPCs, although via non-synaptic junctions. The effect is mediated through glutamatergic and purinergic receptors. The authors conclude that the transmitter filled vesicle release by the electrically active axons is a decisive clue for OPC differentiation and myelination; however, the vesicle release does not necessarily occur at synaptic junctions.

These previous studies investigated regulation of OPCs behavior by neuronal activity in the developing nervous system. Interestingly, these effects also take place in adult rodents. In a study corticospinal axons of adult rats were electrically stimulated, and the effects on proliferation and differentiation of OPCs is the dorsal corticospinal tract were quantified (Li et al., 2010). The electrical stimulation consisted of 15 pulses delivered at 333 Hz, applied every 2 s, for 6 hours / day, over ten days. All in all, the animals received 108000 trains of pulses (that adds up to 1620000 electrical pulses over 10 days), adding to the already existing electrical activity of axons

occurring upon natural behavior. This is a very strong stimulation paradigm, and this activity normally would not occur in physiological conditions. However, these experiments are still very useful as an evidence that increased neuronal activity causes higher proliferation rate of OPCs. It also increased the likelihood of actively proliferating OPCs to start the differentiation process and become an OL (Li et al., 2010).

Another brain region was investigated in Gibson et al 2014, with a different method. To study the effect of neuronal activity on OPC proliferation and differentiation they stimulated projection neurons of the premotor cortex in Thy1::channelrhodopsin 2 (ChR2) mice (Arenkiel et al., 2007) with blue light. They evaluated the effect of additive electrical activity of axons on OPCs in the subcortical white matter tracts. To examine the acute effects, the cortex of the mice were stimulated unilaterally with blue light for 30-s intervals every 2 min over a 30-min period, at 20 Hz (this is 600 action potentials every two minutes, in total 18000 stimulation pulses in half an hour, only one session); and mice were sacrificed 3 (acute effect) or 24 hours (subacute effect) after the stimulation session. For studying chronic effects, the same paradigm was applied, for 7 consecutive days; mice were sacrificed 4 weeks later. They observed increased OPC proliferation and differentiation upon light stimulation, both in the acute and in the chronic group (Gibson et al., 2014).

The previously described experiments used very specific stimulation paradigms which triggered known patterns of axonal firing in addition to the physiological activity. Modulating the firing patterns through less invasive methods and testing whether they have an effect on OPC proliferation are also necessary. Modifications in the natural environmental input change neuronal firings patterns, and as a consequence they also alter the proliferation of OPCs (Ehninger et al., 2011). Ehninger et al. showed that both enriched environment and increased physical activity promotes larger proliferation rate of OPCs in mice (Ehninger et al., 2011). Mangin et al. did a different experiment: they deprived OPCs from their synaptic input from thalamocortical fibers in the barrel cortex by whisker lesion. The lesion reduces thalamocortical input to OPCs. This led to a more uniform OPC distribution in the barrel cortex, but also *increased* the proliferation of OPCs (Mangin et al., 2012). In this case,

glutamatergic input seems to be blocking OPC proliferation and / or migration.

These studies describing the axonal activity on OPC behavior apply very different methods and protocols. Therefore it is challenging to draw general conclusions from them. But it is apparent that neuronal activity might increase *or* decrease OPC proliferation and / or differentiation. Stimulating neurons with the same number of action potentials but with different patterns leads to the transcription of very different gene sets (Lee et al., 2017). This study raises the possibility that the temporal distribution of the electrical activity is a crucial factor in gene expression regulation. Would OPCs detect differences in the firing patterns of their presynaptic axons? Would they decode the different firing patterns differently, and translate them into distinct behavior (proliferation or differentiation)? In my thesis I describe our findings on how OPCs detect repetitive axonal firing, and how OPCs behave in vivo upon different stimulation patters consisting of the same amount of stimulation pulses (Nagy et al., 2017).

Aims of the doctoral studies

Part I. Identify the most efficient method to estimate the quantal physiological parameters of the axon – OPC glutamatergic synapses

The axon – OPC synapses have been investigated for almost twenty years now. However, reports on the quantal amplitude (and consequently the synaptic strength) show a large variation (Table 1). This is a problem because: 1. Conclusions from different studies are difficult to interpret together, as the basic unit of quantal amplitude differs greatly. 2. Alterations in synaptic strength of neuron – neuron contacts often indicate or trigger pathological conditions (Bliss et al., 2014). This might be the case for axon – OPC synapses as well, but the great variation in the reported quantal amplitude prevents the direct detection of such cases. Therefore I aimed to find a reliable reference measurement for the quantal amplitude.

The axon – OPC synapses have low release probability. This makes it technically challenging to record quantal events (which are the miniature excitatory postsynaptic current triggered by one single transmitter-filled vesicle), and investigate the functional quantal properties of the postsynaptic sites at axon – OPC synapses. To circumvent this, several pharmacological and electrophysiological approaches were used previously by different research groups to increase the miniature excitatory postsynaptic current (mEPSC) frequency at these structures (Table 1).

My hypothesis was that the reported differences in quantal amplitude mainly come from the variations in the method to trigger higher occurrence of miniature events. As the first aim of my doctoral work I wanted to answer the following questions: Do the different methods contribute to the large variation in the reported quantal amplitude? What would be most efficient method to enhance the occurrence of quantal events? Which method would trigger kinetically similar EPSCs to the spontaneous mEPSCs?

Answering these questions helps us to standardize the magnitude of the quantal amplitude at axon – OPC synapses, find the most efficient method to detect them at other systems than the mouse corpus callosum, and enable us to compare various further studies in different experimental conditions.

Part II. Test whether OPCs can distinguish between different axonal firing activities

Curiously, there are no detailed comparative studies in the literature investigating the AMPA receptor mediated responses of OPCs to repetitive axonal firing. This is surprising, because it is rare that a glutamatergic projection neuron of the corpus callosum only fires single action potential (Ramos et al., 2008; Zhu and Connors, 1999). Hence OPCs receiving glutamatergic synaptic input from neurons most likely usually detect short burst or trains of action potentials. OPCs show paired-pulse facilitation in brain slice experiments (Ge et al., 2006; Passlick et al., 2016), and even able to follow high rate (50 Hz) of firing of the axons (Kukley et al., 2007). It would be crucial to know if and how OPCs respond to the various axonal firing patterns, since experimental data shows that axonal activity influences the behavior of OPCs (Barres and Raff, 1993; Gibson et al., 2014; Li et al., 2010), and different firing patterns may have completely different effect on OPCs. The neurons projecting axons through the corpus callosum vary their firing frequency, the number of action potentials fired within a burst or a train, and the time gap between the bursts (Ramos et al., 2008; Zhu and Connors, 1999). As OLs myelinate axons based on their activity (Demerens et al., 1996; Fields, 2015), their precursors need to have a structure to detect neuronal firing. The nature and the position of glutamatergic axon – OPCs synapses make these structures prime candidates for such function. However, the detailed analysis of how OPCs detect repetitive axonal firing is lacking.

My hypothesis was that glutamate release triggered by different repetitive stimulation patterns would elicit very dissimilar responses in OPCs. I tested this by voltage-clamp experiments in OPCs in ex vivo brain slices, while electrically stimulated the callosal axons with different stimulation patterns. I applied slower, physiological (5 Hz, 25 Hz) and faster, more pathological (100 Hz, 300 Hz) frequencies; in short (2 or 5 pulses) and longer (20 pulses) trains. With this I aimed to answer the following questions: How would OPCs detect long trains of slower frequency? Would there be any difference of the responses of the OPCs upon lower and faster stimulation firing

patterns? Do OPCs show synaptic depression upon faster or slower stimulation trains? Would the asynchronous or delayed release be present at all at these synapses upon shorter trains?
Answering these questions shows that OPCs can follow a very diverse axonal firing patterns; and makes it predictable how OPCs would detect glutamate release in vivo in certain behavioral states of the animals.

Part III. Test *in vivo* whether the different axonal firing patterns influence the differentiation and proliferation of OPCs in dissimilar ways

It has been established that changes in neuronal activity affects OPC behavior and fate. Upon neuronal stimulation increased proliferation and differentiation of OPCs were described (Gibson et al., 2014; Li et al., 2010). In enriched environment or upon increased physical activity of mice OPCs proliferate faster, but do not differentiate more (Ehninger et al., 2011). Curiously, sensory deprivation reduces glutamatergic input of OPCs, still the OPC proliferation increases (Mangin et al., 2012) Therefore it still remained unclear whether in vivo what kind of neuronal firing patterns increase or decrease the proliferation and differentiation of OPCs. It was also not clear whether the modulation of proliferation and differentiation of OPCs by neuronal activity is an all-or-none effect, or it is graded. It adds to the confusion that these studies use different brain regions and different experimental protocols.
My goal here was to apply different stimulation paradigms in the same model system and under the same conditions, and then examine how they modulate the proliferation and differentiation of OPCC. Hence I implanted stimulation electrodes into the corpus callosum of the mice, and applied three different stimulation paradigms in freely behaving mice, and assessed how the fate and behavior of OPCs was affected.

Part IV. Investigate whether the functional properties of AMPA receptors in axon – OPC synapses regulate proliferation and differentiation of OPCs

Various studies described opposite results whether AMPA receptor activation modulates OPC proliferation and differentiation. In brain slice cultures, the AMPA receptor activation seemed to reduce, and AMPA receptor blockage seemed to increase OPC proliferation (Yuan et al., 1998). Opposite to this, in vivo knock out of AMPA subunits did not seem to influence proliferation and differentiation (Kougioumtzidou et al., 2017). It is also unclear whether the ionotropic function alone, and / or the downstream signaling cascade elements of the AMPA receptor activation pathway play a more significant role. Both scenarios are possible: while the ionotropic function would influence the cell cycle through its effect on the membrane potential (Blackiston et al., 2009); several signal transduction mechanisms can be activated directly or indirectly via AMPA receptors (Auger and Ogden, 2010; Bao et al., 2016; Henley and Wilkinson, 2013; Kessels and Malinow, 2009). Hence we took a different and completely new approach to elucidate the function of AMPA receptors expressed by OPCs: we modified or perturbed the physiological properties of already existing callosal axon – OPCs synapses, then quantified the changes of OPC proliferation and differentiation.

Corpus callosum as a model system

The corpus callosum is the major white matter tract connecting the two hemispheres of the mammalian cortex (Ramos et al., 2008). The majority of axons in the corpus callosum originate from pyramidal cells of the cortical layers II/III (supragranular cells) and V/VI (infragranular cells) (Fame et al., 2011; Ramos et al., 2008). These axons are the presynaptic partners in the neuron-OPC glutamatergic signaling in the corpus callosum (Kukley et al., 2007; Ziskin et al., 2007). The pyramidal cells projecting through the corpus callosum are heterogeneous in their electrophysiological properties (Ramos et al., 2008; Zhu and Connors, 1999). Upon current injection in brain slices, these neurons fire action potentials with a very wide range,

from below 1 Hz up to 400 Hz (Zhu and Connors, 1999). Upon current injection both supragranular and infragranular pyramidal cells can fire trains of action potentials, consisting up to 15-20 action potentials, with up to 100 Hz rate (Ramos et al., 2008). The firing range is different in freely behaving, awake mouse: pyramidal cells responding to whisker vibration in the barrel cortex had mostly firing rate below 60 Hz; and most often they fired in the 5-10 Hz or 20-40 Hz range, depending on the cortical layer (O'Connor et al., 2010).

The corpus callosum is an optimal model system for my investigations for the following reasons:

1. It has been established that OPCs receive glutamatergic input in the corpus callosum.

2. Corpus callosum is a system where glutamatergic synaptic input to OPC can be investigated in isolation. Although OPCs in the corpus callosum express functional $GABA_A$ receptors (Berger et al., 1992), I could not detect GABAergic synaptic input, which could influence the results of the experiments and make the interpretation of those results more challenging.

3. The corpus callosum is easily accessible for both in situ and in vivo experiments.

Part I. Identify the most efficient method to estimate the quantal physiological parameters of the neuron-OPC glutamatergic synapses

Comparison of six different techniques to trigger quantal events at neuron – OPC synapses in the corpus callosum

The synaptic strength (I) between a single neuron and an OPC is defined by the equation:

$$I = q * n_{ves} * p_{ves} * N$$

Where q is the quantal amplitude (the amplitude of the current evoked by a single transmitter-filled vesicle), n_{ves} is the number of vesicles released at a single connection, p_{ves} the probability of vesicle release, and N is the number of synaptic connections between the single axon and a single OPC.

The general approach to estimate *q* is the recordings of miniature excitatory postsynaptic currents (mEPSC). A mEPSC is a postsynaptic event triggered by a single glutamate vesicle released by the presynaptic neuron.

My findings about properties of dEPSCs at neuron-OPC synapses in **Publication 1** gave me the idea to look into the details of the quantal transmission at axon – OPC synapses. I found it curious that the reported values for the parameters of quantal transmission can vary so drastically (Table 1).

The axon – OPC synapses have low release probability (Kukley et al., 2007; Nagy et al., 2017). This results in a very low spontaneous quantal release rate of single vesicles from presynaptic axons (Figure 1A, G, I). The low spontaneous release rate makes the estimation of *q* problematic and challenging, because hundreds of mEPSCs are needed to reliably measure quantal amplitude, rise- and decay-times. Therefore the voltage-clamp recordings from OPCs have to be stable for a very long time (multiple hours) to acquire enough mEPSC. To circumvent this, investigators applied various methods to increase the efficiency of data acquisition (Table 1), but the differences in the estimated quantal amplitude are substantial. It is not clear, whether these differences stem from:

1. Different species used
2. Regional differences in the brain
3. Use of different age groups within the same species
4. Variations in the experimental protocols (e.g. holding potential, ionic composition of pipette and bath solutions)
5. Method of analysis

Therefore we performed whole-cell patch-clamp recordings of OPCs in mouse brain slices to study quantal amplitude q at glutamatergic axon – OPC synapses in corpus callosum. We standardized the species (mouse), strain (NG2DsRedBAC transgenic mice), age (postnatal day 19-22), brain region (corpus callosum), experimental and analysis protocols. We compared how different approaches promoting supposed mEPSCs affects the value of q. We tested the following experimental paradigms:

(1) Spontaneous mEPSCs in OPCs during bath application of tetrodotoxin (TTX, 1 µM), from here called "mEPSC" (Kukley et al., 2007; Nagy et al., 2017);

(2) Recording mEPSCs as in (1) but in the presence of ruthenium red (RR, 100 µM) in the extracellular solution, from here called mEPSC, from here called "RR" (Kukley et al., 2010; Lin et al., 2005);

(3) Recording mEPSCs as in (1) but triggered by local pressure-induced application of hypertonic solution, from here called "sucrose" (De Biase et al., 2010);

(4) Electrical stimulation of (presumably) a single callosal axon, contacting the patched OPC (i.e. minimal stimulation paradigm), with 20 pulses at 100 Hz and recording delayed excitatory postsynaptic currents (dEPSCs) occurring after cessation of stimulation, from here called "dEPSC – minimal" (Nagy et al., 2017);

(5) Recording dEPSCs as in (4) but using higher stimulation intensity in order to activate multiple rather than single callosal axons contacting the recorded OPC, from here called "dEPSC – non-minimal";

(6) Recording dEPSCs as in (4) but under conditions where in the bath solution 2 mM Ca^{2+} was substituted for 3 mM Sr^{2+}, and Mg^{2+} was reduced from 2 to1 mM (Fig.1c) , from here called "Strontium" (Bekkers and Clements, 1999; Lin et al., 2005).

All these experimental paradigms have been used previously to study neuron – neuron and neuron – OPC synapses.

Sucrose, Strontium and Ruthenium red change the kinetic parameters of mEPSCs at axon – OPC synapses

The selected methods worked as expected: they all increased the occurrence of postsynaptic events in OPCs compared to mEPSC (Figure 1G-I): 0.076±0.015 Hz for mEPSC, 0.59±0.15 Hz for RR, 46.44±15.8 Hz for sucrose, 42.1±12.19 Hz for dEPSC – minimal, 69.6±11.62 Hz for dEPSC – non-minimal, and 63.8±18.35 Hz for dEPSC – Strontium.

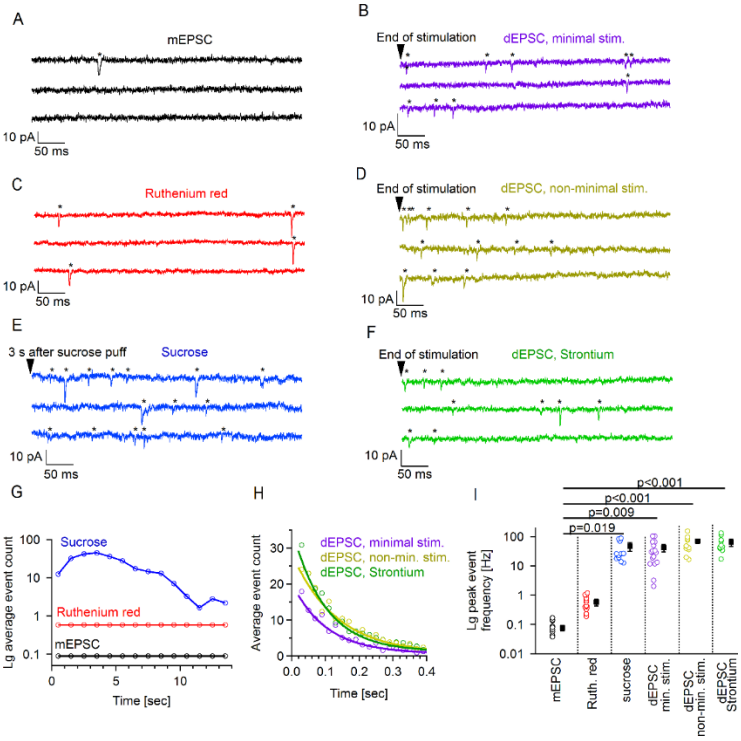

Figure 1. All applied methods increased EPSC occurrence frequency compared to mEPSC

A-F: Representative example traces from voltage clamp recordings of OPCs at -80 mV holding potential for each method. G: Time-course of average event frequency of mEPSC (black), Ruthenium red (red) and sucrose (blue). In the case of sucrose "0" time point represents the time of the fast application of the hypertonic solution. H: Time course of the dEPSC occurrence for minimal stimulation (purple), non-minimal stimulation (yellow), and Strontium (green). "0" time point represents 10 ms after the end of the electrical stimulation train. I: average event frequency of EPSC occurrence for each investigated method. Note that each investigated method increased the frequency of recorded events, therefore making the experiment more time-efficient. One-way ANOVA $F(5,64)=10.227$, $p<0.01$; significant post-hoc Dunnett's test p values are indicated on the graph.

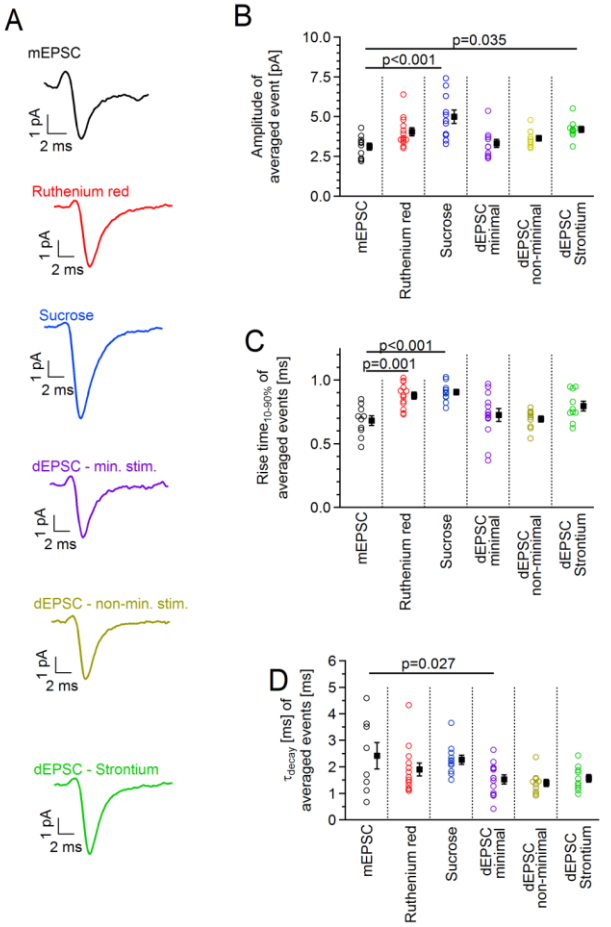
A
mEPSC
1 pA
2 ms
Ruthenium red
Sucrose
dEPSC - min. stim.
dEPSC - non-min. stim.
dEPSC - Strontium
B
Amplitude of averaged event [pA]
p=0.035
p<0.001
C
Rise time10-90% of averaged events [ms]
p<0.001
p=0.001
D
τdecay [ms] of averaged events [ms]
p=0.027
mEPSC
Ruthenium red
Sucrose
dEPSC minimal
dEPSC non-minimal
dEPSC Strontium

We also observed that some of the methods changed the amplitude and the kinetics of the recorded events. The mESPC mean event amplitude was 3.1±0.2 pA. This increased significantly upon the application of sucrose (5.0±0.4 pA) or Strontium (4.2±pA) (Figure 2B). Furthermore, the rise time of synaptic events was also increased significantly by sucrose (0.91±0.02 ms) and RR (0.88±0.03 ms) (Figure 2C) compared to mEPSC (0.68±0.03 ms). These two findings indicated that the events recorded in the presence of sucrose or RR are not necessarily identical to the mEPSCs.

Analyzing the mean EPSC waveform recorded from a given cell (as in Figure 2) is common when studying synaptic currents. This can be somewhat misleading because averaging many events might bias the mean waveform towards the more frequent shapes, thus outlier shapes are neglected. This is a problem because outliers may carry important information regarding the details of the synaptic transmission. Also, if the recorded events come from two or more sources, averaging them will mask this. In any case, the mean EPSC waveform will lose some of the information which might be important in estimating *q*. Therefore we analyzed further the amplitude distribution of the individual synaptic events in OPCs (Figure 3 A-F and Figure 4A). The amplitude distribution histogram of mEPSCs had its peak at 2.9 pA (Figure 3A). Sucrose had its peak at 3.8 pA (roughly 36 % increase) (Figure 3C), and Strontium had its peak at 3.7 pA (roughly 28 % increase) (Figure 3F). This indicates that Sucrose and Strontium shift the EPSCs to larger amplitudes. We also characterized the

Figure 2. Sucrose, Strontium and Ruthenium red change the kinetics of the EPSCs compared to mEPSC.

A: Averaged EPSC waveforms. First all events recorded from single cells were averaged. Then these averaged waveforms were averaged across cells method by method. B: Amplitude of the mean waveform for each analyzed cell One-way ANOVA $F(5,59)=6.229$, $p<0.001$; significant post-hoc Dunnett's test p values are indicated on the graph. C: Same as B, but for 10-90% rise-time. One-way ANOVA $F(5,64)=7.583$, $p<0.001$; significant post-hoc Dunnett's test p values are indicated on the graph. D: Same as B, but for τ_{decay} for for each analyzed cell. One-way ANOVA $F(5,64)=2.852$, $p=0.023$; significant post-hoc Dunnett's test p values are indicated on the graph.

individual histograms by their skewness. If the skewness value is 1, then it means that the EPSC event amplitude has a Gaussian distribution. All experimental approaches were skewed towards the larger amplitudes. Skewed distribution to the larger values may indicate intrinsic variations in quantal size (Zhou and Hablitz, 1997) that can come from variability in the number of transmitter molecules in a single vesicle (Bekkers et al., 1990), variability in post-synaptic receptor density (Edwards, 1995), or occasional multi-quantal release (Ulrich and Luscher, 1993). Interestingly, we could not detect any significant differences between the methods in the skewness of the amplitude distribution (Figure 3 G). We also calculated the coefficient of variation (CV) of the amplitude and did not find any significant differences there either (Figure 3 H). These findings indicate that the increase in the mean amplitude probably was not only caused by more frequent occurrence of larger events, as that would increase the skewness and CV of amplitude at the Sucrose or Strontium, respectively.

We performed further statistical comparison of the amplitude distribution of the events (Figure 4A) with the Kolmogorov-Smirnov test. This test quantifies the distance between two cumulative distribution functions. Only dEPSC recorded upon minimal stimulation were similar to mEPSCs in their amplitude distribution. All other methods triggered events with different amplitude distribution. The distribution curve upon RR and Sucrose shifted to larger amplitudes, which means that: 1. the smaller events of "mEPSC" were missing, *and* 2. the larger events became more frequent (Figure 4A). This could be because of changes in single-channel AMPA receptor conductance, and/or more frequent multi-vesicle event occurrence. Upon Strontium the smaller events were missing, but really large events did not become more frequent, as indicated by the overlap between the mEPSC and Strontium conditions at the largest amplitudes (Figure 4A). This implies that all events were slightly larger compared to the mEPSC events.

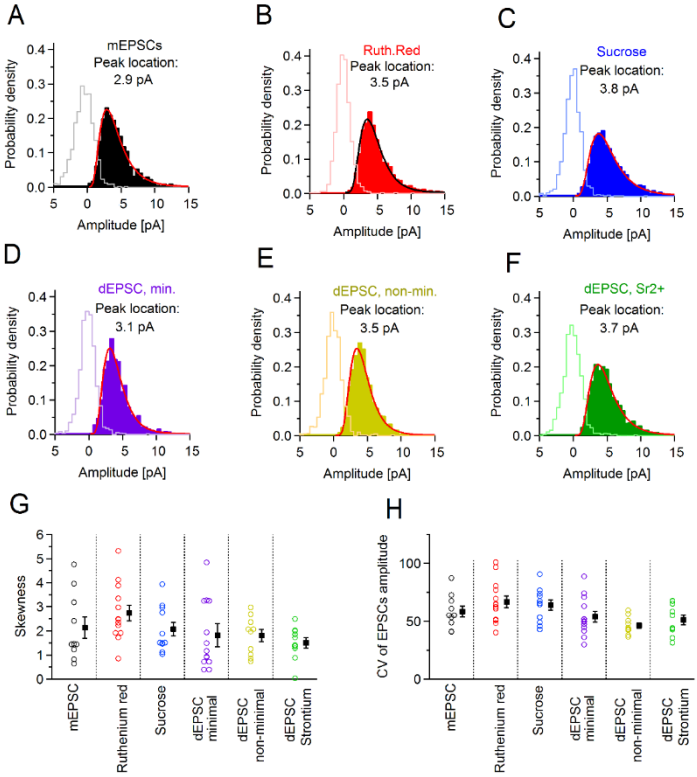

Figure 3. Ruthenium red, Sucrose, dEPSC – non-minimal, and Strontium shift the amplitude distribution histogram peak to higher values compared to mEPSC. A-F: Amplitude distribution histograms for each investigated method. First the histograms were built for each recorded cell, then for representation these histograms were averaged across cells method by method. The peak location was calculated by lognormal fit (represented by the continuous lines) on the averaged histograms. "Empty" histograms represent noise distribution. G: Skewness of the histograms for each analyzed cell. One-way ANOVA $F(5,49)=1.305$, $p=0.277$. H: Coefficient of variation of EPSC amplitude for each analyzed cell. One-way ANOVA $F(5,49)=2.010$, $p=0.094$.

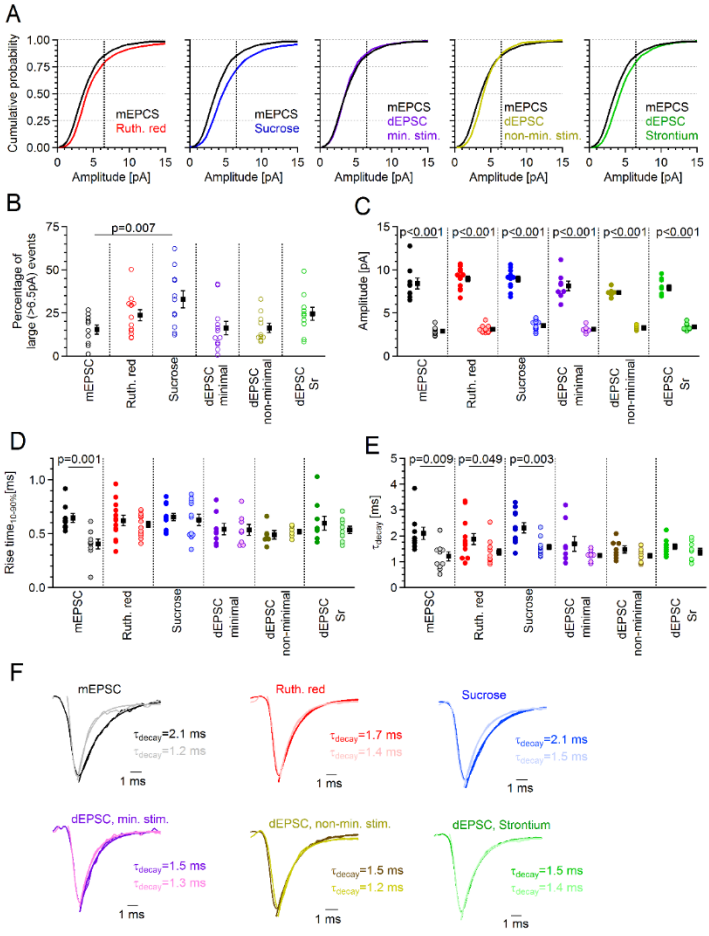

Figure 4. EPSC amplitude is increased significantly compared to mEPSC upon Ruthenium red, Sucrose, dEPSC – non-minimal, and Strontium recordings.
A: Cumulative amplitude distribution histograms for each investigated method overlaid with the histogram of mEPSC. First the histograms were built for each recorded cell, and then these histograms were averaged across cells method by method. (Continued on the bottom of the next page)

Taken these results together, reports of quantal amplitudes based on RR, sucrose or Strontium, are probably overestimating the quantal amplitude. One source of larger events can be the multi-quantal release: when more than one vesicle is released simultaneously. Multi-quantal events generally have slower kinetics (rise- and decay times) (Rudolph et al., 2011). We therefore divided the recorded EPSC to large and small fraction (Figure 4B-F), to test the possibility that the larger events arise from multi-quantal release. Our threshold of small vs. large events was 6.5 pA. This threshold was selected because on the amplitude distribution histogram of the mEPSCs (Figure 3A) there is a "gap" there. The "smaller" events (their amplitudes distributed left from the gap) give a Gaussian distribution. My theory for this is that these small events are the "true" quantal events, and the tail of the histogram (right from the gap) origins from the above mentioned factors (variability in the number of transmitter molecules in a single vesicle, variability in post-synaptic receptor density, occasional multi-quantal release). Our observation was that in the case of the sucrose the proportion of large events is significantly higher (33±5%) than in mEPSC (15±3%) (Figure 4B). Although RR (24±3%) and Strontium (25±4%) both increased the proportion of large events as well, the increase was not statistically significant compared to mEPSCs. The decay time-constants of the large EPSCs were significantly larger in the case of mEPSC, RR and sucrose (Figure 4E). This shows that the existence of large events in these paradigms can be partially explained by the higher frequency of multi-quantal release. In the case of the other methods, the kinetics of

(Continuation from previous page) Dotted line represents 6.5 pA, the threshold of large and small events. Kolmogorov-Smirnov test was used for statistical comparison. mEPSC vs. RR: $p<0.001$; mEPSC vs. sucrose: $p<0.001$; mEPSC vs. dEPSC – minimal: $p=1$; mEPSC vs. dEPSC – non-minimal: $p<0.001$; mEPSC vs. dEPSC – Strontium: $p<0.001$. B: Proportion of large events within each method for each analyzed cell. One-way ANOVA $F(5,65)=3.494$, $p=0.008$; significant post-hoc Dunnett's test p values are indicated on the graph. C: Mean amplitude of large (full circles) and small (empty circles) events. Paired t-test was used to compare large vs. small values. D: Mean 10-90% rise-time of lage (full circles) and small (empty circles) events. Paired t-test was used to compare large vs. small values. E: Mean 10-90% rise-time of large (full circles) and small (empty circles) events. Paired t-test was used to compare large vs. small values. F: Average event waveform for large (darker line) and small (lighter line) EPSCs, normalized for their amplitude. First large and small events were separated and averaged cell by cell, then these averaged EPSC waveforms were averaged across cells method by method for the figure

the large vs. small EPSCs did not differ significantly, therefore the amplitude increase upon Strontium was caused by some other factor than increase in multi-quantal release.

AMPA receptor single-channel conductance is affected by Ruthenium red, sucrose and Strontium

It is also possible that some of the tested methods alter the synaptic function on the post-synaptic site of axon – OPC synapses. In general, larger conductance of single channels at the postsynapse will be translated into larger amplitudes of quantal events (Chater and Goda, 2014; Momiyama et al., 2003). The conductance of the AMPA receptors on the OPCs might be affected by the various methods through some unknown mechanism, thus altering the amplitude of the EPSCs. To test whether the AMPA receptor conductance changes upon the tested conditions, we performed peak scaled non-stationary fluctuation analysis (NSFA) based on (Hartveit and Veruki, 2007) (Figure 5). As earlier, we divided the EPSCs to large and small events with a threshold of 6.5 pA, and estimated the single channel conductance of AMPA receptors for large and small events separately. Calculating single channel conductance was not possible for the large events within mEPSCs, because there were not enough large events to do so.

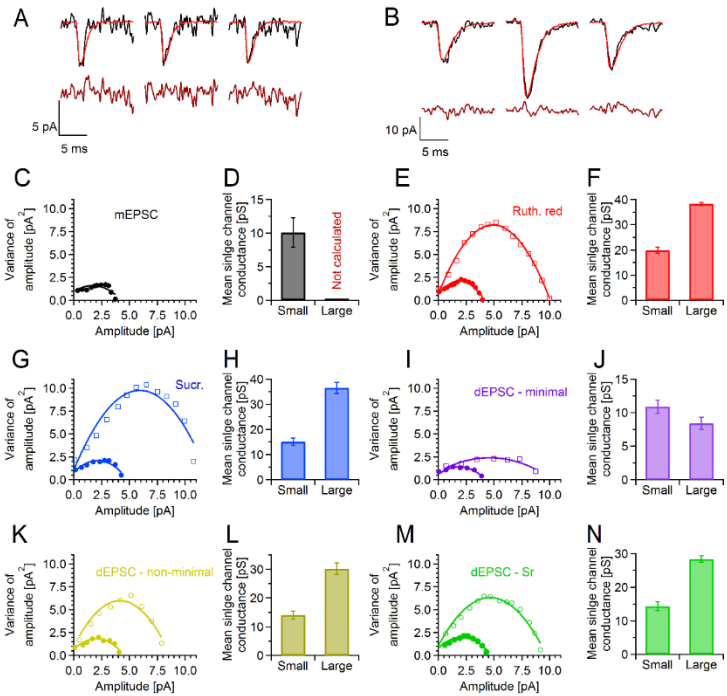

Figure 5. Non-stationary fluctuation analysis reveals altered single-channel conductance upon Ruthenium red, sucrose, and Strontium compared to mEPSC.

A: Upper row: three example small EPSC events (black) overlaid by the peak-scaled mean event waveform (red). Bottom row: Residual noise acquired by subtracting the red trace from the black trace in the upper row, for each three events, respectively. B: Same as "A", except for large EPSC events. C: Small mEPSC variance of amplitude plotted against amplitude; fitted by parabola function. D: Calculated single channel conductance for AMPA receptors upon mEPSC events. E: As in C, for Ruthenium red, filled circles represent the small events, empty squares represent the large events. F: As in D, for Ruthenium red. G-H: as in E-F, only for sucrose. I-J: as in E-F, only for dEPSC – minimal. K-L: as in E-F, only for dEPSC – non-minimal.

The estimated single channel conductance was 10.1±2.2 pS during small mEPSC events. Estimated conductance values were comparable with mEPSC upon small events from sucrose (15.1±1.5 pS), dEPSC – minimal (10.9±1 pS), dEPSC – non-minimal (14.1±1.4 pS) and dEPSC – Strontium (14.4±1.3 pS). However, upon RR single channel conductance of AMPA receptors during small events was considerably increased i.e. 19.9±1.2 pS. Interestingly, during large events, RR (38.3±1.2 pS), sucrose (36.6±2.2 pS), dEPSC – non-minimal (30.1±2 pS) and dEPSC – Strontium (28.4±1 pS) all significantly increased the single channel conductance compared to the corresponding values upon small events. The exception was dEPSC – non-minimal, where the estimated conductance (8.4±0.9 pS) during large events was comparable with the small events (11 pS). These calculations are comparable with the literature, where upon single-vesicle events AMPA receptors exhibit 6-8 pS single channel conductance, and larger events have higher (13-27 pS) conductance (Swanson et al., 1997).

The NSFA gave us the following very important insights: 1. single channel conductance is altered by RR. 2. The calculated conductance values are drastically different for most methods upon large and small events. It is possible that upon small and large events a different set of channels are activated. 3. dPESC – minimal stimulation is an exception from this rule: it has comparable single channel conductance values upon both small and large events with the mEPSC events.

Taking all results in Part I. together, it appears that it is only the dEPSC – minimal stimulation that gives increased occurrence of synaptic event while maintaining similar kinetics of events (amplitude, rise and decay times) and un-altered single channel conductance, compared to mEPSC. These criteria together indicate that the dEPSC – minimal stimulation events were indeed most likely quantal, triggered by only single glutamate-filled vesicles. This makes this method a prime candidate for an efficient substitution of mEPSCs recording. Although acquiring results with the other investigated methods can be valuable, the data analysis and result interpretation need much more care. I would like to emphasize that the detected differences between the investigated methods do not explain the large variability of quantal amplitude in the literature (see Table 1). Most likely the different approaches in data analysis (event

detection algorithm, setting different threshold for event amplitude) contribute greatly to the inconsistencies of the reported values. It would be also interesting to study whether the trends are present at neuron – neuron synapses. As these methods were originally adapted from the investigations of the neuronal synapses, similar distortion of quantal amplitude and single channel conductance changes are expected as at axon – OPC synapses.

Part II. Test in situ whether OPCs can distinguish between different axonal firing activities

Axon – OPC synaptic signaling is facilitated by repetitive axonal activity

There are two types of glutamate release onto OPCs when the callosal axons are stimulated by trains of pulses: 1. synchronous or phasic release, which is time-locked to the action potential, and follows it within a few milliseconds ((Kukley et al., 2007; Ziskin et al., 2007) and **Publication 1**) 2. Asynchronous or delayed release; which continues for up to hundreds of milliseconds after the train of action potentials stops ((Kukley et al., 2007) and **Publication 1**).

To investigate whether the responses of OPC change upon different patterns of stimulation we employed whole-cell patch-clamp recordings of OPCs in live brain slices. We used six stimulation paradigms: 2 pulses at 25 Hz; 5 pulses at 5, 25, and 100 Hz; and 20 pulses at 25 and 100 Hz (**Publication 1,** Fig. 1-4 and 6). We observed two components of presynaptic facilitation, and they were always present independently from the applied stimulation paradigm at the axon – OPC synapses.

Short-term facilitation of phasic responses at axon – OPC synapses

The phasic responses of OPC were always facilitated upon train stimulation, although to a various degree, depending on the paradigm (**Publication 1** Fig. 1, 3 and 6). In addition, the glutamate release became desynchronized, as the train of stimulation progressed (**Publication 1** Fig. 3, 6). The mean amplitude of the responses in OPCs (when including the failures) increased as the train of stimulation progressed (**Publication 1**, Fig. 1, 3, 6). The degree of facilitation depended on the type of stimulation paradigm. For example, upon stimulation with 5 or 20 pulses at 100 Hz, the peak response amplitude was reached at the 3-4th stimulation pulses, and then decayed back to the amplitude of the first response (**Publication 1**, Fig. 1, 3). In contrast, upon stimulation with 20 pulses at 25 Hz the amplitude reached its peak by the 4-5th pulse, and remained consistently high throughout the train of pulses (**Publication 1**, Fig.

3). The *potency* of the responses (the mean amplitude excluding the failures) remained consistent during the stimulation train (**Publication 1**, Fig. 1M, 3C, H), while the response probability (defined as the number of responses divided by the number of trials at each stimulation pulse) followed the shape of the mean amplitude (**Publication 1**, Fig. 1L, 3B, G). Taking together, these findings indicated that the short-term facilitation is caused by the increased release probability at the axon – OPC synapses, and is of presynaptic origin. We did not observe any postsynaptic plasticity (facilitation or depression) in these experiments.
Most often, the accumulation of presynaptic Ca^{2+} is a major reason for this type of facilitation in neuronal synapses (Regehr, 2012). To test whether this is also the case at axon-OPC synapses, we applyed EGTA-AM, a cell permeable slow Ca^{2+}-chelator (Smith et al., 1984), which prevents Ca^{2+}-concentration build-up in the presynaptic site (Swandulla et al., 1991). EGTA-AM did not affect the amplitude of the first response during train stimulations, meaning that the basal synaptic transmission was unaffected (**Publication 1,** Fig. 2F). However, it did abolish the previously observed facilitation completely, by preventing the increase in response probability (**Publication 1,** Fig. 2F). This means that, as in neurons, the facilitation at axon – OPC synapses is also caused by presynaptic $[Ca^{2+}]_i$ build-up.

Increased probability of quantal glutamate release after stimulation trains

The second component of the presynaptic facilitation we observed was an increase of quantal glutamate release after the train of stimulation. This was reflected in a higher occurrence of dEPSCs after train stimulation. The extent of the delayed responses was dependent on both the length of the stimulation train and the inter-pulse interval within the train (**Publication 1** Fig. 4, 6). The occurrence of dEPSCs increased with higher stimulation pulse numbers when the inter-pulse interval was kept constant (**Publication 1** Fig. 4A). The most likely reason for this was that upon longer stimulation trains more Ca^{2+} could build up in the presynaptic site, because the slow Ca^{2+}-buffering capacity of the axons cannot reduce

the $[Ca^{2+}]_i$ to baseline level during the short inter-pulse intervals. When we compared experiments in which we applied the same number of pulses per train but varied the inter-pulse interval, we found that trains with shorter inper-pulse intervals were more efficient in triggering high number of dEPSCs (**Publication 1** Fig. 4D). Both components of the presynaptic plasticity (phasic facilitation and increased dEPSC-occurrence) were present in both adolescent and in adult mice (**Publication 1** Fig. 4, 6). The decay time-constant of the dEPSC occurrence varied between 10-150 ms, depending on the stimulation paradigm (**Publication 1** Fig. 4C, F, I, Fig. 6G). This probably reflects the time-course of presynaptic $[Ca^{2+}]_i$ in callosal axons. For example, the decay time-constant of the callosal Ca^{2+}-transients upon single-pulse electrical stimulation was reported around 70 ms (Kukley et al., 2007). The presynaptic $[Ca^{2+}]_i$ dynamic is most likely different upon the various stimulation patterns (Kreitzer et al., 2000; Scott, 2007). For instance, the stimulation paradigm of 5 pulses at 5 Hz the inter-pulse interval is short enough to trigger some presynaptic $[Ca^{2+}]_i$-build up, as the Ca^{2+} level does not return to baseline within 200 ms. This results in a small rate of dEPSC occurrence. But upon 25 or 100 Hz stimulation the $[Ca^{2+}]_i$ build-up is much more efficient, the axon cannot decrease the $[Ca^{2+}]_i$ fast enough, therefore the delayed release becomes much more pronounced than at 5 Hz.

So far we have only considered differences in the facilitation from stimulus to stimulus during the train (**Publication 1** Fig. 1K; 3A, C; 6A), and this type of analysis disregards the "time factor", the differences in inter-pulse intervals upon the different stimulation patterns. To estimate the "real-time" effect of the facilitated responses of OPCs we analyzed synaptic charge transfer through AMPA/kainate receptors in OPCs upon axonal stimulation (during and after the train) and plotted it versus real time. The bioelectrical signals received by OPCs upon the various paradigms were remarkably different (**Publication 1** Fig. 5). Although the total transmitted charge did not differ significantly during the train (**Publication 1** Fig. 5B), the charge-transfer distribution over time was diverse (**Publication 1** Fig. 5A). Upon longer inter-pulse interval stimulation paradigms (5 and 25 Hz) the transmitted charge oscillated with the stimulation frequencies, and resulted in a prolonged charge transmission process. On the other hand, at 100 Hz stimulation the

charge is transmitted in "bulk", resulting in one large local ion delivery which was over quickly.

Axon – OPC synapses employ the same voltage-gated calcium channels as neuron – neuron synapses

The basis of glutamate-filled vesicle release is the action potential dependent Ca^{2+} entry into the presynaptic sites on the axons, mediated by voltage-gated Ca^{2+} channels (VGCCs). It was not clear whether the phasic and the delayed release of glutamate release are mediated by the same set of VGCC. In our work, we identified for the first time the types of VGCCs mediating glutamate release at axon – OPC synapses in the corpus callosum, with pharmacological methods (**Publication 1,** Fig. 2). We voltage-clamped OPCs in the corpus callosum, triggered glutamatergic responses by electrical stimulation of axons, and applied blockers of different VGCCs via the bath. The phasic responses were sensitive to bath application of both ω-conotoxin-GVIa (selective blocker of N-type VGCCs) and to ω-agatoxin-IVA (selective blocker of P/Q-type VGCCs). Both blockers impaired the glutamatergic transmission to the same degree. The average response amplitude to the first stimulation pulse within the train decreased because of the drop in response probability, and during the train the phasic amplitudes reached their peak later (**Publication 1,** Fig. 2D-E). This was probably caused by the slower accumulation of presynaptic Ca^{2+}. We observed similar effect on the delayed release: both antagonists decreased the rate of dEPSC occurrence (**Publication 1,** Fig. 2M-N). Simultaneous application of the two antagonists did not block the synaptic transmission completely; therefore some other type of channels may also play a role in the glutamate release at these synaptic sites. Alternatively, Ca^{2+}-independent transmitter release might also occur, as is known to happen at some neuron – neuron synapses. It is also possible that in different brain regions the glutamate release is mediated by different types of VGCCs, as is the case with neurons (Schlick et al., 2010).

Part III. Test in vivo whether the different axonal firing patterns influence the differentiation and proliferation of OPCs in dissimilar ways

Specific patterns of in vivo stimulation of callosal axons alter the differentiation of callosal OPCs in freely behaving mice

To test whether elevated action potential activity of callosal axons modifies the behavior of callosal OPCs in vivo, we implanted an array of stimulation electrodes to the corpus callosum of adult mice and stimulated callosal axons using different stimulation paradigms. The tip of the electrode array was positioned into the corpus callosum, beneath the primary motor area (stereotaxic coordinates from Bregma: Rostral-caudal: -1.06 mm, lateral: 0.8 mm, vertical: 1.3 mm). Each mouse was stimulated only in one session. The paradigms consisted of 20 pulses for 36 trains, separated by 5 minutes (total duration 3 hours). We applied 3 different paradigms: 5 Hz, 25 Hz and 300 Hz. As a control group, we used mice with electrodes implanted, but the stimulator was switched off when the animals were connected to it. The animals were sacrificed 3 or 7 days after the stimulation (**Publication 1** Fig.7).

First we tested whether the differentiation of OPCs into OLs was affected differently by the applied stimulation patterns (**Publication 1** Fig.7). We found that 5 Hz stimulation was the most efficient in triggering differentiation over seven days, because we observed significant increase of pre-OL density (**Publication 1** Fig.7H). 300 Hz stimulation did not affect the pre-OL density, while the 25 Hz paradigm caused a slight, statistically not significant increase in pre-OL density compared to the controls. None of the stimulation paradigms changed the density of the OPCs or the OLs seven days after the stimulation. We observed a slight, but statistically significant reduction of OPC density by the 300 Hz stimulation paradigm, three days after the stimulation session (**Publication 1** Fig.S2A). There are three likely reasons for this reduction: 1. OPCs commit apoptosis at a higher rate; 2. OPCs differentiated more readily; 3. OPCs reduce their proliferation upon 300 Hz stimulation. We can rule out the increased apoptotic activity, as we did not observe a rise Caspase-3 labeling in

the corpus callosum (**Publication 1** Fig.S3). We observed a small rise in pre-OL density 3 days after the stimulation sessions (**Publication 1** Fig.S2B), which indicates larger differentiation rate. The proliferation dynamics I discuss below.
These results show that stimulation of callosal axons at low frequencies acts as a differentiation signal for the OPCs, and particularly 5 Hz stimulation is efficient in triggering the differentiation process.

Higher frequencies of callosal stimulation promote OPC proliferation

We also tested whether the callosal stimulation affected the proliferation of OPCs. Right after the stimulation sessions the mice received EdU (5-ethynyl-2´-deoxyuridine) in their drinking water for 48 hours. This compound is built into the DNA as a thymidine analogue, thus labeling the proliferating cells.
We counted the number of EdU+ cells in the stimulated region of the corpus callosum, and determined the proportion of EdU+ OPCs. All applied stimulation paradigms increased the number of EdU+ OPCs compared to the control group, over seven days (**Publication 1** Fig.8E), but this effect was statistically significant only upon the 25 Hz and 300 Hz stimulations. Remarkably, the 5 Hz stimulation, which was so effective in triggering differentiation, did not increase significantly the proliferation rate of the OPCs. Furthermore, the stimulation also increased the density of EdU+ OLs, which means that the newly born OPCs are more likely to turn into OLs than the resting ones (**Publication 1** Fig.8). This increased proliferation rate did not result in increased OPC density compared to the sham (**Publication 1** Fig.7G), which could mean that 1. OPCs differentiated; 2. OPCs migrated away; 3. OPCs died; or 4. the time frame of our experiment is not sufficiently long to see the effect of increased proliferation in the OPC density. We can rule out increased cell death, because we did not see increased cell death in the corpus callosum after the stimulation (**Publication 1** Fig.S3). Therefore the unchanged density of OPCs despite increased proliferation is most likely due to a combination of the other mentioned factors.

Taking together the results of our in vivo experiments, we can conclude that lower stimulation frequencies of callosal axons are more effective in triggering OPCs differentiation, while higher frequency stimulation patterns rather promote proliferation of OPCs.

Part IV. Investigate whether the functional properties of AMPA receptors in axon – OPC synapses regulate the proliferation and differentiation of OPCs

Retrovirus can introduce gene alterations in the oligodendrocyte-lineage

To study functional role of AMPA receptors in the regulation of proliferation and differentiation of OPCs we aimed to modify the ion channel function of AMPA receptors of OPCs in the corpus callosum. We conducted these experiments in 2-3 weeks old mice, as at this age the OPC proliferation rate is high (Psachoulia et al., 2009; Young et al., 2013), and they also differentiate rapidly into myelin-forming OL (**Publication 2** Fig. 1C). We used retroviral gene delivery approach (Tashiro et al., 2007), and introduced three modified GluA2 subunit into OPCs in vivo: 1. Ca^{2+}-permeable: expression of the unedited GluA2(R583Q)-GFP subunit, where arginine(R)583 is replaced by glutamine(Q), aiming to create exclusively Ca^{2+}-permeable AMPARs (Hume et al., 1991) 2. Pore-dead: expression of GluA2(R583E)-GFP subunit, where the arginine(R)583 is replaced by glutamic acid (E). This disables ionic function of mutant GluA2-containing AMPARs (Dingledine et al., 1992) 3. Over-expression of C-tail: overexpression of the cytoplasmic carboxyl-terminal (GluA2(813-862)) of GluA2, which in neurons this perturbs the trafficking and postsynaptic placement of the endogenous GluA2 subunits (Bassani et al., 2009). Targeting the AMPA receptors based on their GluA2 content was possible because in the investigated age group OPCs actively express this subunit (**Publication 2** Fig. 2D and Fig. S1A-B).

We first verified the integration of the introduced GluA2 subunits with point-mutation into the membrane/postsynaptic site of axon – OPC synapses, using voltage-clamp experiments (**Publication 2 Fig**. 2). We used two approaches: recording of the I-V curve and recording of quantal axon-glia EPSCs. AMPA receptors that lack the edited GluA2 subunit are highly Ca^{2+}-permeable (Hume et al., 1991), and their I-V curve shows strong inward rectification in the presence of intracellular polyamines (Bowie and Mayer, 1995). To study Ca^{2+}-permeability of AMPA receptors at axon – OPC synapses we

analyzed the I-V relationship upon all introduced constructs. We found that the Ca^{2+}-permeable and pore-dead mutants had strong inward rectifying curves (**Publication 2 Fig**. 2D-E). This indicates that both constructs were expressed by the OPCs and modified subunits replaced the endogenous AMPA receptors. Upon the GFP and the c-tail constructs the AMPA receptors showed no inward rectification, and were very similar to the non-transduced control cells (**Publication 2 Fig**. 2D-E, Fig.S1A-B). This suggests that the endogenous AMPA receptor content of the axon – OPC synapses was unaffected by the c-tail. To study the alterations in the strength of axon – OPC synapses we recorded quantal EPSCs. We decided that recording dEPSCs would be the best and most efficient method, based on our findings in Part I. We analyzed the amplitude distribution of the dEPSCs (**Publication 2 Fig**. 2F-H, Fig. S1C-E), and calculated single channel conductance of AMPA receptors from these events (**Publication 2** Fig. 2I-J**.**). The amplitude of dEPSCs was increased in OPCs expressing the Ca^{2+}-permeable and pore-dead constructs compared to the GFP construct (**Publication 2** Fig. 2F-H). NSFA revealed that single channel conductance was also increased in OPCs expressing the Ca^{2+}-permeable and pore-dead constructs compared to the GFP construct (**Publication 2** Fig. 2I-J). The single channel conductance is larger in AMPA receptors which lack the edited GluA2 subunit (Swanson et al., 1997). Taken together, our results indicate that the modified GluA2-subunints were successfully expressed, and the OPCs inserted them into their post-synaptic sites. C-tail did not affect dEPSC amplitude, single-channel conductance or the rectification of the I-V curve. These results suggest that this construct did not alter the ionotropic function of the AMPA receptors at the axon – OPC synapses.

All manipulations of GluA2 subunit altered the proportion of OPCs and OLs within the oligodendrocyte lineage

We counted the transduced (GFP+) OPCs and OLs five days after the viral injection (**Publication 2** Fig. 3). All three manipulations of GluA2 subunit (pore-dead, Ca^{2+}-permeable and C-tail) increased the percentage of OPCs and decreased the ratio of the OLs (**Publication 2** Fig. 3G, L) within the GFP+ cell population (**Publication 2** Fig.

3E), compared to the control GFP-construct. The ratio of pre-OLs remained the same in all four experimental groups. The changes observed in cells over-expressing the C-tail were surprising and somewhat unexpected, because C-tail did not alter the physiological parameters of the axon – OPC synapses. The C-tail connects the AMPA receptors to their intracellular binding partners (Henley, 2003); therefore it is possible that the over-expression of the C-tail interferes with the downstream signaling cascade of the AMPA receptors; thus preventing or sidetracking natural OPC differentiation.

Pore-mutant subunit containing AMPA receptors increase OPC proliferation

Several mechanisms may contribute to the increased ratio of OPCs to OLs in our experiments ((**Publication 2** Fig. 3): 1. Increased cell death of OLs; 2. Increased proliferation of OPC; 3. OPCs have lower probability to transition towards OL fate. We could rule out the first mechanism, as we did not observe increased labelling for the apoptotic marker caspase-3 in the corpus callosum in any of the experimental group (**Publication 2** Fig. S3F-K). To assess the second possibility we used two approaches: we injected EdU to the mice at the 3-5th day after the virus injection, and counted EdU+GFP+ cells; and performed immunohistochemistry for Ki67(**Publication 2** Fig. 4), a marker which is present throughout the cell cycle (Gerdes et al., 1984). We found that expressing the GluA2 subunit with pore-mutations resulted in increased fraction of cycling (EdU+GFP+) cells within the population of infected (GFP+) cells (**Publication 2** Fig. 4C). The observed increase in GFP+ EdU+ cells results from an increase in the number of EdU+ OPCs (**Publication 2** Fig. 4D). The retrovirus targeted those OPCs which were in the cell cycle at the time of virus-injection. Thus the GFP+ cells are actively in the cell cycle or just completed one. The EdU only labels freshly synthetized DNA. Therefore GFP+EdU+ labeling is possible only if a cell continued cycling after its transduction with retrovirus. The increased fraction of EdU+NG2+ cells within GFP+ population upon pore mutations of AMPARs (Publication 2 Fig.4D) suggests that the expression of these subunit types drove OPCs to continue to cycle. In addition we found

that only the pore-dead mutation increased the EdU+ fraction of transfected OPCs (GFP+NG2+EdU+) significantly (**Publication 2** Fig. 4E), suggesting that the pore-dead construct was more efficient in driving further proliferation than the Ca^{2+}-permeable. This was supported by our finding that only the pore-dead construct increased the GFP+NG2+EdU+Ki67+ proportion within the previously-cycling population of OPCs (GFP+NG2+EdU+) (**Publication 2** Fig. 4G) on the 5th day of the experiment. The GFP+NG2+EdU+Ki67+ OPCs represent the population which was still actively cycling at the time of the sacrifice.

Overexpression of the C-tail did not alter the proliferation of OPCs (**Publication 2** Fig. 4C-E, G), but the proportion of OPCs was still higher upon this construct than in the GFP control (**Publication 2** Fig. 3E). These together suggest that C-tail indeed perturbs the differentiation of OPCs without driving significant increase in their proliferation.

Taken everything together in this section, two mechanisms may explain the increased ratio of OPCs upon the different constructs: either the transduced cells differentiate slower (or even leave the cell cycle to the G0 phase without differentiating); or OPCs proliferate rather than differentiate. Combining the differentiation and proliferation data (**Publication 2** Fig. 3H, FigS4) revealed that both EdU+ and EdU- OPCs contributed to the increased ratio of OPCs within the GFP+ cells, for all manipulations. Upon the pore-dead construct the EdU+ population was larger than the EdU-; for the C-tail and the Ca^{2+}-permeable the EdU- population was higher than the EdU+ (although to a different degree). These results together suggest that the AMPA receptors at axon – OPC synapses do modulate the fate of OPCs; and depending on the exact construct they can contribute to both mechanisms, i.e. lowering differentiation rate and increasing the proliferation.

Discussion and outlook

In my doctoral studies I have shown that OPCs give very different synaptic responses to dissimilar patterns of repetitive neuronal stimulation. As indicated by the AMPA receptor-mediated responses of OPCs, axons dynamically modulate the quantity and temporal profile of glutamate release at axon – OPC synapses in the corpus callosum. To my knowledge, we were the first to analyze in details the responses of OPCs to different repetitive neuronal firing patters. Our data provide new important pieces of information, because, in spite of the fact that cortical neurons often fire repetitively (Ramos et al., 2008; Vijayan et al., 2010; Zhu and Connors, 1999), and changes of neurotransmitter release at neuronal synapses during repetitive activity have been studied extensively (Balakrishnan and Mironov, 2018; Hennig, 2013; Kim and McCormick, 1998; Regehr, 2012; Wu and Borst, 1999; Zhang et al., 2011), no information has been previously available with this regard for axon – OPC synapses.

I also demonstrated in vivo that different patterns of axonal stimulation translate to distinct behavior of callosal OPCs: some frequencies promote differentiation of OPCs, while others rather enhance their proliferation. This is a remarkable finding because the studies before usually focused on testing only one stimulation frequency, and even used different brain regions for their studies.

We also found that physiological properties of the AMPA receptors at the axon – OPC synapses also play a crucial role in the regulation of the proliferation and differentiation of the OPCs.

These data together suggest that both pre- and post-synaptic properties of axon – OPC synapses play a key part in modulating the cellular fate and behavior of OPCs.

In my doctoral work, I have also provided an important *methodological* contribution to research on axon – OPC synapses: I have shown that the methods utilized by different researchers to increase the occurrence of quantal axon – OPC currents with a goal to investigate the properties these synapses are not interchangeable. I found that despite the pharmacological approaches (such as application of ruthenium red, high-osmolarity solutions or Strontium) are useful for increasing the frequency of quantal events, they might also change fundamental parameters of the glutamatergic synaptic transmission at axon – OPC contacts, i.e. quantal amplitude, rise- and

decay-times, or single channel conductance of AMPA receptors. Contrariwise, the dEPSC elicited by minimal electrical stimulation of callosal axons mirrored the amplitude distribution, rise- and decay-kinetics of spontaneous mEPSCs. Upon dEPSC events the estimated single channel conductance remained similar to the conductance upon mEPSCs. Therefore recording dEPSC with the purpose of quantal event detection is time-efficient; and dEPSC resemble greatly the "gold standards" of quanal events, the spontaneous miniature EPSCs.

Specific patterns of neuronal activity promote OPC proliferation and / or differentiation

The dynamic modulation of the myelination process is a type of plasticity of the CNS. This modern concept became widely established in the last few years (Fields, 2015). The formation of myelin coincides with the acquisition of new cognitive and motoric skills in humans (Bengtsson et al., 2005; Fields, 2008; Nagy et al., 2004); and also in rodents new myelin formation is a prerequisite of motoric learning (McKenzie et al., 2014). The new myelin sheaths are generated by OPCs differentiating into OLs (Emery, 2010), therefore it is crucial to understand what signals drive OPC differentiation and proliferation upon neuronal activity.

OPCs are one of the major proliferating cell types of the adult CNS. The continuous proliferation and differentiation capability of OPCs are crucial for the healthy functioning of the adult brain. OPCs provide a constant renewing basis (Psachoulia et al., 2009; Young et al., 2013) for myelination even in adulthood.

Mounting evidence *in vivo* suggest that the proliferation and the differentiation of OPCs are regulated by the activity of the nearby axons. Blocking action potentials in the optic nerve reduces the proliferation of OPCs (Barres and Raff, 1993). Enhancing the neuronal activity with electrical stimulation (Li et al., 2010; Nagy et al., 2017) or with optogenetic methods (Gibson et al., 2014) supports increased rate of proliferation and differentiation of OPCs. From these three studies (Gibson et al., 2014; Li et al., 2010; Nagy et al., 2017 (**Publication 1**)), we can draw several important conclusions. *First*, stimulation *frequency* is an important aspect in the regulation

of OPC proliferation: 333 Hz (Li et al., 2010); 20 Hz (Gibson et al., 2014); and 25 Hz and 300 Hz (**Publication 1** Fig.7-8.), all increased the rate of OPC proliferation, but to a different degree (**Publication 1** Fig.8.). However, 5 Hz stimulation did not increase the proliferation of OPCs (**Publication 1** Fig.7-8.). The 20 Hz stimulation (Gibson et al., 2014) seems more efficient in triggering proliferation and differentiation than the 25 Hz (**Publication 1** Fig.8.), despite the small frequency difference. However, as s*econd* conclusion, we can state that the effect of the stimulation seems to be graded, more pulses translate to a stronger effect: a total 18000 stimulation pulses in half an hour (Gibson et al., 2014), or 1620000 electrical pulses over 10 days (Li et al., 2010) were more efficient in triggering proliferation than 720 pulses delivered over three hours (**Publication 1** Fig.7-8.). This would also explain why 20 Hz stimulation applied by Gibson et al. was more efficient in triggering stimulation than the 25 Hz stimulation applied in our study. *Third*, lower frequencies of stimulation are more effective in triggering differentiation: 20 Hz (Gibson et al., 2014) and 5 Hz (**Publication 1** Fig.7-8.) both increased the differentiation rate significantly, while 25 Hz and 300 Hz failed to do so (**Publication 1** Fig.7-8.)(Nagy et al., 2017)(Nagy et al., 2017)(Nagy et al., 2017)(Nagy et al., 2017)(Nagy et al., 2017)(Nagy et al., 2017)(Nagy et al., 2017)(Nagy et al., 2017). *Fourth*, newly born OPCs (indicated by their EdU+ labeling) more readily respond by differentiation to these manipulations, as indicated by the increased ratio of EdU+ OL upon 20 Hz (Gibson et al., 2014), 5 Hz, 25 Hz and 300 Hz (**Publication 1** Fig.7-8.) stimulation paradigms.

The adaptation of these conclusions to more natural manipulations of the neuronal activity is challenging. Increased physical activity or enriched environment promotes OPC proliferation in the amygdala, and also influences their differentiation (Ehninger et al., 2011), but it is problematic to predict what kind of neuronal activity the OPCs detect in these "brain states" (exploration or physical activity vs. "baseline"). For example, regularly spiking pyramidal neurons of the barrel cortex have an average firing rate of 8 Hz, but upon whisker-vibration this can reach up to 35 Hz (Vijayan et al., 2010). This firing range is close to our tested paradigms (5 Hz and 25, Hz), but what the OPCs actually detect and *decode* from this dynamically changing activity is uncertain. To complicate things further, while whisker-lesion reduces the glutamatergic input to OPCs in the barrel cortex, it

increases OPC proliferation. Further investigations are necessary to identify the properties of neuronal signaling to OPCs *in vivo*. For example, patch-clamping OPCs in the barrel cortex *in vivo* while stimulating the whiskers would reveal precisely what OPCs can detect in the exploratory state of a mouse.

OPCs can distinguish different patterns of axonal stimulation via their glutamatergic synapses

The physiology and location of glutamatergic synapses on OPCs make them a prime candidate for detecting neuronal signals and translate it to various cellular processes. We think that OPCs are able to distinguish the distinct firing patterns of their presynaptic neurons (**Publication 1,** Fig.1, 3-5.) because: 1. the degree of the short-term facilitation of the *phasic* synaptic transmission at axon – OPC synapses depends on the number and frequency of pulses during repetitive axonal stimulation. 2. The *delayed* release of glutamate at the axon – OPC synapses depends on the frequency of the firing and the number of action potentials as well. 3. The temporal distribution of the charge transferred through the AMPA receptors in OPCs, as well as the pattern of the charge oscillations differ: at higher axonal stimulation frequencies (100 Hz) the charge goes through the receptors in one large bulk, whereas upon lower stimulation frequencies (5 Hz and 25 Hz) it oscillates according to this frequency of the stimulation.

Predicting how OPCs decode these type of oscillations can vary according to how we consider these signals. Activation of AMPA receptors can be simply seen as a bioelectrical signal to OPCs: the AMPA receptor activation will lead to depolarization because the resting membrane potential of the OPC. The temporal pattern of membrane potential changes, e.g. during repetitive neuronal activity, may contribute to the bioelectrical control of cell cycle (Blackiston et al., 2009), e.g. through DNA-synthesis inhibition (LoTurco et al., 1995); or inversely, by stimulating the proliferation through cyclin-dependent kinase 2 activation (Seo et al., 2006). In neurons, same amount but different timing of electrical activity triggers transcription of dissimilar genes (Lee et al., 2017). Similarly, the exact nature of temporal and spatial distribution of the membrane depolarization may

play a significant role in the regulation of cell cycle and differentiation of OPCs.

Physiological properties of AMPA receptor at axon – OPC synapses modulate OPC proliferation and differentiation

Several signal transductions pathways could be triggered downstream of AMPA receptor activation (Henley and Wilkinson, 2013; Qin et al., 2005). For example, AMPA receptor activation can influence the mitogen-activated protein kinase pathway (Kuroda et al., 2001), which directly modulates cell cycle and cellular fate. In neurons, the C-tail of the AMPA receptor is responsible for the binding of intracellular partner-molecules, and the over-expression of the C-tail perturbs the subunit trafficking (Bassani et al., 2009). We found that over-expression of the C-tail of the GluA2 subunit in OPCs significantly impairs their differentiation, without changing the ionic currents through the AMPA receptors (**Publication 2** Fig.2). This suggests that not just the bioelectrical signaling and / or ionic currents through AMPA receptors play a role in regulating the differentiation of OPCs (see below), but the intracellular binding partners of AMPA receptors are just as important (Henley, 2003) in the signal transduction. The underlying downstream signaling cascade is yet to be identified.

One can look at the repeated activation of AMPA receptors as a purely bioelectrical signal (see previous section), but the type of ions which the AMPA receptor channels are letting through can be also important. AMPA receptors are mainly permeable for K^+ and Na^+, but depending on their subunit composition, AMPA receptors can be permeable for Ca^{2+} as well (Hume et al., 1991). Migration (Tong et al., 2009) and differentiation (Cheli et al., 2015) of OPCs is known to be dependent on intracellular Ca^{2+}-dynamics, and therefore it may be influenced by Ca^{2+}-permeability of AMPA receptors activated by neuronal firing. Ca^{2+}-permeability of AMPA receptors could be also crucial for the regulation of proliferation for OPCs, for example Ca^{2+} is a vital modulator of proliferation of neuronal progenitors (Jansson and Åkerman, 2014), tumor cells (Cui et al., 2017), and endothelial cells (Moccia et al., 2012). AMPA receptors in callosal OPCs in young mice are impermeable for Ca^{2+} (Ziskin et al., 2007), and the OPCs have short cell-cycle time and proliferate quickly (Psachoulia

et al., 2009; Young et al., 2013). In the adult mice, callosal OPCs express Ca^{2+}-permeable AMPA receptors, while having much longer cell cycle phases and lower differentiation capabilities. This may indicate that the Ca^{2+}-permeability is a key feature of AMPA receptors in controlling the proliferation and differentiation of OPCs. We tested this hypothesis by transducing the OPCs with different retroviral vectors. The expression of unedited GluA2(R583Q)-GFP subunit ("Ca^{2+}-permeable"), or the expression of the of the GluA2(R583E)-GFP subunit ("pore-dead") (**Publication 2** Fig.2) both lead to increased expression of Ca^{2+}-permeable AMPA receptors (**Publication 2** Fig.2) at the axon – OPC synapses, which drove the OPCs towards proliferation instead of differentiation (**Publication 2** Fig.3-4). Interestingly, we detected a very wide range of rectification indices both in intact (**Publication 2** Fig. S1B) and in GFP-transduced OPCs (**Publication 2** Fig. 2E). This means that in physiological conditions some OPCs express more Ca^{2+}-permeable AMPA receptors than the others. This would imply that there are more subpopulations of OPCs. Based on our findings (**Publication 2** Fig. 3-4), it is plausible that OPCs with higher rectification indices more likely proliferate, thus providing continuous self-renewal for the OPC population; while other OPCs with lower rectification indices more likely differentiate, and responsible for myelin generation. There is independent, indirect evidence for this: based on transcriptomic analysis of oligodendrocyte lineage cells (Marques et al., 2016), there are two distinct populations of oligodendrocyte precursors: the OPCs and the "differentiation-committed oligodendrocyte precursors" (COPs). The differences are subtle and most of the transcriptomic content is similar. However, COPs express less cell-cycle related markers than OPCs, and increase the expression of genes involved in migration. Most likely in our study the "OPCs" were a pooled population of OPCs and COPs.

The specific patterns of axonal firing and *AMPA receptor properties regulate together the proliferation and differentiation of OPCs*

In adult naïve mice most callosal OPCs have Ca^{2+}-permeable AMPA receptors (Ziskin et al., 2007). Making the APMA receptors into Ca^{2+}-permeable in mice pups therefore mimics the "adult" phenotype of OPCs. Our results indicate that the higher proportion of Ca^{2+}-

permeable AMPA receptors lead to decreased differentiation and increased proliferation (**Publication 2** Fig. 3-4). We stimulated the callosal axons in adult animals (**Publication 1** Fig. 7-8), yet the OPCs responded readily by differentiation to callosal stimulation of 5 Hz, without significant increase in OPC proliferation. This suggests that the two factors (presynaptic activation pattern and type of postsynaptic AMPA receptor) together determine the final behavior of the OPCs. This also raises the possibility that the optimal axon-activation patterns for promoting OPC proliferation or differentiation are fundamentally different in young mice and older mice; just because of the different AMPA-receptor set of the OPCs.

Final remarks

So how do the axonal activity and AMPA receptor activation translate into OPC proliferation or differentiation? Through which signal transduction mechanism(s) the OPCs decode the information? These questions are still not answered. It also still has to be discovered which neuronal firing patterns in vivo are the most efficient in triggering / blocking proliferation and differentiation of OPCs. The exact role of AMPA receptor in OPCs for regulation of these cellular processes also should be further investigated. Other key factors released by neurons could affect behavior and function of OPCs, will have to be identified, not just in vitro, but in vivo as well. It is almost certain that glutamate release is not the only cue from axons that is important for OPCs: co-release of other factors, such as ATP (Wake et al., 2015), adenosine, or nitric-oxide (Garthwaite et al., 2015) may also play an important role in vivo. In future studies, the intracellular signaling pathways leading to proliferation and differentiation will have to be dissected. One possibility might be to look at the transcriptional changes in the OPCs upon various axonal stimulation paradigms. In this way, a gene network, switched on in OPCs by the different patterns of neuronal activity and leading to either proliferation or differentiation can be identified. The role of Ca^{2+} in the signal transduction pathways will also have to be further clarified. Although from our studies the Ca^{2+}-permeability of the AMPA receptors seems to be crucial in the regulation of OPC proliferation

and differentiation, we cannot rule out that other intracellular calcium sources contribute or amplify the effect through their Ca^{2+}-release.
It is vital to understand in details the mechanisms leading to proliferation or differentiation of OPCs, as here may lay the key for healing severe pathological conditions, such as multiple sclerosis or certain types of glioblastomas. Such research directions, based on the results presented here, might be able to open new perspectives in treating these severe oligodendroglia-related diseases.

Abbreviations

AMPA: α-amino-3-hydroxy-5-methyl-4-isoxazolepropionic acid

ATP: adenosine triphosphate

Atx: ω-Agatoxin-IVA

BrdU: 5-bromo-2'-deoxyuridine

Casp-3: caspase 3

CD68: cluster of differentiation 68

CC1: anti-adenomatous polyposis coli clone 1

CNS: central nervous system

COP: differentiation-committed oligodendrocyte precursor

Ctx: ω-Conotoxin-GVIA

dEPSC: delayed excitatory postsynaptic current

DNQX: 6,7-dinitroquinoxaline-2,3-dione

DRG: dorsal root ganglion

EdU: 5-ethynyl-2´-deoxyuridine

EGTA-AM: ethylene glycol tetraacetic acid acetoxymethyl ester

EPSC: excitatory postsynaptic current

GABA: gamma-aminobutyric acid

GFP: green fluorescent protein

mEPSC: miniature excitatory postsynaptic current

NG2: neural/glial antigen 2 proteoglycan

NSFA: non-stationary fluctuation analysis

OL: myelinating oligodendrocyte

OPC: oligodendrocyte precursor cell

pre-OL: premyelinating oligodendrocyte

PDGF-Rα: receptor alpha for platelet-derived growth factor

PLP/DM20: proteolipid protein 1

TTX: tetrodotoxin

VGCC: voltage-gated calcium channel

Appendix

Materials and Methods for Part I: "Identify the most efficient method to estimate the quantal physiological parameters of the neuron-OPC glutamatergic synapses"

Electrophysiology: All patch-clamp recordings were performed as described in details in **Publication 1** (Nagy et al., 2017) and / or in **Publication 2** (Chen et al., 2018).

Briefly: Recording solution: Ringer solution containing (in mM): 124 NaCl, 3 KCl, 1.25 $NaH_2PO_4*H_2O$, 2 $MgCl_2$, 2 $CaCl_2$, 26 $NaHCO_3$, 10 glucose; 300 mOsm/kg; 7.4 pH; gassed with carbogen. Patch-pipettes had 5-7 MOhm resistance, and were filled with (in mM): 125 K-gluconate, 2 Na_2ATP, 2 $MgCl_2$, 0.5 EGTA, 10 HEPES, 20 KCl, 3 NaCl; 280–290 mOsm/kg, titrated to pH 7.3 with KOH. All recordings of synaptic currents were performed in the presence of NMDA-receptor antagonist (RS)-3-(2-Carboxypiperazin-4-yl)-propyl-1-phosphonic acid (CPP) and $GABA_A$-receptor antagonist (RS)-3-(2-Carboxypiperazin-4-yl)-propyl-1-phosphonic acid (gabazine, 5 μM). All drugs were added to Ringer solution and perfused via the bath or applied locally. The following experimental paradigms were applied:

1. mEPSC: TTX was perfused in order to block action potentials, and spontaneous EPSC events were recorded
2. RR: same as 1., but in addition 100 μM ruthenium red was perfused

3. Sucrose: local application of 500 mM through a patch pipette with 3-4.5 µm opening, by pneumatic drug ejection system with microJECT (PDES; NPI Electronic)
4. dEPSC – minimal: electrical stimulation of single axons with 20 pulses at 100 Hz, as described in Publication 1 (Nagy et al., 2017)
5. dEPSC – non-minimal: as in 4., but with higher stimulation intensity
6. Strontium: as in 4., but in the Ringer solution Ca^{2+} was removed, Mg^{2+} was reduced to 1 mM, and 3 mM Sr^{2+} was added.

All data analysis was performed as described in Nagy et al. 2017. The amplitude histograms (both conventional and cumulative) were built for each recorded cell individually, and then the resulting histograms were averaged for the graphs.

Skewness was defined for the histogram of each cell as:

$$Skewness = \frac{1}{V\_npnts} \sum_{i=0}^{V_{npnts}-1} \left[\frac{Yi - \overline{Y}}{\sigma}\right]^3$$

Where *V_npnts* = number of EPSC events recorded from one cell; *Yi* = amplitude of single EPSC; $\overline{Y}$ = mean of single EPSC amplitudes for the given cell; σ = standard deviation of the mean of the amplitude.

Coefficient of variance of the amplitude was defined as:

$$CV = \frac{\overline{A}}{\sigma} \text{x} 100$$

Where $\overline{A}$ =mean amplitude of events recorded from single cells; σ = standard deviation of the mean of the amplitude.

Number of cells included in Part I. of the thesis: mEPSC: 10; RR: 13; Sucrose: 11; dEPSC – minimal stimulation: 16; dEPSC – non-minimal stimulation: 10; Strontium: 10. To avoid pseudo-replications, we did not perform the same type of experiment from

brain slices the same mouse. Occasionally, we recorded different protocols from the same cell. A total number of 57 cells were included in the analysis.

Non-stationary fluctuation analysis (NSFA): to estimate single-channel conductance of AMPA receptors we performed peak-scaled NSFA based on (Hartveit and Veruki, 2007). The analysis flow is described in details in Chen et al 2018. The differences are: we analyzed the EPSC events separately for small (<6.5 pA) and large (>6.5 pA) events. The numbers of analyzed EPSC events were: 112 small events from 10 cells for mEPSC; 300 small and 170 large events from 9 cells for RR; 185 small and 114 large events from 7 cells for sucrose; 182 small and 87 large events from 12 cells for dEPSC – minimal; 113 small and 69 large events from 10 cells for dEPSC – non-minimal; 166 small and 182 large events from 7 cells for dEPSC – Strontium. In the mEPSC group there were not enough large events, even after we pooled the experimental data from 10 cells, therefore we could not analyze single-channel conductance of large mEPSC events.
For the other publications included in this thesis, the Materials and Methods are described within the publications (see below!).

References

Arenkiel, B.R., Peca, J., Davison, I.G., Feliciano, C., Deisseroth, K., Augustine, G.J., Ehlers, M.D., Feng, G., 2007. In Vivo Light-Induced Activation of Neural Circuitry in Transgenic Mice Expressing Channelrhodopsin-2. Neuron 54, 205–218. doi:10.1016/j.neuron.2007.03.005

Auger, C., Ogden, D., 2010. AMPA receptor activation controls type I metabotropic glutamate receptor signalling via a tyrosine kinase at parallel fibre-Purkinje cell synapses. J. Physiol. 588, 3063–74. doi:10.1113/jphysiol.2010.191080

Balakrishnan, S., Mironov, S.L., 2018. Regenerative glutamate release in the hippocampus of Rett syndrome model mice. PLoS One 13, e0202802. doi:10.1371/journal.pone.0202802

Bao, H., Ran, P., Zhu, M., Sun, L., Li, B., Hou, Y., Nie, J., Shan, L., Li, H., Zheng, S., Xu, X., Xiao, C., Du, J., 2016. The Prefrontal Dectin-1/AMPA Receptor Signaling Pathway Mediates The Robust and Prolonged Antidepressant Effect of Proteo-β-Glucan from Maitake. Sci. Rep. 6, 28395. doi:10.1038/srep28395

Barres, B.A., Koroshetz, W.J., Swartz, K.J., Chun, L.L., Corey, D.P., 1990. Ion channel expression by white matter glia: the O-2A glial progenitor cell. Neuron 4, 507–24. doi:10.1016/0896-6273(90)90109-S

Barres, B.A., Raff, M.C., 1993. Proliferation of oligodendrocyte precursor cells depends on electrical activity in axons. Nature 361, 258–260. doi:10.1038/361258a0

Bassani, S., Valnegri, P., Beretta, F., Passafaro, M., 2009. The GLUR2 subunit of AMPA receptors: Synaptic role. Neuroscience 158, 55–61. doi:10.1016/J.NEUROSCIENCE.2008.10.007

Baumann, N., Pham-Dinh, D., 2001. Biology of Oligodendrocyte and Myelin in the Mammalian Central Nervous System. Physiol. Rev. 81, 871–927. doi:10.1152/physrev.2001.81.2.871

Bekkers, J.M., Clements, J.D., 1999. Quantal amplitude and quantal variance of strontium-induced asynchronous EPSCs in rat dentate granule neurons. J. Physiol. 516 (Pt 1), 227–48. doi:10.1111/J.1469-7793.1999.227AA.X

Bekkers, J.M., Richerson, G.B., Stevens, C.F., 1990. Origin of variability in quantal size in cultured hippocampal neurons and hippocampal slices. Proc. Natl. Acad. Sci. U. S. A. 87, 5359–62.

Bengtsson, S.L., Nagy, Z., Skare, S., Forsman, L., Forssberg, H., Ullén, F., 2005. Extensive piano practicing has regionally specific effects on white matter development. Nat. Neurosci. 8, 1148–1150. doi:10.1038/nn1516

Berger, T., 1995. AMPA-type glutamate receptors in glial precursor cells of the rat corpus callosum: Ionic and pharmacological properties. Glia 14, 101–114. doi:10.1002/glia.440140205

Berger, T., Walz, W., Schnitzer, J., Kettenmann, H., 1992. GABA- and glutamate-activated currents in glial cells of the mouse corpus callosum slice. J. Neurosci. Res. 31, 21–27. doi:10.1002/jnr.490310104

Bergles, D.E., Jabs, R., Steinhäuser, C., 2010. Neuron-glia synapses in the brain. Brain Res. Rev. 63, 130–7. doi:10.1016/j.brainresrev.2009.12.003

Bergles, D.E., Roberts, J.D.B., Somogyi, P., Jahr, C.E., 2000. Glutamatergic synapses on oligodendrocyte precursor cells in the hippocampus. Nature 405, 187–191. doi:10.1038/35012083

Blackiston, D.J., McLaughlin, K.A., Levin, M., 2009. Bioelectric controls of cell proliferation: ion channels, membrane voltage and the cell cycle. Cell Cycle 8, 3527–36. doi:10.4161/cc.8.21.9888

Bliss, T.V.P., Collingridge, G.L., Morris, R.G.M., 2014. Synaptic plasticity in health and disease: introduction and overview. Philos. Trans. R. Soc. Lond. B. Biol. Sci. 369, 20130129. doi:10.1098/rstb.2013.0129

Bowie, D., Mayer, M.L., 1995. Inward rectification of both AMPA and kainate subtype glutamate receptors generated by polyamine-mediated ion channel block. Neuron 15, 453–62.

Chater, T.E., Goda, Y., 2014. The role of AMPA receptors in postsynaptic mechanisms of synaptic plasticity. Front. Cell. Neurosci. 8, 401. doi:10.3389/fncel.2014.00401

Cheli, V.T., Santiago González, D.A., Spreuer, V., Paez, P.M., 2015. Voltage-gated Ca2+ entry promotes oligodendrocyte progenitor cell maturation and myelination in vitro. Exp. Neurol. 265, 69–83. doi:10.1016/j.expneurol.2014.12.012

Chen, T.-J., Kula, B., Nagy, B., Barzan, R., Gall, A., Ehrlich, I., Kukley, M., 2018. In Vivo Regulation of Oligodendrocyte Precursor Cell Proliferation and Differentiation by the AMPA-Receptor Subunit GluA2. Cell Rep. 25, 852–861.e7. doi:10.1016/j.celrep.2018.09.066

Chittajallu, R., Aguirre, A., Gallo, V., 2004. NG2-positive cells in the mouse white and grey matter display distinct physiological properties. J. Physiol. 561, 109–22. doi:10.1113/jphysiol.2004.074252

Cui, C., Merritt, R., Fu, L., Pan, Z., 2017. Targeting calcium signaling in cancer therapy. Acta Pharm. Sin. B 7, 3–17. doi:10.1016/j.apsb.2016.11.001

Dawson, M.R., Polito, A., Levine, J.M., Reynolds, R., 2003. NG2-expressing glial progenitor cells: an abundant and widespread population of cycling cells in the adult rat CNS. Mol. Cell. Neurosci. 24, 476–488. doi:10.1016/S1044-7431(03)00210-0

De Biase, L.M., Nishiyama, A., Bergles, D.E., 2010. Excitability and synaptic communication within the oligodendrocyte lineage. J. Neurosci. 30, 3600–11. doi:10.1523/JNEUROSCI.6000-09.2010

Demerens, C., Stankoff, B., Logak, M., Anglade, P., Allinquant, B., Couraud, F., Zalc, B., Lubetzki, C., 1996. Induction of myelination in the central nervous system by electrical activity.

Proc. Natl. Acad. Sci. U. S. A. 93, 9887–92.

Dimou, L., Simon, C., Kirchhoff, F., Takebayashi, H., Götz, M., 2008. Progeny of Olig2-expressing progenitors in the gray and white matter of the adult mouse cerebral cortex. J. Neurosci. 28, 10434–42. doi:10.1523/JNEUROSCI.2831-08.2008

Dingledine, R., Hume, R.I., Heinemann, S.F., 1992. Structural determinants of barium permeation and rectification in non-NMDA glutamate receptor channels. J. Neurosci. 12, 4080–7. doi:10.1523/JNEUROSCI.12-10-04080.1992

Edwards, F.A., 1995. Anatomy and electrophysiology of fast central synapses lead to a structural model for long-term potentiation. Physiol. Rev. 75, 759–787. doi:10.1152/physrev.1995.75.4.759

Ehninger, D., Wang, L.-P., Klempin, F., Römer, B., Kettenmann, H., Kempermann, G., 2011. Enriched environment and physical activity reduce microglia and influence the fate of NG2 cells in the amygdala of adult mice. Cell Tissue Res. 345, 69–86. doi:10.1007/s00441-011-1200-z

Emery, B., 2010. Regulation of oligodendrocyte differentiation and myelination. Science 330, 779–82. doi:10.1126/science.1190927

Fame, R.M., MacDonald, J.L., Macklis, J.D., 2011. Development, specification, and diversity of callosal projection neurons. Trends Neurosci. 34, 41–50. doi:10.1016/j.tins.2010.10.002

Fields, R.D., 2015. A new mechanism of nervous system plasticity: activity-dependent myelination. Nat. Rev. Neurosci. 16, 756–767. doi:10.1038/nrn4023

Fields, R.D., 2008. White matter in learning, cognition and psychiatric disorders. Trends Neurosci. 31, 361–70. doi:10.1016/j.tins.2008.04.001

Freeman, S.A., Desmazières, A., Fricker, D., Lubetzki, C., Sol-Foulon, N., 2016. Mechanisms of sodium channel clustering and its influence on axonal impulse conduction. Cell. Mol. Life

Sci. 73, 723–35. doi:10.1007/s00018-015-2081-1

Fröhlich, N., Nagy, B., Hovhannisyan, A., Kukley, M., 2011. Fate of neuron-glia synapses during proliferation and differentiation of NG2 cells. J. Anat. 219, 18–32. doi:10.1111/j.1469-7580.2011.01392.x

Garthwaite, G., Hampden-Smith, K., Wilson, G.W., Goodwin, D.A., Garthwaite, J., 2015. Nitric oxide targets oligodendrocytes and promotes their morphological differentiation. Glia 63, 383–399. doi:10.1002/glia.22759

Ge, W.-P., Yang, X.-J., Zhang, Z., Wang, H.-K., Shen, W., Deng, Q.-D., Duan, S., 2006. Long-term potentiation of neuron-glia synapses mediated by Ca2+-permeable AMPA receptors. Science 312, 1533–7. doi:10.1126/science.1124669

Gerdes, J., Lemke, H., Baisch, H., Wacker, H.H., Schwab, U., Stein, H., 1984. Cell cycle analysis of a cell proliferation-associated human nuclear antigen defined by the monoclonal antibody Ki-67. J. Immunol. 133, 1710–5.

Gibson, E.M., Purger, D., Mount, C.W., Goldstein, A.K., Lin, G.L., Wood, L.S., Inema, I., Miller, S.E., Bieri, G., Zuchero, J.B., Barres, B.A., Woo, P.J., Vogel, H., Monje, M., 2014. Neuronal activity promotes oligodendrogenesis and adaptive myelination in the mammalian brain. Science 344, 1252304. doi:10.1126/science.1252304

Griffiths, I., Klugmann, M., Anderson, T., Yool, D., Thomson, C., Schwab, M.H., Schneider, A., Zimmermann, F., McCulloch, M., Nadon, N., Nave, K.A., 1998. Axonal swellings and degeneration in mice lacking the major proteolipid of myelin. Science 280, 1610–3. doi:10.1126/SCIENCE.280.5369.1610

Hartline, D.K., Colman, D.R., 2007. Rapid Conduction and the Evolution of Giant Axons and Myelinated Fibers. Curr. Biol. 17, R29–R35. doi:10.1016/J.CUB.2006.11.042

Hartveit, E., Veruki, M.L., 2007. Studying properties of neurotransmitter receptors by non-stationary noise analysis of

spontaneous postsynaptic currents and agonist-evoked responses in outside-out patches. Nat. Protoc. 2, 434–448. doi:10.1038/nprot.2007.47

Henley, J.M., 2003. Proteins interactions implicated in AMPA receptor trafficking: a clear destination and an improving route map. Neurosci. Res. 45, 243–54.

Henley, J.M., Wilkinson, K.A., 2013. AMPA receptor trafficking and the mechanisms underlying synaptic plasticity and cognitive aging. Dialogues Clin. Neurosci. 15, 11–27.

Hennig, M.H., 2013. Theoretical models of synaptic short term plasticity. Front. Comput. Neurosci. 7, 45. doi:10.3389/fncom.2013.00045

Hossain, S., Liu, H.-N., Fragoso, G., Almazan, G., 2014. Agonist-induced down-regulation of AMPA receptors in oligodendrocyte progenitors. Neuropharmacology 79, 506–514. doi:10.1016/J.NEUROPHARM.2013.12.020

Hume, R.I., Dingledine, R., Heinemann, S.F., 1991. Identification of a site in glutamate receptor subunits that controls calcium permeability. Science 253, 1028–31.

Isaac, J.T.R., Ashby, M.C., McBain, C.J., 2007. The role of the GluR2 subunit in AMPA receptor function and synaptic plasticity. Neuron 54, 859–71. doi:10.1016/j.neuron.2007.06.001

Jansson, L.C., Åkerman, K.E., 2014. The role of glutamate and its receptors in the proliferation, migration, differentiation and survival of neural progenitor cells. J. Neural Transm. 121, 819–836. doi:10.1007/s00702-014-1174-6

Káradóttir, R., Hamilton, N.B., Bakiri, Y., Attwell, D., 2008. Spiking and nonspiking classes of oligodendrocyte precursor glia in CNS white matter. Nat. Neurosci. 11, 450–6. doi:10.1038/nn2060

Kessels, H.W., Malinow, R., 2009. Synaptic AMPA receptor

plasticity and behavior. Neuron 61, 340–50. doi:10.1016/j.neuron.2009.01.015

Kim, U., McCormick, D.A., 1998. The functional influence of burst and tonic firing mode on synaptic interactions in the thalamus. J. Neurosci. 18, 9500–16. doi:10.1523/JNEUROSCI.18-22-09500.1998

Klugmann, M., Schwab, M.H., Pühlhofer, A., Schneider, A., Zimmermann, F., Griffiths, I.R., Nave, K.A., 1997. Assembly of CNS myelin in the absence of proteolipid protein. Neuron 18, 59–70. doi:10.1016/S0896-6273(01)80046-5

Kougioumtzidou, E., Shimizu, T., Hamilton, N.B., Tohyama, K., Sprengel, R., Monyer, H., Attwell, D., Richardson, W.D., 2017. Signalling through AMPA receptors on oligodendrocyte precursors promotes myelination by enhancing oligodendrocyte survival. Elife 6. doi:10.7554/eLife.28080

Kreitzer, A.C., Gee, K.R., Archer, E.A., Regehr, W.G., 2000. Monitoring presynaptic calcium dynamics in projection fibers by in vivo loading of a novel calcium indicator. Neuron 27, 25–32. doi:10.1016/S0896-6273(00)00006-4

Kukley, M., Capetillo-Zarate, E., Dietrich, D., 2007. Vesicular glutamate release from axons in white matter. Nat. Neurosci. 10, 311–320. doi:10.1038/nn1850

Kukley, M., Nishiyama, A., Dietrich, D., 2010. The Fate of Synaptic Input to NG2 Glial Cells: Neurons Specifically Downregulate Transmitter Release onto Differentiating Oligodendroglial Cells. J. Neurosci. 30, 8320–8331. doi:10.1523/JNEUROSCI.0854-10.2010

Kuroda, S., Schweighofer, N., Kawato, M., 2001. Exploration of signal transduction pathways in cerebellar long-term depression by kinetic simulation. J. Neurosci. 21, 5693–702.

Lee, P.R., Cohen, J.E., Iacobas, D.A., Iacobas, S., Fields, R.D., 2017. Gene networks activated by specific patterns of action potentials in dorsal root ganglia neurons. Sci. Rep. 7, 43765.

doi:10.1038/srep43765

Li, Q., Brus-Ramer, M., Martin, J.H., McDonald, J.W., 2010. Electrical stimulation of the medullary pyramid promotes proliferation and differentiation of oligodendrocyte progenitor cells in the corticospinal tract of the adult rat. Neurosci Lett. 479.

Lin, S., Huck, J.H.J., Roberts, J.D.B., Macklin, W.B., Somogyi, P., Bergles, D.E., 2005. Climbing Fiber Innervation of NG2-Expressing Glia in the Mammalian Cerebellum. Neuron 46, 773–785. doi:10.1016/J.NEURON.2005.04.025

LoTurco, J.J., Owens, D.F., Heath, M.J.S., Davis, M.B.E., Kriegstein, A.R., 1995. GABA and glutamate depolarize cortical progenitor cells and inhibit DNA synthesis. Neuron 15, 1287–1298. doi:10.1016/0896-6273(95)90008-X

Mangin, J.-M., Li, P., Scafidi, J., Gallo, V., 2012. Experience-dependent regulation of NG2 progenitors in the developing barrel cortex. Nat. Neurosci. 15, 1192–1194. doi:10.1038/nn.3190

Marques, S., Zeisel, A., Codeluppi, S., van Bruggen, D., Mendanha Falcão, A., Xiao, L., Li, H., Häring, M., Hochgerner, H., Romanov, R.A., Gyllborg, D., Muñoz Manchado, A., La Manno, G., Lönnerberg, P., Floriddia, E.M., Rezayee, F., Ernfors, P., Arenas, E., Hjerling-Leffler, J., Harkany, T., Richardson, W.D., Linnarsson, S., Castelo-Branco, G., 2016. Oligodendrocyte heterogeneity in the mouse juvenile and adult central nervous system. Science 352, 1326–1329. doi:10.1126/science.aaf6463

McKenzie, I.A., Ohayon, D., Li, H., de Faria, J.P., Emery, B., Tohyama, K., Richardson, W.D., 2014. Motor skill learning requires active central myelination. Science 346, 318–22. doi:10.1126/science.1254960

Miron, V.E., Kuhlmann, T., Antel, J.P., 2011. Cells of the oligodendroglial lineage, myelination, and remyelination. Biochim. Biophys. Acta - Mol. Basis Dis. 1812, 184–193.

doi:10.1016/J.BBADIS.2010.09.010

Moccia, F., Dragoni, S., Lodola, F., Bonetti, E., Bottino, C., Guerra, G., Laforenza, U., Rosti, V., Tanzi, F., 2012. Store-dependent Ca(2+) entry in endothelial progenitor cells as a perspective tool to enhance cell-based therapy and adverse tumour vascularization. Curr. Med. Chem. 19, 5802–18.

Momiyama, A., Silver, R.A., Hausser, M., Notomi, T., Wu, Y., Shigemoto, R., Cull-Candy, S.G., 2003. The density of AMPA receptors activated by a transmitter quantum at the climbing fibre-Purkinje cell synapse in immature rats. J. Physiol. 549, 75–92. doi:10.1113/jphysiol.2002.033472

Nagy, B., Hovhannisyan, A., Barzan, R., Chen, T., Kukley, M., 2017. Different patterns of neuronal activity trigger distinct responses of oligodendrocyte precursor cells in the corpus callosum. doi:10.1371/journal.pbio.2001993

Nagy, Z., Westerberg, H., Klingberg, T., 2004. Maturation of White Matter is Associated with the Development of Cognitive Functions during Childhood. J. Cogn. Neurosci. 16, 1227–1233. doi:10.1162/0898929041920441

Nave, K.-A., 2010. Myelination and support of axonal integrity by glia. Nature 468, 244–252. doi:10.1038/nature09614

Nishiyama, A., Lin, X.-H., Giese, N., Heldin, C.-H., Stallcup, W.B., 1996. Co-localization of NG2 proteoglycan and PDGF ?-receptor on O2A progenitor cells in the developing rat brain. J. Neurosci. Res. 43, 299–314. doi:10.1002/(SICI)1097-4547(19960201)43:3<299::AID-JNR5>3.0.CO;2-E

O'Connor, D.H., Peron, S.P., Huber, D., Svoboda, K., 2010. Neural Activity in Barrel Cortex Underlying Vibrissa-Based Object Localization in Mice. Neuron 67, 1048–1061. doi:10.1016/J.NEURON.2010.08.026

Passlick, S., Trotter, J., Seifert, G., Steinhäuser, C., Jabs, R., 2016. The NG2 Protein Is Not Required for Glutamatergic Neuron–NG2 Cell Synaptic Signaling. Cereb. Cortex 26, 51–57.

doi:10.1093/cercor/bhu171

Peters, A., Palay, S.L., Webster, H.D., 1978. The fine structure of the nervous system: The neurons and supporting cells. Ann. Neurol. 4, 588–588. doi:10.1002/ana.410040660

Peyron, F., Timsit, S., Thomas, J.-L., Kagawa, T., Ikenaka, K., Zalc, B., 1997. In situ expression of PLP/DM-20, MBP, and CNP during embryonic and postnatal development of the jimpy mutant and of transgenic mice overexpressing PLP. J. Neurosci. Res. 50, 190–201. doi:10.1002/(SICI)1097-4547(19971015)50:2<190::AID-JNR8>3.0.CO;2-A

Psachoulia, K., Jamen, F., Young, K.M., Richardson, W.D., 2009. Cell cycle dynamics of NG2 cells in the postnatal and ageing brain. Neuron Glia Biol. 5, 57. doi:10.1017/S1740925X09990354

Qin, Y., Zhu, Y., Baumgart, J.P., Stornetta, R.L., Seidenman, K., Mack, V., van Aelst, L., Zhu, J.J., 2005. State-dependent Ras signaling and AMPA receptor trafficking. Genes Dev. 19, 2000–15. doi:10.1101/gad.342205

Ramos, R.L., Tam, D.M., Brumberg, J.C., 2008. Physiology and morphology of callosal projection neurons in mouse. Neuroscience 153, 654–63. doi:10.1016/j.neuroscience.2008.02.069

Ransom, B.R., Christian, C.N., Bullock, P.N., Nelson, P.G., 1977. Mouse spinal cord in cell culture. II. Synaptic activity and circuit behavior. J. Neurophysiol. 40, 1151–62. doi:10.1152/jn.1977.40.5.1151

Ransom, B.R., Neale, E., Henkart, M., Bullock, P.N., Nelson, P.G., 1977. Mouse spinal cord in cell culture. I. Morphology and intrinsic neuronal electrophysiologic properties. J. Neurophysiol. 40, 1132–1150. doi:10.1152/jn.1977.40.5.1132

Rasband, M.N., Peles, E., 2015. The Nodes of Ranvier: Molecular Assembly and Maintenance. Cold Spring Harb. Perspect. Biol. 8, a020495. doi:10.1101/cshperspect.a020495

Regehr, W.G., 2012. Short-term presynaptic plasticity. Cold Spring Harb. Perspect. Biol. 4, a005702. doi:10.1101/cshperspect.a005702

Rudolph, S., Overstreet-Wadiche, L., Wadiche, J.I., 2011. Desynchronization of Multivesicular Release Enhances Purkinje Cell Output. Neuron 70, 991–1004. doi:10.1016/j.neuron.2011.03.029

Schlick, B., Flucher, B.E., Obermair, G.J., 2010. Voltage-activated calcium channel expression profiles in mouse brain and cultured hippocampal neurons. Neuroscience 167, 786–98. doi:10.1016/j.neuroscience.2010.02.037

Schwenk, J., Baehrens, D., Haupt, A., Bildl, W., Boudkkazi, S., Roeper, J., Fakler, B., Schulte, U., 2014. Regional diversity and developmental dynamics of the AMPA-receptor proteome in the mammalian brain. Neuron 84, 41–54. doi:10.1016/j.neuron.2014.08.044

Scott, R., 2007. Use-dependent control of presynaptic calcium signalling at central synapses. J. Anat. 210, 642–50. doi:10.1111/j.1469-7580.2007.00728.x

Seo, M., Kim, Y.-S.Y., Lee, Y.-I., Kim, S.-Y., Ahn, Y.-M., Kang, U.G., Roh, M.-S., Kim, Y.-S.Y., Juhnn, Y.-S., 2006. Membrane depolarization stimulates the proliferation of SH-SY5Y human neuroblastoma cells by increasing retinoblastoma protein (RB) phosphorylation through the activation of cyclin-dependent kinase 2 (Cdk2). Neurosci. Lett. 404, 87–92. doi:10.1016/J.NEULET.2006.05.061

Smith, P.D., Liesegang, G.W., Berger, R.L., Czerlinski, G., Podolsky, R.J., 1984. A stopped-flow investigation of calcium ion binding by ethylene glycol bis(beta-aminoethyl ether)-N,N'-tetraacetic acid. Anal. Biochem. 143, 188–95.

Steinhäser, C., Jabs, R., Kettenmann, H., 1994. Properties of GABA and glutamate responses in identified glial cells of the mouse hippocampal slice. Hippocampus 4, 19–35. doi:10.1002/hipo.450040105

Swandulla, D., Hans, M., Zipser, K., Augustine, G.J., 1991. Role of residual calcium in synaptic depression and posttetanic potentiation: fast and slow calcium signaling in nerve terminals. Neuron 7, 915–26. doi:10.1016/0896-6273(91)90337-Y

Swanson, G.T., Kamboj, S.K., Cull-Candy, S.G., 1997. Single-channel properties of recombinant AMPA receptors depend on RNA editing, splice variation, and subunit composition. J. Neurosci. 17, 58–69. doi:10.1523/JNEUROSCI.17-01-00058.1997

Tasaki, I., 1939. The electro-saltatory transmission of the nerve impulse and the effect of narcosis upon the nerve fiber. J. Physiol. 127, 211–227. doi:10.1152/ajplegacy.1939.127.2.211

Tashiro, A., Zhao, C., Gage, F.H., 2007. Retrovirus-mediated single-cell gene knockout technique in adult newborn neurons in vivo. Nat. Protoc. 1, 3049–3055. doi:10.1038/nprot.2006.473

Tong, X., Li, X., Zhou, B., Shen, W., Zhang, Z., Xu, T., Duan, S., 2009. Ca(2+) signaling evoked by activation of Na(+) channels and Na(+)/Ca(2+) exchangers is required for GABA-induced NG2 cell migration. J. Cell Biol. 186, 113–28. doi:10.1083/jcb.200811071

Ulrich, D., Luscher, H.R., 1993. Miniature excitatory synaptic currents corrected for dendritic cable properties reveal quantal size and variance. J. Neurophysiol. 69, 1769–1773. doi:10.1152/jn.1993.69.5.1769

Usowicz, M.M., Gallo, V., Cull-Candy, S.G., 1989. Multiple conductance channels in type-2 cerebellar astrocytes activated by excitatory amino acids. Nature 339, 380–383. doi:10.1038/339380a0

Vijayan, S., Hale, G.J., Moore, C.I., Brown, E.N., Wilson, M., 2010. Activity in the barrel cortex during active behavior and sleep. J. Neurophysiol. 103, 2074–84. doi:10.1152/jn.00474.2009

Wake, H., Ortiz, F.C., Woo, D.H., Lee, P.R., Angulo, M.C., Fields, R.D., 2015. Nonsynaptic junctions on myelinating glia promote

preferential myelination of electrically active axons. Nat. Commun. 6, 7844. doi:10.1038/ncomms8844

Wu, L.-G., Borst, J.G.G., 1999. The Reduced Release Probability of Releasable Vesicles during Recovery from Short-Term Synaptic Depression. Neuron 23, 821–832. doi:10.1016/S0896-6273(01)80039-8

Young, K.M., Psachoulia, K., Tripathi, R.B., Dunn, S.-J., Cossell, L., Attwell, D., Tohyama, K., Richardson, W.D., 2013. Oligodendrocyte dynamics in the healthy adult CNS: evidence for myelin remodeling. Neuron 77, 873–85. doi:10.1016/j.neuron.2013.01.006

Yuan, X., Eisen, A.M., McBain, C.J., Gallo, V., 1998. A role for glutamate and its receptors in the regulation of oligodendrocyte development in cerebellar tissue slices. Development 125, 2901–14.

Zhang, B., Sun, L., Yang, Y.-M., Huang, H.-P., Zhu, F.-P., Wang, L., Zhang, X.-Y., Guo, S., Zuo, P.-L., Zhang, C.X., Ding, J.-P., Wang, L.-Y., Zhou, Z., 2011. Action potential bursts enhance transmitter release at a giant central synapse. J. Physiol. 589, 2213–27. doi:10.1113/jphysiol.2010.200154

Zhou, F.M., Hablitz, J.J., 1997. Rapid kinetics and inward rectification of miniature EPSCs in layer I neurons of rat neocortex. J. Neurophysiol. 77, 2416–26. doi:10.1152/jn.1997.77.5.2416

Zhu, J.J., Connors, B.W., 1999. Intrinsic Firing Patterns and Whisker-Evoked Synaptic Responses of Neurons in the Rat Barrel Cortex. J. Neurophysiol. 81, 1171–1183. doi:10.1152/jn.1999.81.3.1171

Ziskin, J.L., Nishiyama, A., Rubio, M., Fukaya, M., Bergles, D.E., 2007. Vesicular release of glutamate from unmyelinated axons in white matter. Nat. Neurosci. 10, 321–30. doi:10.1038/nn1854

III. Publications and Statement of Contribution

Publication 1. Different patterns of neuronal activity trigger distinct responses of oligodendrocyte precursor cells in the corpus callosum.

Nagy B., Hovhannisyan A., Barzan R., Chen T-J., Kukley M. (2017) PLOS Biol. 2017 Aug 22;15(8):e2001993.

Framework: In this original research paper we established that in brain slices, oligodendrocyte precursor cells (OPCs) can decode the different firing patterns of callosal axons via their glutamatergic synapses. By in vivo stimulation of the corpus callosum, we confirmed that low axonal stimulation frequencies trigger OPC differentiation, while high frequencies promote OPCs proliferation. Thus, the different stimulation patterns of axons modulate behavior of OPCs in distinct ways. This suggests that axons can regulate their own myelination.

Contributions: MK, AH and me conceptualized the study. I performed 60 % of all patch-clamp recordings. The patch-clamp data analysis was optimized with a series of trial analysis by me, AH, and MK. The formal and final analysis of the patch-clamp data was analyzed by me (~80%) and MK (~20%).

I independently established the surgical procedures, the in vivo setup where I conducted the experiments, and all in vivo experimental paradigms. This involved preparing all electrode arrays for implantation, performing surgeries, in vivo stimulations, and the tissue preparations for immunohistochemistry. I optimized the EdU administration to the living mice, adjusted the EdU-visualization protocol, the CD68-immunostaining protocol, and the caspase-3 immunostaining protocol.

I made roughly 90 % of the immunohistochemistry staining, and made all confocal imaging experiments. The rest of the staining was executed by TJC and MK. I performed approximately the 50% of the cell counting. The other half of the cell counting was done by RB.

I performed all statistical analysis and made all figures with help and feedback from MK, TJC, RB and AH. I and MK wrote the original draft; we reviewed and edited it after the peer-review process.

PLOS BIOLOGY

RESEARCH ARTICLE

Different patterns of neuronal activity trigger distinct responses of oligodendrocyte precursor cells in the corpus callosum

Balint Nagy[1,2¤a]*, Anahit Hovhannisyan[1,2¤b], Ruxandra Barzan[1,2¤c], Ting-Jiun Chen[1,2], Maria Kukley[1]*

1 Group of Neuron Glia Interaction, Werner Reichardt Centre for Integrative Neuroscience, University of Tübingen, Tübingen, Germany, **2** Graduate Training Centre of Neuroscience, University of Tübingen, Tübingen, Germany

¤a Current address: Institute of Science and Technology Austria, Klosterneuburg, Austria
¤b Current address: SCIPP Biomed, University of California, Santa Cruz, Santa Cruz, United States of America
¤c Current address: Optical Imaging Group, Institute for Neural Computation, Ruhr-University of Bochum, Universitätsstraße, Bochum, Germany
* Maria.Kukley@uni-tuebingen.de (MK); nagyblint@yahoo.com (BN)

OPEN ACCESS

Citation: Nagy B, Hovhannisyan A, Barzan R, Chen T-J, Kukley M (2017) Different patterns of neuronal activity trigger distinct responses of oligodendrocyte precursor cells in the corpus callosum. PLoS Biol 15(8): e2001993. https://doi.org/10.1371/journal.pbio.2001993

Academic Editor: Charles ffrench-Constant, The University of Edinburgh, United Kingdom of Great Britain and Northern Ireland

Received: January 12, 2017

Accepted: July 18, 2017

Published: August 22, 2017

Data Availability Statement: All relevant data are within the paper and its Supporting Information files.

Funding: Deutsche Forschungsgemeinschaft http://www.dfg.de (grant number EXC307). MK received funding for her research group and for this work from the Werner Reichardt Centre for Integrative Neuroscience (CIN) at the Eberhard Karls University of Tübingen. The CIN is an Excellence Cluster funded by the Deutsche

Abstract

In the developing and adult brain, oligodendrocyte precursor cells (OPCs) are influenced by neuronal activity: they are involved in synaptic signaling with neurons, and their proliferation and differentiation into myelinating glia can be altered by transient changes in neuronal firing. An important question that has been unanswered is whether OPCs can discriminate different patterns of neuronal activity and respond to them in a distinct way. Here, we demonstrate in brain slices that the pattern of neuronal activity determines the functional changes triggered at synapses between axons and OPCs. Furthermore, we show that stimulation of the corpus callosum at different frequencies in vivo affects proliferation and differentiation of OPCs in a dissimilar way. Our findings suggest that neurons do not influence OPCs in "all-or-none" fashion but use their firing pattern to tune the response and behavior of these nonneuronal cells.

Author summary

Oligodendrocytes are glial cells of the central nervous system. One of their major tasks is to enwrap neuronal axons with myelin, providing electrical insulation of axons and a dramatic increase in the speed of nerve impulse propagation. Oligodendrocytes develop from oligodendrocyte precursor cells (OPCs). Self-renewal of OPCs, their differentiation into oligodendrocytes, and the process of myelin synthesis are influenced by neuronal activity. Furthermore, OPCs receive glutamatergic synaptic input from neurons. Neuronal activity in vivo is highly variable depending on the brain region, input stimulus, and/or behavioral task that an animal or human has to perform in everyday life. Therefore, it is important to understand whether different types of neuronal activity affect development and function of oligodendrocyte lineage cells in a distinct way. In this study, we demonstrate that the

Forschungsgemeinschaft (DFG) within the framework of the Excellence Initiative (EXC 307). The funder had no role in study design, data collection and analysis, decision to publish, or preparation of the manuscript. Deutsche Forschungsgemeinschaft http://www.dfg.de (grant number KU2569/1-1). Received by MK. The funder had no role in study design, data collection and analysis, decision to publish, or preparation of the manuscript.

Competing interests: The authors have declared that no competing interests exist.

Abbreviations: AMPA, alpha-amino-3-hydroxy-5-methyl-4-isoxazolepropionic acid; Atx, ω-Agatoxin-IVA; Casp-3, caspase 3; CD68, cluster of differentiation 68; Cdk5, cyclin-dependent-kinase-5; CNS, central nervous system; Ctx, ω-Conotoxin-GVIA; EdU, 5-ethynyl-2´-deoxyuridine; EPSC, excitatory postsynaptic current; GTP, guanosintriphosphat; MAPK, mitogen-activated protein kinase; mEPSC, miniature excitatory postsynaptic current; NF-kappaB, nuclear factor k-light-chain-enhancer of activated B cells; OL, oligodendrocyte; OPC, oligodendrocyte precursor cell; pre-OL, premyelinating oligodendrocyte; VGCC, voltage-gated Ca^{2+} channel.

amount and the timing of glutamate release at synapses between neurons and OPCs, the properties of the subsequent ionic current through glutamate receptors in OPC membrane, as well as the extent of OPCs' self-renewal and differentiation into oligodendrocytes differ depending on the frequency and duration of neuronal activity. Hence, the pattern of neuronal activity rather than just presence or absence of activity is an important parameter that determines development and function of oligodendroglial cells.

Introduction

Oligodendrocyte precursor cells (OPCs) are the glial cells of the central nervous system (CNS) that give rise to myelinating oligodendrocytes (OLs) during development and in the adult brain and hence play an important role in establishing and maintaining the healthy function of the CNS. Neurons and OPCs seek to establish functional and structural contacts with each other, and through those contacts, neurons influence the behavior of OPCs. Thus, both in grey and white matter areas of the brain, neurons build functional synapses with OPCs [1], and axon-glia signaling at these synapses is thought to influence proliferation and differentiation of OPCs [2]. However, neurons also release neurotransmitter-filled vesicles at nonsynaptic junctions with OPCs, and this release underlies the preferential choice of electrically active versus inactive axons for myelination by OLs [3]. Furthermore, changing neuronal activity in animals in vivo, e.g., via electrical/optical stimulation of axonal tracts, placing animals into an enriched environment, or letting the animals learn new motor skills, affects proliferation of OPCs and their development into OLs [4–7]. Beautiful experiments performed in zebrafish in vivo demonstrate that neuronal activity also promotes extension and stabilization of prospective myelin sheaths [8] and regulates the myelinating capacity of single OLs [9]. It remains unknown, however, whether each type of neuronal activity influences OPCs in a similar way or whether OPCs discriminate different types of activity, allowing neurons to tune their influence in a pattern-specific manner.

OPCs residing in the corpus callosum, the white matter tract connecting the two hemispheres of the mammalian brain, are involved in axon-glia signaling with cortical pyramidal neurons of layers II/III and V [10–12]. These neurons comprise a morphologically and electrophysiologically heterogeneous population of cells and project to different targets. In response to a behavioral task or to sensory stimulus in vivo, cortical neurons fire trains or bursts of action potentials, and their discharge rates both ex vivo and in vivo can be highly variable. Upon current injection, these neurons can fire at frequencies ranging from <1 Hz to 400 Hz, while in behaving animals in vivo, they most often fire at theta (5–8 Hz) or beta/low-gamma (20–60 Hz) frequencies [13–17]. In neuronal networks, information about the characteristics of the task or stimulus is encoded in the neuronal firing rate (rate code) and/or timing (temporal code), which underlies the accuracy and reproducibility of the response [18]. Remarkably, recent research also indicates that specific patterns of action potentials differentially regulate many genes in neurons [19]. If specific patterns of neuronal activity are also conveyed to neuron-OPC networks, then the response of OPCs to neuronal activity should differ depending on the length and/or frequency of neuronal firing.

Here, we tested this hypothesis by studying changes at axon-OPC synapses in brain slices as well as proliferation and differentiation of callosal OPCs in vivo in response to different patterns of axonal stimulation. We found that neurotransmitter release rate, quantitative and temporal properties of synaptic charge transfer, as well as short-term plasticity at axon-OPC synapses in the corpus callosum are remarkably different depending on the type of presynaptic

axonal activity. Furthermore, we demonstrate that the extent of changes in differentiation, proliferation, and turnover of callosal OPCs triggered by axonal stimulation in vivo also depends on the stimulation paradigm. Our findings suggest that neurons do not influence the OL lineage cells in an "all-or-none" fashion but use their firing pattern to tune the response and behavior of these nonneuronal cells.

Results

Phasic and delayed glutamate release occurs at axon-OPC synapses upon axonal stimulation with trains of 20 pulses at 100 Hz

Our first step on the way to understanding the response of OPCs to different patterns of neuronal activity was to study functional changes at axon-OPC synapses upon repetitive axonal stimulation in situ. We performed whole-cell patch-clamp recordings of callosal OPCs in brain slices prepared from postnatal day 19–22 (P19-P22) NG2-DsRed mice and stimulated callosal axons electrically with trains of stimuli. The recorded cells had membrane resistance of 767 ± 157 MOhm ($n = 36$) and showed voltage-gated outward K^+ currents upon depolarization ($n = 36$), identifying them as OPCs [20–22]. We initially used the paradigm of 20 pulses at 100 Hz. The response of OPCs to train stimulation of axons consisted of two kinetically distinct components: phasic excitatory postsynaptic currents (EPSCs) during the train and delayed EPSCs, which occurred after the final stimulus in the train and continued for several hundreds of milliseconds (Fig 1A). To exclude the possibility that delayed axon-glia EPSCs are triggered by polysynaptic activation of callosally projecting neurons or result from dissimilar conduction velocities in individual fibers, we performed all subsequent experiments in slices where the corpus callosum has been isolated from the cortex (see Materials and methods) and used the minimal stimulation paradigm (Fig 1A and 1B), designed to stimulate a single axon contacting the recorded cell [10, 23]. Under these conditions, we were still able to record phasic and delayed axon-glial EPSCs, although we observed more failures of release during the train and fewer delayed events after the train.

The amplitude distribution histogram of unitary axon-glia EPSCs (without failures) could be fitted with lognormal function and showed one peak at 2.8 pA ($n = 20$; Fig 1B–1D), which was comparable to the histogram peak of miniature EPSCs (mEPSCs) at 2.2 pA ($n = 4$; Fig 1H–1J). Unitary EPSC amplitude distribution was skewed towards larger values (Kolmogorov-Smirnov test, $p < 0.001$), indicating that more than one vesicle can be released at a single axon-OPC connection [10]. The initial average amplitude of phasic axon-glia EPSCs (including failures) was 1.58 ± 0.33 pA, and the failure rate estimated from minimal stimulation was 73 ± 5% ($n = 14$ cells, Fig 1K and 1L), which is similar to the values reported previously [10]. The EPSC amplitude showed progressive facilitation at the beginning of the train, doubled by the third pulse, and returned to baseline by the end of the train ($n = 14$, Fig 1K). The release probability displayed comparable dynamic, while the response potency remained mostly unaltered ($n = 14$, Fig 1L and 1M), pointing to the fact that activity-dependent synaptic enhancement at axon-OPC synapses during the train is of presynaptic origin.

In addition to facilitation of phasic release, repetitive axonal stimulation increased the likelihood of spontaneous axon-glia EPSCs after the train. The rate of these delayed EPSCs decayed monoexponentially with a time constant of 98.7 ms (Fig 1N). The amplitude distribution histogram of delayed events was similar to the histograms of unitary EPSCs and mEPSCs: it could be fitted with lognormal function and showed one peak at 3.3 pA ($n = 14$ cells; Fig 1E–1G). The 10%–90% rise time and decay time constant of unitary, delayed, and mEPSCs were also comparable (Fig 1O and 1P). Hence, each delayed axon-glia EPSC likely represents a quantal response, as it is assumed for neuronal synapses [23].

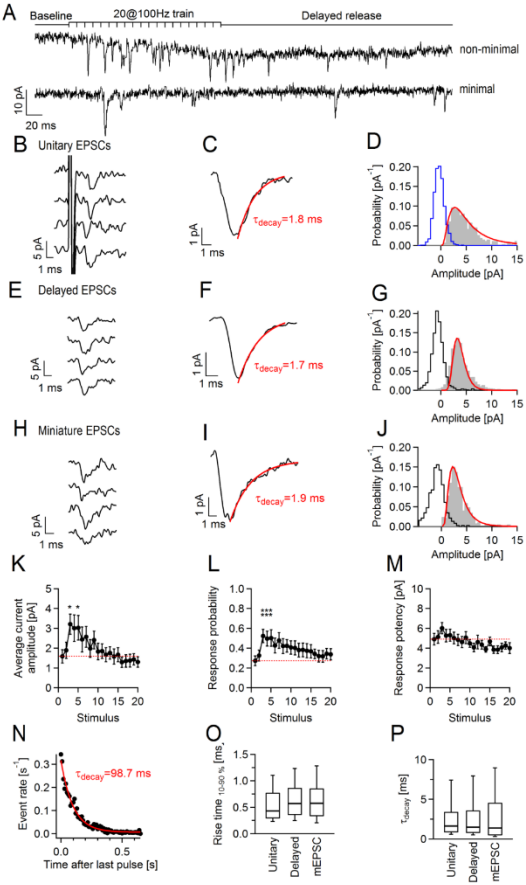
A
Baseline
20@100Hz train
Delayed release
non-minimal
minimal
10 pA
20 ms
B Unitary EPSCs
5 pA
1 ms
C
1 pA
1 ms
τdecay=1.8 ms
D
Probability [pA-1]
Amplitude [pA]
E Delayed EPSCs
F
τdecay=1.7 ms
G
H Miniature EPSCs
I
τdecay=1.9 ms
J
K
Average current amplitude [pA]
Stimulus
L
Response probability
M
Response potency [pA]
N
Event rate [s-1]
τdecay=98.7 ms
Time after last pulse [s]
O
Rise time 10-90 % [ms]
Unitary
Delayed
mEPSC
P
τdecay [ms]

Fig 1. Phasic and delayed currents occur in callosal oligodendrocyte precursor cells (OPCs) upon train stimulation of callosal axons with 20 pulses at 100 Hz. (A) Representative example traces showing phasic and delayed currents in OPCs (holding potential [V_h] = −80 mV) upon nonminimal (top) and minimal (bottom) stimulation of callosal axons. **(B–J)** Unitary, delayed, and miniature excitatory postsynaptic currents (EPSCs) in OPCs. **(B, E, H)** Original example events. **(C, F, I)** Average current waveforms generated by averaging of **(C)** 34 unitary events without failures, **(F)** 170 delayed events, and **(I)** 106 miniature events. Red lines indicate monoexponential fits to the decaying phase of the current. **(D, G, J)** Amplitude distribution histograms fitted with lognormal function (red line). Total of **(D)** 265 unitary events from 20 OPCs, **(G)** 2,089 delayed events from 14 OPCs, and **(J)** 370 miniature events from 4 OPCs were pooled for each histogram. Blue empty histogram in **(D)** represents amplitude distribution histogram of 894 failures pooled from the same 20 OPCs that were used for the histogram of responses. Black empty histograms in **(G, J)** indicate noise distribution. **(K–M)** Average current amplitude including failures, response probability, and response potency during minimal stimulation train. Each point represents the mean value from 14 cells for a given stimulus. To ease visualization of facilitation, a dashed red line is drawn at the level corresponding to the value at the first stimulus. One-way ANOVA with post hoc Dunnett's test was used to compare the values for each stimulus to the value measured at the first stimulus (S1 Table). Each point represents mean ± SEM. **(N)** Average rate of delayed events after the minimal stimulation train. 1,702 events from 14 cells were pooled for this histogram. Red line indicates monoexponential fit to the events rate. **(O–P)** Rise time and decay time constants of unitary, delayed, and miniature EPSCs (mEPSCs) in OPCs. The values were measured on the same events used for the amplitude distribution histograms in (**D, G, J**). One-way ANOVA (S1 Data). $*p < 0.05$, $**0.001 < p < 0.01$, $***p < 0.001$. Box and whisker plots: the bottom and top of each box represent 25th and 75th percentiles of the data, respectively, while whiskers represent 10th and 90th percentiles. The midline represents the median. The numerical data used in K–M and O–P are included in S2 Data.

https://doi.org/10.1371/journal.pbio.2001993.g001

Phasic and delayed axon-glia EPSCs were blocked by tetrodotoxin (TTX) (0.5 μM, $n = 3$, not shown) or by 6-cyano-7-nitroquinoxaline-2,3-dione (CNQX) (10 μM, $n = 3$, not shown), indicating that they depend on action potential propagation and are mediated by alpha-amino-3-hydroxy-5-methyl-4-isoxazolepropionic acid (AMPA)/kainate receptors.

Phasic and delayed release at axon-OPC synapses depends on P/Q- and N-type voltage-gated Ca^{2+} channels

As activity-dependent Ca^{2+} entry into callosal axons plays a crucial role for vesicle fusion and neurotransmitter release at axon-OPC synapses [10], our next goal was to find out whether phasic and delayed release at these synapses depends on the same types of voltage-gated Ca^{2+} channels (VGCCs). We recorded callosal OPCs, stimulated axons electrically, and bath-applied a selective blocker of N-type VGCCs ω-conotoxin-GVIa (Ctx) (1 μM) or a selective blocker of P/Q-type VGCCs ω-agatoxin-IVA (Atx) (0.5 μM). Ctx reduced the initial mean amplitude of axon-glia EPSCs by 95% (control 1.93 ± 0.69 pA, Ctx 0.09 ± 0.30 pA, Fig 2A and 2D), while Atx reduced it by 88% (control 1.78 ± 0.44 pA, Atx 0.2 ± 0.05 pA, Fig 2B and 2E). Each toxin also caused a decrease of the average axon-glia current amplitude during the train, which was especially pronounced during the first 5–10 stimuli (Fig 2D and 2E). Changes in the probability of axon-glia responses upon application of each toxin followed a similar time course during the train as changes in the current amplitude (Fig 2G and 2H), while the response potency was largely unaffected (Fig 2J and 2K). Peak rate of delayed axon-glia EPSCs was also significantly reduced upon application of Ctx (6.3 ± 1.1 Hz before versus 3.3 ± 0.8 Hz after toxin application, Fig 2M), or Atx (13.2 ± 5.2 Hz before versus 4.5 ± 1.2 Hz after toxin application, Fig 2N). Simultaneous application of the two blockers strongly reduced but did not completely abolish phasic or delayed axon-glia EPSCs (S1 Fig).

Taken together, these findings indicate that both phasic and delayed glutamate release at axon-OPC synapses in the corpus callosum is mainly mediated by N- and P/Q-types of VGCCs. However, a small component of release may be mediated by other subtypes of axonal Ca^{2+} channels or may be Ca^{2+} independent.

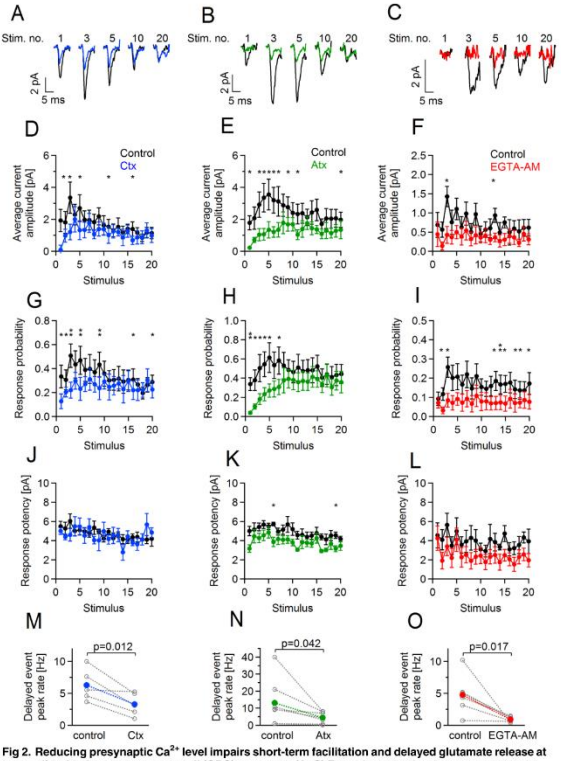

Fig 2. Reducing presynaptic Ca^{2+} level impairs short-term facilitation and delayed glutamate release at axon–oligodendrocyte precursor cell (OPC) synapses. (A–C) Example traces showing average currents (including failures) in three OPCs in response to the 1st, 3rd, 5th, 10th, and 20th stimuli in the train: under control conditions (before drug application, black), after 15 min perfusion of **(A)** ω-Conotoxin-GVIA (Ctx, 1 μM), **(B)** ω-Agatoxin-IVA (Atx, 0.5 μM), **(C)** after 10 min perfusion of ethylene glycol tetraacetic acid acetoxymethyl ester (EGTA-AM) (20 μM) via the bath. **(D–L)** Average current amplitude including failures, response probability, and response potency upon each stimulus of the train during control conditions and after perfusion of Ctx ($n = 5$ cells), Atx ($n = 5$ cells), and EGTA-AM ($n = 6$ cells). Each point represents mean ± SEM. Paired *t* test. (S2 Table, S3 Table and S4 Table). $*p < 0.05$, $**0.001 < p < 0.01$. **(M–O)** Peak rate of delayed currents in OPCs during control conditions and after perfusion of **(M)** Ctx, **(N)** Atx, **(O)** EGTA-AM. Each grey point represents an average peak rate in an individual experiment. Each point in color represents the mean peak rate within the experimental group, i.e., control, Ctx, Atx, and EGTA-AM. Paired *t* test (S3 Data). Throughout the figure: concentration of a

given drug is the same. The shown traces during drug application are taken from the time period when the drug effect on the amplitude of the evoked currents or rate of delayed currents was on the steady state. The numerical data used in D–O are included in S4 Data.

https://doi.org/10.1371/journal.pbio.2001993.g002

Accumulation of free Ca^{2+} in callosal axons underlies activity-dependent facilitation at axon-OPC synapses during the train and delayed release after the train

Accumulation of presynaptic Ca^{2+} plays an important role in triggering activity-dependent enhancement of synaptic efficacy at neuronal synapses [24]. Hence, after determining the source of Ca^{2+} mediating glutamate release at axon-OPC synapses, we tested whether accumulation of residual presynaptic Ca^{2+} underlies the facilitation of release during and after the train. We loaded callosal axons with ethylene glycol tetraacetic acid acetoxymethyl ester (EGTA-AM) (20 μM), a membrane-permeant high-affinity Ca^{2+} buffer with a slow Ca^{2+} binding kinetic [25], and studied the effects of EGTA-AM on phasic and delayed release. EGTA-AM did not significantly change either the mean amplitude of the first axon-glia EPSC in the train or its probability (Fig 2C and 2I), indicating that the basal transmission at axon-glia synapses relies on Ca^{2+} microdomains rather than on free residual axonal Ca^{2+} and that the distance between Ca^{2+} entry site and Ca^{2+} sensor is small [10]. In contrast, short-term synaptic enhancement during the train was completely abolished in the presence of EGTA-AM (Fig 2F). This effect was of presynaptic origin because EGTA-AM caused significant increase in the number of failures after each stimulus in the train, while the response potency remained unaffected (Fig 2I and 2L). EGTA-AM also caused significant reduction of the peak rate of delayed axon-glia EPSCs (4.8 ± 1.3 Hz before versus 0.9 ± 0.2 Hz after EGTA-AM application, Fig 2O).

Thus, repetitive stimulation of callosal axons triggers the rise of residual intra-axonal Ca^{2+}level, which mediates facilitation of glutamate release at axon-OPC synapses during the train as well as delayed release after the train.

Activity-dependent changes at axon-OPC synapses during the train differ depending on the stimulation paradigm

Having demonstrated that OPCs detect phasic and delayed glutamate release at synapses with neurons, we next investigated how these two components of release depend on the stimulation paradigm and whether OPCs distinguish differences in release. We used 6 stimulation paradigms: 2 pulses at 25 Hz; 5 pulses at 5, 25, and 100 Hz; and 20 pulses at 25 and 100 Hz and first focused on release during the train. Upon stimulation of callosal axons with 5 pulses at 5, 25, or 100 Hz, the average amplitude of phasic axon-glia EPSCs showed progressive facilitation, which reached its maximum at third–fifth pulse, but the facilitation rate did not depend on the stimulation paradigm: 2.88 ± 0.8 for 5 pulses at 5 Hz ($n = 5$), 3.75 ± 0.9 for 5 pulses at 25 Hz ($n = 11$), and 2.67 ± 0.7 for 5 pulses at 100 Hz ($n = 19$) (Fig 3A). For all three paradigms, the facilitation was of presynaptic origin (Fig 3B and 3C). If longer trains (20 pulses) were applied, the time course and the amount of synaptic facilitation were determined by the stimulation paradigm: facilitation was larger and more sustained upon stimulation at 25 Hz ($n = 6$) versus 100 Hz ($n = 14$) (Fig 3D–3F). As the response potency remained constant during the trains (Fig 3H), differences in synaptic enhancement between the two stimulation paradigms can be explained by the distinct changes in the probability of glutamate release (Fig 3G).

Repetitive axonal stimulation leads to buildup of presynaptic Ca^{2+} at axon-OPC synapses (Fig 2), which, in analogy to neuronal synapses, may contribute not only to short-term plasticity but also to activity-dependent desynchronization of phasic release [26–28]. We therefore

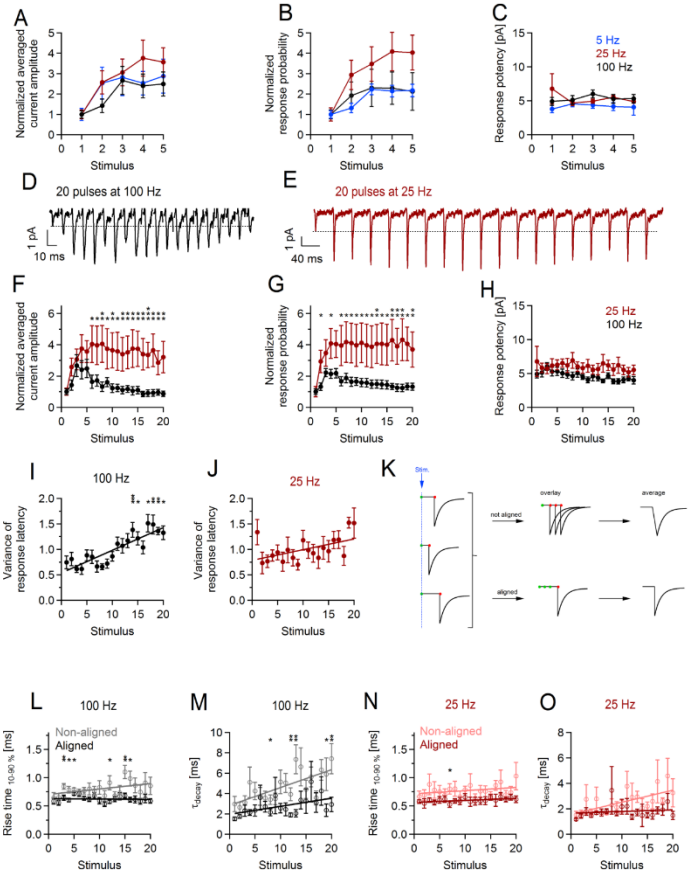

Fig 3. Short-term facilitation and desynchronization of glutamate release at axon-glia synapses during the train depend on the stimulation paradigm. (A–B) Normalized average current amplitude including failures and response probability and **(C)** absolute

response potency during minimal stimulation train of 5 pulses at 5 Hz ($n = 5$ cells), 25 Hz ($n = 11$ cells), or 100 Hz ($n = 19$ cells). Each point represents mean ± SEM. The values for each stimulus were compared between the different paradigms with one-way ANOVA. No statistically significant differences were found (S5 Data). **(D, E)** Example traces showing average currents (including failures) in two oligodendrocyte precursor cells (OPCs) upon minimal stimulation with 20 pulses at **(D)** 100 Hz and **(E)** 25 Hz. Fifty sweeps were averaged for each paradigm. Stimulation artifacts are truncated for clarity. Dotted lines are drawn at the level corresponding to the peak amplitude of the first response within the train. **(F, G)** Normalized average current amplitude including failures and response probability and **(H)** absolute response potency during minimal stimulation train of 20 pulses at 25 Hz ($n = 6$ cells) or at 100 Hz ($n = 14$ cells). Independent sample *t* test (S5 Table). **(I, J)** Average variance of onset latency of the phasic responses during the stimulation train of 20 pulses at **(I)** 100 Hz ($n = 14$ cells) or **(J)** 25 Hz ($n = 6$ cells). Paired *t* test was used to compare the value for each stimulus to the value at the first stimulus (S6 Table). **(K)** Schematic drawing explaining two approaches for generating average current waveforms used to study desynchronization of release during the train. The results of this analysis are shown in panels **(L–O)**. Bottom row ("aligned"): events are aligned on the time of their onset (red dot) and then averaged. Top row ("not aligned"): average event is generated from the raw traces, which are by default aligned on the stimulation time (green dot) but not on their onset. If desynchronization of release occurs during the train while properties of individual events do not change, it is expected that (1) kinetics of the average nonaligned event is slower at the end of the train than at the beginning, and (2) kinetics of the average aligned event does not change during the train. **(L, N)** Average rise time and **(M, O)** average decay time constant of aligned and nonaligned responses (excluding failures) after each stimulus within the train of 20 pulses at **(L, M)** 100 Hz or **(N, O)** 25 Hz. Average aligned and average nonaligned events for each stimulus were generated as explained in **(K)**. The same cells were used as in **(F–J)**. Independent sample *t* test was used to compare the values from nonaligned and aligned averages for each stimulus (S7 Table). $*p < 0.05$; $**0.001 < p < 0.01$. The numerical data used in A–C, F–J, and L–O are included in S6 Data.

https://doi.org/10.1371/journal.pbio.2001993.g003

investigated whether activity-dependent desynchronization of glutamate release occurs at axon-OPC synapses and how it differs depending on the stimulation paradigm. We found that the variance of the onset latency of phasic axon-glia EPSCs increased by 80% over the time course of the 100 Hz but not 25 Hz stimulation train (Fig 3I and 3J), pointing to desynchronization of release. To substantiate this finding, for each stimulus of the train we took the same set of phasic axon-glia EPSCs and averaged them either as they have been recorded ("non-aligned") or after aligning them on the event onset ("aligned") (Fig 3K). In case of 100 Hz stimulation, the kinetics of the average EPSC generated from the nonaligned events was slower compared to the aligned events, and this difference was more pronounced at the end than at the beginning of the train ($n = 14$, Fig 3L and 3M), designating broadening of the release timing during the train. A similar tendency was observed for 25 Hz stimulation, but the differences were not statistically significant ($n = 6$, Fig 3N and 3O).

Thus, activity-dependent synaptic enhancement and desynchronization of release at axon-OPC synapses differ depending on the stimulation paradigm, and OPCs discriminate the differences.

Delayed glutamate release at axon-OPC synapses depends on the stimulation paradigm

We next investigated how different stimulation paradigms affect delayed release at axon-OPC synapses. If we stimulated the axons at 25 Hz, the peak rate of delayed axon-glia EPSCs was higher when longer trains were applied: 0.8 ± 0.2, 1.8 ± 0.4, and 6.1 ± 1.9 Hz after 2, 5, and 20 pulses, respectively (Fig 4A). A similar result was obtained when we stimulated the axons at 100 Hz and compared 5 versus 20 pulses (Fig 4D & 4G). If we kept the number of pulses in the train constant and varied their frequency, the peak rate of delayed events was larger for higher stimulation frequencies (Fig 4D and 4G), although there was no difference between the stimulation at 25 versus 100 Hz. The rate of delayed events decayed monoexponentially to the basal rate of spontaneous axon-glia EPSCs, which was 0.31 ± 0.05 Hz (Fig 4B, 4E and 4H). For the same stimulation frequency, the decay time constant was larger for longer than for shorter trains (Fig 4B and 4C). In contrast, when the number of pulses was the constant parameter, the dependence of the decay time constant on the stimulation frequency was less pronounced (Fig 4E, 4F, 4H and 4I). The mean amplitude, rise, and decay time of the delayed axon-glia EPSCs were comparable in all cells, indicating that these parameters are not influenced by the type of prior axonal activity (not shown).

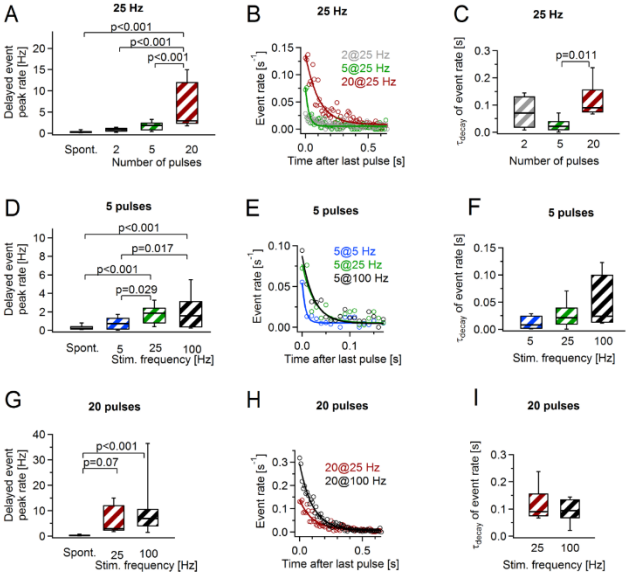

Fig 4. The rate and the time course of delayed glutamate release at axon-oligodendrocyte precursor cell (OPC) synapses depend on the stimulation paradigm. (A) Average peak rate of the delayed events after the stimulation with 2 pulses ($n = 6$ cells), 5 pulses ($n = 6$ cells), or 20 pulses ($n = 8$ cells) at 25 Hz. The box "Spont." shows the frequency of the spontaneous events recorded before each stimulation train. One-way ANOVA (S7 Data). **(B)** Average rate of delayed events after the stimulation with 2, 5, or 25 pulses at 25 Hz. Solid lines indicate monoexponential fits to the events rate. The same cells used as in **(A)**. **(C)** Average decay time constants of the delayed events rate after the stimulation with 2, 5, or 20 pulses at 25 Hz. The same cells used as in **(A).** One-way ANOVA (S7 Data). **(D)** Data and statistical comparisons are as in **(A)** but for the stimulation paradigms of 5 pulses at 5 Hz ($n = 7$ cells), 25 Hz ($n = 7$ cells), and 100 Hz ($n = 6$ cells). One-way ANOVA (S7 Data). **(E)** Data as in **(B)** but for the stimulation paradigms of 5 pulses at 5, 25, and 100 Hz. The same cells used as in **(D)**. **(F)** Data and statistical comparisons are as in **(C)** but for the stimulation paradigms of 5 pulses at 5, 25, and 100 Hz. The same cells used as in **(D)**. One-way ANOVA (S7 Data). **(G)** Data and statistical comparisons are as in **(A)** but for the stimulation paradigms of 20 pulses at 25 Hz ($n = 8$ cells) and 100 Hz ($n = 13$ cells). One-way ANOVA (S7 Data). **(H)** Data as in **(B)** but for the stimulation paradigms of 20 pulses at 25 and 100 Hz. The same cells used as in **(G)**. **(I)** Data and statistical comparisons are as in **(C)** but for the stimulation paradigms of 20 pulses at 25 and 100 Hz. The same cells used as in **(G)**. One-way ANOVA (S7 Data). Box and whisker plots: the bottom and top of each box represent 25th and 75th percentiles of the data, respectively, while whiskers represent 10th and 90th percentiles. The midline represents the median. The numerical data used in A, C, D, F, G, and I are included in S8 Data.

https://doi.org/10.1371/journal.pbio.2001993.g004

Thus, the delayed glutamate release differs depending on the number of stimuli in the train and the stimulation frequency, and OPCs can distinguish these differences.

Temporal profile of synaptic charge transfer at axon-OPC synapses differs depending on the stimulation paradigm

When studying facilitation of transmitter release at axon-OPC synapses, we have so far considered only changes in the amount of facilitation from stimulus to stimulus in the train (Fig 3A and 3F) but not in real time. To fill this gap, we analyzed synaptic charge transfer through AMPA/kainate receptors in OPCs upon axonal stimulation (during and after the train) and plotted it versus real time. We found that the temporal profile of charge transfer, i.e., its distribution over time, was determined by the stimulation paradigm (Fig 5A) and was entirely different even for those paradigms in which the amount of facilitation and the total synaptic charge transfer were similar (Figs 3A & 5A). For instance, although the same amount of charge was transferred during stimulation with 5 pulses at 5 Hz and at 25 Hz (Fig 5B) and the amount of facilitation was comparable (Fig 3A), in the former case, the transfer of synaptic charge oscillated at 5 Hz and was completed after 810 ms (Fig 5A, blue trace), while in the latter case, the transfer of charge oscillated at 25 Hz and was completed already after 170 ms (Fig 5A, red trace). Similar differences were also observed when we compared stimulation with 20 pulses at 25 Hz (Fig 5A, second red trace) versus 100 Hz (Fig 5A, black trace).

When comparing the relative contribution of charge transfer during and after the stimulation train, we found that, independently of the stimulation paradigm, 85%–98% of charge transfer occurred during the train (Fig 5D, Fig 5B & 5C). At four tested paradigms, the delayed glutamate release contributed only 2%–3% of total charge transfer. The largest contribution of 14% was taking place upon stimulation of axons with 20 pulses at 100 Hz (Fig 5D). This is similar to the situation at some neuronal synapses but not at the others [29].

In adult animals, phasic and delayed glutamate release at axon-OPC synapses also depends on the stimulation paradigm

Repetitive axonal stimulation (20 pulses at 25, 100, or 300 Hz) triggered phasic and delayed glutamate release at axon-OPC synapses also in adult (P50–53) mice (Fig 6). In contrast to juvenile mice, we observed little/no difference in presynaptic facilitation of phasic axon-glia EPSCs between 25 and 100 Hz stimulation paradigms; however, the amount of facilitation was lower for 300 Hz stimulation (Fig 6A–6D). (Note that the temporal profile of charge transfer is expected to differ between all three paradigms [Fig 5]). The incidence of delayed EPSCs was transiently elevated after cessation of stimulation, similar as it occurred in the juvenile mice. The delayed events occurred over a slightly longer time window and their peak rate was higher for 25 and 100 Hz stimulation versus 300 Hz trains (Fig 6E–6H). Hence, changes in glutamate release at axon-OPC synapses are determined by the stimulation paradigm also in adult mice, but the effect of a given paradigm may differ from that in the juvenile animals.

Differentiation and proliferation of OPCs in vivo depend on the pattern of transient changes in axonal activity

Having demonstrated that response of OPCs to repetitive axonal stimulation in brain slices differs depending on the stimulation pattern, we were wondering whether also in vivo OPCs respond to different stimulation paradigms in a distinct way. We implanted an electrode array into the corpus callosum of adult mice and transiently changed the activity of callosal axons in freely behaving animals by stimulating the corpus callosum at 5 Hz, 25 Hz, or 300 Hz (Fig 7A and 7B). Importantly, none of the stimulation paradigms triggered an unusual behavior or seizures in any of the animals. We then assessed changes in proliferation and differentiation of OPCs 7 days after the stimulation (Fig 7C–7F).

PLOS BIOLOGY

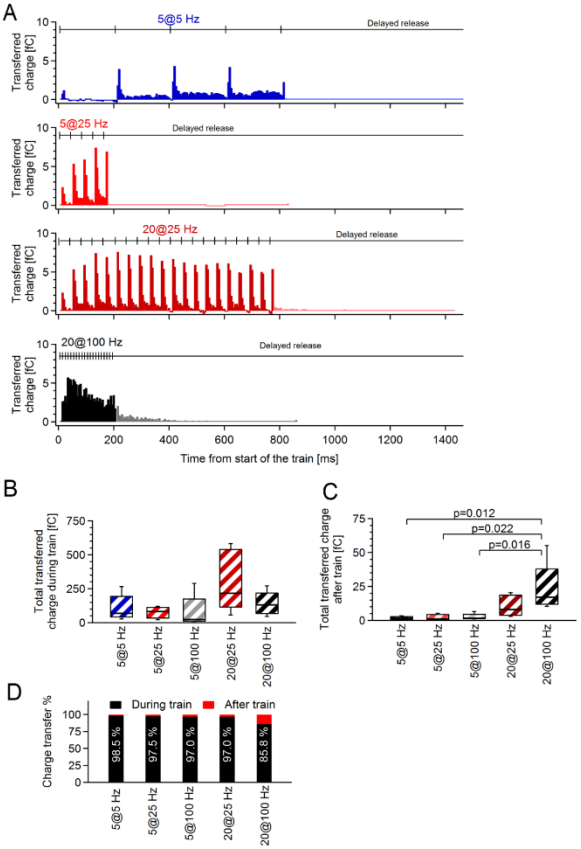

Fig 5. The time course and the amount of synaptic charge transfer through alpha-amino-3-hydroxy-5-methyl-4-isoxazolepropionic acid (AMPA) receptors at axon–oligodendrocyte precursor cell (OPC) synapses depend on the stimulation paradigm. (A) Average synaptic charge transfer upon stimulation of callosal axons with trains of four different frequencies and durations plotted versus real time. Each color (blue, red, dark red, or

black) represents mean charge transfer from $n = 5$ cells (5 pulses at 5 Hz), $n = 5$ cells (5 pulses at 25 Hz), $n = 5$ cells (20 pulses at 25 Hz), and $n = 10$ cells (20 pulses at 100 Hz). Charge transfer is shown in 5-ms bins. Note that plotting charge transfer versus real time allows observing not only the amount of synaptic facilitation but also its distribution over time, and it differs dramatically depending on the stimulation paradigm (Fig 3A & 3D). **(B)** Total average synaptic charge transfer during the stimulation trains of different frequencies and durations. Both phasic and asynchronous charge transfer during the trains are considered for these bar graphs. The same cells used as in **(A)**. One-way ANOVA (S9 Data). **(C)** Total synaptic charge transferred by the delayed currents occurring after the stimulation trains of different frequencies and durations. The same cells used as in **(A)**. One-way ANOVA (S9 Data). **(D)** Percentage contribution of synaptic charge transferred during (phasic + asynchronous charge) and after (delayed charge) the stimulation trains of different frequencies and durations. White numbers on the bars indicate the proportion of charge transferred during the train. Box and whisker plots: the bottom and top of each box represent 25th and 75th percentiles of the data, respectively, while whiskers represent 10th and 90th percentiles. The midline represents the median. The numerical data used in B–C are included in S10 Data.

https://doi.org/10.1371/journal.pbio.2001993.g005

Stimulation of axons at 5 Hz and to a lesser extent at 25 Hz, but not at 300 Hz, resulted in substantial increase in the density of premyelinating OLs (pre-OLs): 1,551 ± 380 cells/mm^3 in sham-treated animals versus 3,625 ± 911 cells/mm^3 upon 5 Hz stimulation versus 2,488 ± 421 cells/mm^3 upon 25 Hz stimulation versus 1,230 ± 387 cells/mm^3 upon 300 Hz stimulation (Fig

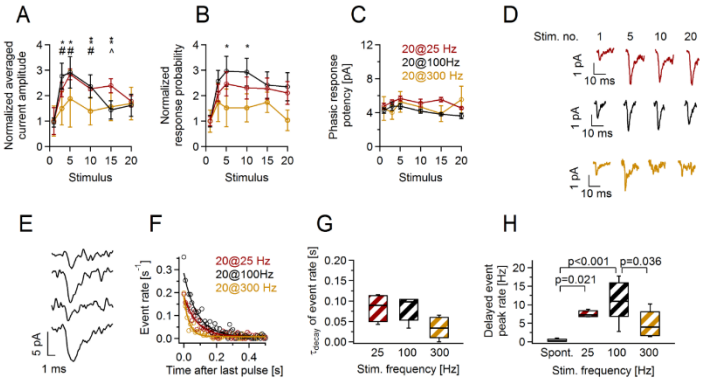

Fig 6. Activity-dependent changes at axon-oligodendrocyte precursor cell (OPC) synapses are determined by the stimulation paradigm also in the adult (P50–53) mice. (A–C) Normalized average **(A)** current amplitude including failures, **(B)** probability of responses, and **(C)** absolute potency of responses upon each stimulus of the minimal stimulation train of 20 pulses at 25 Hz ($n = 4$ cells), 100 Hz ($n = 6$ cells), or 300 Hz ($n = 5$ cells). One-way ANOVA (S11 Data). 25 Hz versus 300 Hz stimulation: *$p < 0.05$, **$0.001 < p < 0.01$. 100 Hz versus 300 Hz stimulation: #$p < 0.05$. 25 Hz versus 100 Hz stimulation: ^$p < 0.05$ **(D)** Example traces showing average currents (including failures) in 3 OPCs in response to the 1st, 5th, 10th, and 20th stimulus of the minimal stimulation train of 20 pulses at 25 Hz, 100 Hz, and 300 Hz. At least 15 trials were averaged to generate each example trace. **(E)** Original example traces showing delayed currents in callosal OPC (holding potential [V_h] = −80 mV) occurring after the stimulation train of 20 pulses at 25 Hz. **(F)** Average rate of delayed currents occurring after the stimulation train of 20 pulses at 25 Hz, 100 Hz, or 300 Hz. Solid lines indicate monoexponential fits to the events rate. **(G)** Average decay time constants of the delayed event rate after the stimulation train with 20 pulses at 25 Hz, 100 Hz, or 300 Hz. One-way ANOVA (S11 Data). **(H)** Average peak rate of the delayed events after the stimulation with 20 pulses at 25 Hz, 100 Hz, or 300 Hz. The box "Spont." shows the frequency of the spontaneous events recorded before each stimulation train. One-way ANOVA (S11 Data). Box and whisker plots: the bottom and top of each box represent 25th and 75th percentiles of the data, respectively, while whiskers represent 10th and 90th percentiles. The midline represents the median. The numerical data used in A–C and G–H are included in S12 Data.

https://doi.org/10.1371/journal.pbio.2001993.g006

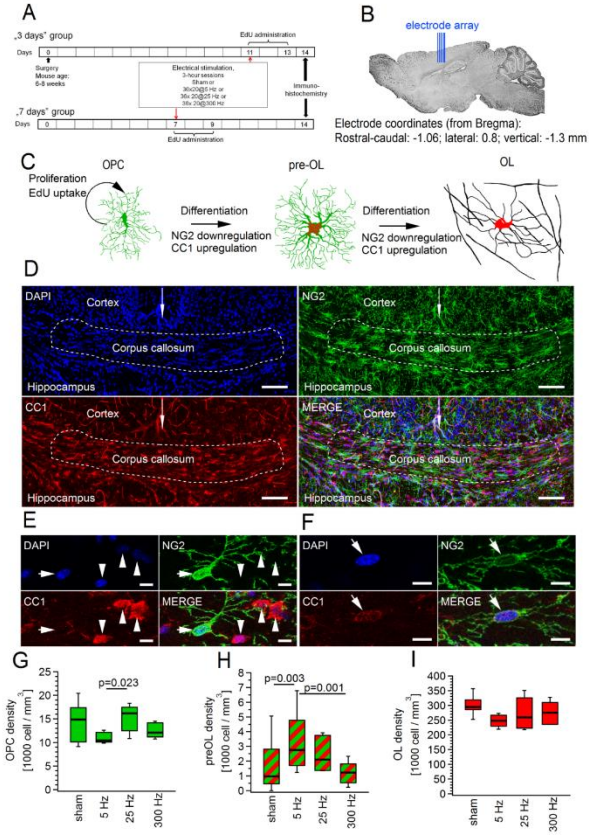

Fig 7. Transient stimulation of callosal axons in vivo at 5 Hz but not at 25 Hz or 300 Hz promotes differentiation of oligodendrocyte precursor cells (OPCs) into oligodendrocytes (OLs). (A) Scheme describing experimental design for studying effects of callosal stimulation in vivo on proliferation and differentiation of OPCs. **(B)** Scheme showing sagittal section of mouse brain and the position of an electrode array used for electrical stimulation of the corpus callosum. **(C)** Schematic drawings of the investigated cell types. For cell counting, OPCs were identified

as NG2$^+$CC1$^-$ cells, premyelinating OLs (pre-OLs) as NG2$^+$CC1$^+$ cells, and myelinating OLs as NG2$^-$ cells expressing CC1 in their soma. Within the OL lineage, 5-ethynyl-2´-deoxyuridine (EdU) only labels proliferating OPCs. However, the progeny of an EdU$^+$ OPC will be EdU$^+$. **(D)** Coronal sections of the corpus callosum. Maximum intensity projection (from 14 successive confocal planes) showing triple channel immunofluorescent labelling with DAPI (top left, blue), NG2 (top right, green), CC1 (bottom left, red), and the overlay of 3 channels (bottom right). White dashed line denotes the middle region of the corpus callosum used for cell counting. White arrow indicates midline of the brain. Scale bars: 100 μm. **(E)** As in **(D)**, but higher magnification example of one NG2$^+$CC1$^-$ OPC (arrow) and three NG2$^-$CC1$^+$ OLs (arrowheads). Maximum intensity projection was generated from a *z*-stack of 3 successive confocal planes. Note that some processes of an NG2$^+$ OPC are clearly visible. Scale bars: 10 μm. **(F)** As in **(E)**, but an example of one NG2$^+$CC1$^+$ pre-OL (arrow). Note that the expression level of NG2 is weaker than in OPCs, and the expression level of CC1 is weaker than in OLs (Fig 7E). Scale bars: 10 μm. **(G–I)** Average density of **(G)** OPCs, **(H)** pre-OLs, and **(I)** OLs in corpus callosum upon electrical stimulation of callosal axons at 5 Hz ($n = 5$ mice, total 13 slices), 25 Hz ($n = 5$ mice, total 16 slices), or 300 Hz ($n = 5$ mice, total 17 slices) versus sham-stimulated controls ($n = 7$ mice, total 25 slices). Note that differentiation rate was significantly increased by 5 Hz but not by 25 Hz or 300 Hz stimulation **(H)**. Nested ANOVA and post hoc Tukey were used for statistical analysis (S13 Data). Box and whisker plots: the bottom and top of each box represent 25th and 75th percentiles of the data, respectively, while whiskers represent 10th and 90th percentiles. The midline represents the median. The numerical data used in G–I are included in S14 Data.

https://doi.org/10.1371/journal.pbio.2001993.g007

7H). At the same time, none of the 3 stimulation paradigms significantly altered the density of OPCs or mature OLs (Fig 7G and 7I). To explore whether corresponding alterations might have occurred at earlier time points after the stimulation, we have also counted cells 3 days after the stimulation. We found, however, that the changes took the same path at that time point: stimulation triggered differentiation of OPCs, and 25 Hz stimulation was more effective with this respect than 300 Hz stimulation (S2 Fig). Hence, at this earlier time point, we restricted our analysis to only two stimulation paradigms. The density of OPCs 3 days after the stimulation was reduced compared to sham-treated animals (S2 Fig); this was most likely the consequence of their differentiation rather than cell death, as we have not observed caspase 3 (Casp-3)–positive OPCs in the corpus callosum (see below).

We next studied the effect of three different stimulation paradigms on proliferation of OPCs (Fig 8A). Stimulation of callosal axons at 25 Hz or 300 Hz triggered a statistically significant increase in the density of proliferating cells in the corpus callosum, while 5 Hz stimulation appeared less effective (Fig 8B). Furthermore, a clear trend was observed for 25 Hz stimulation being more efficient with this respect than 300 Hz: we counted 3,260 ± 839 cells/mm^3 in the sham-treated group, 7,651 ± 930 cells/mm^3 (130% increase) upon 25 Hz stimulation, and 5,652 ± 854 cells/mm^3 (70% increase) upon 300 Hz stimulation. The ratio of 5-ethynyl-2´-deoxyuridine (EdU$^+$) oligodendroglial cells within the total population of cycling cells in the corpus callosum was also enhanced after the stimulation (Fig 8C). The major cause of this enhancement was the rise in the number of EdU$^+$ myelinating OLs (Fig 8D). Interestingly, upon stimulation of axons at 5 Hz, we observed a clear trend to enhanced numbers of pre-OLs versus sham-treated animals, versus the group of animals stimulated at 25 Hz and also at 300 Hz (Fig 8D). Hence, pre-OLs may also contribute to the higher ratio of EdU$^+$ oligodendroglial cells within the total population of cycling cells after electrical stimulation.

We next evaluated the fraction of EdU$^+$ cells within the population of OPCs and within the population of OLs, separately. Stimulation of axons at 25 Hz or 300 Hz caused a statistically significant increase in the proportion of proliferating (EdU$^+$) OPCs within the OPC population, while 5 Hz stimulation was less effective (Fig 8E). Furthermore, all stimulation paradigms promoted differentiation of the newly born (EdU$^+$) OPCs into OLs. This was reflected in the higher numbers of the EdU$^+$ OLs within the total population of OLs in stimulated versus sham-treated mice (Fig 8F). The 5 Hz (248% increase) and the 25 Hz stimulation paradigms (230% increase) were slightly more effective with this respect than 300 Hz stimulation (160% increase).

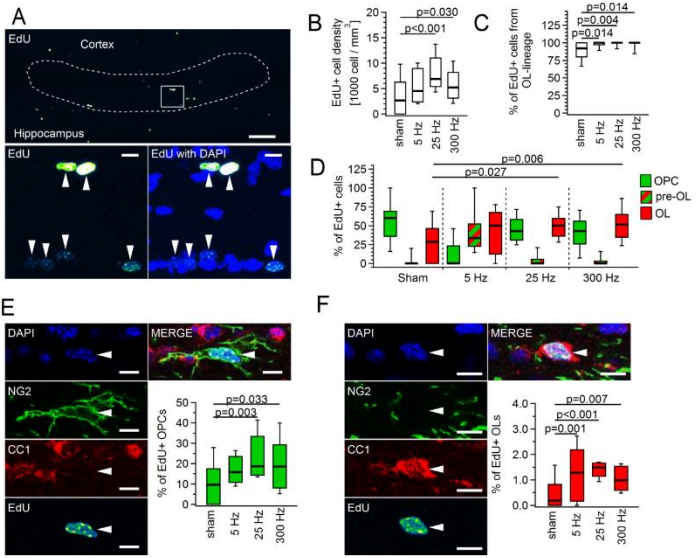

Fig 8. Callosal stimulation in vivo enhances proliferation rate of oligodendrocyte precursor cells (OPCs) and promotes differentiation of newly born OPCs into oligodendrocytes (OLs). (A) Coronal sections of corpus callosum. Maximum intensity projection image (from 14 successive confocal planes) showing fluorescent 5-ethynyl-2′-deoxyuridine (EdU) labelling in corpus callosum. White dashed line marks the region of interest used for cell counting. Top panel: overview. Scale bar: 100 μm. Bottom panels: higher magnification of the area marked by the white square at the top panel; left, EdU (false color look-up table (LUT) "Green Fire Blue"); right, overlay of EdU and DAPI (blue) channels. Arrowheads indicate EdU$^+$ cells. Scale bar: 10 μm. **(B)** Density of EdU$^+$ cells in corpus callosum. **(C)** Proportion of OL lineage cells (OPCs + pre-OLs + OLs) labelled with EdU, within the total population of EdU$^+$ cells. **(D)** Proportion of EdU$^+$ OPCs (green), premyelinating OLs (pre-OLs) (red-green) and OLs (red) within the total population of EdU$^+$ cells. **(E)** Single layer confocal image showing quadruple channel fluorescent labelling with DAPI (blue), NG2 (green), CC1 (red), and EdU (false color LUT "Green Fire Blue"), and the overlay of four channels (top right). The arrowhead indicates an EdU$^+$ OPC. Scale bars: 10 μm. The box plot shows proportion of EdU$^+$ OPCs within the total OPCs population. **(F)** Single layer confocal image showing quadruple-channel fluorescent labelling with DAPI (blue), NG2 (green), CC1 (red), and EdU (false color LUT "Green Fire Blue"), and the overlay of four channels (top right). The arrowhead points to an EdU$^+$ OL. Scale bar: 10 μm. The box plot shows proportion of EdU$^+$ OLs within the total OLs population. Throughout this figure, the same mice and slices were analyzed as in Fig 7. Nested ANOVA and post hoc Tukey test were used for statistical analysis (S15 Data). Box and whisker plots: the bottom and top of each box represent 25th and 75th percentiles of the data, respectively, while whiskers represent 10th and 90th percentiles. The midline represents the median. The numerical data used in B–F are included in S14 Data.

https://doi.org/10.1371/journal.pbio.2001993.g008

Our findings so far suggest that, depending on the paradigm, electrical stimulation promotes proliferation and/or differentiation of OPCs in the corpus callosum. These effects may be mediated by direct axon-OPC contacts and/or by diffusible substances, e.g., neurotransmitters, growth factors, etc. Alternatively, however, the primary effect of callosal stimulation may be the death of OPCs and/or OLs; proliferation and differentiation may then occur as a

consequence of this effect. To test for this, we performed staining of brain slices for a cell death marker cleaved Casp-3, as it has been done previously (Gibson et al. 2014) [5]. We chose to stain for Casp-3 three days after the stimulation because in mouse models of diseases, Casp-3 is detectable 24 hours after the onset and stays for at least 7 days [30]. Similar to the study of Gibson et al., we have not observed any Casp-3–expressing cells in the middle part of the corpus callosum (which we used for counting oligodendroglial cells) in any of the stimulated animals (independently of the stimulation paradigm) and also not in sham-treated mice: $n = 3$ animals for 25 Hz (not shown); $n = 3$ animals for 300 Hz (S3 Fig); $n = 2$ sham-treated animals (S3 Fig). At the site of electrode implantation in the cortex, some Casp-3–positive cells were present (S3 Fig). Hence, our stimulation paradigms are most likely too mild to trigger cell death in the corpus callosum, and the observed effects of stimulation on proliferation and/or differentiation of OPCs are unlikely to be triggered by cell death.

Taken together, increased density of pre-OLs upon 5 Hz stimulation and increased ratio of EdU^+ OPCs upon 25 Hz and 300 Hz stimulation suggest that some frequencies (5 Hz in our case) are more efficient at triggering differentiation, while other frequencies (25 Hz and 300 Hz in our case) are more efficient at triggering proliferation.

Microglia was not activated in the stimulated corpus callosum

To check if callosal stimulation triggered activation of microglia, we sacrificed the animals 3 days after the stimulation and performed cluster of differentiation 68 (CD68) staining. The time point of 3 days was chosen because several independent studies on brain trauma have demonstrated that activated microglia are observed 12 hours after trauma and stay in the brain tissue for up to 2–4 weeks [31–33]. We could not find CD68-positive cells in the middle part of the corpus callosum (which we used for counting oligodendroglial cells) in either stimulated or sham-treated animals (S4 Fig; n numbers are as for Casp-3 above). At the same time, we observed microglia activation at the site of electrodes implantation (close to the cortical surface) and along the track of the electrodes reaching down to the external capsule/corpus callosum (S4 Fig). Importantly, the distance between the microglia activation site and the nearest area used for cell counting was at least 500–600 μm. Hence, even if microglia release factors which could influence oligodendroglial behavior, the concentration of these factors at the cell-counting site is expected to be significantly diminished by diffusion. Therefore, in our study, microglia activation most likely had no/little effects on the proliferation and differentiation of OPCs.

Discussion

In this study, we showed that different patterns of repetitive neuronal activity modulate the quantitative and/or temporal profile of neurotransmitter release, probability of release, and synaptic charge transfer at axon-OPC synapses in corpus callosum in a distinct way. Although repetitive firing is common in cortical neurons in vivo and has been intensively studied by neuronal physiologists, this is the first report investigating how functional modifications at synapses between neurons and glial cells depend on the rate and duration of repetitive neuronal activity. In addition, we demonstrated that the extent of changes in differentiation, proliferation, and turnover of callosal OPCs triggered by axonal stimulation in vivo can be influenced by the stimulation paradigm.

We observed 2 major types of alterations at axon-OPC synapses in response to repetitive axonal activity: (1) short-term facilitation of glutamate release during stimulation accompanied by desynchronization of release and (2) temporary increase of quantal glutamate release after cessation of stimulation. Both phenomena are explained by a transient enhancement of

neurotransmitter release probability from callosal axons and are not age dependent. Remarkably, changes in the amount and the timing of synaptic charge transfer triggered by phasic and delayed glutamate release are determined by the pattern of neuronal activity, i.e., the number and frequency of pulses in the stimulation train. These findings suggest that when OPCs convert synaptic input into the intracellular events, the temporal prevalence and in some cases also spatial distribution (e.g., diffusion of ions) of these events will vary depending on the type of neuronal activity. It is largely unknown how OPCs process and decode synaptic input from neurons, but several signal transduction mechanisms can be considered. Firstly, the resting membrane potential of an OPC is usually between −70 mV and −90 mV [22, 34], and therefore synaptic input will result in transient membrane depolarization and can be regarded as purely an electrical signal. Together with other factors, bioelectrical signaling may contribute to the mitotic control mechanisms in the OPCs [35], for example, to changes in DNA synthesis as reported for neuronal progenitors or neuroblastoma cells [36, 37]. Secondly, as ionotropic glutamate receptors are permeable for Na^+ and K^+ (and also for Ca^{2+} in OPCs of the adult animals), synaptic input will trigger ion fluxes through the OPC membrane and changes in the intracellular concentration of ions in the OPCs. The quantitative and temporal profile of AMPA-receptor–mediated ionic charge transfer at axon-OPC synapses depend on the stimulation paradigm and on the degree of facilitation/desynchronization of transmitter release at these synapses (Fig 5). Hence, quantitative, temporal, and perhaps also spatial alterations in the intracellular concentration of Na^+, K^+, and Ca^{2+} will depend on these factors as well. Alterations in ion concentration may be further boosted or curtailed by activation/inactivation of ion exchanges, voltage-gated ion channels expressed by OPCs and/or by Ca^{2+} release from internal stores [38–40]. Hence, it is very likely that such cellular processes as migration, proliferation, and/or maturation of OPCs, which rely on an intracellular concentration of ions, in particular Ca^{2+} [38, 41, 42], will be affected differently depending on the type of neuronal activity and changes in axon-OPC synaptic input. For neurons, it has been recently demonstrated that different patterns of action potential firing recruit intracellular Ca^{2+}, expression of genes, and signaling pathways differently; furthermore, some firing patterns may affect certain pathways/genes but not others [19]. Among these pathways/genes are, for example, mitogen-activated protein kinase (MAPK) and integrin pathways, cyclin-dependent-kinase-5 (Cdk5), nuclear factor k-light-chain-enhancer of activated B cells (NF-kappaB), Rac-Rho guanosintriphosphat (GTP)-binding proteins, etc. [19]. Many of these pathways/genes also play an important role in proliferation, migration, and/or differentiation of OPCs, and hence may be differently regulated depending on axon-OPC synaptic input. Thirdly, axon-OPC synaptic signaling may trigger activation of enzymatic pathways in OPCs, e.g., initiate cleavage of NG2 proteoglycan by secretases and thus alter plasticity and/or subunit composition of AMPA receptors at axon-OPC synapses [43]. The initiation and/or extent of these alterations may as well depend on the type/strength of axon-OPC synaptic input. Thus, neurons can use axon-OPC synapses to tune their communication with OPCs and to affect various signal transduction mechanisms in OPCs and behavior of OPCs, in keeping with the type of electrical activity. Additionally, the release of other molecules that are known to influence OL lineage cells, e.g., ATP, adenosine, growth factors, nitric oxide [44–46], may also be modulated depending on the neuronal firing paradigm. This idea further extends the modern concept of activity-dependent development and function of OL lineage cells [47] by suggesting that pattern of activity may be more important than the activity per se. As stated by this concept, proliferation and differentiation of OPCs as well as myelination of axons by OLs can be modified by neuronal activity in vitro and in vivo [47–49]. For instance, electrical or optical stimulation of cortical neurons/axons in vivo results in altered proliferation and differentiation of OPCs in the brain

or spinal cord [4, 5]. Environmental enrichment or physical activity enhances the number of newborn OPCs and/or myelination in the amygdala, cerebral cortex, hippocampus, and brain white matter [6, 7, 50–52], while social isolation impairs myelination [53]. Early sensory experience modulates proliferation and distribution of OPCs in the barrel cortex during development [54]. Furthermore, changes in myelination occur and may be required during learning in animals and humans [47]. To tune the changes in myelination to neuronal function, it is expected that one type of neuronal activity is more efficient than another in triggering alterations in the behavior of myelinating glia in vivo. A few studies indicate that this indeed may be the case for Schwann cells in culture [55–57]; however, no in vivo evidence regarding OPCs or OLs has been available with this respect. We transiently changed the activity of callosal axons in adult freely behaving mice in vivo using electrical stimulation at 5 Hz, 25 Hz, and 300 Hz. We considered these interventions mild because each animal underwent only one session of stimulation, and neither of the animals showed signs of pathological behavior during/after the stimulation. The effects of the three stimulation paradigms on the OL lineage cells were not the same. Stimulation at 5 Hz was more efficient than stimulation at 25 Hz or 300 Hz in triggering differentiation of OPCs, as we observed an increase in the density of pre-OLs upon 5 Hz stimulation (Figs 7 and 8). On the other hand, 25 Hz or 300 Hz stimulation resulted in a higher mean density of proliferating cells than 5 Hz stimulation (Fig 8). These data suggest that if firing of neurons within the network in vivo changes as, for instance, a function of the input strength or type, the behavior of OL lineage cells within this network will also be tuned depending on the input properties. In brain slices the amount and the timing of glutamate release at axon-OPC synapses differ when axons are stimulated at 5, 25, or 300 Hz (Figs 3 & 6). Therefore, it is tempting to speculate that axon-OPC communication at synapses is one of the factors that mediate the observed difference in the behavior of OPCs in vivo upon callosal stimulation with different frequencies. Other mechanisms may include nonsynaptic signaling by different molecules [47] or direct structural interactions between axons and OPCs. It would be of future interest to discover the patterns of neuronal activity that can most efficiently strengthen or weaken proliferation, differentiation, and/or turnover of OPCs in vivo and to ascertain the role of axon-OPC synapses in these processes. This research may open new perspectives to therapy of demyelinating disorders where remyelination strongly relies on the increased proliferation and differentiation of OPCs or certain types of gliomas in which, on the contrary, reduction of cell proliferation is expected to improve the disease prognosis.

Materials and methods

Ethics statement

All experiments were performed in accordance with the guidelines of the Animal Care and Use Committee at the University of Tübingen. All experimental protocols were approved by the Regierungspräsidium Tübingen. All efforts were made to minimize the suffering of the animals. For surgery, the animals were anesthetized with a mixture of isoflurane and oxygen (3%–5% v/v), and metacam (1 mg/kg body weight) was injected subcutaneously in order to prevent pain suffering of the animals. Before decapitation, the animals were anesthetized with a mixture of isoflurane and oxygen (3% v/v).

Animals

NG2DsRedBAC transgenic mice [11] were used in all experiments. Breeding pairs were originally obtained from The Jackson Laboratory (stock 008241) and bred in house. Mice were kept in 12–12 hours of light-dark cycle; food and water were available ad libitum.

Slice preparation

Coronal brain slices containing corpus callosum were prepared from 19–22- or 50–53-day-old mice of both sexes. Mice were anesthetized with a mixture of isoflurane and oxygen (3% v/v) and decapitated. The brain was dissected in ice-cold N-methyl-D-glucamine (NMDG)-based solution containing (in mM): 135 NMDG, 1 KCl, 1.2 KH_2PO_4, 20 choline bicarbonate, 10 glucose, 1.5 $MgCl_2$, and 0.5 $CaCl_2$ (pH 7.4, 310 mOsm), gassed with carbogen (95% O_2, 5% CO_2). 270-μm-thick coronal brain slices were cut in the same solution using Leica VT 1200S vibratome. The slices were transferred to the 32˚C Haas-type interface incubation chamber and perfused with Ringer solution containing (in mM): 124 NaCl, 3 KCl, 1.25 $NaH_2PO_4{\cdot}H_2O$, 2 $MgCl_2$, 2 $CaCl_2$, 26 $NaHCO_3$, 10 glucose; 300 mOsm/kg; 7.4 pH; gassed with carbogen. The chamber was gradually cooled down to room temperature.

Electrophysiology

At least 1 hour after the preparation, individual slices were transferred to the submerged recording chamber mounted on a stage of an upright microscope (FN-1, Nikon, Japan) equipped with infrared differential interference contrast (IR-DIC) filters and a fluorescence light source. The slices were kept at room temperature and superfused continuously (about 2 ml/min) with gassed Ringer solution. OPCs were selected for recordings based on their red fluorescence and were distinguished from pericytes based on their morphology. Patch pipettes were pulled from borosilicate glass capillaries (Science Products, Germany) on a vertical puller (Model PC10, Narishige, Japan). Pipettes had resistance of 5–7 MOhms when filled with internal solution containing (in mM): 125 K-gluconate, 2 Na_2ATP, 2 $MgCl_2$, 0.5 EGTA, 10 HEPES, 20 KCl, 3 NaCl; 280–290 mOsm/kg, titrated to pH 7.3 with KOH. Cells were voltage clamped at the holding potential V_h = −80 mV with an EPC-8 amplifier (HEKA, Germany) and V_h was corrected for a −13 mV liquid junction potential before seal formation. Liquid junction potential was calculated using the software JPCalc for Windows (Peter H. Barry, Sydney, Australia). Series resistance was not compensated. After establishing the whole-cell configuration, 10 depolarizing voltage steps (increment +10 mV) were applied to each cell from V_h = −80 mV, and corresponding current responses were recorded in order to verify that the selected cell was an OPC [21]. Evoked synaptic currents were elicited with isolated pulse stimulator (A-M Systems, Model 2100, Science Products, Germany) using a monopolar glass electrode (resistance 5–6 MΩ) filled with Ringer solution and placed at 50–250 μm from the recorded cell. Single or paired (40 ms interpulse interval) biphasic rectangular pulses of 100–250 μs duration were applied every 15–30 s. Trains of stimuli were applied each 30 s. Minimal stimulation was performed as described by us previously [10] in brain slices where the corpus callosum was isolated from the cortex by 4 cuts: 2 parallel and 2 perpendicular to the orientation of callosal axons. The rationale for doing this was to exclude the possibility that delayed axon-glia currents are triggered by polysynaptic activation of callosally projecting neurons or result from dissimilar conduction velocities in individual callosal fibers. When recording stimulated and spontaneous synaptic currents, we applied a voltage step of −10 mV at the beginning of each sweep in order to monitor the dynamic of the series resistance. Whole-cell currents in response to voltage steps were low-pass filtered at 10 kHz and digitized with a sampling frequency of 20 kHz (ITC-18, HEKA Instruments Inc, USA). All synaptic currents were low-pass filtered at 1 kHz and digitized with a sampling frequency of 10 kHz. Data acquisition was performed using Recording Artist (written by Rick Gerkin, Arizona State University, USA) running under Igor Pro 6.3 (WaveMetrics, Lake Oswego, USA). All recordings of evoked or spontaneous synaptic currents were performed in the presence of NMDA-receptor antagonist (RS)-3-(2-Carboxypiperazin-4-yl)-propyl-1-phosphonic acid (CPP, 10 μM, Tocris) and

$GABA_A$-receptor antagonist (RS)-3-(2-Carboxypiperazin-4-yl)-propyl-1-phosphonic acid (gabazine, 5 μM, Sigma). Miniature synaptic currents were recorded in the presence of 10 μM CPP, 5 μM gabazine, and 0.5–1 μM tetrodotoxin citrate (TTX, Abcam). To verify that synaptic currents are mediated by ionotropic glutamate receptors, we used 6-Cyano-7-nitroquinoxaline-2,3-dione (CNQX, 10 μM, Abcam). To test the role of calcium and VGCCs for synaptic currents in OPCs, we used ethylene glycol tetraacetic acid acetoxymethyl ester (EGTA-AM, 20 μM, Invitrogen), N-type calcium channels blocker Ctx (1 μM, Alomone Labs), or P/Q-type calcium channels blocker Atx (0.5 μM, Alomone Labs). Before applying Ctx or Atx, Albumin Fraction V (BSA, 0.1%, Carl Roth) was perfused via the bath for at least 25 minutes. All drugs were dissolved in Ringer solution and applied via the bath. All patch-clamp recordings were performed at room temperature using Ringer solution unless indicated differently.

Analysis of electrophysiology data

Only those recordings were considered for the analysis in which the offset drift by the end of the experiment was smaller than ±5 mV and the change of the series resistance was <30% of the original value. The series resistance was between 20 and 40 MΩ.

To study stimulated and spontaneous synaptic currents in OPCs, 30–100 sweeps of 5 s length were analyzed per cell. No additional digital filtering was applied to the recorded sweeps before the analysis. Each sweep was cut into 2 pieces: one containing the events during the train and the second containing the delayed events after the train. The detection and the subsequent analysis of the events during and after the train were performed separately.

For the pharmacology experiments, at least 50 sweeps were recorded before the drug perfusion. EGTA-AM effect was analyzed after at least 10 minutes of drug perfusion. Ctx or Atx effects were analyzed after at least 15 minutes of drug perfusion.

Analysis of the events during the train. Stimulus artifact was removed using the following procedure: for each recorded cell, the sweeps containing failure in response to the first stimulus in the train were collected and averaged (failure was defined as an absence of postsynaptic response after a stimulation pulse); the part of the averaged sweep from the beginning of the first stimulus in the train until the end of the first interstimulus interval was cut out; a new sweep ("train of failures") was generated by concatenating the cut piece of the train n times, in which n = number of stimuli in the original train; the "train of failures" was subtracted from each recorded sweep.

The detection of the events was performed in the stimulus-artifact–subtracted sweeps containing a 1-s-long pretrain baseline. The events were detected using a deconvolution-based algorithm [58] in FBrain, a customized program running under IgorPro 6 (WaveMetrics, Lake Oswego, USA). FBrain was kindly provided by Peter Jonas Lab (IST Austria, Klosterneuburg). The deconvolution trace was passed through a band-pass filter at 0.1 to 200 Hz. The event detection template had the rise time of 0.5 ms, the decay time constant of 4 ms, and the amplitude of −3 pA. The event detection threshold (θ) was set to 3.9 times the standard deviation of a Gaussian function fitted to the all-point histogram of the deconvolved trace [58]. All events detected by the algorithm were inspected visually, and those events that clearly did not show the kinetic of a typical EPSC (i.e., fast rise and slower exponential decay) were manually removed from the subsequent analysis. The subsequent analysis was performed using custom-written macros in IgorPro.

We defined phasic events during the train as those events for which onset was located within the 6 ms after the stimulus onset. The events for which onset occurred later than 6 ms within the same interstimulus interval were defined as asynchronous events during the train and were further considered only for the analysis of the charge transfer (see below). To

estimate the amplitude of each phasic event, we used the following procedure: the baseline was adjusted to the time interval from the beginning of each stimulus until the event onset; the peak center of each event was determined as a minimum (i.e., where the first derivative of the sweep crosses zero) within the interval of 7.5 ms after the stimulus onset; the values of the current in the peak center and in 2 points around it were averaged in order to obtain the measurement of the current amplitude. Hence, response was defined in our study as an EPSC for which onset is located <6 ms after the stimulus and whose peak is located <7.5 ms after the stimulus.

To estimate the amplitude of each failure, a similar procedure was used, with the exception that "the peak center" was determined not as a minimum but as one point randomly selected by the algorithm within the interval of 7.5 ms after the stimulus onset. Hence, a failure was defined in our study as a situation in which, after a stimulation pulse, we did not observe an EPSC with an onset located <6 ms after the stimulus and with peak located <7.5 ms after the stimulus.

For each stimulation paradigm in each cell, the amplitude of phasic currents after a given stimulus was calculated as the mean amplitude of all responses and all failures after this stimulus. Potency was calculated as the mean amplitude of all responses after a given stimulus, excluding the failures. Response probability was calculated as the number of responses after this stimulus divided by the total number of trials in the stimulation paradigm. To calculate the average amplitude, potency, and response probability (after a given stimulus) across all cells for a given stimulation paradigm, the corresponding mean values were averaged. To calculate the normalized average amplitude and response probability, the corresponding average value after a given stimulus was divided by the average value after the first stimulus. To study the kinetics of phasic events, 10%–90% rise time and weighted decay time constant (after double-exponential fit) were measured for each event. The latency of each phasic response was determined as the temporal location of the point where the deconvolved trace crossed the event detection threshold in FBrain. For each stimulation paradigm in each cell, the variance of the latency of phasic responses after a given stimulus was calculated as a square of the standard deviation of the latencies of all events after this stimulus. For the analysis of charge transfer during the train, the full length of each interstimulus interval (containing phasic and asynchronous currents) was considered. The baseline was adjusted to the time interval from the beginning of each stimulus until the event onset; hence, only the transient currents after each stimulus were taken into consideration. Each interstimulus interval was split into 5-ms-long bins and trapezoidal integration was performed on each bin. To calculate the total charge transfer during the train, the charge values after each stimulus within the train were summed.

Recording and analysis of 300 Hz trains. As indicated above, we defined phasic events during the train as those events whose onset was located within the 6 ms after the stimulus onset. However, in case of 300 Hz trains, the interstimulus interval is only about 3.3 ms long. Hence, to make the analysis of 300 Hz trains comparable to the other stimulation paradigms, we recorded 300 Hz trains consisting of 1, 3, 5, 10, 15, or 20 pulses. In each case, we analyzed the phasic responses for which onset was located within the 6 ms after the last stimulus of the train, and we considered them as events occurring after the 1st, 3rd, 5th, 10th, 15th, and 20th stimulus of the train. These events were then compared to the events after the corresponding stimuli of the other recording paradigms.

Analysis of delayed and mEPSCs. The delayed events were defined as those whose onset occurred later than 10 ms after the last stimulus of the train. The detection of delayed events was performed using a deconvolution-based algorithm in a similar way as described above for the events during the train. The amplitude, rise time, and decay time were measured as described above. To build the time course of the delayed events rate, the following procedure

was used: the onset of each event was determined in FBrain as described above; the number of events within the successive 10-ms-long bins was counted up to 650 ms after the last stimulus of the train and plotted versus time. The resulting histogram was normalized to the number of analyzed sweeps. The peak rate of the delayed events was calculated as the mean frequency of the events on the interval from 10 to 110 ms after the last stimulus in the train. To estimate the charge transferred by the delayed currents, the following procedure was used: each delayed event was isolated and the baseline was adjusted to the time interval of 5 ms before the event onset, trapezoidal integration was performed over the time course of an event to obtain the charge value, and the charge transfer by the individual events and the values of the onset of these events were then used to construct the average time course of charge transfer for a given cell in 5-ms-long bins.

Amplitude distribution histograms of miniature, unitary, and delayed events. To construct the amplitude distribution histograms, we pooled the amplitude values of all unitary, delayed, or miniature EPSCs from several recorded cells. The respective numbers of pooled cells and events are indicated in Fig 1. The bin size for each histogram is 0.5 pA, and each histogram is normalized onto the probability density using the built-in function in IgorPro. The fit with lognormal function was done automatically in IgorPro.

To estimate the amplitude of the noise, we used the following procedure: the peak center of each event was determined as described above; one anchoring point located 3 ms before the peak center of each event (i.e., before the event onset) was defined; the second anchoring point was selected 1 ms after the first anchoring point. The values of the current in 2 points around each anchoring point were averaged, and one average was subtracted from another. The resulting value was considered as noise measurement for a given event. This procedure of noise estimation imitates the measurement of the event amplitude. The values of the noise were collected for all events and the histograms of noise amplitude distribution were constructed using similar parameters as described above for the events amplitude.

Surgery, in vivo stimulation, and EdU application

Adult male mice (6–8 weeks old) from the NG2DsRedBAC transgenic mouse line, but not expressing the transgene, were anesthetized with a mixture of isoflurane and oxygen (3%–5% v/v) and fixed in the stereotaxic frame (Stoelting, USA). The depth of the anaesthesia was verified by testing the reaction of the mouse to a toe pinch. Bepanthen (Bayer) was applied to the eyes in order to protect them from dehydration. Metacam (1 mg/kg body weight, Boehringer Ingelheim) was injected subcutaneously in order to prevent pain suffering of the animals. The body temperature was monitored using a rectal thermometer and kept at 36˚C using the heating pad. The skin above the skull was disinfected, a small cut was made, and Xylocaine (2%, Astra Zeneca) was applied locally. The surface of the skull was cleaned with bone scraper and hydrogen peroxide (3%). Two windows were opened in the skull using a dental drill (NSK Mio drill): on the right side, a small longitudinal window was opened for the implantation of an electrode array used for stimulation, and on the left side, a larger window was opened for the recording of field potentials. An array of 5 electrodes was implanted into the right side of the corpus callosum using the following coordinates: posterior −1.06, lateral 0.8, and ventral 1.3 mm from Bregma and was fixed with dental cement (IvoclarVivadent). The electrode array was self-made: glass-coated platinum wires (Thomas Recording, Germany) were sharpened (outer diameter: 80 μm, platinum diameter: 25 μm, impedance was about 500 kΩ), and 5 of them were arranged parallel to each other. The distance between the tips was 250 μm. To verify that action potentials propagate through the middle part of the corpus callosum used for subsequent counting of cells, we exposed the surface of the cortex contralateral to the implanted

electrode array and attached the recoding ball electrode to it. We then applied low frequency stimulation to the array and tested whether we were able to record field potentials at the contralateral side. This was possible in each mouse. In some animals, we applied TTX (1 μM) or CNQX (10 μM) in saline onto the surface of the cortex to verify that the field potential was dependent on the action potentials and ionotropic glutamate receptor activation. Each drug inhibited the field potential. These animals were not used for further experiments.

After the surgery, mice recovered from anesthesia fast and were returned to their home cages. One week ("7 days group") or 11 days ("3 days group") after surgery, mice were briefly anesthetized to connect the stimulator. This way, all mice were sacrificed 14 days after the surgery, and therefore any possible long-term impact of the surgical procedure was expected to be similar in all animals. Each mouse was stimulated in its home cage, where it was allowed to move freely. Each mouse underwent one of the following types of stimulation: (a) sham, i.e., the mouse was connected to the stimulator but the system was switched off, (b) 20 pulses at 5 Hz were applied every 5 minutes 36 times, (c) 20 pulses at 25 Hz were applied every 5 minutes 36 times, or (d) 20 pulses at 300 Hz were applied every 5 minutes 36 times. Every mouse underwent only 1 stimulation session, which lasted 3 hours, i.e., 36 stimulations at 5-min intervals. Video monitoring was performed for the majority of animals during the whole stimulation session. If, in rare cases, the electrodes got disconnected from the mouse, the mouse was excluded from the subsequent analysis. After the end of the stimulation session, each mouse was taken back to its original housing room. From that moment on and during the following 48 hours, the drinking water of each mouse contained 0.2 mg/ml 5-ethynyl-2'-deoxyuridine (EdU, Thermo Fisher) [59].

Immunohistochemistry

One week or 3 days after the stimulation session, mice were sacrificed, the brain was removed, and 300-μm-thick coronal slices were cut using the Leica VT 1200S vibratome. The cutting was performed in a solution of the following composition (in mM): 87 NaCl, 2.5 KCl, 1.25 NaH_2PO4^+H2O, 7 $MgCl_2$, 0.5 $CaCl_2$, 25 $NaHCO_3$, 25 glucose, and 75 sucrose. The slices were fixed overnight at 4˚C in 4% paraformaldehyde which was dissolved in 10 mM phosphate-saline buffer (PBS). Then, the 300-μm-thick slices were washed, embedded into agar, and resectioned in PBS to 30-μm-thick slices using Microtome (HM 650V, Thermo Fischer Scientific). All stainings were performed on 30-μm free-floating slices placed into multiwell plates. For EdU visualization, we followed the protocol recommended by Thermo Fisher Scientific. For antigen retrieval, we incubated the slices in 10 mM citric acid (pH = 6.0) at 37˚C. After washing, we applied blocking solution containing 0.1 M Tris-buffer saline (TBS), 3% Albumin Fraction V, and 0.2% Triton-X for 1 hour at 37˚C. Primary antibody was incubated overnight in 0.1 M TBS (pH = 7.6) containing 0.2% Triton-X. The following primary antibody was used: rabbit or guinea pig anti-NG2 (1:500, gift from Bill Stallcup, Burnham Institute, La Jolla, USA), mouse anti-APC (1:50, Ab-7, CC-Calbiochem), rabbit anti-Cleaved-Casp-3 (1:500, Cell Signalling Technology), rat anti-CD68 (1:100, Serotec). Detection was performed using the following secondary antibody: goat anti-rabbit Alexa Fluor 488 (1:1,000, Invitrogen), goat anti–guinea pig Alexa Fluor 633 (1:1,000, Invitrogen), goat anti-mouse Alexa Fluor 555 (1:500, Invitrogen), goat anti-rat Alexa Fluor 488 (1:1,000, Invitrogen). Secondary antibody was applied for 3 hours at 37˚C. For counterstaining of the nuclei, we used Diamidino-2-phenylindole dihydrochloride (DAPI, 0.2 μg, Sigma).

Image acquisition

Laser scanning microscope (LSM) 710 system (Zeiss, Germany) was used for image acquisition. Images containing corpus callosum were acquired and saved as z-stacks with a 16-bit

pixel depth. Each z-stack was 11–21 μm thick and consisted of 12–22 z-slices, and the z-step was 1 μm. Each layer of a z-stack was acquired as a multiple tile scan (vertical x horizontal: 2 x 5 images) in which each tile was 512 x 512 pixels in size. Pixel size was 0.42 x 0.42 μm. Each tile scan represented a triple-channel fluorescence image, in which channels were acquired sequentially in ZEN software using 40x oil-immersion objective (NA = 1.3). The following excitation laser lines and emission-detection ranges were used: for DAPI excitation 405 nm, emission 414–490 nm; for Alexa-488 excitation 488 nm, emission 497–556 nm; for Alexa-555 excitation 561 nm, emission 569–633 nm; for Alexa-633 excitation 633 nm, emission 650–740 nm. The beam splitters for each dye matched the excitation laser lines. The pinhole was set to 1 airy unit for each channel. Laser power, detector gain, and offset were adjusted such that in the final scan (averages from 2), we had good signal-to-background-noise ratio. All images presented in the figures are representative examples and have not been additionally processed with any software after acquisition. For presentation purposes, the color of the far red channel used for visualizing EdU signals has been changed in the figures to "Green Fire Blue" LUT in ImageJ in order to distinguish it from the red channel.

Cell counting

We counted cells in unprocessed z-stack images using ImageJ (NIH, USA). The corpus callosum was identified based on the maximum intensity projection of the CC1 and DAPI staining. To define the lateral borders of the region of interest used for counting, in each coronal slice we determined the midline and outlined the area of the corpus callosum approximately 500 μm to each side from the midline, i.e., the region of interest was approximately 1 mm broad. In dorso-ventral direction, we considered the full thickness of the corpus callosum, which was easily identifiable based on the visualization of the cortex and the hippocampus. Anterior and posterior borders for counting were approximately from −0.5 mm to 1.5 mm from Bregma.

For the cells located close to the predefined border of the region of interest, only those cells were included into the analysis whose nucleus touched the border. OPCs were identified as $NG2^+CC1^-$ cells, pre-OLs as $NG2^+CC1^+$ cells, and myelinating OLs as $NG2^-$ cells expressing CC1 in their soma. The following groups of animals were used: (1) sham-treated mice ($n = 7$), (2) mice stimulated at 25 Hz and sacrificed 3 days after the stimulation ($n = 3$), (3) mice stimulated at 300 Hz and sacrificed 3 days after the stimulation ($n = 3$), (4) mice stimulated at 5 Hz and sacrificed 7 days after the stimulation ($n = 5$), (5) mice stimulated at 25 Hz and sacrificed 7 days after the stimulation ($n = 5$), and (6) mice stimulated at 300 Hz and sacrificed 7 days after the stimulation (n = 5). Cells were counted in 2–4 slices from each mouse: in total, 25 slices from sham-treated; 11 slices from 25 Hz, 3 days; 10 slices from 300 Hz, 3 days; 13 slices from 5 Hz, 7 days; 16 slices from 25 Hz, 7 days; and 17 slices from 300 Hz, 7 days groups. After counting, the data was normalized to the volume in which the counting was performed.

Statistics

All data acquisition was randomized (animals for in vivo stimulation, cells during patch-clamp experiments). Throughout the study, we made all efforts to avoid pseudoreplications, both when performing experiments in slices and in vivo. For patch-clamp recordings, we used in total 32 mice of the age P19–22 (Figs 1–5) and 13 mice of the age P50–53 (Fig 6). If several OPCs were recorded on the same day from the same animal, different slices were used and different stimulation paradigms were applied. In some cases, multiple stimulation paradigms were applied while recording from the same cell. During the data analysis, we verified again that all recordings for a given stimulation paradigm always stem from a different mouse. In

this sense, the "n" numbers given in the text reflect simultaneously the number of cells and the number of animals. For in vivo experiments, cells were counted in 2–4 slices per animal; the counts within one animal were averaged and treated as one data point for the ANOVA.

Statistical analysis was performed using SPSS, including tests for homoscedasticity and normal distribution. Where 2 groups were compared, independent *t* tests were used. Pharmacology data was tested with paired *t* test (control versus drug conditions). When more than 2 data sets were compared, we used one-way ANOVA with post hoc Bonferroni or Dunnett's test. For evaluating the in vivo experiments, we used nested-ANOVA design (stimulation group: fixed factor; mice: random factor; cell density per slice: dependent variable, "nested" in mice) with post hoc Tukey test.

In all graphs, statistically significant differences are indicated as follows: $^{*}p < 0.05$, $^{**}0.001 < p < 0.01$, $^{***}p < 0.001$, or the p values are written on the graph.

Box and whisker plots: the bottom and top of each box represent 25th and 75th percentiles of the data, respectively, while whiskers represent 10th and 90th percentiles. The midline represents the median. For graphs other than box plots, each point represents the mean ± SEM unless indicated differently in the corresponding figure legend. Data in text is also represented as mean ± SEM.

Supporting information

S1 Fig. Simultaneous application of ω-Conotoxin-GVIA and ω-Agatoxin-IVA reduces synaptic transmission but does not abolish it completely. (A-C) Average current amplitude including failures, response probability, and response potency upon each stimulus of the train during control conditions and after perfusion of ω-Conotoxin-GVIA (Ctx) and ω-Agatoxin-IVA (Atx). n = 3 cells from 3 mice. Each point represents mean±SEM. Paired T-test (S8 Table). $^{*}p<0.05$; $^{**}0.001<p<0.01$. **(D)** Peak rate of delayed currents in OPCs during control conditions and after perfusion of ω-Conotoxin-GVIA and ω-Agatoxin-IVA. Each grey point represents an average peak rate in an individual experiment. Each point in color represents the mean peak rate within the experimental group. Paired T-test (S16 Data). The numerical data used in A-D are included in S17 Data.
(TIF)

S2 Fig. Effect of electrical stimulation on the number and differentiation of OPCs three days after the stimulation session. (A-B) Average density of **(A)**OPCs and **(B)**pre-OLs in corpus callosum upon electrical stimulation of callosal axons at 25 Hz (n = 3 mice, total 11slices) or 300 Hz (n = 3 mice, total 10 slices), vs. sham-treated control animals (n = 7 mice, total 25 slices). Note that differentiation rate was significantly increased by 25 Hz but not by 300 Hz stimulation **(B)**. Nested ANOVA and post-hoc Tukey were used for statistical analysis (S18 Data). Box- and whisker plots: the bottom and top of each box represent 25^{th} and 75^{th} percentiles of the data, respectively; while whiskers represent 10^{th} and 90^{th} percentiles (sometimes the whiskers are not visible). The midline represents the median. The numerical data used in A-B are included in S19 Data.
(TIF)

S3 Fig. Cell death was not observed in the corpus callosum three days after the stimulation at 300 Hz, and also not in sham-treated animals. (A-C) Sham-treated animal: Coronal section of corpus callosum showing double channel immunofluorescent labelling with DAPI (**A**, blue), Caspase-3 (**B**, red), and the overlay of two channels (**C**). Left column: Overview image taken with an open pinhole. The dashed and white squares indicate the region of electrode implantation and the region of interest used for counting of oligodendroglial cells, respectively.

These regions are shown at a higher magnification in the middle- and right-column images. Note that cell counting area is far away from injury site. ctx = cortex, cc = corpus callosum, hc = hippocampus. Scale bars: 500 μm. Middle column: Higher magnification of the area indicated on the left image with the dashed square. The image shows the site of cortical injury caused by electrode implantation. Single confocal plane. Scale bars: 100 μm. Right column: Higher magnification of the area indicated on the left image with the white square. The image shows the region of corpus callosum with white dashed line denoting the region of interest where counting of oligodendroglial cells was performed. Single confocal plane. Scale bars: 100 μm. **(D-F)** As in **(A-C)** but for 300 Hz stimulation. Note that in **E** (left panel) the right part of the corpus callosum appears brighter. This is due to the folding of the slice and not due to the positive labelling with caspase-3, as revealed by the single confocal image of that region (right panel). Note that in both sham-treated and stimulated animal caspase-3-expressing cells are visible only at the injury site, but not in corpus callosum. All images are representative examples. Samples from the group of mice received stimulation at 25 Hz (not shown) followed very similar pattern, i.e. caspase-3-expressing cells appeared at the injury site, but not in the corpus callosum.
(TIF)

S4 Fig. Microglia activation was not observed in the corpus callosum three days after the stimulation at 300 Hz, and also not in sham-treated animals. (A-C) Sham-treated animal: Coronal section of corpus callosum from a showing double channel immunofluorescent labelling with DAPI (**A**, blue), CD68 (**B**, red), and the overlay of two channels (**C**). Left column: Overview image taken with an open pinhole. The dashed and white squares indicate the region of electrode implantation and the region of interest used for counting of oligodendroglial cells, respectively. These regions are shown at a higher magnification in the middle- and right-column images. Note that cell counting area is far away from injury site. ctx = cortex, cc = corpus callosum, cc = hippocampus. Scale bars: 500 μm. Middle column: Higher magnification of the area indicated on the left image with the dashed square. The image shows the site of cortical injury caused by electrode implantation. Single confocal plane. Scale bars: 100 μm. Right column: Higher magnification of the area indicated on the left image with the white square. The image shows the region of corpus callosum with white dashed line denoting the region of interest where counting of oligodendroglial cells was performed. Single confocal plane. Scale bars: 100 μm. **(D-F)** As in **(A-C)** but for 300 Hz stimulation. Note that in both sham-treated and stimulated animal CD68-expressing cells are visible only at the injury site, but not in corpus callosum. All images are representative examples. Samples from the group of mice received stimulation at 25 Hz (not shown) followed very similar pattern, i.e. CD68-expressing cells appeared at the injury site, but not in the corpus callosum.
(TIF)

S1 Table. Details on statistical analysis relevant to Fig 1.
(DOCX)

S2 Table. Details on statistical analysis relevant to Fig 2E and 2F.
(DOCX)

S3 Table. Details on statistical analysis relevant to Fig 2G–2I.
(DOCX)

S4 Table. Details on statistical analysis relevant to Fig 2J–2L.
(DOCX)

S5 Table. Details on statistical analysis relevant to Fig 3F–3H.
(DOCX)

S6 Table. Details on statistical analysis relevant to Fig 3I–3J.
(DOCX)

S7 Table. Details on statistical analysis relevant to Fig 3L–3O.
(DOCX)

S8 Table. Details on statistical analysis relevant to S1 Fig.
(DOCX)

S1 Data. Details on statistical analysis relevant to Fig 1.
(DOCX)

S2 Data. Excel spreadsheets containing numerical data relevant to Fig 1.
(XLSX)

S3 Data. Details on statistical analysis relevant to Fig 2.
(DOCX)

S4 Data. Excel spreadsheets containing numerical data relevant to Fig 2.
(XLSX)

S5 Data. Details on statistical analysis relevant to Fig 3.
(DOCX)

S6 Data. Excel spreadsheets containing numerical data relevant to Fig 3.
(XLSX)

S7 Data. Details on statistical analysis relevant to Fig 4.
(DOCX)

S8 Data. Excel spreadsheets containing numerical data relevant to Fig 4.
(XLSX)

S9 Data. Details on statistical analysis relevant to Fig 5.
(DOCX)

S10 Data. Excel spreadsheets containing numerical data relevant to Fig 5.
(XLSX)

S11 Data. Details on statistical analysis relevant to Fig 6.
(DOCX)

S12 Data. Excel spreadsheets containing numerical data relevant to Fig 6.
(XLSX)

S13 Data. Details on statistical analysis relevant to Fig 7.
(DOCX)

S14 Data. Excel spreadsheets containing numerical data relevant to Fig 7 and Fig 8.
(XLSX)

S15 Data. Details on statistical analysis relevant to Fig 8.
(DOCX)

S16 Data. Details on statistical analysis relevant to S1 Fig.
(DOCX)

S17 Data. Excel spreadsheets containing numerical data relevant to S1 Fig.
(XLSX)

S18 Data. Details on statistical analysis relevant to S2 Fig.
(DOCX)

S19 Data. Excel spreadsheets containing numerical data relevant to S2 Fig.
(XLSX)

Acknowledgments

We thank Bill Stallcup (Burnham Institute, USA) for the gift of NG2 antibodies, Rick Gerkin (Arizona State University, USA) for help with setting up the acquisition software, and Alejandro Pernía-Andrade (IST, Klosterneuburg, Austria) for help with setting up FBrain. We thank Jeffrey Diamond (Bethesda, Maryland, USA) and the members of Kukley's laboratory Bartosz Kula and Friederike Pfeiffer for comments on the earlier version of the manuscript.

Author Contributions

Conceptualization: Balint Nagy, Anahit Hovhannisyan, Maria Kukley.

Data curation: Balint Nagy, Maria Kukley.

Formal analysis: Balint Nagy, Anahit Hovhannisyan, Ruxandra Barzan, Ting-Jiun Chen, Maria Kukley.

Funding acquisition: Maria Kukley.

Investigation: Balint Nagy, Anahit Hovhannisyan, Ruxandra Barzan, Ting-Jiun Chen, Maria Kukley.

Methodology: Balint Nagy, Anahit Hovhannisyan, Ruxandra Barzan.

Project administration: Maria Kukley.

Software: Maria Kukley.

Supervision: Maria Kukley.

Validation: Balint Nagy, Anahit Hovhannisyan, Ruxandra Barzan, Ting-Jiun Chen, Maria Kukley.

Visualization: Balint Nagy, Maria Kukley.

Writing – original draft: Balint Nagy, Maria Kukley.

Writing – review & editing: Balint Nagy, Maria Kukley.

References

1. Frohlich N, Nagy B, Hovhannisyan A, Kukley M. Fate of neuron-glia synapses during proliferation and differentiation of NG2 cells. J Anat. 2011; 219(1):18–32. https://doi.org/10.1111/j.1469-7580.2011.01392.x PMID: 21592101
2. Gallo V, Mangin JM, Kukley M, Dietrich D. Synapses on NG2-expressing progenitors in the brain: multiple functions? J Physiol. 2008; 586(16):3767–81. https://doi.org/10.1113/jphysiol.2008.158436 PMID: 18635642
3. Wake H, Ortiz FC, Woo DH, Lee PR, Angulo MC, Fields RD. Nonsynaptic junctions on myelinating glia promote preferential myelination of electrically active axons. Nat Commun. 2015; 6:7844. https://doi.org/10.1038/ncomms8844 PMID: 26238238; PubMed Central PMCID: PMCPMC4532789.

4. Li Q, Brus-Ramer M, Martin JH, McDonald JW. Electrical stimulation of the medullary pyramid promotes proliferation and differentiation of oligodendrocyte progenitor cells in the corticospinal tract of the adult rat. Neurosci Lett. 2010; 479(2):128–33. S0304-3940(10)00628-2 [pii]; https://doi.org/10.1016/j.neulet.2010.05.043 PMID: 20493923

5. Gibson EM, Purger D, Mount CW, Goldstein AK, Lin GL, Wood LS, et al. Neuronal activity promotes oligodendrogenesis and adaptive myelination in the mammalian brain. Science. 2014; 344 (6183):1252304. https://doi.org/10.1126/science.1252304 PMID: 24727982; PubMed Central PMCID: PMCPMC4096908.

6. Ehninger D, Wang LP, Klempin F, Romer B, Kettenmann H, Kempermann G. Enriched environment and physical activity reduce microglia and influence the fate of NG2 cells in the amygdala of adult mice. Cell Tissue Res. 2011; 345(1):69–86. https://doi.org/10.1007/s00441-011-1200-z PMID: 21688212

7. McKenzie I, Ohayon D, Li H, de Faria J, Emery B, Tohyama K, et al. Motor skill learning requires active central myelination. Science. 2014; 346:318–22. 0.1126/science.1254960. https://doi.org/10.1126/science.1254960 PMID: 25324381

8. Hines JH, Ravanelli AM, Schwindt R, Scott EK, Appel B. Neuronal activity biases axon selection for myelination in vivo. Nat Neurosci. 2015; 18(5):683–9. https://doi.org/10.1038/nn.3992 PMID: 25849987; PubMed Central PMCID: PMCPMC4414883.

9. Mensch S, Baraban M, Almeida R, Czopka T, Ausborn J, El Manira A, et al. Synaptic vesicle release regulates myelin sheath number of individual oligodendrocytes in vivo. Nat Neurosci. 2015; 18(5):628–30. https://doi.org/10.1038/nn.3991 PMID: 25849985; PubMed Central PMCID: PMCPMC4427868.

10. Kukley M, Capetillo-Zarate E, Dietrich D. Vesicular glutamate release from axons in white matter. Nat Neurosci. 2007; 10(3):311–20. https://doi.org/10.1038/nn1850 PMID: 17293860

11. Ziskin JL, Nishiyama A, Rubio M, Fukaya M, Bergles DE. Vesicular release of glutamate from unmyelinated axons in white matter. Nat Neurosci. 2007; 10(3):321–30. https://doi.org/10.1038/nn1854 PMID: 17293857

12. Fame RM, MacDonald JL, Macklis JD. Development, specification, and diversity of callosal projection neurons. Trends Neurosci. 2011; 34(1):41–50. https://doi.org/10.1016/j.tins.2010.10.002 PMID: 21129791; PubMed Central PMCID: PMCPMC3053014.

13. O'Connor DH, Peron SP, Huber D, Svoboda K. Neural activity in barrel cortex underlying vibrissa-based object localization in mice. Neuron. 2010; 67(6):1048–61. https://doi.org/10.1016/j.neuron.2010.08.026 PMID: 20869600.

14. Buzsaki G, Mizuseki K. The log-dynamic brain: how skewed distributions affect network operations. Nat Rev Neurosci. 2014; 15(4):264–78. https://doi.org/10.1038/nrn3687 PMID: 24569488; PubMed Central PMCID: PMCPMC4051294.

15. Suter BA, Migliore M, Shepherd GM. Intrinsic electrophysiology of mouse corticospinal neurons: a class-specific triad of spike-related properties. Cereb Cortex. 2013; 23(8):1965–77. https://doi.org/10.1093/cercor/bhs184 PMID: 22761308; PubMed Central PMCID: PMCPMC3698370.

16. Ramos R, Tam D, Brumberg J. Physiology and morphology of callosal projection neurons in mouse. Neuroscience. 2008; 153(3): 654–63. https://doi.org/10.1016/j.neuroscience.2008.02.069 PMID: 18424008

17. Zhu J, Connors B. Intrinsic firing patterns and whisker-evoked synaptic responses of neurons in the rat barrel cortex. J Neurophysiol. 1999; 81(3):1171–83. PMID: 10085344

18. Stein RB, Gossen ER, Jones KE. Neuronal variability: noise or part of the signal? Nat Rev Neurosci. 2005; 6(5):389–97. https://doi.org/10.1038/nrn1668 PMID: 15861181.

19. Lee PR, Cohen JE, Iacobas DA, Iacobas S, Fields RD. Gene networks activated by specific patterns of action potentials in dorsal root ganglia neurons. Sci Rep. 2017; 7:43765. https://doi.org/10.1038/srep43765 PMID: 28256583; PubMed Central PMCID: PMCPMC5335607.

20. Chittajallu R, Aguirre A, Gallo V. NG2-positive cells in the mouse white and grey matter display distinct physiological properties. J Physiol. 2004; 561(Pt 1):109–22. https://doi.org/10.1113/jphysiol.2004.074252 PMID: 15358811

21. Kukley M, Nishiyama A, Dietrich D. The fate of synaptic input to NG2 glial cells: neurons specifically downregulate transmitter release onto differentiating oligodendroglial cells. J Neurosci. 2010; 30 (24):8320–31. 30/24/8320 [pii]; https://doi.org/10.1523/JNEUROSCI.0854-10.2010 PMID: 20554883

22. Maldonado PP, Velez-Fort M, Levavasseur F, Angulo MC. Oligodendrocyte precursor cells are accurate sensors of local K+ in mature gray matter. J Neurosci. 2013; 33(6):2432–42. https://doi.org/10.1523/JNEUROSCI.1961-12.2013 PMID: 23392672.

23. Bekkers JM, Clements JD. Quantal amplitude and quantal variance of strontium-induced asynchronous EPSCs in rat dentate granule neurons. J Physiol. 1999; 516 (Pt 1):227–48. https://doi.org/10.1111/j.1469-7793.1999.227aa.x PMID: 10066937

24. Regehr WG. Short-term presynaptic plasticity. Cold Spring Harb Perspect Biol. 2012; 4(7):a005702. https://doi.org/10.1101/cshperspect.a005702 PMID: 22751149; PubMed Central PMCID: PMCPMC3385958.

25. Smith PD, Liesegang GW, Berger RL, Czerlinski G, Podolsky RJ. A stopped-flow investigation of calcium ion binding by ethylene glycol bis(beta-aminoethyl ether)-N,N'-tetraacetic acid. Anal Biochem. 1984; 143(1):188–95. https://doi.org/10.1016/0003-2697(84)90575-X PMID: 6442108.

26. Lu T, Trussell LO. Inhibitory transmission mediated by asynchronous transmitter release. Neuron. 2000; 26(3):683–94. https://doi.org/10.1016/S0896-6273(00)81204-0 PMID: 10896163

27. Kirischuk S, Grantyn R. Intraterminal Ca2+ concentration and asynchronous transmitter release at single GABAergic boutons in rat collicular cultures. J Physiol. 2003; 548(Pt 3):753–64. https://doi.org/10.1113/jphysiol.2002.037036 PMID: 12640015

28. Rudolph S, Overstreet-Wadiche L, Wadiche JI. Desynchronization of multivesicular release enhances Purkinje cell output. Neuron. 2011; 70(5):991–1004. https://doi.org/10.1016/j.neuron.2011.03.029 PMID: 21658590; PubMed Central PMCID: PMCPMC3148031.

29. Hefft S, Jonas P. Asynchronous GABA release generates long-lasting inhibition at a hippocampal interneuron-principal neuron synapse. Nat Neurosci. 2005; 8(10):1319–28. https://doi.org/10.1038/nn1542 PMID: 16158066

30. Weise J, Engelhorn T, Dorfler A, Aker S, Bahr M, Hufnagel A. Expression time course and spatial distribution of activated caspase-3 after experimental status epilepticus: contribution of delayed neuronal cell death to seizure-induced neuronal injury. Neurobiol Dis. 2005; 18(3):582–90. https://doi.org/10.1016/j.nbd.2004.10.025 PMID: 15755684.

31. d'Avila JC, Lam TI, Bingham D, Shi J, Won SJ, Kauppinen TM, et al. Microglial activation induced by brain trauma is suppressed by post-injury treatment with a PARP inhibitor. J Neuroinflammation. 2012; 9:31. https://doi.org/10.1186/1742-2094-9-31 PMID: 22335939; PubMed Central PMCID: PMCPMC3298794.

32. Thomas TC, Ogle SB, Rumney BM, May HG, Adelson PD, Lifshitz J. Does time heal all wounds? Experimental diffuse traumatic brain injury results in persisting histopathology in the thalamus. Behav Brain Res. 2016. https://doi.org/10.1016/j.bbr.2016.12.038 PMID: 28042008.

33. Vela JM, Yanez A, Gonzalez B, Castellano B. Time course of proliferation and elimination of microglia/macrophages in different neurodegenerative conditions. J Neurotrauma. 2002; 19(11):1503–20. https://doi.org/10.1089/089771502320914723 PMID: 12490014.

34. Kukley M, Kiladze M, Tognatta R, Hans M, Swandulla D, Schramm J, et al. Glial cells are born with synapses. FASEB J. 2008; 22(8):2957–69. https://doi.org/10.1096/fj.07-090985 PMID: 18467596

35. Blackiston D, McLaughlin K, Levin M. Bioelectric controls of cell proliferation: ion channels, membrane voltage and the cell cycle. Cell Cycle. 2009; 8(21):3527–36. https://doi.org/10.4161/cc.8.21.9888 PMID: 19823012

36. LoTurco JJ, Owens DF, Heath MJ, Davis MB, Kriegstein AR. GABA and glutamate depolarize cortical progenitor cells and inhibit DNA synthesis. Neuron. 1995; 15(6):1287–98. https://doi.org/10.1016/0896-6273(95)90008-X PMID: 8845153

37. Seo M, Kim Y, Lee YI, Kim SY, Ahn YM, Kang UG, et al. Membrane depolarization stimulates the proliferation of SH-SY5Y human neuroblastoma cells by increasing retinoblastoma protein (RB) phosphorylation through the activation of cyclin-dependent kinase 2 (Cdk2). Neurosci Lett. 2006; 404(1–2):87–92. https://doi.org/10.1016/j.neulet.2006.05.061 PMID: 16824683.

38. Tong XP, Li XY, Zhou B, Shen W, Zhang ZJ, Xu TL, et al. Ca(2+) signaling evoked by activation of Na(+) channels and Na(+)/Ca(2+) exchangers is required for GABA-induced NG2 cell migration. J Cell Biol. 2009; 186(1):113–28. jcb.200811071 [pii]; https://doi.org/10.1083/jcb.200811071 PMID: 19596850

39. Haberlandt C, Derouiche A, Wyczynski A, Haseleu J, Pohle J, Karram K, et al. Gray matter NG2 cells display multiple Ca2+-signaling pathways and highly motile processes. PLoS ONE. 2011; 6(3):e17575. https://doi.org/10.1371/journal.pone.0017575 PMID: 21455301; PubMed Central PMCID: PMCPMC3063786.

40. Sun W, Matthews EA, Nicolas V, Schoch S, Dietrich D. NG2 glial cells integrate synaptic input in global and dendritic calcium signals. Elife. 2016; 5. https://doi.org/10.7554/eLife.16262 PMID: 27644104; PubMed Central PMCID: PMCPMC5052029.

41. Paez PM, Fulton D, Colwell CS, Campagnoni AT. Voltage-operated Ca(2+) and Na(+) channels in the oligodendrocyte lineage. J Neurosci Res. 2009; 87(15):3259–66. https://doi.org/10.1002/jnr.21938 PMID: 19021296.

42. Cheli VT, Santiago Gonzalez DA, Spreuer V, Paez PM. Voltage-gated Ca2+ entry promotes oligodendrocyte progenitor cell maturation and myelination in vitro. Exp Neurol. 2015; 265:69–83. https://doi.org/10.1016/j.expneurol.2014.12.012 PMID: 25542980; PubMed Central PMCID: PMCPMC4711374.

43. Sakry D, Neitz A, Singh J, Frischknecht R, Marongiu D, Biname F, et al. Oligodendrocyte precursor cells modulate the neuronal network by activity-dependent ectodomain cleavage of glial NG2. PLoS Biol. 2014; 12(11):e1001993. https://doi.org/10.1371/journal.pbio.1001993 PMID: 25387269; PubMed Central PMCID: PMCPMC4227637.

44. Stevens B, Porta S, Haak LL, Gallo V, Fields RD. Adenosine: a neuron-glial transmitter promoting myelination in the CNS in response to action potentials. Neuron. 2002; 36(5):855–68. https://doi.org/10.1016/S0896-6273(02)01067-X PMID: 12467589

45. Ishibashi T, Dakin KA, Stevens B, Lee PR, Kozlov SV, Stewart CL, et al. Astrocytes promote myelination in response to electrical impulses. Neuron. 2006; 49(6):823–32. https://doi.org/10.1016/j.neuron.2006.02.006 PMID: 16543131

46. Garthwaite G, Hampden-Smith K, Wilson GW, Goodwin DA, Garthwaite J. Nitric oxide targets oligodendrocytes and promotes their morphological differentiation. Glia. 2015; 63(3):383–99. https://doi.org/10.1002/glia.22759 PMID: 25327839; PubMed Central PMCID: PMCPMC4309495.

47. Fields RD. A new mechanism of nervous system plasticity: activity-dependent myelination. Nat Rev Neurosci. 2015; 16(12):756–67. https://doi.org/10.1038/nrn4023 PMID: 26585800.

48. Barres BA, Raff MC. Proliferation of oligodendrocyte precursor cells depends on electrical activity in axons. Nature. 1993; 361(6409):258–60. https://doi.org/10.1038/361258a0 PMID: 8093806

49. Demerens C, Stankoff B, Logak M, Anglade P, Allinquant B, Couraud F, et al. Induction of myelination in the central nervous system by electrical activity. Proc Natl Acad Sci U S A. 1996; 93(18):9887–92. https://doi.org/10.1073/pnas.93.18.9887 PMID: 8790426

50. Okuda H, Tatsumi K, Makinodan M, Yamauchi T, Kishimoto T, Wanaka A. Environmental enrichment stimulates progenitor cell proliferation in the amygdala. J Neurosci Res. 2009; 87(16):3546–53. https://doi.org/10.1002/jnr.22160 PMID: 19565652

51. Simon C, Gotz M, Dimou L. Progenitors in the adult cerebral cortex: Cell cycle properties and regulation by physiological stimuli and injury. Glia. 2011; 59(6):869–81. https://doi.org/10.1002/glia.21156 PMID: 21446038

52. Xiao L, Ohayon D, McKenzie IA, Sinclair-Wilson A, Wright JL, Fudge AD, et al. Rapid production of new oligodendrocytes is required in the earliest stages of motor-skill learning. Nat Neurosci. 2016; 19(9):1210–7. https://doi.org/10.1038/nn.4351 PMID: 27455109; PubMed Central PMCID: PMCPMC5008443.

53. Liu J, Dietz K, DeLoyht JM, Pedre X, Kelkar D, Kaur J, et al. Impaired adult myelination in the prefrontal cortex of socially isolated mice. Nat Neurosci. 2012; 15(12):1621–3. https://doi.org/10.1038/nn.3263 PMID: 23143512; PubMed Central PMCID: PMCPMC3729624.

54. Mangin JM, Li P, Scafidi J, Gallo V. Experience-dependent regulation of NG2 progenitors in the developing barrel cortex. Nat Neurosci. 2012; 15(9):1192–4. https://doi.org/10.1038/nn.3190 PMID: 22885848; PubMed Central PMCID: PMCPMC3437334.

55. Itoh K, Stevens B, Schachner M, Fields R. Regulated expression of the neural cell adhesion molecule L1 by specific patterns of neural impulses. Science. 1995; 270:1369–72. https://doi.org/10.1126/science.270.5240.1369 PMID: 7481827

56. Itoh K, Ozaki M, Stevens B, Fields R. Activity-dependent regulation of N-cadherin in DRG neurons: differential regulation of N-cadherin, NCAM, and L1 by distinct patterns of action potentials. J Neurobiol. 1997; 33:735–48. https://doi.org/10.1002/(SICI)1097-4695(19971120)33:6<735::AID-NEU3>3.0.CO;2-A PMID: 9369148

57. Stevens B, Tanner S, Fields RD. Control of myelination by specific patterns of neural impulses. J Neurosci. 1998; 18(22):9303–11. PMID: 9801369

58. Pernia-Andrade AJ, Goswami SP, Stickler Y, Frobe U, Schlogl A, Jonas P. A deconvolution-based method with high sensitivity and temporal resolution for detection of spontaneous synaptic currents in vitro and in vivo. Biophysical journal. 2012; 103(7):1429–39. https://doi.org/10.1016/j.bpj.2012.08.039 PMID: 23062335; PubMed Central PMCID: PMC3471482.

59. Young KM, Psachoulia K, Tripathi RB, Dunn SJ, Cossell L, Attwell D, et al. Oligodendrocyte dynamics in the healthy adult CNS: evidence for myelin remodeling. Neuron. 2013; 77(5):873–85. https://doi.org/10.1016/j.neuron.2013.01.006 PMID: 23473318; PubMed Central PMCID: PMCPMC3842597.

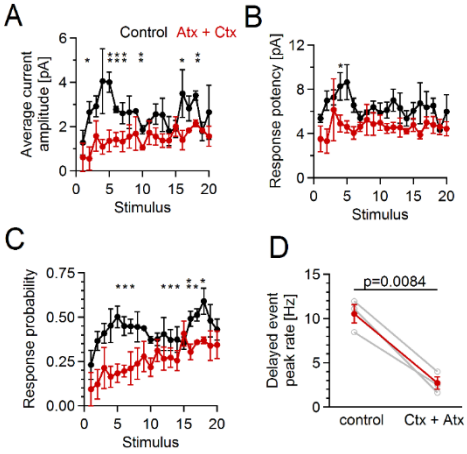

S1 Fig. Simultaneous application of ω-Conotoxin-GVIA and ω-Agatoxin-IVA reduces synaptic transmission but does not abolish it completely.

(A-C) Average current amplitude including failures, response probability, and response potency upon each stimulus of the train during control conditions and after perfusion of ω-Conotoxin-GVIA (Ctx) and ω-Agatoxin-IVA (Atx). n = 3 cells from 3 mice. Each point represents mean±SEM. Paired T-test (S8 Table). *p<0.05; **0.001 **(D)** Peak rate of delayed currents in OPCs during control conditions and after perfusion of ω-Conotoxin-GVIA and ω-Agatoxin-IVA. Each grey point represents an average peak rate in an individual experiment. Each point in color represents the mean peak rate within the experimental group.

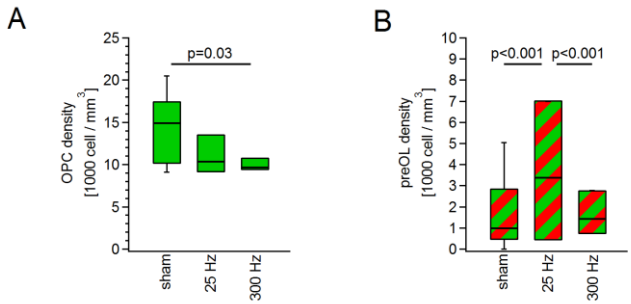

S2 Figure. Effect of electrical stimulation on the number and differentiation of OPCs three days after the stimulation session.

(A-B) Average density of (A)OPCs and (B)pre-OLs in corpus callosum upon electrical stimulation of callosal axons at 25 Hz (n = 3 mice, total 11slices) or 300 Hz (n = 3 mice, total 10 slices), vs. sham-treated control animals (n = 7 mice, total 25 slices). Note that differentiation rate was significantly increased by 25 Hz but not by 300 Hz stimulation (B). Nested ANOVA and post-hoc Tukey were used for statistical analysis (S18 Data). Box- and whisker plots: the bottom and top of each box represent 25th and 75th percentiles of the data, respectively; while whiskers represent 10th and 90th percentiles (sometimes the whiskers are not visible). The midline represents the median.

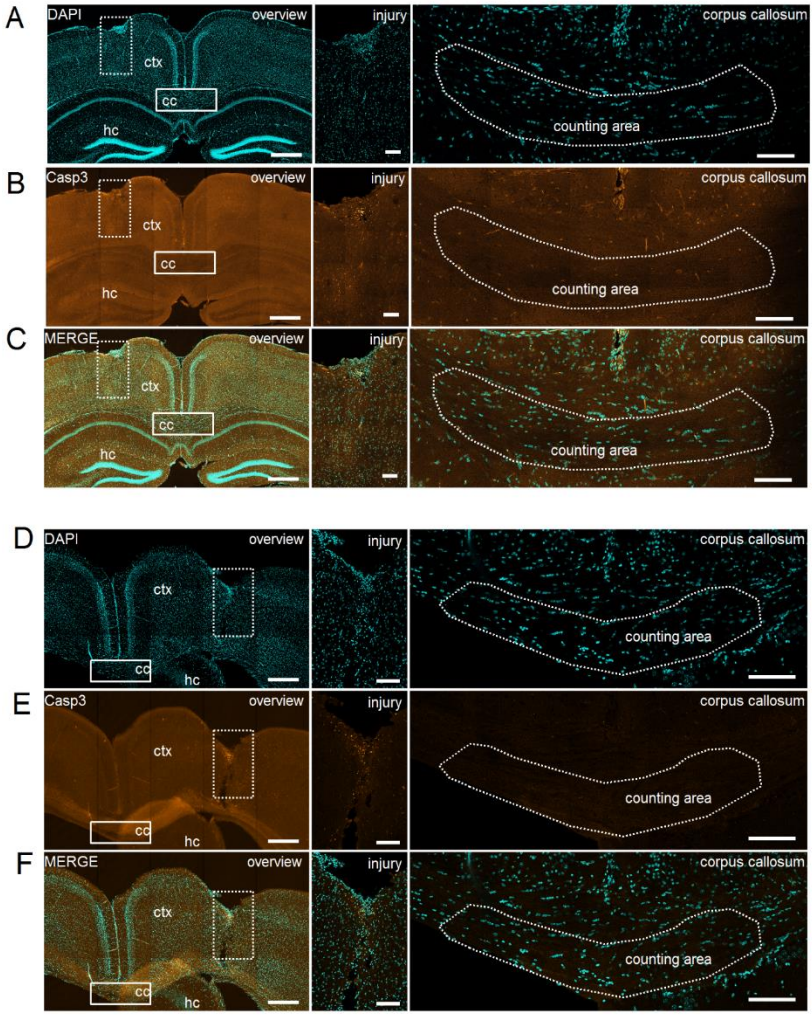
A
DAPI
overview
injury
corpus callosum
ctx
cc
hc
counting area
B
Casp3
overview
injury
corpus callosum
ctx
cc
hc
counting area
C
MERGE
overview
injury
corpus callosum
ctx
cc
hc
counting area
D
DAPI
overview
injury
corpus callosum
ctx
cc
hc
counting area
E
Casp3
overview
injury
corpus callosum
ctx
cc
hc
counting area
F
MERGE
overview
injury
corpus callosum
ctx
cc
hc
counting area

S3 Fig. Cell death was not observed in the corpus callosum three days after the stimulation at 300 Hz, and also not in sham treated animals.

(A-C) Sham-treated animal: Coronal section of corpus callosum showing double channel immunofluorescent labelling with DAPI (A, blue), Caspase-3 (B, red), and the overlay of two channels (C). Left column: Overview image taken with an open pinhole. The dashed and white squares indicate the region of electrode implantation and the region of interest used for counting of oligodendroglial cells, respectively. These regions are shown at a higher magnification in the middle- and right-column images. Note that cell counting area is far away from injury site. ctx = cortex, cc = corpus callosum, hc = hippocampus. Scale bars: 500 μm. Middle column: Higher magnification of the area indicated on the left image with the dashed square. The image shows the site of cortical injury caused by electrode implantation. Single confocal plane. Scale bars: 100 μm. Right column: Higher magnification of the area indicated on the left image with the white square. The image shows the region of corpus callosum with white dashed line denoting the region of interest where counting of oligodendroglial cells was performed. Single confocal plane. Scale bars: 100 μm. **(D-F)** As in (A-C) but for 300 Hz stimulation. Note that in E (left panel) the right part of the corpus callosum appears brighter. This is due to the folding of the slice and not due to the positive labelling with caspase-3, as revealed by the single confocal image of that region (right panel). Note that in both sham-treated and stimulated animal caspase-3-expressing cells are visible only at the injury site, but not in corpus callosum. All images are representative examples. Samples from the group of mice received stimulation at 25 Hz (not shown) followed very similar pattern, i.e. caspase-3-expressing cells appeared at the injury site, but not in the corpus callosum.

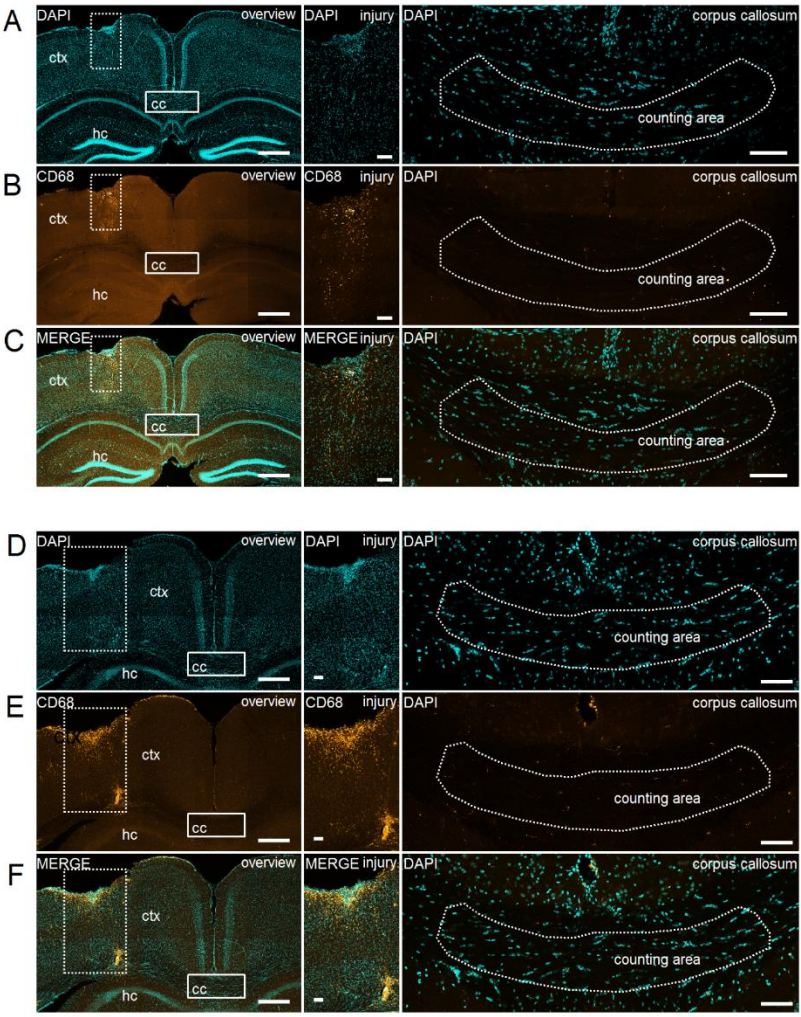
A
DAPI
overview
ctx
cc
hc
DAPI
injury
DAPI
corpus callosum
counting area
B
CD68
overview
ctx
cc
hc
CD68
injury
DAPI
corpus callosum
counting area
C
MERGE
overview
ctx
cc
hc
MERGE
injury
DAPI
corpus callosum
counting area
D
DAPI
overview
ctx
cc
hc
DAPI
injury
DAPI
corpus callosum
counting area
E
CD68
overview
ctx
cc
hc
CD68
injury
DAPI
corpus callosum
counting area
F
MERGE
overview
ctx
cc
hc
MERGE
injury
DAPI
corpus callosum
counting area

S4 Fig. Microglia activation was not observed in the corpus callosum three days after the stimulation at 300 Hz, and also not in sham-treated animals.

(A-C) Sham-treated animal: Coronal section of corpus callosum from a showing double channel immunofluorescent labelling with DAPI (**A**, blue), CD68 (**B**, red), and the overlay of two channels (**C**). Left column: Overview image taken with an open pinhole. The dashed and white squares indicate the region of electrode implantation and the region of interest used for counting of oligodendroglial cells, respectively. These regions are shown at a higher magnification in the middle- and right-column images. Note that cell counting area is far away from injury site. ctx = cortex, cc = corpus callosum, cc = hippocampus. Scale bars: 500 μm. (Continuation from previous page) Middle column: Higher magnification of the area indicated on the left image with the dashed square. The image shows the site of cortical injury caused by electrode implantation. Single confocal plane. Scale bars: 100 μm. Right column: Higher magnification of the area indicated on the left image with the white square. The image shows the region of corpus callosum with white dashed line denoting the region of interest where counting of oligodendroglial cells was performed. Single confocal plane. Scale bars: 100 μm. **(D-F)** As in **(A-C)** but for 300 Hz stimulation. Note that in both sham-treated and stimulated animal CD68-expressing cells are visible only at the injury site, but not in corpus callosum. All images are representative examples. Samples from the group of mice received stimulation at 25 Hz (not shown) followed very similar pattern, i.e. CD68-expressing cells appeared at the injury site, but not in the corpus callosum.

Publication 2. In vivo regulation of oligodendrocyte precursor cell proliferation and differentiation by the AMPA-receptor subunit GluA2.

Chen T-J., Kula B., Nagy B., Barzan R., Gall A., Ehrlich I., and Kukley M. (2018) Cell Reports 2018 25, 1-10

Framework: This is an original research paper. The aim was to study *in vivo* how the functional properties of AMPA receptors in oligodendrocyte precursor cells (OPCs) modulate the proliferation and differentiation of OPCs. To address this aim, we targeted the GluA2 subunit of AMPA receptors in OPCs in the corpus callosum using retroviral approach. We found that introducing unedited or pore-dead GluA2 subunit of AMPA receptors, the modifications which render the receptors Ca^{2+}-permeable, promoted OPC proliferation, and reduced their capability to differentiate into oligodendrocytes. Overexpression of the C-tail of the AMPA receptor in OPCs reduced OPC differentiation, without affecting their proliferation rate.

Contributions: I recorded 10 % of the I-V curve experiments and delayed synaptic events, and analyzed these experiments. I counted cells for the evaluation of the immunohistological data. The rest of the counting was done by RB, T-JC and BK. I participated in the optimization of the electrophysiological data analysis. The rest of the electrophysiological and histological data was recorded and analyzed by T-JC, BK and MK. All the molecular biology was performed by T-JC, with the initial help from AG and IE. In vivo stereotaxic retroviral injection was done by T-JC. Brain preparation and immunohistochemistry were done by T-JC, BK and MK. The statistical analysis was performed by T-JC with the help of BK and me. The figures were prepared by T-JC, with feedback from BK, MK, IE and me. T-JC, IE and MK wrote the original draft and T-JC, BK, RB, IE, MK and me reviewed and edited the final version of manuscript.

Report

Cell Reports

In Vivo Regulation of Oligodendrocyte Precursor Cell Proliferation and Differentiation by the AMPA-Receptor Subunit GluA2

Graphical Abstract

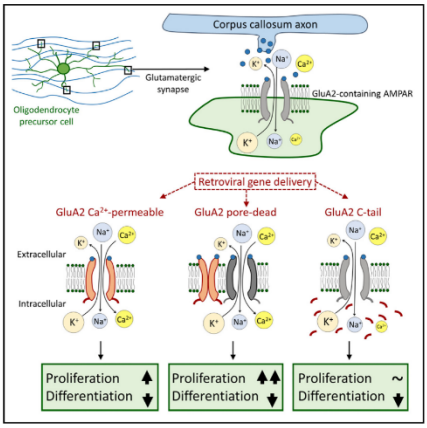

Authors

Ting-Jiun Chen, Bartosz Kula, Bálint Nagy, Ruxandra Barzan, Andrea Gall, Ingrid Ehrlich, Maria Kukley

Correspondence

maria.kukley@uni-tuebingen.de

In Brief

In the brain, oligodendrocyte precursor cells (OPCs) receive glutamatergic AMPA-receptor-mediated synaptic input from neurons. Chen et al. show that modifying AMPA-receptor properties at axon-OPC synapses alters proliferation and differentiation of OPCs. This expands the traditional view of synaptic transmission by suggesting neurons also use synapses to modulate behavior of glia.

Highlights

- AMPA receptors (AMPARs) with modified properties are expressed in OPCs *in vivo*
- Channel-pore mutations of AMPARs affect functional properties of axon-OPC synapses
- Expression of Ca^{2+}-permeable AMPARs alters proliferation and differentiation of OPCs
- Introducing the C-tail of the GluA2 subunit of AMPARs reduces differentiation of OPCs

Chen et al., 2018, Cell Reports 25, 852–861
October 23, 2018 © 2018
https://doi.org/10.1016/j.celrep.2018.09.066

CellPress

OPEN ACCESS CellPress

Cell Reports
Report

In Vivo Regulation of Oligodendrocyte Precursor Cell Proliferation and Differentiation by the AMPA-Receptor Subunit GluA2

Ting-Jiun Chen,[1,2] Bartosz Kula,[1,2] Bálint Nagy,[1,2,3] Ruxandra Barzan,[1,2,8] Andrea Gall,[4,5,6] Ingrid Ehrlich,[4,5,6] and Maria Kukley[1,7,9,*]

[1]Group of Neuron Glia Interaction, Werner Reichardt Centre for Integrative Neuroscience, University of Tübingen, 72076 Tübingen, Germany
[2]Graduate Training Centre of Neuroscience, University of Tübingen, 72074 Tübingen, Germany
[3]Institute of Science and Technology (IST) Austria, 3400 Klosterneuburg, Austria
[4]Learning and Memory Group, Werner Reichardt Centre for Integrative Neuroscience, University of Tübingen, 72076 Tübingen, Germany
[5]Learning and Memory Group, Hertie Institute for Brain Research, University of Tübingen, 72076 Tübingen, Germany
[6]Department of Neurobiology, IBBS, University of Stuttgart, 70569 Stuttgart, Germany
[7]Department of Ophthalmology, Research Institute of Ophthalmology, Faculty of Medicine, University Hospital Tübingen, 72076 Tübingen, Germany
[8]Present address: Optical Imaging Group, Institute for Neural Computation, Ruhr University Bochum, 44801 Bochum, Germany
[9]Lead Contact
*Correspondence: maria.kukley@uni-tuebingen.de
https://doi.org/10.1016/j.celrep.2018.09.066

SUMMARY

The functional role of AMPA receptor (AMPAR)-mediated synaptic signaling between neurons and oligodendrocyte precursor cells (OPCs) remains enigmatic. We modified the properties of AMPARs at axon-OPC synapses in the mouse corpus callosum *in vivo* during the peak of myelination by targeting the GluA2 subunit. Expression of the unedited (Ca^{2+} permeable) or the pore-dead GluA2 subunit of AMPARs triggered proliferation of OPCs and reduced their differentiation into oligodendrocytes. Expression of the cytoplasmic C-terminal (GluA2(813-862)) of the GluA2 subunit (C-tail), a modification designed to affect the interaction between GluA2 and AMPAR-binding proteins and to perturb trafficking of GluA2-containing AMPARs, decreased the differentiation of OPCs without affecting their proliferation. These findings suggest that ionotropic and non-ionotropic properties of AMPARs in OPCs, as well as specific aspects of AMPAR-mediated signaling at axon-OPC synapses in the mouse corpus callosum, are important for balancing the response of OPCs to proliferation and differentiation cues.

INTRODUCTION

In the CNS, neurons are involved in glutamatergic synaptic signaling with oligodendrocyte precursor cells (OPCs). At these neuron-glia synapses, action potentials trigger a fast vesicular release of the neurotransmitter glutamate, which binds to α-amino-3-hydroxy-5-methyl-4-isoxazolepropionic acid receptors (AMPARs) on the OPCs and leads to the activation of a depolarizing current (Bergles et al., 2000). Axon-OPC synapses are present in gray matter and white matter areas of rodent brain (Fröhlich et al., 2011) and human brain (Gallo et al., 2008), but their functional role remains a puzzle. Proliferation and differentiation of OPCs, as well as myelination, are influenced by neuronal activity (Mount and Monje, 2017). Because axon-OPC synapses represent the points of direct structural and functional interaction between the two cell types, they are ideal sites at which the effects of neuronal activity can be conveyed to glial cells. As a consequence, genetic disruption of axon-OPC synapses is expected to affect proliferation or differentiation of OPCs or myelination. However, a study showed that although permanent deletion of AMPARs in OPCs from the onset of mouse development reduced axon-OPC synaptic signaling, it did not alter proliferation and differentiation of OPCs but instead facilitated apoptotic death of oligodendrocytes (OLs) (Kougioumtzidou et al., 2017). In the present study, we used a different strategy to investigate the functional role of axon-OPC synaptic signaling: we aimed at perturbation of the properties of postsynaptic AMPARs in OPCs, rather than at perpetual deletion of these receptors.

AMPARs are large macromolecular complexes that in neurons comprise more than 30 proteins (Schwenk et al., 2014). The core of the AMPAR complex is a tetramer of GluA1–GluA4 subunits, which assemble in different combinations to form a channel pore. The GluA2 subunit is key, because it determines the single-channel conductance (Swanson et al., 1997) and the Ca^{2+} permeability of AMPARs (Hume et al., 1991). Deletion or modification of the GluA2 subunit in neurons results in strong alterations of synaptic function and animal development (Isaac et al., 2007). We expressed the full-length receptors with point mutations in the GluA2 subunit, or the truncated GluA2 subunit, in OPCs *in vivo* and assessed the effects on physiology and function of the oligodendroglial cells.

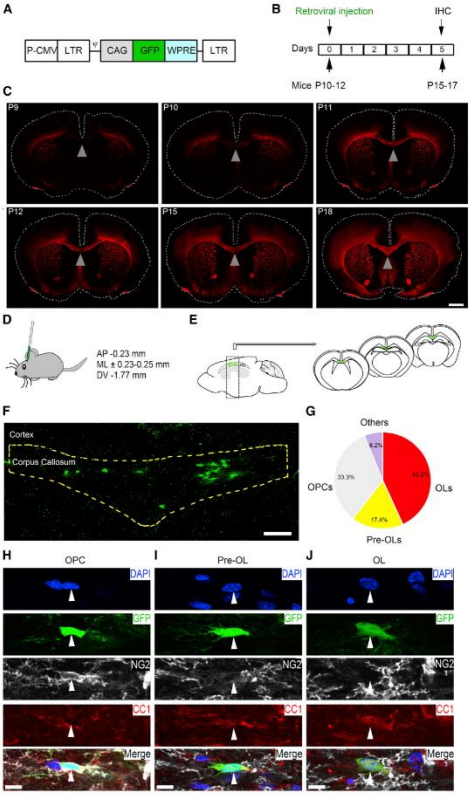

Figure 1. Retroviral Infection Specifically Targets Oligodendroglia Lineage Cells

(A) Scheme of the recombinant retroviral vector. The cytomegalovirus promoter (P-CMV) drives transcription of the viral genome; the chicken-beta actin (CAG) promoter drives expression of GFP. LTR, long terminal repeat; Ψ, viral packing signal; WPRE, Woodchuck hepatitis virus post-transcriptional regulatory element.

(B) Experimental design and timeline. IHC, immunohistochemistry.

(C) Representative images of coronal brain slices stained for myelin basic protein (red). P9, P10, P11, P12, P15, and P18 indicate postnatal days at which slices were prepared. Dashed lines indicate borders of each slice. Arrowheads point to the midline of the corpus callosum. Scale bar: 1 mm.

(D) Stereotaxic coordinates for bilateral virus injection into the corpus callosum. AP, anteroposterior; ML, mediolateral; DV, dorsoventral.

(E) Scheme showing distribution of cells infected with retrovirus (GFP$^+$ cells, green dots) in the corpus callosum. GFP$^+$ cells were found in several 300-μm-thick coronal slices along the rostro-caudal axis.

(F) Maximum intensity projection (6 successive confocal planes) showing GFP$^+$ cells in the corpus callosum (yellow dashed line). Scale bar: 100 μm.

(G) Most GFP$^+$ cells belong to the oligodendroglia lineage (n = 8 animals). OPCs, oligodendrocyte precursor cells; pre-OLs, pre-myelinating oligodendrocytes; OLs, oligodendrocytes.

(H) Maximum intensity projection (3 successive confocal planes) showing quadruple labeling for DAPI, GFP, NG2, CC1, and the merged image. The arrowhead points to an OPC (GFP$^+$NG2$^+$CC1$^-$). Stitches visible in all panels at higher magnification appeared because images have been acquired as multiple tile scans, and the edges of two neighboring tiles have not been stitched properly by the software. Scale bar: 10 μm.

(I) As in (H), but the arrowhead points to a pre-OL (GFP$^+$NG2$^+$CC1$^+$).

(J) As in (H) and (I), but the arrowhead points to an OL (GFP$^+$NG2$^-$CC1$^+$).

RESULTS

Experimental Strategies for Modifying the GluA2-Containing AMPARs in OPCs *In Vivo*

We perturbed the properties of GluA2-containing AMPARs in OPCs in the corpus callosum during the second and third postnatal weeks in mice (Figures 1A, 1B, and 2A–2C), when the OPC division rate is high (Moshrefi-Ravasdjani et al., 2017) and many OPCs differentiate into myelinating OLs, which is reflected in a steep increase of myelin basic protein expression (Figure 1C). The edited GluA2 subunit is present in callosal OPCs during this time window, because the current-voltage (I-V) relationship of AMPAR-mediated excitatory postsynaptic currents (EPSCs) in OPCs shows only slight inward rectification, with an average rectification index (RI) of 0.33 ± 0.058 (Figures S1A and S1B).

To target AMPARs specifically in OPCs, we used a retroviral gene delivery approach (Tashiro et al., 2006) and performed three manipulations (Figures 2A and 2B), which are well

OPEN ACCESS
CellPress

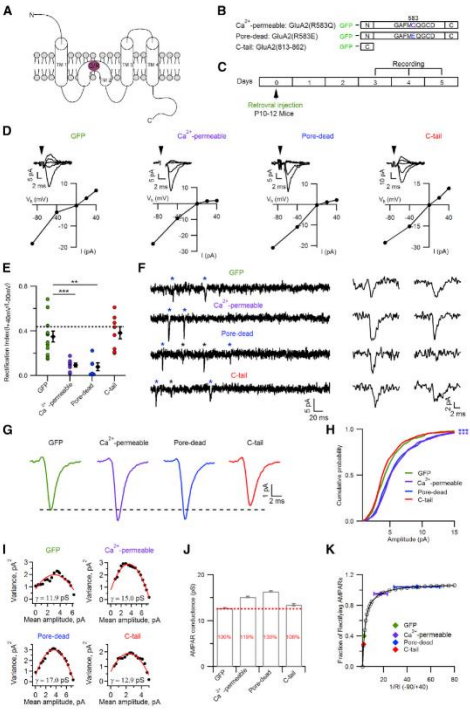

Figure 2. Modifications of the GluA2 Subunit of AMPARs in OPCs Change Rectification and Amplitude of Axon-Glia EPSCs

(A) Scheme of the GluA2 subunit of AMPARs with a Q/R editing site. Q, glutamine; R, arginine; TM, transmembrane domain; N, N terminus; C, C terminus.

(B) Scheme of the mutated and truncated GluA2 subunits fused to GFP and expressed by the viral vector. Amino acid 583 is the site of the point mutation.

(C) Experimental design and timeline for electrophysiological experiments.

(D) Examples of current-voltage (I-V) relationships of evoked EPSCs in OPCs infected with retrovirus expressing GFP or AMPAR-modifying constructs. Black dots represent the average amplitudes of 10 sweeps recorded at each holding potential (V_h). Corresponding averaged sweeps are shown above. Arrowheads indicate time of stimulation; stimulation artifacts are blanked for clarity.

(E) Rectification index (RI) for evoked EPSCs in OPCs infected with retrovirus expressing GFP (n = 12 cells/9 mice), Ca^{2+}-permeable (n = 8 cells/7 mice), pore-dead (n = 6 cells/6 mice), or C-tail (n = 8 cells/6 mice) constructs. Colored dots represent individual cells; black diamonds represent group mean ± SEM. The dashed line indicates the theoretical RI for a linear I-V relationship (0.44). One-way ANOVA ($F(3, 30) = 11.800$, $p = 0.000028$) with post hoc Games-Howell test: GFP versus Ca^{2+} permeable, ***p = 0.001; GFP versus pore dead, **p = 0.002; GFP versus C-tail, p = 0.969.

(F) Representative example traces of delayed EPSCs recorded after cessation of train stimulation in OPCs infected with retrovirus expressing GFP or AMPAR-modifying constructs (V_{hold} = −80 mV). Stars indicate delayed EPSCs; blue stars indicate events shown on the right.

(G) Averaged delayed EPSCs from OPCs expressing GFP (7 cells), Ca^{2+}-permeable (7 cells), pore-dead (8 cells), and C-tail (8 cells) constructs. In each cell, 67 events were randomly selected and averaged. Subsequently, the averages from all cells per group were pooled to generate the average EPSCs.

(H) Cumulative probability distribution of EPSC amplitudes obtained by pooling 67 randomly selected events from each cell within each experimental group. GFP, 469 events (n = 7 cells/6 mice); Ca^{2+} permeable, 469 events (n = 7 cells/6 mice); pore dead, 536 events (n = 8 cells/6 mice); C-tail, 536 events (n = 8 cells/6 mice). Kolmogorov-Smirnov test: GFP versus Ca^{2+} permeable, ***p = 0.00000013492; GFP versus pore dead, ***p = 0.000006; GFP versus C-tail, p = 0.101.

(I) Representative examples of variance-mean plots with parabola fit (red line) for delayed EPSCs recorded in OPCs expressing GFP or AMPAR-modifying constructs. The analysis is based on 85 events in each group. γ is the single-channel conductance estimated from the parabola fit.

(J) Average single-channel conductance (mean ± SEM) of synaptic AMPARs in OPCs expressing GFP or AMPAR-modifying constructs. Red numbers in the bar graphs indicate the average percentage values of single-channel conductance for different manipulations of AMPARs compared to the GFP group (100%, red dashed line).

(K) Estimation of the fraction of rectifying AMPARs (FRR) based on rectification measurements. Open circles and the black curve represent the model for measurements. Colored dots represent values of FRR corresponding to 1/RI (mean ± SEM) for GFP and AMPAR-modifying constructs.

characterized in neurons (Hayashi et al., 2000; Shi et al., 2001): (1) expression of the unedited GluA2(R583Q)-GFP subunit (Ca^{2+}-permeable), aiming to create exclusively Ca^{2+}-permeable AMPARs by replacing arginine(R)583 with glutamine(Q) (Hume et al., 1991) at the channel pore; (2) expression of the GluA2(R583E)-GFP subunit (pore-dead), aiming to reduce the number of functional GluA2-containing AMPARs by replacing arginine(R)583 with glutamic acid(E) in the channel pore

(Dingledine et al., 1992; Shi et al., 2001); and (3) overexpression of the cytoplasmic C-terminal (GluA2(813-862)) of GluA2 (C-tail), a soluble polypeptide of 50 amino acids that in neurons mediates trafficking of receptors to the membrane and interaction with other proteins within the AMPAR complex (Henley, 2003). The C-tail was expected to perturb trafficking of endogenous AMPAR in OPCs (Bassani et al., 2009; Shi et al., 2001). Each construct was tagged with GFP (Figure 2B) to identify infected cells. Recombinant retroviral vectors expressing GFP (control) (Figure 1A) or one of the constructs were stereotaxically injected into the corpus callosum of postnatal day (P) 10–P12 mice (Figures 1B and 1D).

The Retroviral Vector Specifically Targeted Oligodendroglia Lineage Cells

To verify that retroviral vectors specifically targeted OPCs, we counted oligodendroglia lineage cells positive for neuron-glia-antigen-2 (NG2) or adenomatous polyposis coli (APC/CC1) 5 days after injection of the GFP-expressing retrovirus (Figures 1E–1J). 94% of the GFP^+ cells were oligodendroglial cells: 33.35% ± 3.3% were $GFP^+NG2^+CC1^-$ OPCs, 17.4% ± 3.6% were $GFP^+NG2^+CC1^+$ pre-myelinating OLs (pre-OLs), and 43.2% ± 4.2% were $GFP^+NG2^-CC1^+$ mature OLs (Figures 1E–1J). Cells considered pre-OLs in our study are likely earlier pre-OLs than $ENPP6^+$ cells (Xiao et al., 2016), because the latter do not label for platelet-derived growth factor receptor alpha ($PDGFR\alpha$).

Most GFP^+NG2^+ cells were not pericytes: 90% of them were located away from blood vessels and showed a rich tree of processes typical for OPCs (Bergles et al., 2000; Kukley et al., 2007), 8% were in the vicinity of a blood vessel but possessed dichotomized processes, and only 2% were near a blood vessel, had no or few processes (Figures S2A–S2G), and could be pericytes.

Thus, our retroviral vectors specifically and efficiently targeted oligodendroglia lineage cells *in vivo*.

Pore Mutations of the GluA2 Subunit in OPCs Changed Rectification and Amplitude of Axon-Glia EPSCs

Trafficking of full-length AMPARs to the cell surface and integration into the cell membrane are important prerequisites for their delivery to synaptic sites (Borgdorff and Choquet, 2002; Derkach et al., 2007). To verify that receptors with Ca^{2+}-permeable and pore-dead GluA2 subunits were targeted to the cell membrane of OPC, we immunolabeled the GFP fused to the N-terminal domain of the mutant GluA2 subunits (Figure S3A), without cell permeabilization (Kopec et al., 2006). GFP immunoreactivity was localized exclusively to the cell membrane and processes of OPCs (Figures S3B and S3C), confirming that mutant subunits were inserted into the membrane, from which they could be recruited to synapses by lateral diffusion. We did not assess this for the C-tail, because it is not a transmembrane protein.

To investigate changes in Ca^{2+} permeability of AMPARs at axon-OPC synapses, we studied the I-V relationship of evoked EPSCs in $NG2DsRed^+GFP^+$ OPCs recorded in whole-cell, voltage-clamp mode. In each experiment, we verified that the recorded cell had an electrophysiological signature of OPCs (Figure S2H) (Kukley et al., 2010) and was not a pericyte (Kawamura et al., 2002). The I-V relationship of EPSCs in OPCs expressing the GluA2(R583Q)-GFP showed marked inward rectification (RI = 0.093 ± 0.018) (Figures 2D and 2E), as expected for Ca^{2+}-permeable AMPARs (Verdoorn et al., 1991). This suggests that modified GluA2 subunits assembled into tetrameric receptors, trafficked to the postsynaptic sites of axon-OPC synapses, and replaced the endogenous AMPARs. Clear inward rectification (RI = 0.078 ± 0.034) (Figures 2D and 2E) was also observed in OPCs expressing GluA2(R583E)-GFP, indicating that synaptic AMPARs lacked the conducting GluA2 subunit and were Ca^{2+} permeable. The expression of the C-tail did not alter the I-V relationship (RI = 0.38 ± 0.054) (Figures 2D and 2E), suggesting that the delivery of endogenous GluA2-containing AMPARs to synaptic sites was unaffected. To quantify changes of AMPAR properties, we adopted a model for estimating the fraction of rectifying Ca^{2+}-permeable receptors (Stubblefield and Benke, 2010). More than 95% of synaptic AMPARs were rectifying in OPCs expressing the Ca^{2+}-permeable or pore-dead construct, but only 40.18% ± 0.5% and 29.44% ± 0.47% were rectifying in GFP- and C-tail-expressing OPCs, respectively (Figure 2K).

To estimate alterations in the strength of individual axon-OPC synapses, we analyzed the amplitude of quantal EPSCs in OPCs (Nagy et al., 2017) (Figure 2F). The expression of Ca^{2+}-permeable and pore-dead constructs shifted the cumulative histogram toward larger current amplitudes when compared to the GFP group (Figures 2G and 2H) and increased the single-channel conductance of synaptic AMPARs (Figures 2I and 2J). A larger single-channel conductance is expected for AMPARs lacking the functional (edited) GluA2 subunit (Swanson et al., 1997), is in line with the inwardly rectifying I-V relationship (Figures 2D and 2E), and likely underlies the increase in the current amplitude. However, this result differed from that of pyramidal neurons, in which expression of the pore-dead construct reduced the EPSC amplitude (Shi et al., 2001). It is possible that in neurons, AMPARs with pore-dead GluA2 subunits merely replaced endogenous receptors, while in OPCs, the integration of pore-dead subunits was accompanied by insertion of additional functional GluA2-lacking AMPARs. Expression of the C-tail did not affect the quantal EPSC amplitude and single-channel conductance of AMPARs (Figures 2G–2J). Together with the unchanged RI (Figures 2D and 2E), this suggests that the C-tail did not alter the ionotropic function of AMPARs at axon-OPC synapses.

None of the constructs affected presynaptic properties of axon-OPC synapses, because the paired-pulse ratio (PPR) of evoked EPSCs, a parameter reflecting alterations in neurotransmitter release probability (Dobrunz and Stevens, 1997), was unchanged (Figures S3D and S3E). Retroviral infection also did not modify presynaptic release probability or the number and Ca^{2+} permeability of postsynaptic AMPARs in OPCs (Figure S1).

All Manipulations of the GluA2 Subunit Altered the Fraction of OPCs and OLs within the Oligodendroglia Lineage

To investigate changes in OPC differentiation, we counted OPCs, pre-OLs, and mature OLs labeled with specific molecular markers 5 days after the viral injection (Figures 3A–3D). The fraction of OPCs was larger in animals expressing the GluA2 subunit with pore mutations than in the GFP group (Figure 3E), while the proportion of OLs was lower (Figure 3G), suggesting

OPEN ACCESS
CellPress

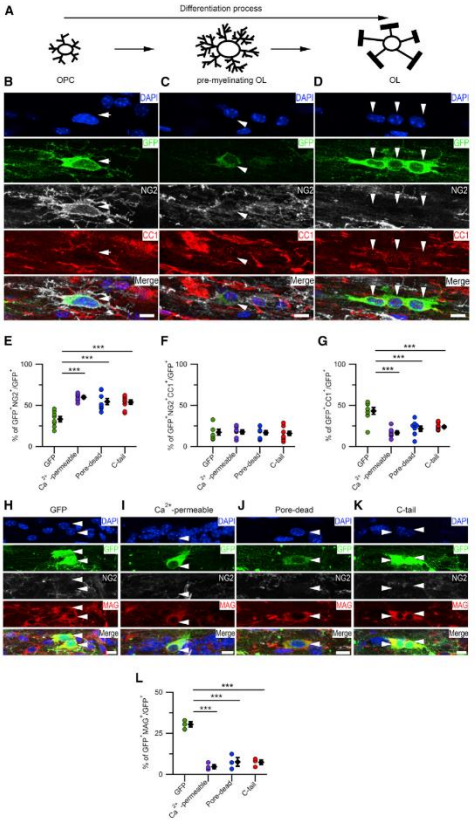

Figure 3. Modifications of the GluA2 Subunit of AMPARs in OPCs Decrease OPC Differentiation

(A) Scheme of the differentiation process in the oligodendroglia lineage.

(B) Maximum intensity projection (3 successive confocal planes) showing examples of OPC ($GFP^+NG2^+CC1^-$) infected with retrovirus expressing the pore-dead construct. Colors are as in Figures 1H–1J. Arrows point to the soma of infected cells. Scale bar: 10 μm.

(C) As in (B), but for a pre-myelinating oligodendrocyte ($GFP^+NG2^+CC1^+$).

(D) As in (B) and (C), but for an oligodendrocyte ($GFP^+NG2^-CC1^+$).

(E) Percentage of OPCs ($GFP^+ NG2^+CC1^-$) among the GFP^+ cells expressing GFP (n = 8), Ca^{2+}-permeable (n = 7), pore-dead (n = 8), and C-tail (n = 9) constructs. Colored dots represent individual animals; black diamonds represent group mean ± SEM. One-way ANOVA ($F(3, 28) = 15.175$, $p = 0.000005$) with post hoc Bonferroni test: GFP versus Ca^{2+}-permeable, ***p = 0.000008; GFP versus pore-dead, ***p = 0.000143; GFP versus C-tail, ***p = 0.000146; Ca^{2+}-permeable versus pore-dead, p = 1.000; Ca^{2+}-permeable versus C-tail, p = 1.000; pore-dead versus C-tail, p = 1.000.

(F) As in (E), but for pre-myelinating oligodendrocytes ($GFP^+NG2^+CC1^+$). One-way ANOVA ($F(3, 28) = 0.077$, $p = 0.972$).

(G) As in (E) and (F), but for oligodendrocytes ($GFP^+NG2^-CC1^+$). One-way ANOVA ($F(3, 28) = 15.557$, $p = 0.000004$) with post hoc Bonferroni test: GFP versus Ca^{2+}-permeable, ***p = 0.000006; GFP versus pore-dead, ***p = 0.000085; GFP versus C-tail, ***p = 0.000253; Ca^{2+}-permeable versus pore-dead, p = 1.000; Ca^{2+}-permeable versus C-tail, p = 0.581; pore-dead versus C-tail, p = 1.000.

(H) Maximum intensity projection (3 successive confocal planes) showing examples of MAG^+ oligodendrocytes (arrowheads) in an animal infected with retrovirus expressing GFP. Scale bar: 10 μm.

(I) As in (H), but for the Ca^{2+}-permeable construct.

(J) As in (H) and (I), but for the pore-dead construct.

(K) As in (H)–(J), but for the C-tail construct.

(L) Proportion of $GFP^+NG2^-MAG^+$ cells among the GFP^+ cells expressing GFP (n = 3 mice), Ca^{2+}-permeable (n = 3 mice), pore-dead (n = 3 mice), and C-tail (n = 3 mice) constructs. Each dot represents one animal; black diamonds represent mean ± SEM for each group. One-way ANOVA ($F(3, 8) = 43.234$, $p = 0.000027$) with post hoc Dunnett's test: GFP versus Ca^{2+}-permeable, ***p = 0.000023; GFP versus pore-dead, ***p = 0.000057; GFP versus C-tail, ***p = 0.000052.

that differentiation of OPCs into OLs was reduced. There was no difference in the percentage of pre-OLs between the groups (Figure 3F). The reduction in OPC differentiation was confirmed by counting the mature OLs expressing myelin-associated glycoprotein (MAG). The proportion of $GFP^+NG2^-MAG^+$ cells among GFP^+ cells was lower in animals expressing the GluA2 subunits with pore mutations than in the GFP group (Figures 3H–3L).

Expression of the C-tail increased the fraction of OPCs and reduced the fraction of OLs within the GFP$^+$ population (Figures 3E–3L). This was surprising, because in contrast to pore mutations, the C-tail did not alter the ionotropic function of AMPARs. It is possible that OPC differentiation was affected because the C-tail interfered with AMPAR signaling via intracellular binding partners of the GluA2 subunit.

The decrease in the fraction of OLs was not a consequence of cell death, because an apoptotic marker, activated caspase-3, was hardly detected in the corpus callosum (Figures S3F–S3K). It was also not a consequence of OPC differentiation into other cell types, because the fraction of oligodendroglia lineage cells within the GFP$^+$ population was comparable in all groups (Figures 3E–3G).

Thus, manipulations of the GluA2 subunit in callosal OPCs perturb normal differentiation of OPCs into OLs.

Pore Mutations of the GluA2-Containing AMPARs Increase Proliferation of OPCs

During the second and third postnatal weeks in mice, many OPCs are actively cycling. Therefore, an increase in the fraction of OPCs (Figure 3E) may be attributable to continued cycling of OPCs at the expense of differentiation (Figure 4A). To test this, we compared the fraction of proliferating GFP$^+$ cells in mice expressing the GFP versus mice expressing the modified GluA2 subunits, or the C-tail. We used two approaches: (1) *in vivo* labeling with 5-ethynyl-2′-deoxyuridine (EdU), which integrates during the S phase, and (2) *ex vivo* labeling for Ki67, which is present during all active phases of the cell cycle (Gerdes et al., 1984).

Pore mutations altering the Ca^{2+} permeability of AMPARs in OPCs resulted in a larger proportion of cycling cells (GFP$^+$EdU$^+$) (Figures 4B and 4C). This was caused by an increase in EdU$^+$ OPCs, because the GFP$^+$ population contained a higher percentage of NG2$^+$EdU$^+$ cells (Figure 4D). In addition, most EdU$^+$ cells were NG2$^+$ in all groups (not shown), indicating that neither of the AMPAR manipulations specifically triggered fast differentiation of EdU$^+$ OPC into OLs.

With our retroviral approach, we initially targeted cycling OPCs (Yamashita and Emerman, 2006). Therefore, the GFP$^+$ population represents cells that are progressing through or have recently completed the cell cycle. EdU injected 3–5 days after the retroviral infection incorporates only into newly synthesized DNA. Therefore, GFP$^+$EdU$^+$ cells denote cells that continued cycling, passed through the S phase again, and underwent another cell division after retroviral infection. An enhanced fraction of EdU$^+$NG2$^+$ cells within GFP$^+$ population upon alteration of Ca^{2+} permeability of AMPARs (Figure 4D) indicates that pore mutations of GluA2 subunit prompted OPCs to re-enter mitosis. If increased Ca^{2+} permeability of AMPARs triggers cell division, but does not promote differentiation, then the population of GFP$^+$NG2$^+$ cells should contain a higher proportion of EdU$^+$ cells. This was only observed for the pore-dead mutation, not the Ca^{2+}-permeable mutation (Figure 4E), suggesting that the former promoted proliferation of OPCs more effectively than the latter. In accordance with this, labeling for Ki67 on the 5th day after viral infection in animals treated with EdU (Figure 4F) showed that the proportion of still-cycling OPCs (GFP$^+$NG2$^+$EdU$^+$Ki67$^+$) within the population of previously cycling OPCs (GFP$^+$NG2$^+$EdU$^+$) was increased only upon expression of the pore-dead mutation (Figure 4G).

Expression of the C-tail did not alter OPC proliferation (Figures 4C–4E and 4G). Therefore, one might expect that the proportion of OPCs is lower after introducing the C-tail than after introducing the GluA2 pore mutations. But this was not the case (Figure 3E), and there was no difference in apoptotic cell death between the manipulations (Figures S3F–S3K). Two mechanisms may underlie an increase in the OPC population: (1) OPCs cycle, rather than differentiate, or (2) OPCs stay longer in the G1 phase or exit the cell cycle but do not differentiate at the usual rate (Figure 4A). When combining the data on differentiation (Figures 3E–3G) and proliferation (Figures 4C–4E and 4G) into a unified model (Figure 4H; Figure S4), we found that EdU$^+$ and EdU$^-$ OPCs contributed to increasing the population of GFP$^+$NG2$^+$ cells for all manipulations (Figure 4H). However, for the pore-dead construct, the fraction of EdU$^+$ OPCs was higher than the fraction of EdU$^-$ OPCs; for the C-tail, the opposite was true; and for the Ca^{2+}-permeable construct, the contribution of those two populations was roughly equal (Figure 4H). This indicates that both mechanisms play a role but that their impact is different depending on the properties of AMPARs. Therefore, axon-OPC synapses are likely involved in regulating the ratio between cycling and non-cycling OPCs.

DISCUSSION

Our major finding is that manipulating the key properties of AMPARs at axon-OPC synapses *in vivo* at the peak of myelination results in altered balance between proliferation and differentiation of OPCs.

In cell culture, AMPARs regulate proliferation and differentiation of OPCs (Fannon et al., 2015; Gallo et al., 1996; Hossain et al., 2014; Yuan et al., 1998), and Ca^{2+}-permeable AMPARs indirectly modulate the expression of genes involved in differentiation and growth (Pende et al., 1994). Ca^{2+} ions are important modulators of proliferation and differentiation of many cells, including neuronal progenitors and tumor and endothelial cells (Cui et al., 2017; Jansson and Åkerman, 2014; Moccia et al., 2012). Our findings *in vivo* suggest that Ca^{2+} permeability of AMPARs may be a key mechanism modulating the development of oligodendroglial cells. During the second and third postnatal weeks in mice, when extensive myelination of axons takes place, OPCs efficiently respond to proliferation and differentiation cues, but it is unknown how OPCs make the choice between the two processes. In GFP controls and in non-injected mice, the RI was highly variable, ranging from 0.15 to 0.68 (Figure 2E; Figure S1B). Hence, during normal development, some OPCs have higher Ca^{2+} permeability of AMPARs than others. Possibly, OPCs with high Ca^{2+} permeability of AMPARs continue cycling, while OPCs with low Ca^{2+} permeability of AMPARs are prone to differentiate. This is also suggested by a study showing that AMPARs in differentiating OPCs have lower Ca^{2+} permeability than in immature OPCs (Zonouzi et al., 2011). Thus, Ca^{2+} permeability of AMPARs is likely a physiological mechanism regulating the choice between proliferation and differentiation of OPCs. Another mechanism may be the subunit composition of AMPARs. We found that the pore-dead mutation of the GluA2

OPEN ACCESS
CellPress

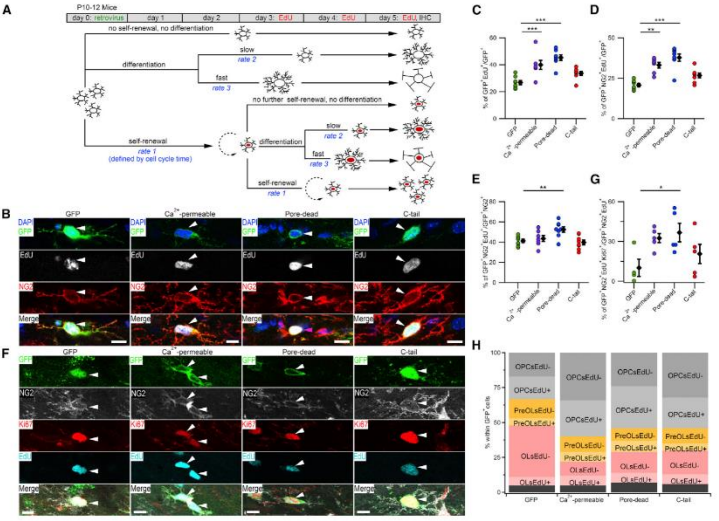

Figure 4. Modifications Rendering AMPARs Ca^{2+} Permeable Increase OPC Proliferation

(A) Scheme illustrating that OPCs infected with retrovirus can follow different developmental fates. Cells with a red nucleus indicate EdU$^+$ cells. IHC, immunohistochemistry.

(B) Maximum intensity projection (2 successive confocal planes) showing examples of quadruple labeling for DAPI (blue), GFP (green), EdU (white), and NG2 (red) and a merged image in animals expressing the GFP, Ca^{2+}-permeable, pore-dead, or C-tail construct. White arrowheads mark GFP$^+$NG2$^+$EdU$^+$ cells. Scale bar: 10 μm.

(C) Proportion of GFP$^+$EdU$^+$ cells among the GFP$^+$ cells expressing the GFP (n = 8 mice), Ca^{2+}-permeable (n = 7 mice), pore-dead (n = 8 mice), and C-tail (n = 8 mice) constructs. Colored dots represent individual animals; black diamonds represent group mean ± SEM. One-way ANOVA ($F(3, 27) = 14.234$, $p = 0.000009$) with post hoc Dunnett's test: GFP versus Ca^{2+}-permeable, ***$p = 0.001$; GFP versus pore-dead, ***$p = 0.000004$; GFP versus C-tail, $p = 0.074$.

(D) As in (C), but for the proportion of GFP$^+$NG2$^+$EdU$^+$ among the GFP$^+$ cells. Kruskal-Wallis test ($H(3) = 21.277$, $p = 0.000092$) with post hoc Dunn's test: GFP versus Ca^{2+}-permeable, **$p = 0.009$; GFP versus pore-dead, ***$p = 0.000084$; GFP versus C-tail, $p = 0.499$.

(E) As in (C) and (D), but for the proportion of GFP$^+$NG2$^+$EdU$^+$ cells among the GFP$^+$NG2$^+$ cells. One-way ANOVA ($F(3, 27) = 5.569$, $p = 0.004$) with post hoc Dunnett's test: GFP versus Ca^{2+}-permeable, $p = 0.838$; GFP versus pore-dead, *$p = 0.007$; GFP versus C-tail, $p = 0.985$.

(F) Maximum intensity projection (3 successive confocal planes) showing examples of quadruple labeling for GFP (green), NG2 (white), Ki67 (red), and EdU (cyan) and a merged image in animals expressing GFP or AMPAR-modifying constructs. The arrowheads point to infected Ki67$^+$EdU$^+$ OPC (GFP$^+$NG2$^+$EdU$^+$Ki67$^+$). Scale bar: 10 μm.

(G) Proportion of GFP$^+$NG2$^+$EdU$^+$ cells labeled for Ki67 among the GFP$^+$ cells expressing the GFP (n = 4 mice), Ca^{2+}-permeable (n = 5 mice), pore-dead (n = 5 mice), or C-tail (n = 5 mice) constructs. Each dot represents one animal; black diamonds represent mean ± SEM for each group. One-way ANOVA ($F(3, 15) = 3.47$, $p = 0.043$) with post hoc Dunnett's test: GFP versus Ca^{2+}-permeable, $p = 0.067$, GFP versus pore-dead, *$p = 0.027$, GFP versus C-tail, $p = 0.53$.

(H) Cumulative bar graphs showing all subpopulations of cells comprising the GFP$^+$ population. Calculations are derived from all data on proliferation and differentiation and are specified in Figure S4. Colored bars indicate oligodendrocyte linage cells; black bars indicate other cells.

subunit triggered stronger changes in OPC proliferation than the Ca^{2+}-permeable mutation (Figures 4E and 4G), although electrophysiological changes at axon-OPC synapses were similar (Figures 2D–2K). An important difference between the pore-dead and the Ca^{2+}-permeable mutations is that ionic conductance is carried only by GluA2-lacking AMPARs in the former case but by AMPARs composed of all subunits (including the unedited GluA2) in the latter case. The downstream signaling cascades may differ depending on the subunit composition, resulting in distinct regulatory mechanisms of the OPC cell cycle.

Regulation of OPC differentiation may also involve the non-ionotropic function of AMPARs, because expression of the C-tail did not alter the AMPAR ionotropic function but did reduce differentiation. AMPAR subunits interact with various binding proteins, including GRIP, TARP, PICK, ABP, SAP97, NSF, and the PLP-integrin-G_i complex (Harlow et al., 2015; Henley, 2003; Henley and Wilkinson, 2016), and many of these interactions involve the cytoplasmic C-tails of AMPAR subunits (Henley, 2003). Expression of the C-tail may have perturbed some of these interactions, for instance, interaction between AMPARs and integrins, which play a key role for differentiation of the oligodendroglial cells (Baron et al., 2005). It will be important to investigate the interaction partners of the GluA2 C-tail in OPCs and to use pharmacological and genetic approaches to identifying the molecular cascades inducing changes in OPC differentiation by non-ionotropic mechanisms.

Proliferation and differentiation of OPCs can be modulated by neuronal activity (Mount and Monje, 2017), and some patterns of activity are more likely to promote proliferation, while others are more likely to promote differentiation (Nagy et al., 2017). Synaptic AMPARs in OPCs are good candidates to transduce the effects of neuronal activity to OPCs. Our findings that different manipulations of AMPARs *in vivo* result in distinct changes in proliferation and differentiation suggest that even the same pattern of neuronal activity may affect OPCs differently depending on the subunit composition of postsynaptic AMPARs in OPCs.

Our manipulations of the established AMPAR signaling in OPCs had a different outcome than elimination of AMPARs from the onset of mouse development (Kougioumtzidou et al., 2017). Proliferation and differentiation of OPCs is likely controlled via several signaling pathways (Huang et al., 2013), with AMPAR signaling being one of them. Germline deletion of AMPARs in OPCs may trigger compensatory mechanisms, resulting in normal proliferation and lineage progression of OPCs in the postnatal brain (Kougioumtzidou et al., 2017). This is less likely in our study, because we induced acute alterations at axon-OPC synapses. Another difference is that we specifically targeted and analyzed the dividing OPCs, while Kougioumtzidou et al. (2017) investigated the entire population of OPCs (cycling OPCs and cells in the G0 phase). AMPAR signaling may play a more prominent role in proliferating OPCs, which have to transfer synaptic contacts to their daughter cells (Ge et al., 2009; Kukley et al., 2008), making the effects of AMPAR modifications more evident in these cells.

Our findings have important implications for future research on the properties and function of AMPARs in OPCs during diseases. Injury triggers trafficking of GluA2-lacking (Ca^{2+}-permeable) AMPARs to the membrane in neurons, and this process can be initiated by inflammatory molecules (Yin et al., 2012). Similar events may take place in OPCs during inflammatory demyelination, spinal cord injury, and other pathological conditions. Therefore, investigating and manipulating properties and downstream signaling of AMPARs in OPCs during diseases is important for opening new therapeutic avenues.

STAR★METHODS

Detailed methods are provided in the online version of this paper and include the following:

SUPPLEMENTAL INFORMATION

Supplemental Information includes four figures and can be found with this article online at https://doi.org/10.1016/j.celrep.2018.09.066.

ACKNOWLEDGMENTS

We thank Eberhart Zrenner (Tübingen) for his trust and support, Bill Stallcup (Burnham Institute, USA) for NG2 antibodies, Rick Gerkin (Arizona State University, USA) for help with acquisition software, Alejandro Pernia-Andrade (Klosterneuburg, Austria) for help with FBrain, Fred Gage (The Salk Institute, USA) and Roberto Malinow (University of California, USA) for plasmids, and Friederike Pfeiffer for comments on the manuscript. This work was supported by Deutsche Forschungsgemeinschaft (DFG) grant KU2569/1-1 (to M.K.); DFG project EXC307 Centre for Integrative Neuroscience (CIN), including grant Pool Project 2011-12 (jointly to M.K. and I.E.); and the Charitable Hertie Foundation (to I.E.). CIN is an Excellence Cluster funded by the DFG within the framework of the Excellence Initiative for 2008–2018. M.K. is supported by the Tistou & Charlotte Kerstan Foundation.

AUTHOR CONTRIBUTIONS

Conceptualization, T.-J.C., I.E., and M.K.; Methodology, T.-J.C., B.K., B.N., A.G., I.E., and M.K.; Software, M.K.; Validation, T.-J.C., B.K., B.N., R.B., and M.K.; Formal Analysis, T.-J.C., B.K., B.N., and M.K.; Investigation, T.-J.C., B.K., B.N., R.B., and M.K.; Writing – Original Draft, T.-J.C., I.E., and M.K.; Writing – Review & Editing, T.-J.C., B.K., B.N., R.B., I.E., and M.K.; Visualization, T.-J.C. and M.K.; Supervision, I.E. and M.K.; Funding Acquisition, I.E. and M.K.

DECLARATION OF INTERESTS

The authors declare no competing interests.

Received: November 13, 2017
Revised: August 9, 2018
Accepted: September 19, 2018
Published: October 23, 2018

REFERENCES

Baron, W., Colognato, H., and Ffrench-Constant, C. (2005). Integrin-growth factor interactions as regulators of oligodendroglial development and function. Glia *49*, 467–479.

Bassani, S., Valnegri, P., Beretta, F., and Passafaro, M. (2009). The GLUR2 subunit of AMPA receptors: synaptic role. Neuroscience *158*, 55–61.

OPEN ACCESS
CellPress

Bergles, D.E., Roberts, J.D., Somogyi, P., and Jahr, C.E. (2000). Glutamatergic synapses on oligodendrocyte precursor cells in the hippocampus. Nature *405*, 187–191.

Borgdorff, A.J., and Choquet, D. (2002). Regulation of AMPA receptor lateral movements. Nature *417*, 649–653.

Cui, C., Merritt, R., Fu, L., and Pan, Z. (2017). Targeting calcium signaling in cancer therapy. Acta Pharm. Sin. B *7*, 3–17.

Derkach, V.A., Oh, M.C., Guire, E.S., and Soderling, T.R. (2007). Regulatory mechanisms of AMPA receptors in synaptic plasticity. Nat. Rev. Neurosci. *8*, 101–113.

Dingledine, R., Hume, R.I., and Heinemann, S.F. (1992). Structural determinants of barium permeation and rectification in non-NMDA glutamate receptor channels. J. Neurosci *12*, 4080–4087.

Dobrunz, L.E., and Stevens, C.F. (1997). Heterogeneity of release probability, facilitation, and depletion at central synapses. Neuron *18*, 995–1008.

Fannon, J., Tarmier, W., and Fulton, D. (2015). Neuronal activity and AMPA-type glutamate receptor activation regulates the morphological development of oligodendrocyte precursor cells. Glia *63*, 1021–1035.

Fröhlich, N., Nagy, B., Hovhannisyan, A., and Kukley, M. (2011). Fate of neuron-glia synapses during proliferation and differentiation of NG2 cells. J. Anat. *219*, 18–32.

Gallo, V., Zhou, J.M., McBain, C.J., Wright, P., Knutson, P.L., and Armstrong, R.C. (1996). Oligodendrocyte progenitor cell proliferation and lineage progression are regulated by glutamate receptor-mediated K+ channel block. J. Neurosci. *16*, 2659–2670.

Gallo, V., Mangin, J.M., Kukley, M., and Dietrich, D. (2008). Synapses on NG2-expressing progenitors in the brain: multiple functions? J. Physiol. *586*, 3767–3781.

Ge, W.P., Zhou, W., Luo, Q., Jan, L.Y., and Jan, Y.N. (2009). Dividing glial cells maintain differentiated properties including complex morphology and functional synapses. Proc. Natl. Acad. Sci. USA *106*, 328–333.

Gerdes, J., Lemke, H., Baisch, H., Wacker, H.H., Schwab, U., and Stein, H. (1984). Cell cycle analysis of a cell proliferation-associated human nuclear antigen defined by the monoclonal antibody Ki-67. J. Immunol. *133*, 1710–1715.

Harlow, D.E., Saul, K.E., Komuro, H., and Macklin, W.B. (2015). Myelin proteolipid protein complexes with αv integrin and AMPA receptors *in vivo* and regulates AMPA-dependent oligodendrocyte progenitor cell migration through the modulation of cell-surface GluR2 expression. J. Neurosci. *35*, 12018–12032.

Hartveit, E., and Veruki, M.L. (2007). Studying properties of neurotransmitter receptors by non-stationary noise analysis of spontaneous postsynaptic currents and agonist-evoked responses in outside-out patches. Nat. Protoc. *2*, 434–448.

Hayashi, Y., Shi, S.H., Esteban, J.A., Piccini, A., Poncer, J.C., and Malinow, R. (2000). Driving AMPA receptors into synapses by LTP and CaMKII: requirement for GluR1 and PDZ domain interaction. Science *287*, 2262–2267.

Henley, J.M. (2003). Proteins interactions implicated in AMPA receptor trafficking: a clear destination and an improving route map. Neurosci. Res. *45*, 243–254.

Henley, J.M., and Wilkinson, K.A. (2016). Synaptic AMPA receptor composition in development, plasticity and disease. Nat. Rev. Neurosci. *17*, 337–350.

Hossain, S., Liu, H.N., Fragoso, G., and Almazan, G. (2014). Agonist-induced down-regulation of AMPA receptors in oligodendrocyte progenitors. Neuropharmacology *79*, 506–514.

Huang, H., Zhao, X.F., Zheng, K., and Qiu, M. (2013). Regulation of the timing of oligodendrocyte differentiation: mechanisms and perspectives. Neurosci. Bull. *29*, 155–164.

Hume, R.I., Dingledine, R., and Heinemann, S.F. (1991). Identification of a site in glutamate receptor subunits that controls calcium permeability. Science *253*, 1028–1031.

Isaac, J.T., Ashby, M.C., and McBain, C.J. (2007). The role of the GluR2 subunit in AMPA receptor function and synaptic plasticity. Neuron *54*, 859–871.

Jansson, L.C., and Åkerman, K.E. (2014). The role of glutamate and its receptors in the proliferation, migration, differentiation and survival of neural progenitor cells. J. Neural Transm. (Vienna) *121*, 819–836.

Kawamura, H., Oku, H., Li, Q., Sakagami, K., and Puro, D.G. (2002). Endothelin-induced changes in the physiology of retinal pericytes. Invest. Ophthalmol. Vis. Sci. *43*, 882–888.

Kopec, C.D., Li, B., Wei, W., Boehm, J., and Malinow, R. (2006). Glutamate receptor exocytosis and spine enlargement during chemically induced long-term potentiation. J. Neurosci. *26*, 2000–2009.

Kougioumtzidou, E., Shimizu, T., Hamilton, N.B., Tohyama, K., Sprengel, R., Monyer, H., Attwell, D., and Richardson, W.D. (2017). Signalling through AMPA receptors on oligodendrocyte precursors promotes myelination by enhancing oligodendrocyte survival. eLife *6*, e28080.

Kukley, M., Capetillo-Zarate, E., and Dietrich, D. (2007). Vesicular glutamate release from axons in white matter. Nat. Neurosci. *10*, 311–320.

Kukley, M., Kiladze, M., Tognatta, R., Hans, M., Swandulla, D., Schramm, J., and Dietrich, D. (2008). Glial cells are born with synapses. FASEB J. *22*, 2957–2969.

Kukley, M., Nishiyama, A., and Dietrich, D. (2010). The fate of synaptic input to NG2 glial cells: neurons specifically downregulate transmitter release onto differentiating oligodendroglial cells. J. Neurosci. *30*, 8320–8331.

Moccia, F., Dragoni, S., Lodola, F., Bonetti, E., Bottino, C., Guerra, G., Laforenza, U., Rosti, V., and Tanzi, F. (2012). Store-dependent Ca(2+) entry in endothelial progenitor cells as a perspective tool to enhance cell-based therapy and adverse tumour vascularization. Curr. Med. Chem. *19*, 5802–5818.

Moshrefi-Ravasdjani, B., Dublin, P., Seifert, G., Jennissen, K., Steinhäuser, C., Kafitz, K.W., and Rose, C.R. (2017). Changes in the proliferative capacity of NG2 cell subpopulations during postnatal development of the mouse hippocampus. Brain Struct. Funct. *222*, 831–847.

Mount, C.W., and Monje, M. (2017). Wrapped to adapt: experience-dependent myelination. Neuron *95*, 743–756.

Nagy, B., Hovhannisyan, A., Barzan, R., Chen, T.J., and Kukley, M. (2017). Different patterns of neuronal activity trigger distinct responses of oligodendrocyte precursor cells in the corpus callosum. PLoS Biol. *15*, e2001993.

Pende, M., Holtzclaw, L.A., Curtis, J.L., Russell, J.T., and Gallo, V. (1994). Glutamate regulates intracellular calcium and gene expression in oligodendrocyte progenitors through the activation of DL-alpha-amino-3-hydroxy-5-methyl-4-isoxazolepropionic acid receptors. Proc. Natl. Acad. Sci. USA *91*, 3215–3219.

Perrais-Andrade, A.J., Goswami, S.P., Stickler, Y., Fröbe, U., Schlögl, A., and Jonas, P. (2012). A deconvolution-based method with high sensitivity and temporal resolution for detection of spontaneous synaptic currents *in vitro* and *in vivo*. Biophys. J. *103*, 1429–1439.

Rozov, A., Zilberter, Y., Wollmuth, L.P., and Burnashev, N. (1998). Facilitation of currents through rat Ca2+-permeable AMPA receptor channels by activity-dependent relief from polyamine block. J. Physiol. *511*, 361–377.

Schwenk, J., Baehrens, D., Haupt, A., Bildl, W., Boudkkazi, S., Roeper, J., Fakler, B., and Schulte, U. (2014). Regional diversity and developmental dynamics of the AMPA-receptor proteome in the mammalian brain. Neuron *84*, 41–54.

Shi, S., Hayashi, Y., Esteban, J.A., and Malinow, R. (2001). Subunit-specific rules governing AMPA receptor trafficking to synapses in hippocampal pyramidal neurons. Cell *105*, 331–343.

Stubblefield, E.A., and Benke, T.A. (2010). Distinct AMPA-type glutamatergic synapses in developing rat CA1 hippocampus. J. Neurophysiol. *104*, 1899–1912.

Swanson, G.T., Kamboj, S.K., and Cull-Candy, S.G. (1997). Single-channel properties of recombinant AMPA receptors depend on RNA editing, splice variation, and subunit composition. J. Neurosci. *17*, 58–69.

Tashiro, A., Zhao, C., and Gage, F.H. (2006). Retrovirus-mediated single-cell gene knockout technique in adult newborn neurons *in vivo*. Nat. Protoc. *1*, 3049–3055.

OPEN ACCESS CellPress

Verdoorn, T.A., Burnashev, N., Monyer, H., Seeburg, P.H., and Sakmann, B. (1991). Structural determinants of ion flow through recombinant glutamate receptor channels. Science *252*, 1715–1718.

Xiao, L., Ohayon, D., McKenzie, I.A., Sinclair-Wilson, A., Wright, J.L., Fudge, A.D., Emery, B., Li, H., and Richardson, W.D. (2016). Rapid production of new oligodendrocytes is required in the earliest stages of motor-skill learning. Nat. Neurosci. *19*, 1210–1217.

Yamashita, M., and Emerman, M. (2006). Retroviral infection of non-dividing cells: old and new perspectives. Virology *344*, 88–93.

Yin, H.Z., Hsu, C.I., Yu, S., Rao, S.D., Sorkin, L.S., and Weiss, J.H. (2012). TNF-α triggers rapid membrane insertion of Ca(2+) permeable AMPA receptors into adult motor neurons and enhances their susceptibility to slow excitotoxic injury. Exp. Neurol. *238*, 93–102.

Young, K.M., Psachoulia, K., Tripathi, R.B., Dunn, S.J., Cossell, L., Attwell, D., Tohyama, K., and Richardson, W.D. (2013). Oligodendrocyte dynamics in the healthy adult CNS: evidence for myelin remodeling. Neuron *77*, 873–885.

Yuan, X., Eisen, A.M., McBain, C.J., and Gallo, V. (1998). A role for glutamate and its receptors in the regulation of oligodendrocyte development in cerebellar tissue slices. Development *125*, 2901–2914.

Ziskin, J.L., Nishiyama, A., Rubio, M., Fukaya, M., and Bergles, D.E. (2007). Vesicular release of glutamate from unmyelinated axons in white matter. Nat. Neurosci. *10*, 321–330.

Zonouzi, M., Renzi, M., Farrant, M., and Cull-Candy, S.G. (2011). Bidirectional plasticity of calcium-permeable AMPA receptors in oligodendrocyte lineage cells. Nat. Neurosci. *14*, 1430–1438.

OPEN ACCESS CellPress

STAR★METHODS

KEY RESOURCES TABLE

REAGENT or RESOURCE	SOURCE	IDENTIFIER
Antibodies		
Guinea pig anti-NG2 Antibody	William Stallcup, Sanford Burnham Prebys Medical Discovery Institute, USA	Cat# Anti-NG2, RRID:AB_2572299
Rabbit anti-NG2 Antibody	William Stallcup,Sanford Burnham Prebys Medical Discovery Institute, USA	Cat# NG2-rabbit, RRID:AB_2572298
Anti-APC (Ab-7) Mouse mAb (CC-1) antibody	Millipore	Cat# OP80, RRID:AB_2057371
Cleaved Caspase-3 (Asp175) (5A1E) Rabbit mAb antibody	Cell Signaling Technology	Cat# 9664, RRID:AB_2070042
Anti-GFP Antibody	Abcam	Cat# ab13970, RRID:AB_300798
Rat Anti-Myelin Basic Protein Monoclonal Antibody, Unconjugated, Clone 12	Abcam	Cat# ab7349, RRID:AB_305869
Mouse Anti-Ki-67 Monoclonal Antibody, Unconjugated, Clone B56	BD Biosciences	Cat# 556003, RRID:AB_396287
Mouse Anti-MAG Monoclonal Antibody, Unconjugated	Santa Cruz Biotechnology	Cat# sc-166849, RRID:AB_2250078
Goat anti-Rabbit IgG (H+L) Cross-Adsorbed Secondary Antibody, Alexa Fluor 568	Thermo Fisher Scientific	Cat# A-11011, RRID:AB_143157
Cy5 antibody	Jackson ImmunoResearch Labs	Cat# 111-175-003, RRID:AB_2314269
Goat anti-Rabbit IgG (H+L) Secondary Antibody, Alexa Fluor 405	Thermo Fisher Scientific	Cat# A-31556, RRID:AB_221605
Goat anti-Guinea Pig IgG (H+L) Highly Cross-Adsorbed Secondary Antibody, Alexa Fluor 633	Thermo Fisher Scientific	Cat# A-21105, RRID:AB_2535757
Goat anti-Mouse IgG (H+L) Secondary Antibody, Alexa Fluor 555 conjugate	Thermo Fisher Scientific	Cat# A-21422, RRID:AB_2535844
Fluorescein (FITC)-AffiniPure Donkey Anti-Chicken IgY (IgG) (H+L) (min X Bov,Gt,GP,Sy Hms,Hrs,Hu,Ms,Rb,Rat,Shp Sr Prot) antibody	Jackson ImmunoResearch Labs	Cat# 703-095-155, RRID:AB_2340356
Goat anti-Chicken IgY (H+L) Secondary Antibody, Alexa Fluor 488	Thermo Fisher Scientific	Cat# A-11039, RRID:AB_2534096
Biotin-SP-AffiniPure Goat Anti-Rat IgG (H+L) antibody	Jackson ImmunoResearch Labs	Cat# 112-065-003, RRID:AB_2338168
Cy3-Streptavidin antibody	Jackson ImmunoResearch Labs	Cat# 016-160-084, RRID:AB_2337244
Bacterial and Virus Strains		
XL 10-Gold ultracompetent cells	Stratagene	Cat# 200521
Stbl3 competent cells	ThermoFisher	Cat#C73730
Chemicals, Peptides, and Recombinant Proteins		
Diamidino-2-phenylindole dihydrochloride (DAPI)	Sigma-Aldrich	Cat# D954
Spermine tetrachydrocloride	Sigma-Aldrich	Cat# 1141
(RS)-CPP	Tocris Bioscience	Cat# 0173
Gabazine	Abcam	Cat# ab120042
Tetrodotoxin citrate	Abcam	Cat# ab120055
CNQX disodium salt	Abcam	Cat# ab120044
Cesium methanesulfonate	Sigma-Aldrich	Cat# C1426
Tetraethylammonium (TEA) Chloride	Sigma-Aldrich	Cat# T2265
Experimental Models: Cell Lines		
HEK293T/17	ATCC	Cat# CRL-11268, RRID:CVCL_1926

(*Continued on next page*)

OPEN ACCESS CellPress

Continued

REAGENT or RESOURCE	SOURCE	IDENTIFIER
Experimental Models: Organisms/Strains		
STOCK Tg(Cspg4-DsRed.T1)1Akik/J	The Jackson Laboratory	RRID:IMSR_JAX:008241
C57BL/6	Charles River Laboratories	Strain Code: 027
Oligonucleotides		
Primers for mutagenesis:	Eurofins	N/A
Fwd: CTTGGGTGCCTTTATGGAGCAGGGATGCGATATTTC		
Rev: GAAATATCGCATCCCTGCTCCATAAAGGCACCCAAG		
Primers for cloning of EGFPGluA2(R583Q) and EGFPGluA2(R583E):	Eurofins	N/A
Fwd: TTACCGGTACGACTCACTATAGGCTAGAACTAG		
Rev: TGTTTAAACCCAAGGCCTGCATGCACTGCTTTG		
Primers for cloning of EGFPGluA2(813-862)	Eurofins	N/A
Fwd: TAGCGCT ACCGGT CGCCACCATGGTG		
Rev: TGGTTTAAACACCTCTACAAATGTGGTATGGCTG		
Primers for sequencing of pRetroCAG-EGFPGluA2(R683Q) and pRetroCAG-EGFPGluA2(R683E)	Eurofins	N/A
Fwd: CTGACATTGCAATTGCTCC		
Rev: ACGTTGCTCAGACTGAG		
Primers for sequencing of pRetroCAG-EGFPGluA2(813-862)	Eurofins	N/A
Fwd: TCACATGGTCCTGCTGG		
Fwd: ATCGACTTCAAGGAGGAC		
Recombinant DNA		
pCI-EGFPGluA2(R583Q)	Roberto Malinow, University of California, USA	N/A
pEGFPC1-GluA2(813-862)	Ingrid Ehrlich, University of Tuebingen and University of Stuttgart, Germany	N/A
pRetroCAG-EGFPGluA2(R683Q)	This paper	N/A
pRetroCAG-EGFPGluA2(R683E)	This paper	N/A
pRetroCAG-EGFPGluA2(813-862)	This paper	N/A
pRetroCAG-GFP	Tashiro et al., 2006	N/A
pCMV-gp	Tashiro et al., 2006	N/A
pCMV-vsv-g	Tashiro et al., 2006	N/A
Software and Algorithms		
ZEN Digital Imaging for Light Microscopy	Carl Zeiss	RRID:SCR_013672
ImageJ	National Institutes of Health	RRID:SCR_003070
IBM SPSS Statistics	IBM	RRID:SCR_002865
IGOR Pro	WaveMetrics, Inc	RRID:SCR_000325
Recording Artist (running under IgorPro)	Richard Gerkin, Arizona State University, USA	https://bitbucket.org/rgerkin/recording-artist
FBrain	Peter Jonas, Institute of Science and Technology, Austria	N/A
JCalc for Windows	Peter Barry, Sydney, Australia	N/A
BLASTn https://blast.ncbi.nlm.nih.gov/Blast.cgi?PROGRAM=blastn&PAGE_TYPE=BlastSearch&BLAST_SPEC=MicrobialGenomes&LINK_LOC=blasttab&LAST_PAGE=blastn	NIH/ NCBI	N/A
Other		
Quick Change II XL Site-Directed mutagenesis kit	Stratagene	N/A
Click-iT EdU Alexa Fluor 647 Imaging Kit	Thermo Fisher Scientific	Cat# C10340

OPEN ACCESS CellPress

CONTACT FOR REAGENT AND RESOURCE SHARING

Further information and requests for resources and reagents should be directed to and will be fulfilled by the Lead Contact, Maria Kukley (maria.kukley@uni-tuebingen.de).

EXPERIMENTAL MODEL AND SUBJECT DETAILS

Animals

NG2DsRedBAC transgenic mice (Ziskin et al., 2007) and C57BL/6 mice of both sexes were used in all experiments. Breeding pairs of NG2DsRedBAC transgenic mice were originally obtained from The Jackson Laboratory (stock 008241) and C57BL/6 mice were originally obtained from Charles River. Mice were bred in house and kept in 12–12 hours of light-dark cycle; food and water were available *ad libitum*. All experiments were performed in accordance with current European Union guidelines and approved by the local government authorities for Animal Care and Use (Regierungspraesidium Tuebingen, State of Baden-Wuerttemberg, Germany).

METHOD DETAILS

Molecular biology

pCI-EGFPGluA2(Q583) was a gift from Roberto Malinow (University of California, USA). The plasmids for viral production (pRetroCAG-GFP, pCMV-gp and pCMV-vsv-g) were gifts from Fred Gage (The Salk Institute, USA). The point mutation of GluA2(Q583) to GluA2(Q583E) was introduced using the Quick Change II XL Site-Directed mutagenesis kit (Stratagene). The primers for the point mutation were (5′ to 3′): fwd: CTTGGGTGCCTTTATGGAGCAGGGATGCGATATTTC and rev: GAAATATCGCAT CCCTGCTCCATAAAGG CACCCAAG. All the procedures followed the instruction manual provided by Stratagene. To construct pRetroCAG-GluA2(Q583)-GPF, pRetroCAG-GluA2(Q583E)-GFP and pRetroCAG-GluA2Ctail-GFP, we inserted GluA2(Q583)-GPF, GluA2(Q583E)-GFP and GluA2Ctail-GFP by PCR amplification. PCR primers included PmeI and AgeI restriction sites for insertion into pRetroCAG-GFP. For GluA2(Q583)-GPF and GluA2(Q583E)-GFP the primers were (5′ to 3′): forward TTACCGGTACGACTCACTATAGGCTAGAACTAG, reverse TGTTTAAACCCAAGGCCTGCATGCACTGCTTTG. For GluA2Ctail-GFP the primers were (5′ to 3′): forward TAGCGCTA CCGGTCGCCACCATGGTG, reverse TGGTTTAAACACCTCTACAAATGTGGTATGGCTG. The expression of all constructs was controlled by the chicken-beta actin (CAG) promoter. All plasmids were sequenced to ensure accuracy. For retroviral production, we used procedure described previously (Tashiro et al., 2006) with two modifications: we collected the supernatant 48 and 72 hours after transfection and filtered the supernatant through a 0.45 μm filter (Merck). The viral titers were 10^8-10^9/ml.

Experimental groups of animals

In the majority of experiments, the following 4 groups of animals were used: (1) Animals injected with retrovirus-GFP (called "GFP" throughout the manuscript); (2) Animals injected with retrovirus-GluA2(R583Q)-GPF (called "Ca^{2+}-permeable" throughout the manuscript); (3) Animals injected with retrovirus-GluA2(R583E)-GFP (called "pore-dead" throughout the manuscript); and (4) Animals injected with retrovirus-GluA2(813-862)-GFP (called "C-tail" throughout the manuscript). In some expetriments (see text), a fifth group of mice was used which contained naive animals, i.e., not injected with retrovirus (non-injected). The number of animals (*n*) used in each experiment is indicated in the corresponding figure legends.

Retrovirus injection

10-12 days-old NG2DsRedBAC transgenic mice were anesthetized with a mixture of isoflurane and oxygen (1%–3% v/v) and fixed in the stereotaxic frame (Stoelting, USA). The depth of the anesthesia was monitored by testing the reaction of the mouse to a toe pinch. For analgesia, metacam (1 mg/kg bodyweight, Boehringer Ingelheim) was injected subcutaneously before the surgery. The skin above the skull was disinfected, a small cut was made, and xylocaine (2%, Astra Zeneca) was applied locally. Bilateral injections of the virus into the corpus callosum were performed using the following coordinates (in mm from Bregma): anteroposterior 0.23, mediolateral ± 0.23-0.25, dorsoventral 1.77. For each injection we used a glass micropipette containing ~2.5 μL viral stock solution. The micropipette was connected to a fast pressure application system (PDES-01D-4, NPI Electronic, Germany), and the following parameters were used for injection: pressure 16-20 psi, application duration 60-90 ms. Subsequently, the wound was sutured with silk (Ethicon, USA). After the surgery, mice recovered rapidly from anesthesia and were returned to their home cages with parents.

For electrophysiological experiments we used $DsRed^+$ mice of the NG2DsRedBAC line; for immunohistochemistry and cell counting we used $DsRed^-$ littermates in order to have the red fluorescent channel available for antibody labeling.

In vivo EdU treatment

To study cell proliferation, mice were administrated with 5-ethynyl-2′-deoxyuridine (EdU, Thermo Fisher) (Young et al., 2013) intraperitoneally at a dose of 25 mg/ kg body weight. EdU was applied three times, i.e., on the third, fourth, and fifth day after the viral injection at an interval of 24 hours.

Slice preparation for electrophysiology

For patch-clamp recordings, we used in total 59 mice of the age P12-17. Three to five days after the viral injection mice were anesthetized with a mixture of isoflurane and oxygen (3% v/v) and decapitated. The brain was dissected in the ice-cold N-methyl-D-glucamine (NMDG)-based solution containing (in mM): 135 NMDG, 1 KCl, 1.2 KH_2PO_4, 20 choline bicarbonate, 10 glucose, 1.5 $MgCl_2$, and 0.5 $CaCl_2$ (pH 7.4, 310 mOsm), gassed with carbogen (95% O_2, 5% CO_2). 270-300 μm thick coronal brain slices were cut in the same solution using a Leica VT 1200S vibratome. The slices were transferred to a 32° C Haas-type interface incubation chamber and perfused with Ringer-solution containing (in mM): 124 NaCl, 3 KCl, 1.25 NaH_2PO_4*H_2O, 2 $MgCl_2$, 2 $CaCl_2$, 26 $NaHCO_3$, 10 glucose; 300 mOsm/kg; 7.4 pH; gassed with carbogen. The chamber was gradually cooled down to room temperature.

Patch-clamp recordings

At least one hour after the preparation, individual slices were transferred to a submerged recording chamber mounted on the stage of an up-right microscope (FN-1, Nikon, Japan) equipped with infrared differential interference contrast (IR-DIC) filters and a fluorescence light source. The slices were kept at room temperature and superfused continuously (~2 ml/min) with carbogenated Ringer solution. OPCs were selected for recordings based on fluorescence: red fluorescence (NG2DsRed$^+$ cells) for mice not injected with retrovirus, or green and red double-fluorescence (GFP$^+$NG2DsRed$^+$ cells) for mice injected with retrovirus. Patch pipettes were pulled from borosilicate glass capillaries (Science Products, Germany) on a vertical puller (Model PC10, Narishige, Japan). Pipettes had resistance of 4.8-7 MOhms when filled with K-gluconate-based internal solution containing (in mM): 125 K-gluconate, 2 Na_2ATP, 2 $MgCl_2$, 0.5 EGTA, 10 HEPES, 20 KCl, 3 NaCl; 280-290 mOsm/kg; titrated to pH 7.3 with KOH. Cells were voltage-clamped at a holding potential V_h = −80 mV with an EPC-8 amplifier (HEKA, Germany). The liquid junction potential was calculated using the software JPCalc for Windows (Peter H. Barry, Sydney, Australia) and V_h was corrected for a −13 mV liquid junction potential before seal formation. Series resistance was not compensated. After establishing the whole-cell configuration, ten depolarizing voltage steps (increment +10 mV) were applied to each cell from V_h = −80 mV, and corresponding current responses were recorded in order to verify that the selected cell was an OPC (Kukley et al., 2010). Evoked synaptic currents were elicited with an isolated pulse stimulator (A-M Systems, Model 2100, Science Products, Germany) using mono-polar glass electrode (resistance 5-6 MΩ) filled with Ringer solution and placed at 50-150 μm from the recorded cell (V_h = −80 mV). Paired (40 ms inter-pulse interval) monophasic rectangular pulses of 100-250 μsec duration were applied every 15 s. Trains of stimuli (20 pulses @ 100 Hz or 20 pulses @ 25 Hz) were applied each 15 s.

For I-V curve recordings, we used a Cs-based internal solution containing (in mM): 100 $CsCH_3SO_3H$ (CsMeS), 20 tetraethylammonium (TEA) chloride, 20 HEPES, 10 EGTA, 2 Na_2ATP, and 0.2 NaGTP; 280-290 mOsm/kg; titrated to pH 7.3 with CsOH, and a Ringer solution containing (in mM): 119 NaCl, 2.5 KCl, 1 NaH_2PO_4*H_2O, 1.3 $MgCl_2$, 2.5 $CaCl_2$, 26.2 $NaHCO_3$, 11 glucose; 300 mOsm/kg; 7.4 pH; gassed with carbogen. Spermine (Sigma, 100 μM) was included into the internal solution in all recordings of evoked EPSCs in order to test for the presence of Ca^{2+}-permeable AMPA receptors in OPCs. V_h was corrected for a −7 mV liquid junction potential before seal formation. The cells were held at different potentials (−90, −40, 0, +20, and +40 mV) and 10-15 sweeps were recorded at each potential.

When recording the synaptic currents, we applied a voltage step of −5 mV at the beginning of each sweep to monitor series resistance. Whole-cells currents in response to voltage steps were low-pass filtered at 10 kHz and digitized with a sampling frequency of 20 kHz (ITC-18, HEKA Instruments Inc, USA). All recordings of synaptic currents were low-pass filtered at 1 kHz and digitized with a sampling frequency of 10 kHz. Data acquisition was performed using Recording Artist (Rick Gerkin, Arizona State University, USA) running under Igor Pro 6.3 (WaveMetrics, Lake Oswego, USA). All recordings of evoked synaptic currents were performed in the presence of NMDA-receptor antagonist CPP (10 μM, Tocris) and $GABA_A$ receptor antagonist gabazine (5 μM, Sigma). In some experiments, TTX (0.5 μM, Abcam) or CNQX (10 μM, Abcam) was applied at the end of the recording. All drugs were dissolved in Ringer solution and applied via the bath. All patch-clamp recordings were performed at room temperature.

Immunohistochemistry

For MBP staining, C57BL/6 mice were sacrificed at P9, P10, P11, P12, P15, and P18. For all other stainings, mice were sacrificed 5 days after the retroviral injection. The brain was removed, and 350-400 μm thick coronal slices were cut using the Leica VT 1200S vibratome in the solution of the following composition (in mM): 87 NaCl, 2.5 KCl, 1.25 NaH_2PO_4*H_2O, 7 $MgCl_2$, 0.5 $CaCl_2$, 25 $NaHCO_3$, 25 glucose, 75 sucrose or NMDG-based solution. The slices were fixed overnight at 4°C in 4% paraformaldehyde, dissolved in 10 mM phosphate-saline buffer (PBS). Subsequently, thick slices were washed, embedded into Agar and re-sectioned in PBS to 30 μm thickness using a microtome (HM 650V, Thermo Scientific). All 30 μm thick slices were inspected visually for quality and for presence of GFP-expressing cells using an epi-fluorescence microscope (Axio Imager Z1m, Zeiss, Germany). Slices which did not contain green cells or appeared damaged were discarded. From the remaining pool, 4-12 slices per mouse were selected and used for immunohistochemistry and cell counting. The stainings were performed on 30 μm free floating slices in multi-well plates, or (in few cases) mounted on glass-slides. For antigen retrieval, the slices were incubated in 10 mM citric acid (pH = 6.0) at 37° C. After washing, we applied blocking solution containing: 0.1 M Tris-buffer saline (TBS), 3%–5% Albumin Fraction V (Roth), and 0.2%–0.5% Triton-X (Roth), at 37°C for 1 hour. Slices were incubated with primary antibody overnight in blocking solution. The following primary antibodies were used: rabbit or guinea pig anti-NG2 (1:500, gift from Bill Stallcup, Burnham Institute, La Jolla, USA), mouse anti-APC (1:250, Ab-7, CC-Calbiochem), rabbit anti-Cleaved-Caspase-3 (1:500, Cell Signaling Technology), chicken anti-GFP (1:500, Abcam),

OPEN ACCESS CellPress

rat anti-MBP (1:125, Abcam), mouse anti-ki67 (1:500, BD PharMingen), mouse anti-MAG (1:1000 Santa Cruz Biotechnology). Detection was performed using the following secondary antibodies: goat anti-rabbit Alexa Fluor 568 (1:500, Invitrogen), goat anti-rabbit Cy5 (1:500, Dianova), goat anti-rabbit Alexa Fluor 405 (1:150, Invitrogen), goat anti-guinea pig Alexa Fluor 633 (1:500, Invitrogen), goat anti-mouse Alexa Fluor 555 (1:500, Invitrogen), donkey anti-chicken FITC (1:1000, Dianova), goat anti-chicken Alexa Fluor 488 (1:500, Invitrogen) or goat anti-rat biotin-SP (1:200, Dianova) followed by streptavidin-Cy3 (1:200, Dianova). Secondary antibodies were applied for 3 hours at 37°C. For EdU visualization, the protocol recommended by Thermo Fisher Scientific was used. Diamidino-2-phenylindole dihydrochloride (DAPI, 0.2 μg, Sigma) was used for counterstaining of the cell nuclei.

Image acquisition

A confocal LSM 710 system (Zeiss, Germany) was used for image acquisition. Images containing corpus callosum were acquired and saved as z stacks with 16 bit pixel depth. Each z stack was 6-18 μm thick and consisted of 6-18 z-slices at a step size of 1 μm. Each layer of a z stack was acquired as a tile-scan (vertical x horizontal: 3 × 7 or 2 × 7 images), where each tile was 512 × 512 pixels in size. Pixel size was usually 0.415 × 0.415 μm, with exception of images shown in Figures S3B and S3C, where pixel size was 0.033 × 0.033 μm. Each tile-scan represented a quadruple-channel fluorescence image, where channels were acquired sequentially in ZEN software using 40x oil-immersion objective (NA = 1.3). For images shown in Figures S3B and S3C we used 63x objective (NA = 1.4). The following excitation laser lines and emission detection ranges were used: for DAPI excitation 405 nm, emission 414-490 nm; for FITC excitation 488 nm, emission 497-556 nm; for Alexa-555, Alexa-568 or Cy3 excitation 561 nm, emission 569-633 nm; for Alexa-633 or Alexa-647 excitation 633 nm, emission 650-740 nm. The beam splitters for each dye matched the excitation laser lines. The pinhole was set to 1.07-1.42 airy units and adjusted such that the optical section for each channel was 1.2 μm. The exception are the images shown in Figure 1C, where we used 10x objective and optical section was 12.3 μm. Laser power, detector gain, and offset were adjusted such that in the final scan (average of 2 frames) a good signal to background noise ratio was achieved. For visualization, images presented in the figures were adjusted for brightness/contrast in ImageJ (NIH, USA), as follows: Figure 1F, brightness of GFP staining; Figure 1I, brightness and contrast for NG2 and CC1 staining; Figure 1J, brightness and contrast for CC1; Figure 3B, brightness and contrast for NG2 and CC1 staining for pre-OL; Figure 3H, brightness for NG2 staining; Figure 3J, brightness and contrast for GFP staining; Figure 4B, brightness of EdU staining for GFP group; Figure 4F, brightness for GFP staining in GFP group; Figure S2E, brightness for GFP; Figure S2F, brightness for GFP; Figures S3B and S3C, brightness and contrast for GFP (green; without antibody labeling) and GFP staining (red; non-permeabilized conditions); Figure S3G, brightness and contrast for Caspase3.

QUANTIFICATION AND STATISTICAL ANALYSIS

Analysis of electrophysiology data

Only recordings where the offset drift by the end of the experiment was smaller than ± 5 mV, and the change of the series resistance was < 30% relative to the original value were considered for the analysis. The series resistance was between 20 and 40 MΩ.

Analysis of evoked EPSCs, I-V curve, and paired-pulse ratio

Analysis of evoked EPSCs was performed using custom-written macros in IgorPro. Stimulus artifacts were removed using the following procedure: sweeps containing failures (absence of postsynaptic response) after the first stimulus, or sweeps recorded in the presence of TTX or CNQX, were averaged and the segment of the averaged sweep from time-point of stimulation to last point before the second stimulus was cut out, duplicated and concatenated with itself. The resulting sweep was subtracted from each recorded sweep.

To measure the EPSC amplitude (after first or second pulse), we used the following procedure: For each recorded sweep the baseline was adjusted to the 100-ms segment immediately preceding the stimulation; the peak-center of each event was determined as the time-point at which the first derivative of the sweep crossed zero; the amplitude values of the current in the peak-center and in 4 points around it (2 points to the right and 2 points to the left) were averaged, and the resulting value was taken as current amplitude. The threshold for event detection was determined individually for each recorded sweep and was equal to three times the standard deviation of the noise. In case several EPSCs occurred after a given stimulus, care was taken to measure the amplitude of the first event.

Although we used paired-pulse stimulation in all experiments, in order to generate the I-V curve we considered only the EPSCs occurring after the first pulse. The amplitudes of all recorded sweeps (10 to 15) at a given holding potential (−90, −40, 0, +20, +40 mV, and back to −90 mV) were measured as described above, and averaged. The resulting averages were used to generate the I-V curve in each cell. To calculate the rectification index, the average value of the EPSC amplitude at +40 mV was divided by the average value of the EPSC amplitude at −90 mV.

To determine the paired-pulse ratio, the average amplitude value of the EPSC occurring after the second pulse was divided by the average amplitude value of the EPSC occurring after the first pulse at a holding potential of −90 mV.

Analysis of delayed EPSCs

To study the quantal amplitude of synaptic currents in OPCs, we analyzed the delayed EPSCs occurring in OPCs after the train stimulation of callosal axons with 20 pulses at 25 or 100 Hz. The delayed EPSCs were defined as those with an onset of > 10 ms after the last stimulus of the train. In each recorded cell we collected the delayed EPSCs in 20-160 sweeps of 1.73-2.3 s length each. The EPSCs were detected using a deconvolution-based algorithm (Pernía-Andrade et al., 2012) in FBrain, a customized program running

under IgorPro 6 (WaveMetrics, Lake Oswego, USA). FBrain was kindly provided by Peter Jonas Lab (IST, Klosterneuburg, Austria). Additional digital high-pass (10 Hz) and Notch (50 ± 0.5 Hz) filtering was applied to the recorded sweeps in FBrain before the analysis. The deconvolution trace was passed through a digital band-pass filter at 0.001 to 200 Hz. The event detection template had a rise-time of 0.5 ms, a decay time constant of 4 ms, and amplitude of −3 pA. The event detection threshold (θ) was set to 4.2 times the standard deviation of a Gaussian function fitted to the all-point histogram of the deconvolved trace (Pernía-Andrade et al., 2012). All events detected by the algorithm were inspected visually, and those events which clearly did not show kinetics of typical excitatory postsynaptic currents (i.e., fast rise and exponential decay) were manually removed. The subsequent analysis was performed using custom-written macros in IgorPro.

Cumulative probability histogram of the amplitude of delayed EPSCs

The following procedure was used: (1) The amplitude of all delayed EPSCs was measured in each cell as described above; (2) 67 delayed EPSCs were randomly selected from each cell using the StatsSample procedure in IgorPro; (3) the amplitude distribution of randomly selected events was compared to the amplitude distribution of all events within a given cell using the Kolmogorov-Smirnov test in IgorPro to ensure that the two distributions were similar, and the pool of randomly selected events was representative of the whole population of events. In case the two distributions were different, the random selection was automatically repeated until no difference was found between the distributions; (4) in each cell, steps (2)-(3) were repeated 100 times; (5) for each of the 100 trials, the randomly selected events from all cells within a given experimental group were pooled to generate an EPSCs amplitude distribution per experimental group; (6) for each of the 100 trials this new amplitude distribution of the events in a group of animals expressing one of the GluA2-subunit modifying constructs was compared to the GFP group using the Kolmogorov-Smirnov test in IgorPro. In selected trials, the comparison was repeated using SPSS.

For data presentation in Figure 2H and Figure S1E, we chose one representative example from the 100 random selection trials for each experimental group. The bin size for cumulative probability histograms was 0.5 pA, and each histogram was normalized to probability density using built-in function in IgorPro.

Non-stationary fluctuation analysis (NSFA)

To estimate the single channel conductance of synaptic AMPARs in OPCs we performed peak-scaled non-stationary fluctuation analysis (Hartveit and Veruki, 2007). In each cell, the delayed EPSCs were examined visually and only the events with smooth rise- or decay phase were selected for NSFA. Spearman's rank-order correlation test was applied to verify that there was no drift in the peak amplitude, rise-time, or decay-time of the events during the time-course of each experiment. In addition, we also verified that there was no correlation between rise-time and decay-time constant (Hartveit and Veruki, 2007). If any of the indicated correlations was found, the cell was excluded from the NSFA. On average, 13 events (range 7-17) were selected randomly from each cell (n = 6 cells for GFP, n = 5 for "Ca^{2+}-permeable," n = 7 cells for "pore-dead," and n = 8 for "C-tail"), and were pooled within each experimental group. This resulted in, on average, 82 events (range 57-94) included into the NSFA within each experimental group. The events were aligned on the point of steepest rise, which corresponds to the location of the minimum value of the first time derivative of the event waveform. The mean waveform was calculated from these events and the amplitude of the mean waveform was scaled to the amplitude of each individual event. Subsequently, the scaled mean waveform was subtracted from each individual event, resulting in the noise component for each event, from which the variance was calculated. The background variance was estimated from the segment of the trace before the onset of each event, and was subtracted. The ensemble background-subtracted variance was calculated as an average of variances of all events. The mean amplitude wave was binned into 18 bins, and the corresponding values of the variance wave were then obtained in accordance with this binning (Hartveit and Veruki, 2007). Different number of bins was also tested, but varying the number of bins did not affect the results. Finally, the values of variance were plotted versus the corresponding values of the mean current amplitude. The resulting variance-mean relationship was fitted with the following parabola function in IgorPro:

$$\delta^2(I) = i * I - I^2/N + \delta_{bgr}^2$$

where $\delta^2(I)$ is the variance; i is the (weighted) estimate of a mean single channel current; N is average number of channels opened at the peak, and δ_{bgr}^2 is the background variance. The single-channel conductance (γ) of synaptic AMPAR was calculated from the single-channel current i as:

$$\gamma = i/E$$

where E is the driving force for AMPAR-mediated EPSC, which is −80 mV in our study.

Notably, because we used the peak-scaling method for NSFA, the information on the total number of available channels is lost (Hartveit and Veruki, 2007), the parameter N has no meaning, and is not further analyzed/presented in our study.

The random selection, the pooling process, and all subsequent procedures described above were repeated 100 times for each of our 4 experimental groups, and by 4 researchers, resulting in total of 400 random selections and pooling per experimental group.

All routines for NSFA were custom programmed and were based on the code presented in the supplementary material of Hartveit and Veruki (Hartveit and Veruki, 2007).

OPEN ACCESS
CellPress

Estimation of the fraction of rectifying AMPARs (FRR) based on rectification measurements

To obtain the FFR, we used the equation developed by Stubblefield and Benke (Stubblefield and Benke, 2010), which allows for estimation of the FRR based on rectification measurements. Their rectification indices were calculated as a ratio of EPSC amplitudes recorded at −70 mV and at +40 mV. To match their approach, we took the inverse of our *RI* values (*1/RI*) from Figure 2E and adjusted their equation to model our results as follows:

$$FFR = (1 - 1/RI * F3)/1/RI * (F1 - F3),$$

where *F1* is the maximal block of inwardly rectifying receptors (EPSC at +40 mV/ EPSC at −90mV), extrapolated to be 0.035 (based on (Rozov et al., 1998; Stubblefield and Benke, 2010)). *F3* is the value for linear relationship (F3 = 40/90 = 0.444). This analysis assumes that there is no change in presynaptic function (c.f. Figures S1F and S1G and Figures S3D–S3E).

Cell counting

We counted GFP-labeled infected cells in z stack images using ImageJ Cell Counter plugin (NIH, USA). No contrast or brightness adjustment was made in any of the images, but background subtraction was applied to the green channel before counting. The background fluorescence was measured using the linear 'plot profile' function in ImageJ and the resulting value was subtracted from each pixel of the original image. The ventral and dorsal borders of corpus callosum were identified based on the CC1 or NG2 and DAPI staining. For counting, in each coronal slice we outlined the area of the corpus callosum approximately 500-850 μm laterally on each side from the midline. Thus, the ROI spanned 1-1.4 mm along the mediolateral axis of the corpus callosum and avoided cells in the vicinity of lateral ventricles. Only cells within the ROI and cells whose nucleus was ≥ 50% within its borders were included in the analysis. Cells were counted in 4-12 slices from each mouse and the counts within one animal were summed, resulting in 29 to 486 GFP^+ cells per animal. OPCs were identified as $GFP^+NG2^+CC1^-$ cells, pre-myelinating oligodendrocytes as $GFP^+NG2^+CC1^+$ cells, and myelinating oligodendrocytes as $GFP^+NG2^-CC^+$ cells. To avoid bias, in randomly selected experiments the counting was repeated by one or two additional investigators blind to the experimental group of animals. The differences in counts were minor and did not affect the final results.

Statistics

All data acquisition was randomized (animals for viral injections, cells during patch-clamp experiments). Throughout the study we made all efforts to avoid pseudoreplications, both when performing experiments in slices and *in vivo*. The exact number of cells and animals used in each experiment is given in the figure legends.

Statistical analysis was performed using SPSS, including tests for homoscedasticity and normal distribution. If the datasets had normal distributions and equal variances, one-way ANOVA with post hoc Dunnett's or Bonferroni (Figures 3E–3G) test was used. If the datasets had normal distributions but unequal variances, one-way ANOVA with post hoc Games-Howell test was used. If the datasets were not normally distributed, Kruskal-Wallis with post hoc Dunn's test was used. In all Figures, except the Figures 3E–3G, we were interested only in the comparison between the experimental groups with AMPAR-manipulation and the GFP control group. Therefore, the *p* values in the Figure Legends are shown only for these comparisons. To compare values of rectification index and paired-pulse ratio between cells in non-injected and GFP expressing animals, we tested the datasets for normal distribution and used the 2-tailed Student's t test. To compare cumulative probability histograms of the amplitude of the delayed EPSCs between control (GFP) and each experimental group ("Ca^{2+}-permeable," "pore-dead," or "C-tail"), 100 trials of random selections of events were performed and compared in IgorPro with Kolmogorov-Smirnov test as described above. Comparison of the GFP and "Ca^{2+}-permeable" groups showed that the two distributions were different in all 100 trials therefore, we considered the difference between these two distributions statistically significant. Comparison of the GFP and "pore-dead" groups showed that the two distributions were different in 98 out of 100 trials therefore, we considered the difference between these two distributions statistically significant. Comparison of the GFP and "C-tail" groups showed that the two distributions were different in only 46 out of 100 trials; therefore, we considered the difference between these two distributions not statistically significant. To report the corresponding p values in the figure, we used the Kolmogorov-Smirnov test in SPSS. For all statistical comparisons, significance level was set at $p < 0.05$. Statistically significant differences are indicated by *p* values in the figure legends. * represents $p \leq 0.05$, ** represents $p \leq 0.01$, and *** represents $p \leq 0.001$. For graphs, each point represents an individual data point (cell or animal) and the diamond represents the mean ± SEM. Data in the text report mean ± SEM.

DATA AND SOFTWARE AVAILABILITY

The datasets generated and analyzed in the current study and custom-written macros for electrophysiological analysis are available from the lead author upon request.

Cell Reports, Volume *25*

Supplemental Information

In Vivo Regulation of Oligodendrocyte Precursor Cell Proliferation and Differentiation by the AMPA-Receptor Subunit GluA2

Ting-Jiun Chen, Bartosz Kula, Bálint Nagy, Ruxandra Barzan, Andrea Gall, Ingrid Ehrlich, and Maria Kukley

Supplemental Figures

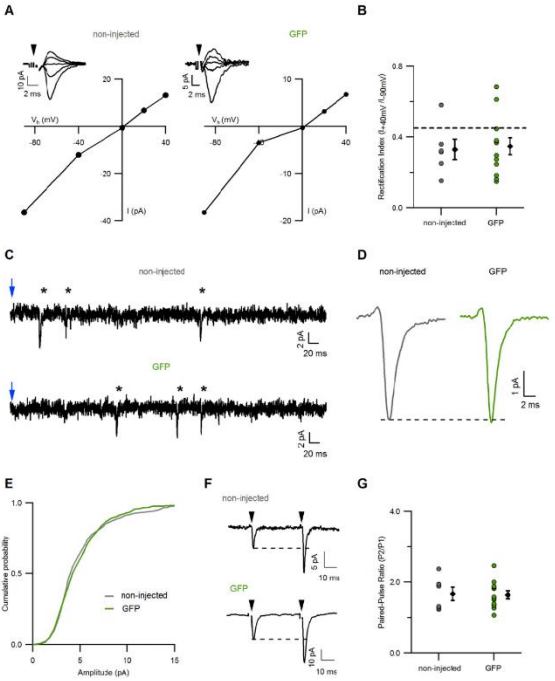

Figure S1. Retroviral infection does not affect AMPAR properties or presynaptic release probability at axon-OPC synapses. Related to Figure 2.

A, Current-voltage (*I-V*) relationship of evoked axon-glia EPSCs recorded in an OPC from a non-injected (*left*) or a GFP-injected (*right*) mouse. Each graph represents one example cell. Each black dot represents the average amplitude of 10 sweeps recorded at a given holding potential (V_h). Corresponding examples of the averaged sweeps are shown above each graph. The arrowheads indicate the time of stimulation. The stimulation artifacts are blanked for clarity. The *I-V* curve for the GFP-expressing cell is the same as shown in Figure 2D.

B, Rectification index for evoked EPSCs recorded in OPCs from non-injected (n=6 cells / 5 mice) or GFP-injected (n=12 cells / 9 mice) animals. Each dot represents one cell. The black diamonds represent mean ± SEM for each group. The dashed line indicates the theoretical rectification index for the linear *I-V* relationship (*RI*=0.44). Two-tailed t-test; t(16)=-0.222, p=0.827. The dataset for the GFP group is the same as shown in Figure 2E.

C, Representative example traces of delayed EPSCs recorded in OPCs from a non-injected (*top*) or GFP-injected (*bottom*) animal after cessation of train stimulation of callosal axons. Stars indicate delayed events. V_{hold}=-80 mV. The blue arrows indicate the end of train stimulation.

D, Averaged delayed EPSCs in OPCs from non-injected (*left*, n=6 cells / 4 mice) or GFP-injected (*right,* n=7 cells / 6 mice) animals. In each cell, 67 events were randomly selected and averaged. Subsequently, the averages from all cells within each experimental group were put together to generate the average EPSC for each group.

E, Cumulative probability distribution histograms of the amplitude of delayed EPSCs. 67 events were randomly selected from each OPC, and the events from all OPCs within each experimental group were pooled; non-infected: 402 events (n= 6 cells / 4 mice); GFP: 469 events (n=7 cells / 6 mice). Kolmogorov-Smirnov test: non-injected mouse vs. GFP group: p=0.47. The dataset for the GFP is the same as in the Figure 2H.

F, Representative example traces showing evoked EPSCs recorded in OPC from a non-injected (*top*) or GFP-injected (*bottom*) mouse. V_h = -90 mV. Each trace represents the average of 30-35 sweeps. The black arrowheads indicate the time-points of stimulation. The stimulation artifacts are blanked for clarity. The dashed lines indicate the peak amplitude of EPSC elicited by the first stimulus.

G, Paired pulse ratio of the evoked EPSCs recorded in the OPCs. Each dot represents one cell. The black diamonds represent mean ± SEM for each group. Non-infected: n=6 cells from 5 mice; GFP: n=12 cells from 9 mice. Two-tailed t-test; t(16)=0.126, p=0.901.

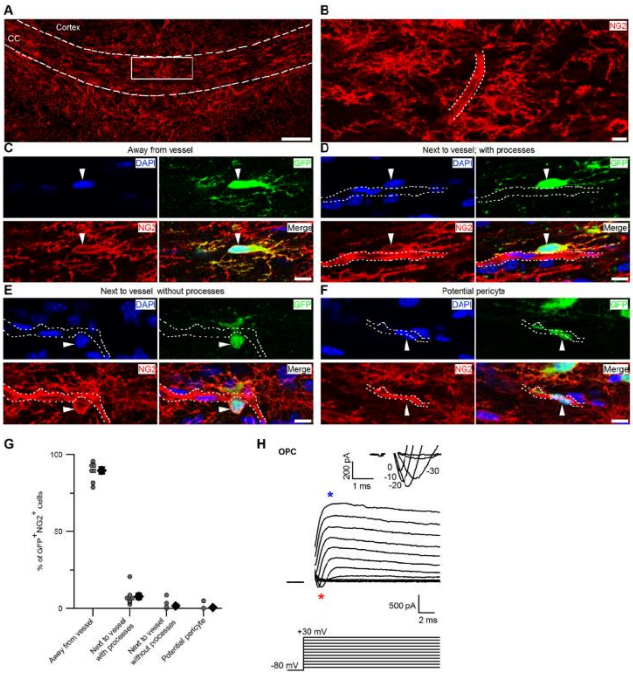

Figure S2. The vast majority of GFP$^+$NG2$^+$ cells are not pericytes. Related to Figure 1 and 2.

A, Maximum intensity projection (4 successive confocal planes) showing NG2 labelling (red) in the corpus callosum. White dashed line indicates the borders of the corpus callosum. White rectangle indicates the region shown at a higher magnification in (**B**). CC; corpus callosum. Scale bar: 100 µm.

B, Higher magnification of the region marked with white rectangle in (**A**). White dashed line indicates an NG2$^+$ blood vessel. Scale bar: 10 µm.

C, Maximum intensity projection (3 successive confocal planes) showing triple labeling for DAPI (blue), GFP (green), NG2 (red), and the merged image. The white arrowhead points to GFP^+NG2^+ cell with multiple processes that is located away from blood vessels. Scale bar: 10 µm.

D, As in (**C**) but the white arrowhead points to GFP^+NG2^+ cell with multiple processes that is located next to a $NG2^+$ blood vessel (outlined with the white dashed line). Stitches visible in all panels at higher magnification appeared because images have been acquired as multiple tile scans, and the edges of two neighboring tiles have not been stitched properly by the software. Scale bar: 10 µm.

E, As in (**C-D**) but the white arrowhead points to GFP^+NG2^+ cell without processes that is located next to an $NG2^+$ blood vessel (outlined with the white dashed line). Scale bar: 10 µm.

F, As in (**C-E**) but the white arrowhead points to potential GFP^+NG2^+ pericyte. Scale bar: 10 µm.

G, Proportion of GFP^+NG2^+ cells with different morphology and location, corresponding to the examples shown in (**C-F**). Analysis was performed in 8 animals from the GFP group. Each dot represents one animal. The black diamonds represent mean ± SEM.

H, Typical current response of a $GFP^+NG2DsRed^+$ OPC to a series of depolarizing voltage steps applied from a holding potential V_h=-80 mV, with an increment of +10 mV. Blue star indicates transient outward K^+ current. Red star indicates Na^+ current shown at an expanded time-scale and after leak subtraction, in the inset above. All $GFP^+NG2DsRed^+$ cells recorded in our study with K^+-gluconate-based internal solution (n=30 cells in 24 animals) showed current responses with transient K^+ and fast Na^+ currents. Fast capacitive transients are truncated for clarity. *Bottom*, Applied voltage-step protocol. V_h is -80 mV; maximal command potential is +30 mV.

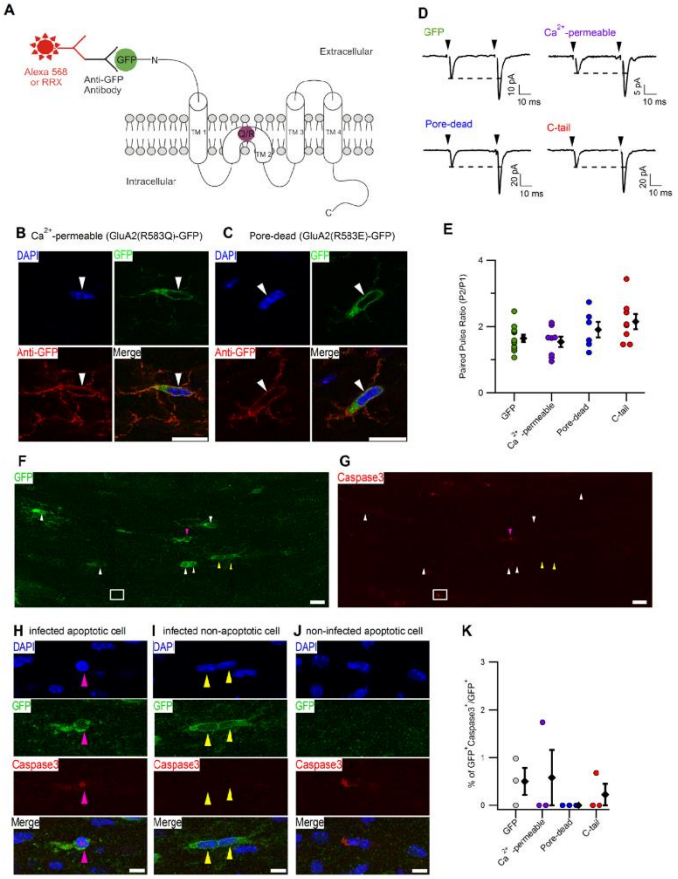
A
Alexa 568 or RRX
GFP
N
Anti-GFP Antibody
Extracellular
Intracellular
TM 1
TM 2
TM 3
TM 4
C
D
GFP
Ca2+-permeable
Pore-dead
C-tail
10 pA
5 pA
20 pA
10 ms
B Ca2+-permeable (GluA2(R583Q)-GFP)
C Pore-dead (GluA2(R583E)-GFP)
DAPI
GFP
Anti-GFP
Merge
E
Paired Pulse Ratio (P2/P1)
F
G
Caspase3
H infected apoptotic cell
I infected non-apoptotic cell
J non-infected apoptotic cell
K
% of GFP+Caspase3+/GFP+

Figure S3. Recombinant GluA2(R583Q)-GFP and GluA2(R583E)-GFP subunits are delivered to the cell membrane of OPCs. Manipulations of postsynaptic GluA2-containing AMPARs in OPCs do not alter the probability of glutamate release at axon-OPC synapses in the corpus callosum. Expression of GFP or AMPAR-modifying constructs in OPCs does not cause apoptotic cell death within the corpus callosum. Related to Figure 2 and 3.

A, Schematic drawing showing the topology of the GluA2 subunit of AMPARs. The magenta dot indicates the Q/R editing site. GFP is fused to the extracellular N-terminal domain. Q: glutamine, R: arginine, TM: transmembrane domain, N: N-terminus, C: C-terminus.

B, Single confocal plane image showing an OPC expressing the GluA2(R583Q)-GFP construct (GFP, green; without antibody labeling), DAPI (blue), and anti-GFP staining (red) in non-permeabilized conditions. White arrowhead points to the cell soma. Anti-GFP staining labels the surface of cell soma and outlines the processes, indicating that GluA2(R583Q)-GFP subunits incorporated into the cell membrane. Scale bar: 5 µm.

C, As in (**B**) but for an OPC expressing the GluA2(R583E)-GFP construct.

D, Representative example traces showing evoked EPSCs recorded in OPCs expressing the GFP or one of the GluA2 subunit modifying constructs. V_h = -90 mV. Each trace represents an average of 10-52 sweeps. Black arrowheads indicate the time-points of stimulation. The stimulation artifacts are blanked for clarity. The dashed lines indicate the peak amplitude of EPSC elicited by the first stimulus.

E, Paired pulse ratio of the evoked EPSCs recorded in OPCs. Each dot represents one cell. The black diamonds represent mean ± SEM from each group. GFP: n=12 cells from 9 mice; "Ca^{2+}-permeable": n=8 cells from 7 mice; "pore-dead": n=6 cells from 6 mice; and "C-tail": n=8 cells from 6 mice. The dataset from GFP is the same as shown in Figure S1F-G. One-way ANOVA, F(3,30)=2.484, p=0.08.

F, Maximum intensity projection (5 successive confocal planes) showing cells expressing "Ca^{2+}-permeable" construct in the corpus callosum. Arrowheads point to infected cells. Magenta arrowhead points to an infected apoptotic cell ($GFP^+Caspase3^+$), magnified in (**H**). Yellow and white arrowheads point to infected non-apoptotic cells ($GFP^+Caspase3^-$); cells marked with yellow arrowheads are magnified in (**I**). White rectangle indicates a non-infected apoptotic cell ($GFP^-Caspase3^+$), magnified in (**J**). Dashed line indicates the borders of corpus callosum. Scale bar: 20 µm.

G, As in (**F**), but for Caspase3 shown in the red channel.

H, Higher magnification of the $GFP^+Caspase3^+$ cell marked with the magenta arrowhead in (**F-G**). The panels show triple labelling for DAPI (blue), GFP (green), caspase3 (red), and merged image. Scale bar: 10 µm.

I, As in (**H**), but for $GFP^+Caspase3^-$ cells marked with the yellow arrowheads in (**F-G**).

J, As in (**H**), but for $GFP^-Caspase3^+$ cell marked the white rectangle in (**F-G**).

K, Proportion of $GFP^+Caspase3^+$ cells amongst the GFP^+ cells expressing GFP (n=3 mice), "Ca^{2+}-permeable" (n=3 mice), "pore-dead" (n=3 mice), or "C-tail" (n=3 mice) constructs. Each dot represents one animal. The black diamonds represent mean ± SEM for each group. Kruskal-Wallis test; H(3)=2.305, p=0.512.

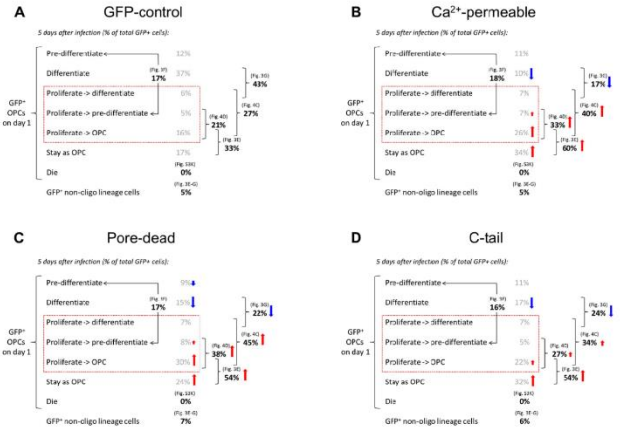

Figure S4. Sub-populations of oligodendroglia lineage cells composing the population of GFP$^+$ cells in animals expressing GFP or AMPAR-modifying constructs. Related to Figure 4.

(A)-(D) Results from Figure 3E-G and Figure 4C-E are combined to calculate the contribution of different sub-populations of oligodendroglia lineage cells to the total population of GFP$^+$ cells (c.f. Figure 4H). Values shown in bold black represent the original measurements; values shown in grey represent results of the calculation. Red rectangles encompass EdU$^+$ cells. Red arrows indicate an increase while blue arrows indicate a decrease in the size of a given cell population compared to the GFP group.

For these calculations, we made several assumptions: (1) For proliferating OPCs, we made an assumption that they differentiate with similar time-course as shown in Figure 1G and Figure 3E-G: after five days 33% are OPCs, 17% are pre-myelinating oligodendrocytes, and 43% are oligodendrocytes. Assuming that one day is required for expression of the constructs, this situation is reached four days after the start of expression. (2) As we counted EdU$^+$ cells two days after the first EdU injection, we made an assumption that at that time-point the cells will be present in the following proportion: 66% (=33% x 2) are OPCs, 17% are pre-myelinating oligodendrocytes (we assumed that their proportion is constant and corresponds to values presented in Figure 3F at all times, because they represent a transient stage), and 22% (~43%/2) are oligodendrocytes.

Publication 3. Fate of neuron-glia synapses during proliferation and differentiation of NG2 cells.

Fröhlich N., Nagy B., Hovhannisyan A., Kukley M. (2011) J Anat. 2011 Jul;219(1):18-32.

Framework: This is a review paper which gives a broad overview on the general morphological and physiological features of the oligodendrocyte precursor cells (OPCs). We highlighted new (in 2010-11) findings on the properties of OPCs in the developing and the adult nervous systems of rodents. We discussed more specifically how unique electrophysiological and synaptic attributes of OPCs change during proliferation and differentiation. In the conclusion sections we drew attention to some of the most interesting questions arising from the reviewed literature, and set a new direction for our research for the following years. I would like to emphasize that with Nagy et al. (2017) and Chen et al. (2018) we successfully answered some of the questions raised in this review.
Contributions: The authors selected on the reviewed themes and research papers together. The outline of this review was decided through discussions. Each author wrote parts of the original manuscript. I wrote parts of the "Introduction", and the sections "Appearance, distribution and progeny of NG2 cells" and "NG2 cells express voltage-gated potassium and sodium channels". The layout and design of the figures were decided together, and NF and MK prepared the illustrations. NF and MK created the final manuscript after the review process.

Journal of Anatomy

J. Anat. (2011) **219**, pp18–32 doi: 10.1111/j.1469-7580.2011.01392.x

REVIEW

Fate of neuron–glia synapses during proliferation and differentiation of NG2 cells

Nicole Fröhlich,[1] Bálint Nagy,[1] Anahit Hovhannisyan[1,2] and Maria Kukley[1]

[1]*Group of Neuron–Glia Interactions, Werner Reichardt Centre for Integrative Neuroscience, University of Tübingen, Tübingen, Germany*

[2]*Group of Retinal Circuits and Optogenetics, Werner Reichardt Centre for Integrative Neuroscience, University of Tübingen, Tübingen, Germany*

Abstract

Progenitor cells expressing proteoglycan NG2 (also known as oligodendrocyte precursor cells or polydendrocytes) are widespread in the grey and white matter of the CNS; they comprise 8–9% of the total cell population in adult white matter, and 2–3% of total cells in adult grey matter. NG2 cells have a complex stellate morphology, with highly branched processes that may extend more than 100 μm around the cell body. NG2 cells express a complex set of voltage-gated channels, AMPA/kainate and/or γ-aminobutyric acid $(GABA)_A$ receptors, and receive glutamatergic and/or GABAergic synaptic input from neurons. In every region of the brain NG2 cells are found as proliferative cells, and the fraction of actively cycling NG2 cells is quite high in young as well as in adult animals. During development NG2 cells either differentiate into myelinating oligodendrocytes (and possibly also few astrocytes and neurons) or persist in the brain parenchyma as NG2 cells. This review highlights new findings related to the morphological and electrophysiological changes of NG2 cells, and the fate of synaptic input between neurons and NG2 cells during proliferation and differentiation of these cells in the neonatal and adult nervous system of rodents.

Key words: cell cycle; glutamate; NG2 glia; oligodendrocytes; proliferation; synaptic transmission.

Introduction

Progenitor cells expressing proteoglycan NG2 [also known as oligodendrocyte precursor cells (OPCs) or polydendrocytes] are widespread in the grey and white matter of the CNS; they comprise 8–9% of the total cell population in adult white matter, and 2–3% of total cells in adult grey matter (Dawson et al. 2003). The fact that a certain population of glial cells in the brain expresses proteoglycan NG2 has been known for more than 20 years (Levine & Card, 1987; Stallcup & Beasley, 1987). NG2-expressing cells rapidly came to light following the discovery of synapse-like associations between these glial cells and neurons in multiple regions of the developing and adult CNS (Bergles et al. 2000; Lin & Bergles, 2004a; Lin et al. 2005). NG2 cells have attracted greater attention, and steady progress in our understanding of their development and lineage progression has been made to date; yet, we still know surprisingly little about physiological properties and function of these cells in normal and diseased brain.

NG2 cells can be identified by the expression of the NG2 chondroitin sulphate proteoglycan and alpha receptor for platelet-derived growth factor (PDGF-Rα). Microvascular pericytes also express the NG2 proteoglycan (Ozerdem et al. 2001; Zhu et al. 2008a; Hamilton et al. 2010), but the two cell types are clearly distinguished by their morphology: NG2-glia are stellate cells with multiple processes, and pericytes are perivascular cells with two or more primary processes extending along blood vessels (Wigley & Butt, 2009).

Electrophysiological studies indicate that NG2 cells express a complex set of voltage-gated channels, including tetrodotoxin (TTX)-sensitive sodium channels and several types of potassium channels (Bergles et al. 2000; Chittajallu et al. 2004; Karadottir et al. 2008; Kukley et al. 2008, 2010; De Biase et al. 2010). Furthermore, NG2 cells in grey and white matter areas of the brain express α-amino-3-hydroxyl-5-methyl-4-isoxazole-propionate (AMPA)/kainate and/or γ-aminobutyric acid $(GABA_A)$ receptors, and receive glutamatergic and/or GABAergic synaptic input from neurons (Bergles et al. 2000; Lin & Bergles, 2004a; Karadottir et al.

Correspondence
Maria Kukley, Werner Reichardt Centre for Integrative Neuroscience (CIN), University of Tübingen, Paul-Ehrlich-Strasse 15-17, 72076 Tübingen, Germany. T: 0049 7071 29 89180; F: 0049 7071 29 5971; E: maria.kukley@cin.uni-tuebingen.de

Accepted for publication *11 April 2011*
Article published online *17 May 2011*

2005; Lin et al. 2005; Kukley et al. 2007; Ziskin et al. 2007). It is not known why neurons have developed dedicated release machinery at specific sites of contact with NG2 glial cells or if neuron–glia synapses are dynamic; although some recent studies have started to probe possible changes that neuron–glia synapses undergo when NG2 cells divide or differentiate (Kukley et al. 2008, 2010; Ge et al. 2009; De Biase et al. 2010).

This review highlights new findings related to the morphological and electrophysiological changes of NG2 cells, and the fate of synaptic input between neurons and NG2 cells during proliferation and differentiation of these cells in the neonatal and adult nervous system of rodents. First, we summarize current knowledge of the morphological and electrophysiological properties of NG2 cells and discuss evidence that NG2 cells receive synaptic input from neurons. Next, we talk about recent discoveries that suggest that NG2 cells maintain synapses with neurons during cell division and pass them onto their progeny. Finally, we emphasize the latest findings related to the fate of neuron–glia synapses upon differentiation of NG2 cells into myelinating oligodendrocytes.

Appearance, distribution and progeny of NG2 cells

To date it is not entirely clear at what point during development the first oligodendroglial progenitors expressing NG2 appear in the CNS. Several reports indicate that the earliest NG2-positive parenchymal cells appear after E14.5 in the mouse or E15–E17 in the rat (Nishiyama et al. 1996; Zhu et al. 2011). Before that time NG2 labelling within the CNS is detected in the developing capillaries, and no areas derived from the neuroepithelium appear to be stained (Nishiyama et al. 1996; Trotter et al. 2010). All the non-vascular NG2-positive cells also express PDGF-Rα. Other studies demonstrate that the earliest oligodendrocyte progenitors are generated in the ventral telencephalon at about E11.5–E12.5 in the mouse, from the ventricular zone of the medial ganglionic eminence (Tekki-Kessaris et al. 2001; Kessaris et al. 2006). These oligodendrocyte progenitors express PDGF-Rα, but it is not clear whether they are also positive for NG2.

The peak in the density of NG2 cells in the rat is reached during the first postnatal week. By this time regional variations in the density of the NG2 cells appear to be less apparent because the entire CNS becomes populated more uniformly by these cells (Nishiyama et al. 1996). Starting from the second postnatal week the density of NG2-immunoreactive cells begins to decrease, although both NG2 and PDGF-Rα molecules continue to be expressed into adulthood.

In the developing and also in the adult brain many NG2 cells develop into myelinating oligodendrocytes. A proportion of NG2 cells fail to differentiate past the stage at which they express NG2 and the lipid antigen O4 and persist in the CNS in a presumably immature form (Dawson et al. 2003; Rivers et al. 2008; Zhu et al. 2008a). Whether NG2 cells are oligodendrocyte precursors with restricted lineage potential or whether they are multipotent progenitors is not well understood. Earlier studies attempting to address the question of the NG2 cells' fate report that NG2 cells (OPC or O-2A progenitors) generate oligodendrocytes, but in addition they also give rise to a number of neurons and/or astrocytes (Belachew et al. 2003; Aguirre & Gallo, 2004; Aguirre et al. 2004; Tamura et al. 2007). Recent advances in gene technology have allowed further evaluation of NG2 cells' fate in the mouse CNS *in vivo* using Cre-loxP fate mapping in different transgenic mouse lines (Dimou et al. 2008; Rivers et al. 2008; Zhu et al. 2008a,b, 2011; Guo et al. 2009; Kang et al. 2010). These studies agree that NG2 cells are capable of generating oligodendrocytes. In addition, some studies reported that NG2 cells are the precursors of astrocytes in ventral areas of the brain and spinal cord (Zhu et al. 2008a,b; Guo et al. 2009). Other findings suggested that NG2 cells can differentiate into principal neurons in the ventral forebrain, dorsal cerebral cortex and hippocampus in the postnatal and adult animals (Rivers et al. 2008; Guo et al. 2009, 2010). At the same time, some investigators point out that NG2 cells remain committed to the oligodendrocyte lineage in postnatal life (Kang et al. 2010) and even following neurodegeneration (Kang et al. 2010). Interestingly, the fate of NG2 cells is likely to be age dependent, because a new study showed that NG2 cells in the postnatal brain generate only NG2 cells or oligodendrocytes, whereas NG2 cells in the embryonic brain generate protoplasmic astrocytes in addition to oligodendrocytes and NG2 cells (Zhu et al. 2011). Thus, it is clear that NG2 cells are the precursors of oligodendrocytes, but conclusions about the alternative fate of these cells remain controversial. This issue is difficult to investigate because of several reasons. First of all, NG2 proteoglycan is a surface marker that is lost before the terminal differentiation of the cells. Therefore, it is not possible to define the lineage potential of NG2-expressing cells based solely on NG2 expression, and the use of multiple markers is necessary to identify what types of progeny NG2 cells can generate. Second, although Cre-loxP technology brought many advantages, caution is needed in interpreting the results of Cre-loxP-mediated fate-mapping experiments (Nishiyama et al. 2009). Even in transgenic animals designed to express Cre recombinase under a specific promoter, transient expression of Cre recombinase in cells distinct from the lineage of interest is possible (Nishiyama et al. 2009). Therefore, confirmation of the fate-mapping results with other lineage-tracing methods is always desirable. The research on fate mapping of NG2 cells is further complicated by the fact that pericytes also express NG2 proteoglycan and, therefore, they and their progeny may be labelled by reporter genes in NG2 transgenic strains. This may bring confusion to the inter-

pretation of data obtained from transgenic strains, especially when taking into account possible neurogenic potential of pericytes recently reported *in vitro* (Dore-Duffy et al. 2006).

Morphological features of NG2 cells based on single-cell fluorescent dye labelling

NG2 glial cells are characterized by a small (10–15 μm) polygonal soma and a multipolar tree of fine processes (Bergles et al. 2000; Chittajallu et al. 2004; Kukley et al. 2007, 2008, 2010; Gallo et al. 2008). The morphology of the NG2 cells differs slightly depending on their location in the brain. In grey matter the cells have a centrally located soma, from which extend several long, slender primary processes, which bifurcate two or more times, to form a symmetrical process field (Fig. 1; Bergles et al. 2000; Chittajallu et al. 2004). In white matter areas of the CNS, for example in the corpus callosum and optic nerve, NG2 cells often have a more polarized appearance, extending processes along the axonal axis (Berry et al. 2002; Butt et al. 2004; Chittajallu et al. 2004; Kukley et al. 2007). Some authors show that NG2 cells in white matter have classic bipolar morphology of neural precursor cells: they possess only few processes that are short in length and are emanating from the opposing poles of the cell body (Chittajallu et al. 2004). However, other studies demonstrate that the process fields of white matter NG2 cells may ramify through the neuropil for distances up to 160–200 μm (Berry et al. 2002). Possible reasons for these discrepancies are not known, but may include different age of experimental animals and/or variations in cell-labelling techniques.

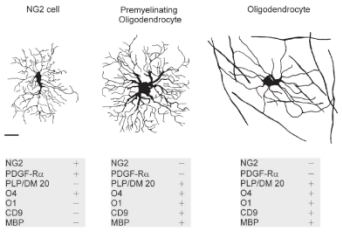

Fig. 1 Morphological comparison of the oligodendrocyte lineage cells. Drawings of an NG2 cell, a premyelinating oligodendrocyte and a myelinating oligodendrocyte. The drawings are traced from Lucifer-Yellow-filled cells in brain slices, and represent the typical morphology of oligodendrocyte lineage cells at different stages of differentiation. The grey panels beneath the drawings list some of the important molecular markers that are present (+) or absent (–) in the oligodendrocytes lineage cells. Scale bar: 10 μm (applies to all three drawings). Upper panel is modified with permission from Kukley et al. (2010).

An interesting morphological feature of NG2 cells in grey and white matter is the occurrence of multiple small varicosities, also called nodules, throughout the length of their processes (Fig. 2a; Butt et al. 1999; Berry et al. 2002; Jabs et al. 2005; Kukley et al. 2010). Functional meaning of those structures has not been identified, but it is possible that these regions indicate points where branching of NG2 cell processes has just started (Chatterjee et al. 2008). Alternatively, varicosities may represent sites of contacts between NG2 cells and other types of cells in the brain. Notably, in primary oligodendrocyte cultures, an intense co-localization of NG2 and a PDZ (postsynaptic density-95/discs large/zona occludens-1) domain protein syntenin-1 is seen at varicosities in NG2 cell processes (Chatterjee et al. 2008). The majority of the PDZ domain-containing proteins are associated with plasma membrane proteins, and they are generally restricted to specific sub-cellular domains such as synapses or cell–cell contact points (Sheng & Sala, 2001; Chatterjee et al. 2008). In neurons, syntenin binds to kainate receptor subunits and to all forms of AMPA receptor subunits, GluR1–4 (Hirbec et al. 2002, 2005). NG2 cells also express different subunits of AMPA receptors (see below). Therefore, it is possible that by interaction with ionotropic glutamate receptors syntenin plays a role in determining the formation and maturation of neuron–glia synapses. It might be of future interest to investigate whether varicosities along NG2 cell processes represent sites of functional input from neurons ('glial spines'), and whether different PDZ domain proteins and receptors for neurotransmitters are mainly targeted to the varicosities *in situ* and *in vivo*.

Are NG2 cells morphologically different from other types of glial cells in the brain, i.e. from astrocytes, microglia and oligodendrocytes? Our observations based on immunohistochemical labelling in hippocampal slices as well as on labelling individual astrocytes and NG2 cells with fluorescent dye Lucifer Yellow during patch-clamp recordings indicate that in grey matter those two cell types are morphologically distinct. Hippocampal astrocytes show large soma and asymmetrically radiating processes that consist of several primary thick processes, from which emanate multiple smaller collateral branching secondary processes, giving them a bushy, spongiform appearance (Fig. 2b; Nishiyama et al. 2005). NG2 cells, in contrast, have smaller soma and numerous irregular fine processes, but the smallest processes of NG2 cells are not as thin as those of the astrocytes, and thus NG2 cells clearly lack sponge-like appearance (Fig. 2a; Nishiyama et al. 2005). Astrocyte processes often end in bulbous swellings, or terminal end-feet, which form the vascular and pial glia limitans. In contrast, NG2-glial processes taper to an end and do not appear to contribute to the glia limitans (Nishiyama et al. 2005). It is so far not clear whether those morphological differences hold true for NG2 cells and fibrous astrocytes in white matter. NG2 cells and astrocytes are also diverse in respect with molecular markers: NG2 cells do not express

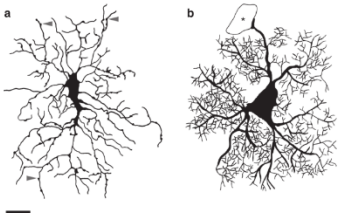

Fig. 2 Morphological comparison between an NG2 cell and a grey matter astrocyte. Drawings of an NG2 cell (a) and an astrocyte (b) represent typical morphological appearance of the two cell types in brain slices. The drawing of the NG2 cell is traced from a Lucifer-Yellow-filled cell. Arrowheads point to varicosities present along the processes of the NG2 cell. Drawing of the grey matter astrocyte is a collage based on anti-GFP staining of astrocytes in brain slices from GFP/GFAP transgenic mouse. The asterisk indicates a blood vessel. Note the difference in the size of the soma, the thickness of the main and finer processes, as well as in the branching of fine processes. Scale bar: 10 μm (applies to both drawings). Part (a) is modified with permission from Kukley et al. (2010).

glial fibrillary acidic protein (GFAP) or the glial glutamate–aspartate transporter, which are expressed by astrocytes; while astrocytes in turn do not express NG2, PDGF-Rα and O4 (Levison et al. 1999; Zhou et al. 2006; Nishiyama et al. 2009; Kukley et al. 2010).

Clear differences in the number, length and appearance of the processes as well as in the size of cell soma have been observed between NG2 cells and more mature cells of the oligodendrocyte lineage, and in striking contrast to mature oligodendrocytes NG2 cells do not bear myelin sheathes (Fig. 1; Trapp et al. 1997; De Biase et al. 2010; Kukley et al. 2010). NG2 cells appear negative for the molecular markers of the more mature cells of the oligodendroglial lineage, such as proteolipid protein (PLP) and/or its splice variant DM20, myelin basic protein, 2,3-cyclic nucleotide 3-phosphodiesterase, galactocerebroside O1 and tetraspanin CD9 (Polito & Reynolds, 2005; Nishiyama et al. 2009; Kukley et al. 2010). Notably, some premyelinating oligodendrocytes may still carry residual amounts of NG2 proteoglycan, indicating that they are indeed the descendants of NG2 cells.

NG2 cells are likely to hold some morphological similarities with ramified microglial cells. To date, no direct comparison of morphological properties of these two cell types has been performed based on single-cell dye labelling under identical experimental conditions. Some insights into the morphological structure of ramified microglia come from reconstructions of Lucifer Yellow-filled cells in brain slices of the adult mice (Boucsein et al. 2003), and from the *in vivo* 2-photon imaging of microglial cells in adult EGFP-CX3CR1 transgenic mice (Davalos et al. 2005; Nimmerjahn et al. 2005). Similar to NG2 cells, microglial cells have small cell soma from which numerous thin and highly ramified processes extend symmetrically (Boucsein et al. 2003; Davalos et al. 2005; Nimmerjahn et al. 2005). In contrast to NG2 cells, microglia cell processes lack small nodules but display highly motile filopodia-like protrusions of variable shape, typically forming bulbous endings under normal conditions and/or during injury (Davalos et al. 2005; Nimmerjahn et al. 2005). The double-labelling immunohistochemical studies have established that NG2 cells are clearly distinct from resting or activated microglia: NG2 cells are negatively stained with the markers of the microglial cells, for example 4H1, CD68, F4/80 or OX42 (Nishiyama et al. 1997, 2002; Horner et al. 2002; Kukley et al. 2010).

Thus, NG2 cells possess some unique morphological features that could be their individual hallmarks; in brain slices NG2 cells can be reliably distinguished from other cells on the basis of their morphology and antigenic expression.

NG2 cells express voltage-gated potassium and sodium channels

NG2 cells in grey and white matter express different types of voltage-gated channels. Depolarizing voltage steps from the resting potential elicit both rapidly inactivating and sustained outward K^+ currents (Knutson et al. 1997; Chittajallu et al. 2002, 2004; Kukley et al. 2010). These currents consist of conventional 'A-type' and 'delayed rectifier' type K^+ currents that are antagonized by 4-aminopyridine and tetraethylammonium, respectively (Chittajallu et al. 2004). The functional role of voltage-activated K^+ channels in NG2 cells is not entirely clear. Cell proliferation studies and electrophysiological analysis in cultured cells and in brain slices have suggested that potassium channels may have a prominent role in the oligodendrocyte lineage cell proliferation (Gallo et al. 1996; Knutson et al. 1997; Yuan et al. 1998; Ghiani et al. 1999). It has been observed that over-expression of Kv1.3 or Kv1.4 subunits of potassium channel increases oligodendrocyte lineage cell proliferation in the absence of mitogens, whereas Kv1.6 over-expression inhibits mitogen-induced cell cycle progression (Vautier et al. 2004). Thus, it is possible that K^+ channels in NG2 cells are in some way involved in the regulation and/or modulation of the cell cycle. Interestingly, the amplitude of voltage-gated outward potassium currents begins to decrease as NG2 cells stop dividing and start to differentiate (Kukley et al. 2010).

In addition to the outward K^+ currents, NG2 cells also exhibit inward K^+ currents to a variable degree (Lin & Bergles, 2002; Chittajallu et al. 2004). These currents are likely to result from the activity of both ATP-sensitive K^+ channels and inwardly rectifying K^+ channels (Kir). Kir channels in glial cells have been implicated in several functions, which include setting and/or stabilizing the resting membrane potential near the K^+ equilibrium potential, as well as accumulation, buffering or siphoning of K^+ released

during neuronal activity (Reimann & Ashcroft, 1999; Lin & Bergles, 2002).

Most authors agree on the fact that NG2 cells carry voltage-gated sodium channels (NaV channels), yet there is some disagreement concerning the proportion of NG2 cells that express NaV (Bergles et al. 2000; Chittajallu et al. 2004; Jabs et al. 2005; Karadottir et al. 2008; De Biase et al. 2010; Kukley et al. 2010; Maldonado et al. 2011). A recent study aimed to define the prevalence of NaV channel expression and excitability within the NG2 cell population in grey and white matter throughout development (De Biase et al. 2010). Whole-cell voltage-clamp recordings in acute brain slices prepared from NG2-DsRed mice of different ages (P5–P8, P12–P15, P20–P26, P40–P45) revealed that all NG2 cells in corpus callosum, hippocampus, molecular layer of the cerebellum and cerebellar white matter exhibit TTX-sensitive NaV channel-mediated currents (De Biase et al. 2010). These data suggest that NaV channel expression is a universal property of NG2 cells in both grey and white matter regions of the developing and mature brain. At the same time, other studies point towards heterogeneity of the NG2 cell population in the brain with respect to expression of NaV channels and define two classes of NG2 glial cells: one type lacks voltage-gated Na^+ channels completely (~ 30% of all NG2 cells); whereas the other type expresses a sufficient number of NaV channels to generate Na^+ currents upon depolarization of cell membrane (Karadottir et al. 2008). Importantly, relatively high passive membrane conductance of some NG2 cells, for example in the adult brain, may mask Na^+ currents in these cells (Maldonado et al. 2011). Using an effective way to increase membrane resistance (e.g. bath application of barium) may help in uncovering Na^+ currents in NG2 cells (Maldonado et al. 2011). Maldonado et al. (2011) have recently applied this approach to demonstrate that the large majority, if not all NG2 cells, of the somatosensory cortex express voltage-gated Na^+ channels regardless of the age of the animal.

Expression of NaV channels by NG2 glial cells has raised the question whether these cells are able to generate action potentials. Apparently the peak amplitude of the Na^+ current in NG2 cells is > 10 times smaller than that observed in mature neurons under similar conditions (Chittajallu et al. 2004; De Biase et al. 2010; Kukley et al. 2010). The small number of these channels and the comparatively large K^+ conductances present prevents the initiation of regenerative spikes in NG2 cells (De Biase et al. 2010; Kukley et al. 2010). But it should be noted that some NG2 cells in the cortex and corpus callosum may generate a single spike upon depolarization (Chittajallu et al. 2004; Ge et al. 2009; De Biase et al. 2010; Maldonado et al. 2011). However, these spikes do not meet the criteria normally used to define action potentials in neurons. Action potentials are regenerative, all-or-none events, with a discrete threshold of activation (normally of about −45 to −55 mV), constant amplitude, and a peak depolarization that approaches the sodium equilibrium potential (E_{Na}; Kandel et al. 2000; Squire et al. 2003). Single spikes observed in NG2 cells exhibit a more depolarized threshold for activation (−22 ± 1 mV), their amplitudes increase with larger current injections, and they do not substantially overshoot 0 mV (Chittajallu et al. 2004; Ge et al. 2009; De Biase et al. 2010). In addition, NG2 cells that exhibit spikes are unable to sustain repetitive firing with continued depolarization and they do not exhibit spontaneous firing (De Biase et al. 2010; Maldonado et al. 2011; but see Karadottir et al. 2008). If NG2 cells do not use NaV channels for firing typical action potentials, what could be the functional meaning of these channels in NG2 glia? The influx of positive charge through the Na^+ channels could boost other depolarizing stimuli, allowing activation of other voltage-dependent channels (Lin & Bergles, 2004b). Alternatively, in the absence of excitability, the Na^+ influx through these channels could regulate the efficiency of the Na^+/K^+ ATPase or Na^+-dependent transporters (Lin & Bergles, 2004b). Recent data demonstrate that Na^+ channels mediate Ca^{2+} influx via Na^+/Ca^{2+} exchangers in NG2 cells upon GABA induction of membrane depolarization (Tong et al. 2009). The authors go on to show that this unique Ca^{2+}-signalling pathway is involved in the migration of NG2 cells (Tong et al. 2009). They further speculate that any ligand that induces sufficient membrane depolarization in NG2 cells may elevate intracellular Ca^{2+} by activating the Na^+ channel–Na^+/Ca^{2+} exchanger pathway. This induces NG2 cell migration by triggering the Ca^{2+}-dependent mechanisms required for cell migration, including cytoskeletal reorganization, cell mobility, membrane traffic, and cell adhesion and de-adhesion (Tong et al. 2009).

The lack of ability to fire bona fide action potentials does not necessarily imply that NG2 cells do not possess any output signalling and can not be involved in the information processing. Action potentials may be absent from the responses of NG2 cells because these cells have relatively short processes (up to 100–200 μm) and do not convey signals over long distances, analogous to, for example, bipolar cells in distal retina (Dowling, 1987). Therefore, electrotonic spread of the potential changes might be sufficient for information to reach from one end of the cell to the other. NG2 cells may use graded potentials rather than action potentials to distinguish a wide range of signal intensities, for example in analogy to various types of cells in the retina that use graded potentials rather than action potentials for fine intensity discriminations (Dowling, 1987).

NG2 cells express AMPA/kainate and $GABA_A$ receptors, and receive synaptic input from neurons

The first demonstration of glutamate-activated channels in glia goes back to 1989, when multiple conductance channels activated by L-glutamate, quisqualate or kainate have been

reported in type-2 astrocytes in culture (Usowicz et al. 1989). At that time it has been suggested that glial cells possess glutamate receptors, which could be activated by glutamate released from axons and may, therefore, be important for formation and maintenance of the nodes of Ranvier (Usowicz et al. 1989). Follow-up studies revealed that glutamate or kainate, agonists at AMPA/kainate receptors, elicit inward currents in O-2A cells acutely isolated from the optic nerve (Barres et al. 1990), in 'complex cells' from hippocampal slices (Steinhauser et al. 1994) and in glial precursor cells in the corpus callosum (Berger, 1995). Glial $GABA_A$ receptors were first discovered in cultured astrocytes and cells of oligodendrocyte lineage (Gilbert et al. 1984; Kettenmann et al. 1984), and subsequently in *in situ* preparations, for example in 'complex cells' from slices of the rat hippocampus (Steinhauser et al. 1994) and in glioblasts from the corpus callosum (Berger et al. 1992). Although no immunohistochemical staining for NG2 was performed at that time, it is likely that the large proportion of O-2A cells, 'complex cells', and possibly also callosal precursor cells, investigated in those studies were cells now known as NG2 glia. This assumption is based on two major facts. Firstly, a detailed comparison in the developing rodent CNS between the distribution of the NG2 proteoglycan and the PDGF-Rα shows that these two molecules are co-expressed by glial progenitor cells of the O-2A lineage and can serve as reliable markers for identification of O-2A cells *in vivo* (Nishiyama et al. 1996). Secondly, there is now an emerging consensus in the field that 'complex cells' (also termed GluR cells) exhibit many of the properties that have been described for NG2 cells, and that 'complex cells' and NG2 cells represent overlapping populations (Bergles et al. 2010).

The expression of neurotransmitter receptors by NG2 glia inspired thinking of how these receptors become activated *in situ*. Bergles et al. (2000) were the first to demonstrate that upon propagation of single action potentials glutamate is released directly onto NG2 cells' AMPA receptors at neuron–NG2 cell synapses. The authors made whole-cell patch-clamp recordings from NG2 cells in the hippocampus and measured their response to stimulation of afferent excitatory axons. They were able to record inward currents in NG2 cells, which were strongly inhibited by the AMPA/kainate receptor antagonists (Bergles et al. 2000). The quantal nature of these responses and their rapid kinetics indicated that they are produced by the exocytosis of vesicles filled with glutamate directly opposite AMPA receptors on NG2 glia (Bergles et al. 2000). A similar type of fast neuron–glia synaptic signalling has been later discovered between GABAergic interneurons and NG2 cells in the hippocampus (Lin & Bergles, 2004a). Additional evidence from electron microscopic analysis revealed accumulations of small vesicles at contact sites between axons and the processes of NG2 cells in both the young and adult rodent hippocampus (Bergles et al. 2000; Lin & Bergles, 2004a).

Since the first discovery of glutamatergic and GABAergic innervation of NG2 cells, several groups demonstrated that NG2 cells receive synaptic input from neurons in different grey matter areas, including the cerebral cortex, hippocampus, cerebellum, brain stem and ventrobasal thalamus (Chittajallu et al. 2004; Lin & Bergles, 2004a; Lin et al. 2005; Karadottir et al. 2008; Kukley et al. 2008; Muller et al. 2009; De Biase et al. 2010; Parri et al. 2010; Velez-Fort et al. 2010). More surprisingly, unmyelinated axons passing through white matter (e.g. corpus callosum, optic nerve) also establish excitatory glutamatergic synapses with local NG2 cells, and neurotransmitter release along axons in white matter is quite similar to vesicle fusion at synapses: it is reliable, it depends on action potential propagation, involves highly localized calcium microdomain signalling and is strongly calcium cooperative (Kukley et al. 2007; Ziskin et al. 2007).

Do only few NG2 cells receive synaptic input from neurons, or is it a universal property of the whole population of NG2 cells throughout the brain? The data obtained by different groups to date remain controversial. For example, Chittajallu et al. (2004) observed functional AMPA receptors in all NG2 cells in the neocortex, but could detect spontaneous AMPA receptor-mediated synaptic currents only in ~ 6% of these cells. These findings are consistent with a recent report indicating that > 90% of synaptic currents in NG2 cells in the neocortex are GABAergic early in postnatal life (Velez-Fort et al. 2010). In the cerebellum NG2 cells have been shown to fall into two classes: cells expressing Na^+ channels and cells lacking Na^+ channels. Interestingly, these two populations of NG2 cells appeared to sense their environment in different ways: 81% of NG2 cells expressing Na^+ channels showed spontaneous synaptic input; while only 2% of the NG2 cells lacking Na^+ channels showed detectable synaptic events (Karadottir et al. 2008). On the contrary, another study reports that in the cerebellum (both in white matter and in the molecular layer) the ability to receive glutamatergic synaptic input from neurons is a general feature of each and every NG2 cell (De Biase et al. 2010). To obtain an unbiased sample of the NG2 cell population, De Biase et al. used transgenic mice expressing DsRed-T1 under the control of the NG2 promoter (Ziskin et al. 2007; Zhu et al. 2008a). They made whole-cell voltage-clamp recordings from NG2 cells, and focally applied hypertonic solution (500 mM sucrose in artificial cerebral spinal fluid) to force fusion of docked, primed synaptic vesicles from presynaptic membranes in contact with these cells (De Biase et al. 2010). At the earliest postnatal periods examined (P5–P10), hypertonic challenge evoked glutamatergic synaptic responses in the majority of NG2 cells. At later developmental periods (P12–P15, P20–P26, P40–45), hypertonic challenge elicited glutamatergic synaptic responses in all NG2 cells (De Biase et al. 2010). The authors report similar findings for NG2 cells in the hippocampus and corpus callosum (De Biase et al. 2010). It remains unclear why the proportion of synaptically innervated cerebellar NG2 cells found in the study of Karadottir et al. (2008) and that of De Biase et al. (2010) is different. One

possibility could be species differences, because Karadottir et al. (2008) recorded in the rat cerebellum while De Biase et al. (2010) used a transgenic mouse.

Taken together, the controversy on whether or not all NG2 cells throughout the brain receive synaptic input is not completely resolved. It remains to be ascertained whether the proportion of synaptically innervated NG2 cells depends on the brain region and/or on the age of the animal. It is especially interesting to find out whether glutamatergic and GABAergic synaptic inputs onto NG2 cells are differently regulated during development, and whether those two inputs have different meaning for a given NG2 cell contacted by both glutamatergic and GABAergic synapses (e.g. in the hippocampus).

The process of forming a synapse involves complex coordinated cell morphological and structural changes that are instructed through ligand-receptor interactions, intracellular signalling cascades and complex filamentous actin remodelling (Shen & Cowan, 2010). Why do neurons establish synapses with NG2 glial cell and why do NG2 cells attempt to receive synaptic input from neurons? Discovery of the functional importance of neuron–NG2 synapses remains a challenge for future research. So far a number of studies proposed that neuron–glia communication is essential for regulating development of NG2 cells, and suggested that there is a link between activation of neurotransmitter receptors and the proliferation and/or differentiation of NG2 cells (Karadottir & Attwell, 2007). We will discuss these findings in more detail in the following sections of this review.

NG2 cells represent the major cycling cell type in the brain

From the time of birth, NG2 cells are more or less evenly distributed throughout the brain, both in grey matter and white matter (Nishiyama et al. 1996; Dimou et al. 2008; Rivers et al. 2008). Interestingly, in every region of the brain NG2 cells are found as proliferative cells (Dawson et al. 2000, 2003; Horner et al. 2002; Nishiyama et al. 2002; Aguirre et al. 2004), and the fraction of actively cycling NG2 cells (growth fraction) is quite high in young (1–2 weeks old) as well as adult (~ 18 months old) animals (Kukley et al. 2008; Psachoulia et al. 2009). In order to estimate the growth fraction of NG2 cells, Kukley et al. (2008) performed a double staining for NG2 and the proliferating cell nuclear antigen (PCNA), which is only detected in cycling but not in resting cells. At P9 and P11 mouse hippocampus, the authors determined the growth fraction (NG2+ and PCNA+) of NG2 glia to be as large as 48% and 49% (93/194 and 52/106 of NG2 cells), respectively (Kukley et al. 2008). These growth fraction measurements are in keeping with a follow-up report indicating that the growth fraction [defined by cumulative bromodeoxyuridine (BrdU) labeling] of P6 mouse NG2 cells in corpus callosum and cerebral cortex is ~ 55% (Psachoulia et al. 2009).

As an animal grows into adulthood the density of NG2 cells decreases (Nishiyama et al. 1996; Velez-Fort et al. 2009), and the absolute number of cycling NG2 cells declines (Panagiotakos et al. 2007; Velez-Fort et al. 2009). However, although the actual number of proliferating NG2 cells in the adult brain is largely below that of the first postnatal weeks, the fraction of actively cycling NG2 cells changes only slightly with age, being ~ 46% in corpus callosum and ~ 39% in cerebral cortex of 2–18-month-old mice (Psachoulia et al. 2009). Thus, approximately half of all NG2 cells are constantly dividing, independently of the brain area and the age of the animals. Remarkably, recent findings indicate that *all* NG2+ cells in the mature brain, regardless of region, have the ability to divide (Kang et al. 2010). Therefore, it is possible that the total number of cycling NG2 cells in the brain is even higher than suggested previously (Kukley et al. 2008; Psachoulia et al. 2009).

Are there any differences in proliferation parameters of NG2 cells between the neonatal and adult brain? Cumulative BrdU labelling performed in mice of various ages revealed a striking discrepancy in cell cycle time of NG2 cells (Kukley et al. 2008; Rivers et al. 2008; Psachoulia et al. 2009). During the first two postnatal weeks the cell cycle time of NG2 cells in the hippocampus, cerebral cortex and corpus callosum is about 2–3 days, meaning each cycling NG2 cell divides approximately every 48–72 h (Kukley et al. 2008; Psachoulia et al. 2009). As the animal matures, cell cycle time increases steadily, being > 100 days at P540 (Psachoulia et al. 2009). Interestingly, the rate of oligodendrocyte production from NG2 cells declines in parallel with the increase of the NG2 cells' cell cycle duration. In the corpus callosum, for example, the cell cycle slows down ~ 10-fold between P45 and P240, and the rate of oligodendrocyte production slows ~ 20-fold at the same period (Psachoulia et al. 2009).

NG2 cells represent the major cycling cell population in the rodent brain parenchyma. Thus, studies using BrdU labelling and immunohistochemistry show that NG2 cells account for approximately 70% of BrdU-positive cells in the adult cerebral cortex, hippocampus, corpus callosum and spinal cord after a short BrdU pulse (Horner et al. 2000; Dawson et al. 2003; Polito & Reynolds, 2005; Lasiene et al. 2009). Other studies using BrdU labelling, immunohistochemistry and/or transgenic mice where NG2 or Olig2 cells are labelled suggest that virtually all cells (≥ 90%) incorporating BrdU in the brain parenchyma represent NG2 cells (Alonso, 2000; Dayer et al. 2005; Dimou et al. 2008; Mori et al. 2009). NG2+/Olig2+ cells also represent the major cycling population of the healthy adult human brain (Geha et al. 2010).

NG2 cells maintain complex morphology during cell division

NG2 cells in grey and white matter of the rodent brain have a complex morphology, with highly branched processes that may extend more than 100 μm in radial (grey matter)

or bipolar (white matter) shape around the small cell body. At the same time, in the neonatal as well as in the adult brain about 50% of NG2 cells are actively involved in the cell cycle. How does the cell morphology change when an NG2 cell enters the cell cycle? To address this question, patch-clamp recordings from individual hippocampal NG2 cells with mitotic DNA configuration have been carried out, and the cells were filled with a fluorescent dye Lucifer Yellow (Kukley et al. 2008). Subsequent morphological analysis of these dye-filled cells revealed that metaphase and telophase NG2 cells possess a rich tree of branching processes (Kukley et al. 2008). Similar findings have been reported by Ge et al. (2009), who carried out morphological examination of mitotic glial cells positively labelled for NG2 in brain slices (Fig. 3A–C). We, therefore, believe that NG2 cells maintain their complex morphology during division. These findings, however, do not completely exclude the possibility that NG2 cells are able to retract and re-grow some of their processes very quickly, for example in the range of minutes, and at the moment of chromosome separation the cells withdraw many of their processes. Time-lapse imaging of zebrafish OPCs *in vivo* shows that cells can rapidly remove filopodium-like processes, divide and then re-grow their processes again and migrate away from each other (Kirby et al. 2006). *In vivo* time-lapse imaging of mammalian NG2 cells has not been reported to date, and it is unclear whether a similar sequence of events happens during cell division of mammalian NG2 cells. Ge et al. (2009) attempted to perform time-lapse imaging of dividing NG2 cells in acute mouse brain slices, and observed that the soma of the mother cell was splitting into two, while all of the processes remained un-retracted. This result strongly supports the

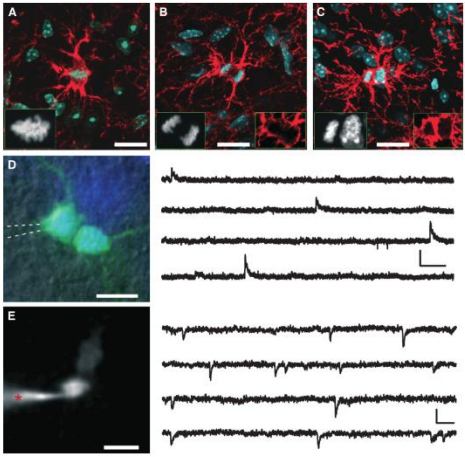

Fig. 3. NG2 cells maintain complex morphology and functional synapses during mitosis. (A–C) Three NG2 cells at different stages of cell division labelled by DAPI (blue) and NG2 antibodies (red) in brain slices prepared from P25 mouse: metaphase (A), anaphase (B) and telophase (C). Note that mitotic cells possess a rich tree of processes, and that NG2 expression is upregulated during mitosis. Scale bars: 20 μm (A–C). Insets show blue and red channels separately. Note the difference between the appearance of the DAPI signal in NG2 cells at different stages of mitosis. (D) Left: dividing NG2 cell showing mitotic chromatin configuration in a live brain slice. The cell is filled with Lucifer Yellow (green) during patch-clamp recordings. Chromatin is labelled with Hoechst 33342 (blue). Patch-pipette is indicated by the dashed white lines. Scale bar: 10 μm. Right: GABAergic synaptic currents recorded from the cell shown on the left (V_h = +30 mV), in the presence of 30 μM CNQX and 100 μM ruthenium red. Scale bar: 400 ms, 20 pA. (E) Left: mitotic NG2 cell filled with Cy5-conjugated dextran (10 kDa) during patch-clamp recordings. Dextran (10 kDa) does not spread through gap junctions, so filling of two cells indicates that the division process is not completed and cells still share the cytoplasm. Asterisk indicates the patch-pipette. Scale bar: 10 μm. Right: glutamatergic synaptic currents recorded from the cell shown on the left (V_h = −80 mV), in the presence of 10 μM bicuculline. Scale bar: 20 ms, 10 pA. (A–C) Modified with permission from Ge et al. (2009). (D,E) Modified with permission from Kukley et al. (2008).

idea that NG2 cells can indeed retain their complex morphology during mitosis. However, the observation of Ge et al. is so far based only on a single example. Future experiments involving time-lapse imaging in transgenic mice where soma and processes of NG2 cells are specifically labelled would be necessary to further investigate this issue.

NG2 cells keep functional synapses during mitosis and pass them onto their progeny

Do NG2 cells maintain synapses with neurons during cell division? To investigate synaptic responses directly in proliferating cells, patch-clamp recordings have been performed from mitotic NG2 cells (metaphase or telophase of mitosis) in acute hippocampal and cortical slices from neonatal (7–12 days old) mice (Kukley et al. 2008). In the presence of AMPA/kainate receptor antagonist 6-cyano-7-nitroquinoxaline-2,3-dione (CNQX, 10 μM), clear GABAergic synaptic currents were detected in NG2 cells with mitotic chromosomes configurations (Fig. 3D; Kukley et al. 2008). On removal of AMPA/kainate receptor antagonists from the extracellular solution and adding $GABA_A$ receptor antagonist bicuculline (10 μM), fast rising and decaying excitatory postsynaptic currents could be recorded in NG2 cells during metaphase and telophase of mitosis (Fig. 3E; Kukley et al. 2008). In line with these findings are the recent data of Ge et al. (2009), who demonstrate that grey and white matter NG2 cells in metaphase and telophase of mitosis receive glutamatergic synaptic input from neurons not only in young but also in older animals (up to 20 weeks old). Furthermore, electron microscopy images show that synaptic terminals contact mitotic NG2 cells, suggesting that during cell division at least some synaptic contacts are maintained (Kukley et al. 2008).

Based on the described evidence it seems likely that NG2 cells in the rodent brain can enter cell cycle and undergo cell division without losing functional GABAergic and glutamatergic synapses. The evidence so far is indirect, because we and other groups have not tracked single synapses on NG2 cells during mitosis in native brain slices or *in vivo*. However, the following facts speak in favour of the inheritance. First, the frequency of synaptic currents is comparable between metaphase and telophase NG2 cells (Kukley et al. 2008). Synaptic currents recorded in telophase NG2 cells are likely to stem from both daughter cells, because in telophase two daughter cells are not completely separated yet and share cell membrane and cytoplasm. Therefore, the invariant frequency of synaptic currents between metaphase and telophase cells most likely indicates that the number of functional synaptic contacts of the parent cell is comparable with the number found in two daughter cells. In addition, the number of glutamate decarboxylase-positive ($GAD65^+$) terminals (putative GABAergic boutons) in each daughter NG2 cell is roughly half of the synaptic terminals found in the parent cell (Kukley et al. 2008). Furthermore, if we assume that the time necessary for the assembly and disassembly of neuron–glia synapses is the same as of neuronal synapses, then AMPA receptor-containing synapses can be eliminated as quickly as 90 min and assembled within 1–2 h of initial axo-dendritic contact (Friedman et al. 2000; Eaton & Davis, 2003; Goda & Davis, 2003). If NG2 cells have to disassemble *all* synapses before cell division and reform *all* of them from scratch after cytokinesis, there should be a period of time equal to at least 1 h when synaptic currents are absent in NG2 cells. However, synaptic currents could be recorded in NG2 cells presumably 30 min before and after chromosome segregation (Kukley et al. 2008).

Taken together, we believe that newly generated NG2 cells can inherit synapses from their parent cell in the postnatal rodent brain. What could be the benefit of inheriting a synapse? Keeping synaptic contacts with dividing NG2 cells may give neurons the opportunity to directly or indirectly regulate proliferation of NG2 cells, for example by influencing the expression of potassium channels during the cell cycle and/or by controlling other intracellular signalling cascades. On the other hand, inheritance of synapses may allow for the direct transfer of environmental interactions to clonal descendants of NG2 cells, which might be important for effective colonization and perhaps future myelination of the developing brain.

Discovery of glutamatergic innervation of dividing NG2 cells (Kukley et al. 2008; Ge et al. 2009) re-opened an essential question regarding the role of glutamate and its receptors for proliferation of the oligodendrocyte lineage cells, which was first addressed 15 years ago (Gallo et al. 1996; Yuan et al. 1998). At that time work performed in dissociated cell cultures and organotypic slice cultures showed that glutamate acts through AMPA/kainate receptors to inhibit O-2A progenitor (presumably NG2 cells) proliferation (Gallo et al. 1996; Yuan et al. 1998). It has been suggested that this effect is mediated by the increase in intracellular Na^+ concentration triggered by the opening of the AMPA channels in the O-2A membrane, and subsequent block of voltage-gated K^+ channels (Gallo et al. 1996; Yuan et al. 1998). Now it turned out that glutamate released from neurons activates AMPA/kainate receptors on dividing NG2 cells in acute brain slices (Kukley et al. 2008; Ge et al. 2009). How can NG2 cells receiving glutamatergic synaptic input divide if glutamate inhibits proliferation? In the earlier studies agonists and antagonists of glutamate receptors have been added to the culture medium for 1–48 h, and therefore cells were constantly exposed to these substances for a prolonged period of time (Gallo et al. 1996; Yuan et al. 1998). Glutamatergic synaptic-like signalling between neurons and NG2 cells under physiological conditions is a much finer 'tool' for exposing glial cells to glutamate and activating their glutamate receptors. Importantly, glutamatergic synaptic signalling can be tuned in time and space both pre- and postsynaptically, and it can perhaps be tuned during the cell cycle of NG2 cells. For example, AMPA receptors

expression on NG2 cells and/or properties of the axonal release machinery could be higher in G1 phase and decreasing in G2/M phase, thereby allowing NG2 cell division. Blocking AMPA/kainate receptors and subsequent increase in cell proliferation described by Yuan et al. (1998) would be an extreme of this situation. It is not known today whether and how surface expression of neurotransmitter receptors on NG2 cells, the number and properties of synapses, the location of synapses along NG2 cell processes and the strength of synaptic input change during the cell cycle of an NG2 cell. It remains to be discovered whether and how glutamatergic synaptic signalling between neurons and glia regulates proliferation of NG2 cells.

Synaptic signalling and glutamate receptor expression are rapidly decreased during differentiation of NG2 cells

During animal development a large proportion of NG2 cells evolve into premyelinating oligodendroglial cells, which then differentiate further into myelinating oligodendrocytes (Trapp et al. 1997; Zhu et al. 2008a,b; De Biase et al. 2010; Kukley et al. 2010). Differentiation of NG2 cells is accompanied by dramatic alterations of the cell morphology and by definite changes of the expression pattern of specific molecular markers (Fig. 1). Detailed morphometric analysis based on single cell dye-filling reveals that premyelinating oligodendrocytes in grey matter display a significantly larger total processes length (2891 ± 177 vs. 1198 ± 190 μm), area covered by the processes (6169 ± 235 vs. 3328 ± 215 μm^2) and diameter of the soma (9.7 ± 0.9 vs. 6.5 ± 0.7 μm) when compared with NG2 cells (Kukley et al. 2010). In contrast to NG2 cells, premyelinating oligodendrocytes are largely negative for NG2 and PDGF-Rα, but are positively stained by the PLP/DM20 antibodies and by O1 antibodies showing labelling of the entire cell surface (Sommer & Schachner, 1981; Trapp et al. 1997; Kukley et al. 2010). Premyelinating oligodendrocytes do not display myelin sheathes (Fig. 1). Mature myelinating oligodendrocytes in the grey matter possess fewer processes than NG2 cells or premyelinating cells, but they clearly show numerous myelin sheathes. Myelin sheathes of hippocampal oligodendrocytes in CA1 stratum radiatum rarely appear as parallel, linear structures like those frequently observed in the white matter. They rather show random orientation, which reflects the orientation of axons in the stratum radiatum (Fig. 1).

Do neurons keep synapses that they have established with NG2 cells when NG2 cells advance through the process of differentiation? Two recent studies used whole-cell patch-clamp recordings from distinct developmental stages of oligodendroglial cells in brain slices to address the question what is the fate of synaptic input upon differentiation of NG2 cells (De Biase et al. 2010; Kukley et al. 2010). The authors employed two separate approaches to identify oligodendroglial cells at distinct stages of differentiation: while De Biase et al. (2010) used NG2-CreER;Z/EG transgenic mice where NG2 cells and their progeny show green fluorescence, Kukley et al. (2010) recorded from C57black/N mice and PLP-GFP mice and applied post-recording immunohistochemistry to prove the identity of the cells. Neuron–glial synapses exhibit a low rate of spontaneous release (Bergles et al. 2000; Chittajallu et al. 2004; Kukley et al. 2008), therefore it might be challenging to measure the innervation of the oligodendroglial cells in distinct stages of differentiation. It would be necessary to employ an approach that reliably brings about high exocytotic activity in the presynaptic nerve terminals contacting glial cells. To date, several manipulations have been extensively used to study vesicular release at neuronal synapses (Trudeau et al. 1996). One method used is to locally apply hypertonic solution (e.g. sucrose), which rapidly increases the quantal release rate to a relatively high level (Rosenmund & Stevens, 1996). Importantly, the pool of quanta defined with stimulation by hypertonic solution is the same as that employed when release is evoked by action potentials (Rosenmund & Stevens, 1996; De Biase et al. 2010). Another tool is application of polyvalent cations, such as lanthanum and ruthenium red (Raastad et al. 1992; Trudeau et al. 1996). The mechanism of action of polyvalent cations is not completely clear, but it has been suggested that they effectively induce quantal neurotransmitter release by binding to an external site on the presynaptic plasma membrane (Trudeau et al. 1996). In two recent studies the authors employed those approaches to study vesicular neurotransmitter release at neuron–glia synapses in different regions of the brain *in situ* (De Biase et al. 2010; Kukley et al. 2010). Whereas bath perfusion of 100 μM ruthenium red or local application of 500 mM sucrose elicited spontaneous synaptic responses in all NG2 cells tested, only a few premyelinating cells showed synaptic currents upon those manipulations, and no currents could be induced in myelinating oligodendrocytes (De Biase et al. 2010; Kukley et al. 2010).

A different way to test for the presence of synaptic input onto a given cell is to record this cell and use extracellular stimulation to synchronously induce action potentials in a large number of nearby axons. After an action potential arrives at a presynaptic terminal membrane depolarization causes rapid and brief opening of voltage-gated Ca^{2+} channels. The localization of Ca^{2+} channels at active zones provides a high, local rise in the Ca^{2+} concentration more than a thousand-fold (to $\sim$ 100 μM) within a few hundred microseconds at the site of transmitter release. This large and rapid local increase is required for the rapid synchronous release of neurotransmitter. When axons were stimulated electrically during recording of an NG2 cell, a robust synchronous compound response to the release of hundreds of synaptic vesicles could be observed in the NG2 cell (Fig. 4a, c; Kukley et al. 2010; see also Bergles et al. 2000). Synaptic response in the NG2 cell appeared with a brief

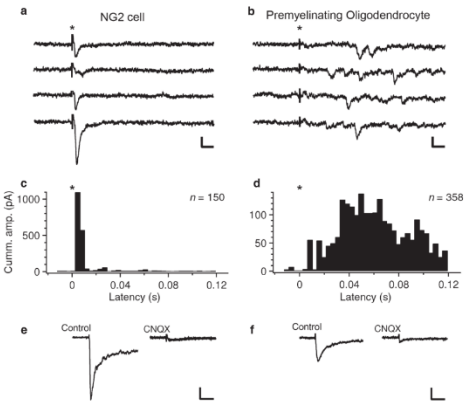

Fig. 4 Synaptic signalling and AMPA/kainate receptor expression is downregulated upon differentiation of NG2 cells. (a,b) Four successive sweeps recorded in an NG2 cell (a) and in a premyelinating oligodendrocyte (b) in response to extracellular electrical stimulation of nearby axons in the presence of 25 μM APV and 10 μM bicuculline (the time point of stimulation is indicated by an asterisk). The holding potential is −80 mV. Synaptic responses in the NG2 cell appear with a brief latency following electrical stimulation, steeply increase to a sharp peak and then rapidly decay back to baseline (a). In a premyelinating oligodendrocyte, synchronous responses briefly after the stimulus are absent; however, there are individual release events appearing late after the stimulation and continuing for hundreds of milliseconds (b). Scale bars: 10 ms, 10 pA. (c,d) Histograms summarize the latency of synaptic currents recorded in three NG2 cells (150 events) and in five premyelinating oligodendrocytes (358 events). The cumulative peak amplitude was calculated for each latency by summing current amplitudes of all events falling into the same latency bin (bin width is 3.75 ms). The asterisks mark the time point of stimulation. (e,f) Whole-cell current responses of an NG2 cell (e) and a premyelinating oligodendrocyte (f) to glutamate un-caging, in the absence (left) or presence (right) of AMPA/kainate receptor antagonist CNQX (30 μM). The holding potential is −80 mV. The current amplitude is smaller in the premyelinating cells compared with NG2 cells. Pre-application of CNQX strongly reduces current response. Scale bar: 20 ms, 20 pA. (A–F) Modified with permission from Kukley et al. (2010).

latency (< 5 ms) following electrical stimulation, steeply increased to a sharp peak (20–80% rise time is < 1 ms) and then rapidly decayed back to baseline (decay time constant is about 2–4 ms; Fig. 4a,c). In contrast to NG2 cells, it was not possible to elicit any synchronous synaptic responses in the mature myelinating oligodendrocytes as well as in the majority of premyelinating oligodendrocytes (Fig. 4b,d). However, in ~ 30% of premyelinating oligodendrocytes small asynchronous responses could be recorded upon electrical stimulation (Fig. 4b,d). Those individual release events typically started to appear as late as 20 ms after the presynaptic stimulation and continued for hundreds of milliseconds (Fig. 4b,d; Kukley et al. 2010). Taken together, during electrical stimulation of axons the dominant component of the synaptic response in an NG2 cell is attributable to phasic neurotransmitter release. In a premyelinating cell only late release events caused by delayed asynchronous release are detected. No synaptic events mediated by release of single neurotransmitter-filled vesicles can be identified in myelinating oligodendrocytes. At neuronal synapses, and probably at neuron–glia synapses as well, phasic neurotransmitter release is driven by a brief strong increase in presynaptic calcium concentration (10–100 μM) local to the calcium channel pore (Heidelberger et al. 1994; Xu-Friedman & Regehr, 2000). Experimentally slowing and reducing the calcium signal seen by the calcium sensor or removing important components of the presynaptic release machinery leads to the appearance of asynchronous synaptic currents and dramatically reduces synchronous transmitter release (Schneggenburger & Neher, 2000; Xu-Friedman & Regehr, 2000; Sun et al. 2007). It is plausible that the asynchronous synaptic currents encountered in some premyelinating oligodendrocytes represent the residual and transient function of the presynaptic release machinery that is in the process of being disassembled.

Notably, recent experimental evidence suggests that also during the re-myelination process in mouse, corpus callosum axonal glutamatergic synapses contact NG2-positive cells (Etxeberria et al. 2010). Similar to the situation in the healthy brain, synaptic connectivity appears to be lost

during differentiation of NG2 cells into mature oligodendrocytes (Etxeberria et al. 2010). The authors suggest that reduction in glutamatergic activity may be necessary for NG2 cells to differentiate into oligodendrocytes, as predicted by the inhibitory influence of glutamate on the differentiation of OPCs (Gallo et al. 1996; Yuan et al. 1998).

Is the loss of synaptic signalling accompanied by changes in surface glutamate receptors during differentiation of NG2 cells? One way to address this question is to investigate the current response of oligodendrocyte lineage cells to the application of glutamate. Recent evidence demonstrates that upon fast application of glutamate by mean of fast photolysis of glutamate (un-caging), NG2 cells and premyelinating oligodendrocytes show clear responses that are prevented by AMPA/kainate receptor antagonists, however, the amplitude of those responses is $\sim$ two–three times smaller in the premyelinating cells compared with NG2 cells (Fig. 4e,f; De Biase et al. 2010; Kukley et al. 2010). Interestingly, the amplitude of AMPA/kainate receptor-mediated current decreases further as premyelinating cells differentiate into mature oligodendrocytes (De Biase et al. 2010; Kukley et al. 2010).

AMPA receptors are not expressed uniformly over the surface of NG2 cells, but rather are clustered into discrete patches along their processes (Bergles et al. 2010). Recently freeze-fracture immunolabelling of brain tissue from transgenic mice in which NG2 cells can be clearly identified through labelling with anti-GFP antibodies has been performed (Bergles et al. 2010). Preliminary results of these experiments showed clusters of AMPA receptor-immunoreactive intra-membrane particles along NG2 cells processes (Bergles et al. 2010). Also, functional mapping of AMPA receptors using two-photon un-caging of MNI-L-glutamate has shown the presence of 'hot spots' along NG2 cell processes where AMPA receptors are enriched (Bergles et al. 2010). These 'hot spots' of AMPA receptors may represent receptors that are accumulated to form functional microdomains opposite the presynaptic glutamatergic terminal boutons that release neurotransmitters. Synaptic clustering of glial neurotransmitter receptors into microdomains could, in analogy to neurons, be crucial for efficient signal transduction. The NG2 proteoglycan has been suggested to play an important role in clustering the glial AMPA receptors towards the site of neuronal glutamate release (Stegmuller et al. 2003; Trotter et al. 2010). NG2 proteoglycan is indirectly associated with the AMPA receptors of NG2-expressing cells as a result of molecular linkage with glutamate receptor interaction protein via a PDZ domain-mediated interaction (Stegmuller et al. 2003). Interestingly, the NG2 proteoglycan is expressed by OPCs but downregulated upon differentiation of the cells into premyelinating oligodendrocytes, which also show lower surface expression of AMPA receptors (Levine et al. 1993; Dawson et al. 2000). Thus, it is possible that downregulation of NG2 proteoglycan contributes to a disruption of postsynaptic AMPA receptor clusters and subsequent removal of AMPA receptors from the postsynaptic glial membrane.

Loss of synaptic signalling and decrease in the number of AMPA receptors upon differentiation of NG2 cells is accompanied by a downregulation of voltage-gated sodium and potassium channels, as demonstrated by electrophysiological experiments (De Biase et al. 2010; Kukley et al. 2010). In accordance with the physiological studies, mRNAs encoding most principal CNS NaV channel subunits (Scn1a, Scn2a1, Scn3a) are significantly lower in mature oligodendrocytes compared with NG2 cells (De Biase et al. 2010).

In summary, as NG2 cells differentiate down an oligodendrocyte lineage dramatic changes in synaptic input occur with the altered expression pattern of neurotransmitter receptors and voltage-gated ion channels on NG2 cells; those changes reflect a rapid decrease in the expression of ion channel and AMPA receptor genes.

Conclusions

NG2 cells are widespread in the grey and white matter of the CNS and, depending on the region they comprise, 2–9% of the total cell population (Dawson et al. 2003). These cells are intriguing because, on one hand they exhibit properties of immature progenitor cells, while on the other hand they show features of differentiated cells that can perhaps perform some essential physiological role on their own. NG2 cells are considered precursor cells because they are able to divide and migrate; during development many NG2 cells evolve into the myelinating oligodendrocytes. Unlike precursor cells, however, NG2 cells show complex ramified morphology, express different types of voltage-gated ion channels, neurotransmitter receptors and receive synaptic input from neurons. The fact that NG2 cells keep cellular processes and synaptic junctions with neurons during cytokinesis and pass them onto the daughter cells indicates that directly from birth NG2 cells are integrated into the complex neuronal circuitry of the CNS. Upon differentiation NG2 cells loose synapses with neurons, so neuronal input in the form of a functional synapse is most likely important exclusively for NG2 cells and not for more mature cells of the oligodendrocyte lineage. The functional role of synaptic input onto NG2 cells remains to be discovered. This is especially exciting if we consider that the total number of NG2 cells within the entire cell population (Dawson et al. 2003) roughly equals the entire number of neurons in the adult brain (2–10% of all cells), and that the total length of processes of an NG2 cell (about 1250 μm) is not much smaller than the total length of the dendritic tree of some neurons (Benavides-Piccione et al. 2006). Those facts indicate that, if the probability of establishing a neuron–neuron or a neuron–glia synapse is the same, the overall number of synaptic contacts that a given neuron receives from other neurons might be only slightly larger than the amount of synapses that a given NG2 glial cell receives from neurons

(at least in some brain areas) and, thus, point to the importance of neuron–glia synapses in the brain. Synaptic input from neurons onto NG2 cells also raises the question whether NG2 cells possess any output signalling, for example release neurotransmitters and/or other molecules that may influence behaviour of neighbouring cells or intercellular communication.

Acknowledgements

We thank Vittorio Gallo (Center for Neuroscience Research, Children's National Medical Center, Washington, USA), Akiko Nishiyama (Department of Physiology and Neurobiology, University of Connecticut, Storrs, USA) and Charles J. Gilbride (Centre for Integrative Neuroscience, University of Tübingen, Germany) for their helpful discussions during the writing of this manuscript. The authors are supported by the Centre for Integrative Neuroscience (Deutsche Forschungsgemeinschaft, EXC 307). NF is supported by the Christiane Nüsslein-Volhard Foundation.

References

Aguirre A, Gallo V (2004) Postnatal neurogenesis and gliogenesis in the olfactory bulb from NG2-expressing progenitors of the subventricular zone. *J Neurosci* **24**, 10 530–10 541.

Aguirre AA, Chittajallu R, Belachew S, et al. (2004) NG2-expressing cells in the subventricular zone are type C-like cells and contribute to interneuron generation in the postnatal hippocampus. *J Cell Biol* **165**, 575–589.

Alonso G (2000) Prolonged corticosterone treatment of adult rats inhibits the proliferation of oligodendrocyte progenitors present throughout white and gray matter regions of the brain. *Glia* **31**, 219–231.

Barres BA, Koroshetz WJ, Swartz KJ, et al. (1990) Ion channel expression by white matter glia: the O-2A glial progenitor cell. *Neuron* **4**, 507–524.

Belachew S, Chittajallu R, Aguirre AA, et al. (2003) Postnatal NG2 proteoglycan-expressing progenitor cells are intrinsically multipotent and generate functional neurons. *J Cell Biol* **161**, 169–186.

Benavides-Piccione R, Hamzei-Sichani F, Ballesteros-Yanez I, et al. (2006) Dendritic size of pyramidal neurons differs among mouse cortical regions. *Cereb Cortex* **16**, 990–1001.

Berger T (1995) AMPA-type glutamate receptors in glial precursor cells of the rat corpus callosum: ionic and pharmacological properties. *Glia* **14**, 101–114.

Berger T, Walz W, Schnitzer J, et al. (1992) GABA- and glutamate-activated currents in glial cells of the mouse corpus callosum slice. *J Neurosci Res* **31**, 21–27.

Bergles DE, Roberts JD, Somogyi P, et al. (2000) Glutamatergic synapses on oligodendrocyte precursor cells in the hippocampus. *Nature* **405**, 187–191.

Bergles DE, Jabs R, Steinhauser C (2010) Neuron–glia synapses in the brain. *Brain Res Rev* **63**, 130–137.

Berry M, Hubbard P, Butt AM (2002) Cytology and lineage of NG2-positive glia. *J Neurocytol* **31**, 457–467.

Boucsein C, Zacharias R, Farber K, et al. (2003) Purinergic receptors on microglial cells: functional expression in acute brain slices and modulation of microglial activation in vitro. *Eur J Neurosci* **17**, 2267–2276.

Butt AM, Duncan A, Hornby MF, et al. (1999) Cells expressing the NG2 antigen contact nodes of Ranvier in adult CNS white matter. *Glia* **26**, 84–91.

Butt AM, Pugh M, Hubbard P, et al. (2004) Functions of optic nerve glia: axoglial signalling in physiology and pathology. *Eye* **18**, 1110–1121.

Chatterjee N, Stegmuller J, Schatzle P, et al. (2008) Interaction of syntenin-1 and the NG2 proteoglycan in migratory oligodendrocyte precursor cells. *J Biol Chem* **283**, 8310–8317.

Chittajallu R, Chen Y, Wang H, et al. (2002) Regulation of Kv1 subunit expression in oligodendrocyte progenitor cells and their role in G1/S phase progression of the cell cycle. *Proc Natl Acad Sci USA* **99**, 2350–2355.

Chittajallu R, Aguirre A, Gallo V (2004) NG2-positive cells in the mouse white and grey matter display distinct physiological properties. *J Physiol* **561**, 109–122.

Davalos D, Grutzendler J, Yang G, et al. (2005) ATP mediates rapid microglial response to local brain injury in vivo. *Nat Neurosci* **8**, 752–758.

Dawson MR, Levine JM, Reynolds R (2000) NG2-expressing cells in the central nervous system: are they oligodendroglial progenitors? *J Neurosci Res* **61**, 471–479.

Dawson MR, Polito A, Levine JM, et al. (2003) NG2-expressing glial progenitor cells: an abundant and widespread population of cycling cells in the adult rat CNS. *Mol Cell Neurosci* **24**, 476–488.

Dayer AG, Cleaver KM, Abouantoun T, et al. (2005) New GABAergic interneurons in the adult neocortex and striatum are generated from different precursors. *J Cell Biol* **168**, 415–427.

De Biase LM, Nishiyama A, Bergles DE (2010) Excitability and synaptic communication within the oligodendrocyte lineage. *J Neurosci* **30**, 3600–3611.

Dimou L, Simon C, Kirchhoff F, et al. (2008) Progeny of Olig2-expressing progenitors in the gray and white matter of the adult mouse cerebral cortex. *J Neurosci* **28**, 10 434–10 442.

Dore-Duffy P, Katychev A, Wang X, et al. (2006) CNS microvascular pericytes exhibit multipotential stem cell activity. *J Cereb Blood Flow Metab* **26**, 613–624.

Dowling JE (1987) *The Retina: an Approachable Part of the Brain*. Cambridge, Mass, Belknap Press of Harvard University Press.

Eaton BA, Davis GW (2003) Synapse disassembly. *Genes Dev* **17**, 2075–2082.

Etxeberria A, Mangin JM, Aguirre A, et al. (2010) Adult-born SVZ progenitors receive transient synapses during remyelination in corpus callosum. *Nat Neurosci* **13**, 287–289.

Friedman HV, Bresler T, Garner CC, et al. (2000) Assembly of new individual excitatory synapses: time course and temporal order of synaptic molecule recruitment. *Neuron* **27**, 57–69.

Gallo V, Zhou JM, McBain CJ, et al. (1996) Oligodendrocyte progenitor cell proliferation and lineage progression are regulated by glutamate receptor-mediated K+ channel block. *J Neurosci* **16**, 2659–2670.

Gallo V, Mangin JM, Kukley M, et al. (2008) Synapses on NG2-expressing progenitors in the brain: multiple functions? *J Physiol* **586**, 3767–3781.

Ge WP, Zhou W, Luo Q, et al. (2009) Dividing glial cells maintain differentiated properties including complex morphology and functional synapses. *Proc Natl Acad Sci USA* **106**, 328–333.

Geha S, Pallud J, Junier MP, et al. (2010) NG2+/Olig2+ cells are the major cycle-related cell population of the adult human normal brain. *Brain Pathol* **20**, 399–411.

Ghiani CA, Yuan X, Eisen AM, et al. (1999) Voltage-activated K+ channels and membrane depolarization regulate accumulation of the cyclin-dependent kinase inhibitors p27(Kip1) and p21(CIP1) in glial progenitor cells. *J Neurosci* **19**, 5380–5392.

Gilbert P, Kettenmann H, Schachner M (1984) Gamma-aminobutyric acid directly depolarizes cultured oligodendrocytes. *J Neurosci* **4**, 561–569.

Goda Y, Davis GW (2003) Mechanisms of synapse assembly and disassembly. *Neuron* **40**, 243–264.

Guo F, Ma J, McCauley E, et al. (2009) Early postnatal proteolipid promoter-expressing progenitors produce multilineage cells in vivo. *J Neurosci* **29**, 7256–7270.

Guo F, Maeda Y, Ma J, et al. (2010) Pyramidal neurons are generated from oligodendroglial progenitor cells in adult piriform cortex. *J Neurosci* **30**, 12 036–12 049.

Hamilton N, Vayro S, Wigley R, et al. (2010) Axons and astrocytes release ATP and glutamate to evoke calcium signals in NG2-glia. *Glia* **58**, 66–79.

Heidelberger R, Heinemann C, Neher E, et al. (1994) Calcium dependence of the rate of exocytosis in a synaptic terminal. *Nature* **371**, 513–515.

Hirbec H, Perestenko O, Nishimune A, et al. (2002) The PDZ proteins PICK1, GRIP, and syntenin bind multiple glutamate receptor subtypes: analysis of PDZ binding motifs. *J Biol Chem* **277**, 15 221–15 224.

Hirbec H, Martin S, Henley JM (2005) Syntenin is involved in the developmental regulation of neuronal membrane architecture. *Mol Cell Neurosci* **28**, 737–746.

Horner PJ, Power AE, Kempermann G, et al. (2000) Proliferation and differentiation of progenitor cells throughout the intact adult rat spinal cord. *J Neurosci* **20**, 2218–2228.

Horner PJ, Thallmair M, Gage FH (2002) Defining the NG2-expressing cell of the adult CNS. *J Neurocytol* **31**, 469–480.

Jabs R, Pivneva T, Huttmann K, et al. (2005) Synaptic transmission onto hippocampal glial cells with hGFAP promoter activity. *J Cell Sci* **118**, 3791–3803.

Kandel ER, Schwartz JH, Jessell TM (2000) *Principles of Neural Science*. New York: McGraw-Hill.

Kang SH, Fukaya M, Yang JK, et al. (2010) NG2+ CNS glial progenitors remain committed to the oligodendrocyte lineage in postnatal life and following neurodegeneration. *Neuron* **68**, 668–681.

Karadottir R, Attwell D (2007) Neurotransmitter receptors in the life and death of oligodendrocytes. *Neuroscience* **145**, 1426–1438.

Karadottir R, Cavelier P, Bergersen LH, et al. (2005) NMDA receptors are expressed in oligodendrocytes and activated in ischaemia. *Nature* **438**, 1162–1166.

Karadottir R, Hamilton NB, Bakiri Y, et al. (2008) Spiking and nonspiking classes of oligodendrocyte precursor glia in CNS white matter. *Nat Neurosci* **11**, 450–456.

Kessaris N, Fogarty M, Iannarelli P, et al. (2006) Competing waves of oligodendrocytes in the forebrain and postnatal elimination of an embryonic lineage. *Nat Neurosci* **9**, 173–179.

Kettenmann H, Gilbert P, Schachner M (1984) Depolarization of cultured oligodendrocytes by glutamate and GABA. *Neurosci Lett* **47**, 271–276.

Kirby BB, Takada N, Latimer AJ, et al. (2006) In vivo time-lapse imaging shows dynamic oligodendrocyte progenitor behavior during zebrafish development. *Nat Neurosci* **9**, 1506–1511.

Knutson P, Ghiani CA, Zhou JM, et al. (1997) K+ channel expression and cell proliferation are regulated by intracellular sodium and membrane depolarization in oligodendrocyte progenitor cells. *J Neurosci* **17**, 2669–2682.

Kukley M, Capetillo-Zarate E, Dietrich D (2007) Vesicular glutamate release from axons in white matter. *Nat Neurosci* **10**, 311–320.

Kukley M, Kiladze M, Tognatta R, et al. (2008) Glial cells are born with synapses. *FASEB J* **22**, 2957–2969.

Kukley M, Nishiyama A, Dietrich D (2010) The fate of synaptic input to NG2 glial cells: neurons specifically downregulate transmitter release onto differentiating oligodendroglial cells. *J Neurosci* **30**, 8320–8331.

Lasiene J, Matsui A, Sawa Y, et al. (2009) Age-related myelin dynamics revealed by increased oligodendrogenesis and short internodes. *Aging Cell* **8**, 201–213.

Levine JM, Card JP (1987) Light and electron microscopic localization of a cell surface antigen (NG2) in the rat cerebellum: association with smooth protoplasmic astrocytes. *J Neurosci* **7**, 2711–2720.

Levine JM, Stincone F, Lee YS (1993) Development and differentiation of glial precursor cells in the rat cerebellum. *Glia* **7**, 307–321.

Levison SW, Young GM, Goldman JE (1999) Cycling cells in the adult rat neocortex preferentially generate oligodendroglia. *J Neurosci Res* **57**, 435–446.

Lin SC, Bergles DE (2002) Physiological characteristics of NG2-expressing glial cells. *J Neurocytol* **31**, 537–549.

Lin SC, Bergles DE (2004a) Synaptic signaling between GABAergic interneurons and oligodendrocyte precursor cells in the hippocampus. *Nat Neurosci* **7**, 24–32.

Lin SC, Bergles DE (2004b) Synaptic signaling between neurons and glia. *Glia* **47**, 290–298.

Lin SC, Huck JH, Roberts JD, et al. (2005) Climbing fiber innervation of NG2-expressing glia in the mammalian cerebellum. *Neuron* **46**, 773–785.

Maldonado PP, Velez-Fort M, Angulo MC (2011) Is neuronal communication with NG2 cells synaptic or extrasynaptic? *J Anat*, doi: 10.1111/j.1469-7580.2011.01350.x.

Mori T, Wakabayashi T, Takamori Y, et al. (2009) Phenotype analysis and quantification of proliferating cells in the cortical gray matter of the adult rat. *Acta Histochem Cytochem* **42**, 1–8.

Muller J, Reyes-Haro D, Pivneva T, et al. (2009) The principal neurons of the medial nucleus of the trapezoid body and NG2(+) glial cells receive coordinated excitatory synaptic input. *J Gen Physiol* **134**, 115–127.

Nimmerjahn A, Kirchhoff F, Helmchen F (2005) Resting microglial cells are highly dynamic surveillants of brain parenchyma in vivo. *Science* **308**, 1314–1318.

Nishiyama A, Lin XH, Giese N, et al. (1996) Co-localization of NG2 proteoglycan and PDGF alpha-receptor on O2A progenitor cells in the developing rat brain. *J Neurosci Res* **43**, 299–314.

Nishiyama A, Yu M, Drazba JA, et al. (1997) Normal and reactive NG2+ glial cells are distinct from resting and activated microglia. *J Neurosci Res* **48**, 299–312.

Nishiyama A, Watanabe M, Yang Z, et al. (2002) Identity, distribution, and development of polydendrocytes: NG2-expressing glial cells. *J Neurocytol* **31**, 437–455.

Nishiyama A, Yang Z, Butt A (2005) Astrocytes and NG2-glia: what's in a name? *J Anat*, **207**, 687–693.

Nishiyama A, Komitova M, Suzuki R, et al. (2009) Polydendrocytes (NG2 cells): multifunctional cells with lineage plasticity. *Nat Rev Neurosci* **10**, 9–22.

Ozerdem U, Grako KA, Dahlin-Huppe K, et al. (2001) NG2 proteoglycan is expressed exclusively by mural cells during vascular morphogenesis. *Dev Dyn* **222**, 218–227.

Panagiotakos G, Alshamy G, Chan B, et al. (2007) Long-term impact of radiation on the stem cell and oligodendrocyte precursors in the brain. *PLoS ONE* **2**, e588.

Parri HR, Gould TM, Crunelli V (2010) Sensory and cortical activation of distinct glial cell subtypes in the somatosensory thalamus of young rats. *Eur J Neurosci* **32**, 29–40.

Polito A, Reynolds R (2005) NG2-expressing cells as oligodendrocyte progenitors in the normal and demyelinated adult central nervous system. *J Anat* **207**, 707–716.

Psachoulia K, Jamen F, Young KM, et al. (2009) Cell cycle dynamics of NG2 cells in the postnatal and ageing brain. *Neuron Glia Biol* **5**, 57–67.

Raastad M, Storm JF, Andersen P (1992) Putative single quantum and single fibre excitatory postsynaptic currents show similar amplitude range and variability in rat hippocampal slices. *Eur J Neurosci* **4**, 113–117.

Reimann F, Ashcroft FM (1999) Inwardly rectifying potassium channels. *Curr Opin Cell Biol* **11**, 503–508.

Rivers LE, Young KM, Rizzi M, et al. (2008) PDGFRA/NG2 glia generate myelinating oligodendrocytes and piriform projection neurons in adult mice. *Nat Neurosci* **11**, 1392–1401.

Rosenmund C, Stevens CF (1996) Definition of the readily releasable pool of vesicles at hippocampal synapses. *Neuron* **16**, 1197–1207.

Schneggenburger R, Neher E (2000) Intracellular calcium dependence of transmitter release rates at a fast central synapse. *Nature* **406**, 889–893.

Shen K, Cowan CW (2010) Guidance molecules in synapse formation and plasticity. *Cold Spring Harb Perspect Biol* **2**, a001842.

Sheng M, Sala C (2001) PDZ domains and the organization of supramolecular complexes. *Annu Rev Neurosci* **24**, 1–29.

Sommer I, Schachner M (1981) Monoclonal antibodies (O1 to O4) to oligodendrocyte cell surfaces: an immunocytological study in the central nervous system. *Dev Biol* **83**, 311–327.

Squire LR, Bloom FE, McConnell SK, et al. (2003) *Fundamental Neuroscience*. USA: Academic Press.

Stallcup WB, Beasley L (1987) Bipotential glial precursor cells of the optic nerve express the NG2 proteoglycan. *J Neurosci* **7**, 2737–2744.

Stegmuller J, Werner H, Nave KA, et al. (2003) The proteoglycan NG2 is complexed with alpha-amino-3-hydroxy-5-methyl-4-isoxazolepropionic acid (AMPA) receptors by the PDZ glutamate receptor interaction protein (GRIP) in glial progenitor cells: implications for glial-neuronal signaling. *J Biol Chem* **278**, 3590–3598.

Steinhauser C, Jabs R, Kettenmann H (1994) Properties of GABA and glutamate responses in identified glial cells of the mouse hippocampal slice. *Hippocampus* **4**, 19–35.

Sun J, Pang ZP, Qin D, et al. (2007) A dual-Ca2+-sensor model for neurotransmitter release in a central synapse. *Nature* **450**, 676–682.

Tamura Y, Kataoka Y, Cui Y, et al. (2007) Multi-directional differentiation of doublecortin- and NG2-immunopositive progenitor cells in the adult rat neocortex in vivo. *Eur J Neurosci* **25**, 3489–3498.

Tekki-Kessaris N, Woodruff R, Hall AC, et al. (2001) Hedgehog-dependent oligodendrocyte lineage specification in the telencephalon. *Development* **128**, 2545–2554.

Tong XP, Li XY, Zhou B, et al. (2009) Ca(2+) signaling evoked by activation of Na(+) channels and Na(+)/Ca(2+) exchangers is required for GABA-induced NG2 cell migration. *J Cell Biol* **186**, 113–128.

Trapp BD, Nishiyama A, Cheng D, et al. (1997) Differentiation and death of premyelinating oligodendrocytes in developing rodent brain. *J Cell Biol* **137**, 459–468.

Trotter J, Karram K, Nishiyama A (2010) NG2 cells: properties, progeny and origin. *Brain Res Rev* **63**, 72–82.

Trudeau LE, Doyle RT, Emery DG, et al. (1996) Calcium-independent activation of the secretory apparatus by ruthenium red in hippocampal neurons: a new tool to assess modulation of presynaptic function. *J Neurosci* **16**, 46–54.

Usowicz MM, Gallo V, Cull-Candy SG (1989) Multiple conductance channels in type-2 cerebellar astrocytes activated by excitatory amino acids. *Nature* **339**, 380–383.

Vautier F, Belachew S, Chittajallu R, et al. (2004) Shaker-type potassium channel subunits differentially control oligodendrocyte progenitor proliferation. *Glia* **48**, 337–345.

Velez-Fort M, Audinat E, Angulo MC (2009) Functional alpha 7-containing nicotinic receptors of NG2-expressing cells in the hippocampus. *Glia* **57**, 1104–1114.

Velez-Fort M, Maldonado PP, Butt AM, et al. (2010) Postnatal switch from synaptic to extrasynaptic transmission between interneurons and NG2 cells. *J Neurosci* **30**, 6921–6929.

Wigley R, Butt AM (2009) Integration of NG2-glia (synantocytes) into the neuroglial network. *Neuron Glia Biol* **5**, 21–28.

Xu-Friedman MA, Regehr WG (2000) Probing fundamental aspects of synaptic transmission with strontium. *J Neurosci* **20**, 4414–4422.

Yuan X, Eisen AM, McBain CJ, et al. (1998) A role for glutamate and its receptors in the regulation of oligodendrocyte development in cerebellar tissue slices. *Development* **125**, 2901–2914.

Zhou M, Schools GP, Kimelberg HK (2006) Development of GLAST(+) astrocytes and NG2(+) glia in rat hippocampus CA1: mature astrocytes are electrophysiologically passive. *J Neurophysiol* **95**, 134–143.

Zhu X, Bergles DE, Nishiyama A (2008a) NG2 cells generate both oligodendrocytes and gray matter astrocytes. *Development* **135**, 145–157.

Zhu X, Hill RA, Nishiyama A (2008b) NG2 cells generate oligodendrocytes and gray matter astrocytes in the spinal cord. *Neuron Glia Biol* **4**, 19–26.

Zhu X, Hill RA, Dietrich D, et al. (2011) Age-dependent fate and lineage restriction of single NG2 cells. *Development* **138**, 745–753.

Ziskin JL, Nishiyama A, Rubio M, et al. (2007) Vesicular release of glutamate from unmyelinated axons in white matter. *Nat Neurosci* **10**, 321–330.

IV. Acknowledgments

First of all I would like to thank my doctoral supervisor, Maria Kukley, for continuous scientific and personal support. I learned a lot about science and myself from you.
The years spent in Tübingen would have been much less fun and bearable without the many wonderful people I got to know. Guo Da, Katja, Hartwig, Flavia, Marco, Cris, Irene, Cora, Saad (and I hope I did not forget anyone…): you were not just colleagues, but also fantastic friends, for which I am very grateful. I'd like to thank especially the members of the Neuron – Glia Interaction Group, Anahit, Bartosz, Charlie, Friederike, Nicole, Ruxandra, Ting-Jiun, for all the fruitful scientific and not-so-scientific discussions we had over the years. I'd like highlight Daniela's excellent technical assistance – without you, the lab would have been much messier.
I would also like to express my gratitude to my family – my parents, brother, grandparents, cousins – for supporting me throughout this experience, no matter how seldom we could be together because I was being over-busy. Thank you for tolerating this (and me).
And lastly, but most importantly, I would like to thank my wife, Krisztina, for always believing in me, and being there for me, through rough times and fun times.